Towards a Greener Future: Sustainable Membrane Fabrication for Wastewater Treatment

by

Md Mizanul Haque Mizan

A thesis submitted in partial fulfillment of the requirements for the degree of

Doctor of Philosophy

Department of Mechanical Engineering
University of Alberta

Abstract

Large-scale membrane technology has seen significant growth over the past 40 years. Despite its advancements, the industry lacks sustainability and cannot be considered entirely environmentally friendly. Membrane manufacturing primarily depends on nonbiodegradable petroleum-based polymers and hazardous solvents. These materials contribute to the energy crisis, pose disposal challenges and present risks to human health and the environment. Given the increasing energy crisis and environmental pollution concerns, the eco-friendly transformation of this engineering sector is imperative. Consequently, there is growing interest in utilizing bio-based polymers to enhance sustainability in membrane fabrication, with a particular focus on biodegradable materials. In the realm of sustainable and green chemistry, the exploration of greener alternative solvents is underway for membrane fabrication. This PhD research aims to develop a more sustainable approach for producing high-performance membranes using biodegradable materials and green solvents.

The first part of the study focused on developing high-performance poly (sodium 4-styrene sulfonate) (PSS) and polyethyleneimine (PEI) based polyelectrolyte complex membranes using an organic solvent-free aqueous phase separation (APS) process. This work aimed to enhance the pure water permeability (PWP) of the membrane, which is a primary concern for APS-based membranes. In order to achieve this goal, two key parameters—monomer mixing ratio and casting solution temperature—were varied. The results showed that nanofiltration and ultrafiltration membranes with different molecular weight cut-off values could be obtained by controlling these parameters. Optimal PSS/PEI monomer mixing ratios of 1:1.65 and 1:1.70 produced nanofiltration membranes with high pure water permeability and excellent divalent salt retention. On the other hand, PSS/PEI monomer ratios of 1:1.75 and 1:1.80 led to ultrafiltration membranes with high BSA retention and increased PWP. The casting solution temperature was found to be a crucial parameter in controlling the phase separation kinetics, resulting in membranes with different pore sizes and permeabilities. The increase in casting solution temperature from 25 to 60°C resulted in ultrafiltration membranes with high BSA retention and increased PWP.

In the second part, an eco-friendly and biodegradable electrospun membrane was fabricated using the electrospinning technique. The goal of this study was to enhance the sustainability of the membrane fabrication process by utilizing biodegradable materials and non-toxic green solvents. This was achieved by using biodegradable polycaprolactone (PCL) and sulfonated kraft lignin (SKL) blend as the membrane material. Additionally, using acetic acid as a benign solvent for preparing the PCL/SKL electrospun membrane prevented secondary pollution and contributed to the overall green approach. The influence of SKL content on the surface morphology, chemical composition, and mechanical properties of the electrospun membrane was studied in detail. Membranes modified with SKL exhibited superhydrophilicity and underwater superoleophobicity, with water contact angles of 0° and underwater oil contact angles over 150°. These membranes demonstrated high pure water flux (800-900 LMH) and effective emulsion flux during gravity-driven filtration, with superior anti-oil-fouling performance. Moreover, the SKL-modified membrane showed consistent performance after several cycles and maintained stability across a wide pH range.

The last part of this research presents a facile and scalable method for fabricating a green and biodegradable PCL/SKL-based ultrafiltration membrane using a nonsolvent-induced phase separation approach. The study examined the impact of SKL content within the PCL matrix using various characterization techniques and evaluated the dye/salt separation performance of the prepared membranes. This is the first exploration of SKL and PCL as compatible materials for preparing biodegradable phase inversion membranes using acetic acid as a green solvent. The proposed method ensures simplicity and scalability in the membrane fabrication process.

The overall findings of this PhD research contribute significantly to advancing sustainability in membrane fabrication processes, offering insights into developing high-performance, eco-friendly membranes with potential applications across various fields.

Keywords: Membrane separation; Sustainable membrane fabrication; Phase separation; Electrospinning; Biopolymeric membranes; Lignin; Biodegradability; Polycaprolactone; Polyelectrolytes; Green Solvents; Fouling resistance

Preface

This dissertation is the original work by Md Mizanul Haque Mizan. The majority of the content in chapters 1, 2, 3, 4, and 5 were published in the following journals and book chapters:

1. **Md.M.H. Mizan,** M. Rastgar, S.A. Aktij, A. Asad, P. Karami, A. Rahimpour, Mohtada Sadrzadeh, Organic solvent-free polyelectrolyte complex membrane preparation: Effect of monomer mixing ratio and casting solution temperature, Published in Journal of Membrane Science, 2023, 668, 121197.
2. **Md.M.H. Mizan**, P. M. Gurave, M. Rastgar, A. Rahimpour, R.K. Srivastava, Mohtada Sadrzadeh, "Biomass to Membrane": Sulfonated Kraft Lignin/PCL Superhydrophilic Electrospun Membrane for Gravity-Driven Oil-in-Water Emulsion Separation, Published in ACS Applied Material & Interfaces, 2023, 15, 35, 41961-41976.
3. **Md.M.H. Mizan**, M. Rastgar, H. Sultana, Mohtada Sadrzadeh, Green polycaprolactone/sulfonated kraft lignin phase inversion membrane for dye/salt separation, Published in Journal of Membrane Science, 2024, 702, 122806.
4. **Md.M.H. Mizan**, F.R. Omi, H. Sultana, Mohtada Sadrzadeh, Bio-sourced and biodegradable materials for membrane fabrication, (Chapter 7 in Green membrane technologies toward environmental sustainability), 2023, Elsevier.
5. **Md.M.H. Mizan**, F. Seyedpour, Mohtada Sadrzadeh, Exploring biomimetic membranes: applications and challenges, (Chapter 5 in Green membrane technologies toward environmental sustainability), 2023, Elsevier.

DEDICATED TO MY PARENTS

SUFIA BEGUM AND MD ABDUL JALIL

FOR YOUR ENDLESS LOVE

LOVE YOU!

Acknowledgement

Completing this Ph.D. thesis has been a journey of immense personal and professional growth, and I am deeply indebted to many individuals who have supported and guided me throughout this process.

First and foremost, I would like to express my deepest gratitude to my supervisor, Dr. Mohtada Sadrzadeh. I am deeply thankful to Dr. Sadrzadeh for offering me the opportunity to pursue a PhD under his supervision in 2021. Your unwavering support, insightful guidance, and invaluable expertise have been the cornerstone of this research. Your patience and encouragement have helped me navigate the complexities of this study and have inspired me to strive for excellence. I extend my sincere thanks to the members of my dissertation committee, Dr. Cagri Ayranci and Dr. Marc Secanell Gallart. My sincere gratitude to Dr. Ahmad Rahimpour and Dr. Masoud Rastgar for the time and effort you invested in reviewing my work and for your invaluable suggestions.

I am also thankful to my colleagues and friends at the Advanced Water Research Laboratory (AWRL) in the Mechanical Engineering Department. The collaborative environment and intellectual discussions have contributed significantly to my academic development. Special thanks to Pooria Karami, Amirul Islam, Farah Rahman Omi, Pramod M. Gurave, Sadegh Aghapour, Asad Asad, Amirhossein Taghipour, Zahra Zandi, Amir Aghaei, Nazanin Chitgar, Fatemeh Seyedpour Taji, Kazem Moradi, Afrouz Yousefi, Elham Jashni, Aria Khalili, Mehrasa Yassari, Arura Hu, Longxin Jiang, Laleh Shamaei, Hamadia Sultana, Meng Zhou, Behnam Khorshidi, Farhan Afzal, Mahfuja Akter, Nusrat Sharmin, Taposh Saha for your camaraderie and support during the challenging times of research.

A special note of thanks goes to all the participants of this Ph.D. research. Your willingness to contribute your time and insights has been crucial to the success of this study. I sincerely appreciate your involvement and contributions.

I would like to acknowledge the financial support (Alberta Innovates Graduate Student Scholarship, AIGSS) provided by Alberta Innovates of the Alberta government, Canada. This research would not have been possible without your generous funding and support. I also

acknowledge the financial support for this research from Canada's Oil Sands Innovation Alliance (COSIA) and the Natural Sciences and Engineering Research Council of Canada (NSERC).

I owe a great deal of gratitude to my family. To my parents, Sufia and Abdul Jalil, your unconditional love, encouragement, and belief in my abilities have been my driving force. To my siblings, Masud, Reza, Samira, and Zahin, thank you for your constant support and understanding.

Finally, I would like to express my heartfelt appreciation to my beloved wife, Afia Zahin. Your unwavering support, patience, and understanding have been my anchor throughout this journey. Your belief in me and your encouragement has been instrumental in helping me persevere and complete this thesis.

To all those who have supported me in any way during this journey, whether mentioned here or not, I extend my deepest gratitude. This thesis is a testament to your collective support and belief in my capabilities.

Table of Contents

List of Tables

List of Figures

Abbreviation

AA	Acetic acid
AC	Alternating current
AFM	Atomic force microscopy
AGNIQUE AMD 3L	N,N-dimethyl lactamide
APS	Aqueous phase separation
ATR-FTIR	Attenuated total reflectance-Fourier transform infrared
BSA	Bovine serum albumin
CA	Cellulose acetate
CS	Chitosan
Cyrene^{TM}	Dihydrolevoglucosenone
DC	Direct current
DMAC	Dimethyl acetamide
DMI	Dimethyl Isobromide
DMF	Dimethyl formamide
DMSO	Dimethyl Sulfoxide
[EMIM]OAc	1-ethyl-3-methylimidazolium acetate
[EMIM]DEP	1-ethyl-3-methylimidazolium dimethylphosphate
FDR	Flux decline rate
FRR	Flux recovery ratio
HSP	Hansen solubility parameters
LBL	Layer-by-layer
LNF	Loose nanofiltration
MO	Methyl orange
MWCO	Molecular weight cut-off
NF	Nanofiltration
PAA	Poly(acrylic acid)
PAH	Poly (allylamine hydrochloride)
PBAT	Poly (butylene adipate-co-terephthalate)
PBS	Poly (butylene succinate)
PCL	Polycaprolactone

PDADMAC	Poly(diallyldimethylammonium chloride)
PDMAEMA	Poly(2-(dimethylamino)ethyl methacrylate)
PEC	Polyelectrolyte Complex
PEI	Poly(ethyleneimine)
PEs	Polyelectrolytes
PHA	Polyhydroxyalkanoate
PLA	Poly (lactic acid)
PSS	Poly-(sodium 4-styrenesulfonate)
Q4VP	Quarternized poly (4-vinylpyridine)
QVP-C2	Poly(N-ethyl-4-vinylpyridinium)
RB	Reactive black 5
RED	Relative energy difference
RR	Reactive red 120
R_o	Radius of solubility sphere
R_a	HSP distance between two molecules
R_{ir}	Irreversible fouling ratio
R_r	Reversible fouling ratio
SIPS	Solvent evaporation-induced phase separation
SKL	Sulfonated kraft lignin
TIPS	Thermally-induced phase separation
TUF	Tight ultrafiltration
UWOCA	Underwater contact angle
VIPS	Vapor-induced phase separation
WCA	Water contact angle

Nomenclature

A_m	Effective membrane surface area
C_R	concentration of retentate
C_f	Concentration of feed
C_p	Concentration of permeate
D	Diffusion coefficient of salt in bulk solution
d	Fiber diameter
ε	Porosity
ΔG_{mix}	Gibbs free energy of mixing
ΔH_{mix}	Enthalpy of mixing
J_w	Initial water flux
J_1	Flux after the first cycle
J_2	Flux after the second cycle
Mw	Molecular weight
r	Average pore size
R	Salt rejection
R_a	Average roughness
R_q	Root mean square roughness
SAD	Surface area difference
P	Permeability
ΔP	Transmembrane pressure
ΔS_{mix}	Entropy of mixing
Δt	Time interval
δ	Solubility parameter
ρ	Density of water

Chapter 1

Introduction

1.1 Water demand and membrane technology

Water scarcity is one of the significant threats in the 21st century. Among 71% of the water on the earth's surface, only 1% can be accessed as freshwater, and the rest are seawater [1]. The increasing demand for clean water due to rapid population growth and economic development also reduces accessible freshwater sources per capita. Almost half of the population (about 4 billion people) live under conditions of limited freshwater supply for at least one month per year, which is expected to increase to 4.8-5.7 billion people by 2050 [2]. Therefore, there is an urgent need for more freshwater resources and energy-efficient wastewater treatment technologies. Wastewater treatment technologies are divided into three main categories: (i) physical methods, which include adsorption, membrane filtration, media filtration (using sand, gravel, and walnut shell), evaporation, distillation, and air flotation; (ii) chemical methods, such as chemical oxidation (utilizing ozone, chlorine, iodine, hydrogen peroxide, and permanganate) and electrochemical processes; and (iii) biological methods, including anaerobic reactors, activated sludge, aerated lagoons, and wetlands [3]. Among these, the most widely used for industrial and residential wastewater treatment are adsorption, chemical oxidation, biological treatment, and membrane processes. Adsorption, utilizing materials like activated carbon and zeolites, effectively removes pollutants such as organic matter, oil, and grease. However, its limitations include low adsorption capacity and environmental and cost concerns related to adsorbent disposal and regeneration [4]. Chemical oxidation decomposes pollutants through radical reactions facilitated by chemicals like ozone and hydrogen peroxide, but high salt concentrations and radical scavengers in some wastewater hinder its efficiency. Additionally, it is energy-intensive and may not completely remove low-concentration contaminants like pharmaceuticals and microplastics. Biological methods are mainly effective for municipal wastewater but face challenges with complex industrial effluents due to the harsh conditions that may harm microorganisms [4]. Membrane technology has become a widely implemented and rapidly growing separation technology over the past few decades. It has several advantages over conventional technologies, for example, easy installation and operation, low energy consumption, low chemical usage, low space requirement, and reduced environmental effects [5]. Moreover, membrane-based separation processes are more energy efficient and considered a low environmental impact route for many applications such as energy conversion [6], clean water production [7], gas barrier, food processing [8,9] and molecular separation [10].

A membrane is a selective barrier that allows certain substances to pass while retaining others in the presence of a certain driving force (i.e., pressure, concentration, electrical potential gradient, and temperature) [11]. Currently, the primary membrane separation processes for wastewater treatment and desalination include microfiltration, ultrafiltration, nanofiltration, and reverse osmosis (**Figure 1.1**). Microfiltration removes particles larger than 100 nm, such as oil, grease, and bacteria. Ultrafiltration targets solutes between 10-100 nm, including some viruses and organic matter. Nanofiltration filters solutes from 1-10 nm, effectively removing divalent ions for water softening. Reverse osmosis membranes, being dense and nonporous, separate even the smallest monovalent ions.

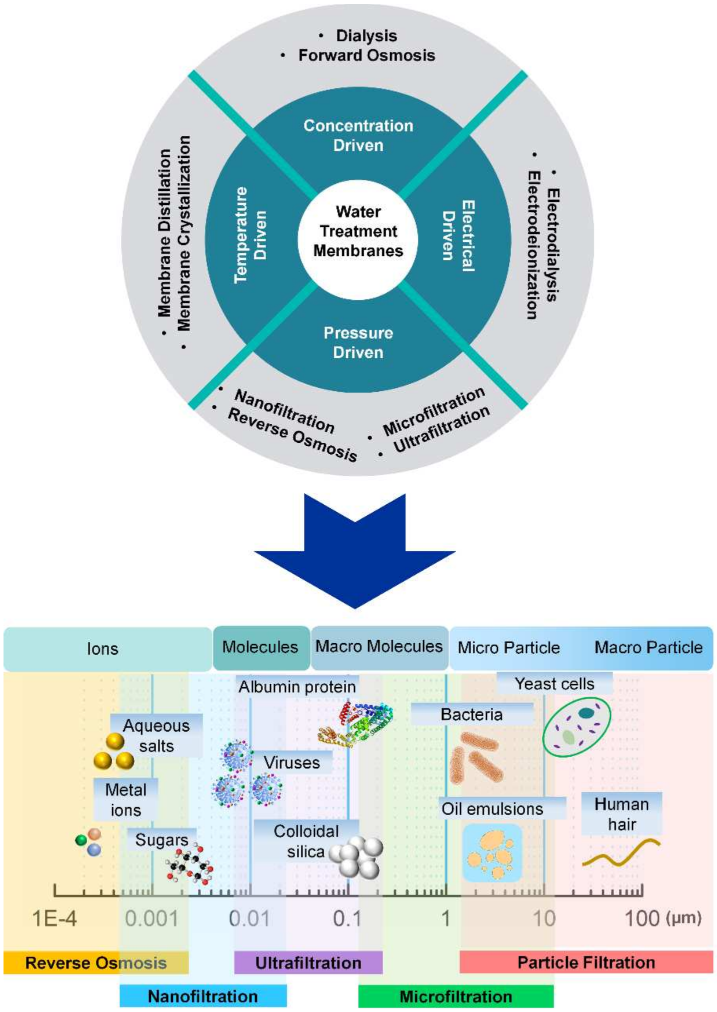

Figure 1.1. Types of membrane separation processesbased on different driving forces. The Schematic also shows the most used pressure-driven membranes and their respective pore sizes. Reproduced with permission from Elsevier [3].

Based on membrane materials, membranes are classified as inorganic, organic (mainly polymeric), and mixed matrix membranes. Among them, polymeric membranes have the advantages of high transport properties and low cost [11].

1.2 Motivation

Although the membrane process itself is recognized as a sustainable technology, the fabrication process of polymeric membranes cannot be considered fully green as it involves non-degradable polymer and generates a considerable amount of waste [12,13]. The fabrication steps of these membranes primarily relied on fossil-based polymers (e.g., polysulfone [14], polyacrylonitrile [15], polyamide-imide [16], and polyvinylidene fluoride [17]) and toxic organic solvents (e.g., dimethylformamide (DMF) [18], dimethylacetamide (DMAc) [19], and N-methyl-pyrrolidone (NMP) [20]), raising environmental concerns due to their toxicity, poor degradability at the end of their life cycle and potential for secondary pollution during recycling. Almost 50 billion liters of wastewater containing these toxic solvents are generated from the membrane industries annually [13,21]. These solvents are now added to the REACH list of the European Chemical Agency [22–24]. In the near future, these will be banned from being used as solvents in industrial membrane fabrication. Therefore, substituting hazardous solvents could effectively solve this problem and make the process greener. With the increasing interest in sustainable and green chemistry, new environmentally friendly solvents (e.g., Cyrene^{TM} [25], dimethyl isosorbide [26], and sulfolane [27]) are explored for membrane fabrication. However, the shift from traditional solvents to more eco-friendly alternatives depends not only on the accessibility of these options but also on the compatibility between the selected green solvents and the polymers employed in membrane fabrication [5]. Given the rising energy crisis and environmental pollution issues, the eco-friendly transformation of this engineering sector has become crucial. Hence, there is a growing interest in using bio-based polymers as raw materials and nontoxic solvents to improve sustainability in membrane fabrication.

1.3 Membrane fabrication techniques

Several well-established techniques, such as sintering, track-etching, template leaching, phase inversion, interfacial polymerization, solution coating, etc., can be used to prepare selective, high flux, and defect-free membranes with symmetric or asymmetric structures [28]. Among the various available techniques, phase inversion (also known as phase separation) stands out as the most adaptable approach for preparing membranes, enabling the attainment of diverse morphologies. Much research has already been conducted on phase inversion membranes over the last six decades, as shown in **Figure 1.2**. The subsequent section provides a detailed description of the membrane fabrication through the phase separation technique. Comprehensive information about alternative methods for membrane fabrication can be explored in other sources [13,29].

1.3.1 Phase separation techniques

The phase inversion technique, pioneered by Loeb and Sourirajan in the 1960s, is the foundation for synthesizing the most commercially available membranes in membrane technology [11]. A thermodynamically stable polymer solution undergoes a controlled transition from a liquid to a solid state in this process. A liquid-liquid demixing phenomenon precedes the solidification. After a specific period following the initiation of demixing, the phase with the highest polymer concentration undergoes solidification through mechanisms such as gelation, vitrification, or crystallization [29]. Consequently, the polymer-lean phase contributes to the formation of pores in the solidified material, while the polymer-rich phase forms the solid membrane matrix.

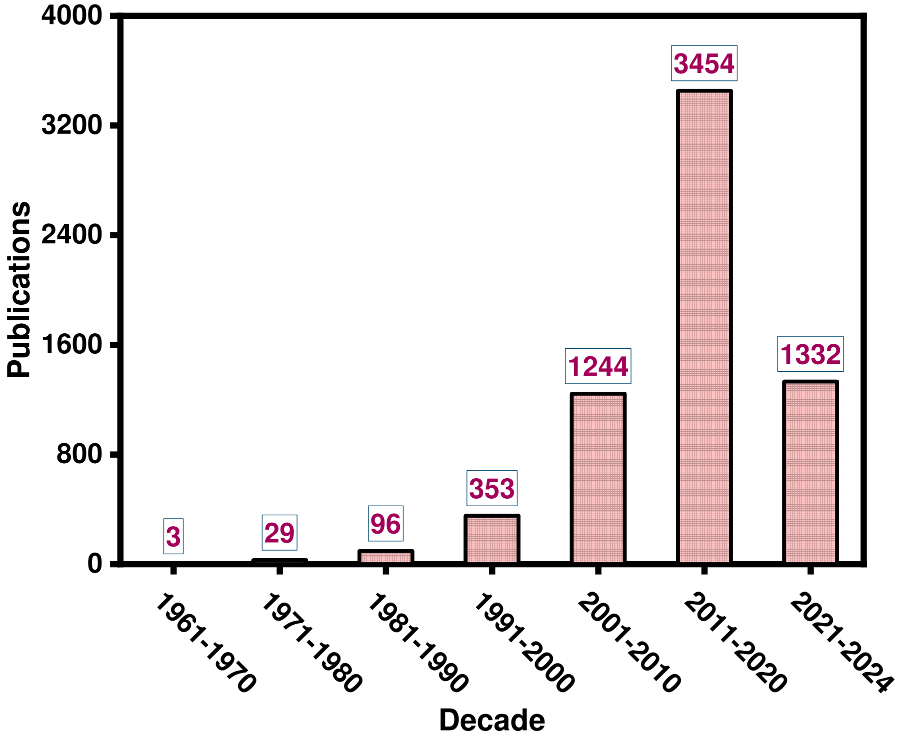

Figure 1.2. The number of publications searched as "Phase inversion membranes" in Scopus.

This demixing can occur by [29]:

- **Loeb-Sourirajan or Immersion Precipitation Process:** In this method, also known as nonsolvent induced phase separation (NIPS), the polymer solution is cast and then immersed in a non-solvent, typically water. This immersion leads to the precipitation of a film through the solvent-nonsolvent exchange, involving water uptake and solvent loss.
- **Vapor Absorption Process:** In this vapor-induced phase separation (VIPS), the cast polymer solution is exposed to a humid atmosphere, causing the absorption of water vapor and the subsequent precipitation of polymeric film.
- **Thermal Gelation:** This technique, also known as thermally induced phase separation (TIPS), involves the precipitation of the polymer film due to the cooling of a hot cast polymer solution.
- **Controlled Evaporation:** In evaporation-induced phase separation (EIPS), precipitation occurs in this method through the evaporation of a volatile solvent from the cast polymer solution, containing a mixture of volatile solvent and less volatile non-solvent solution.

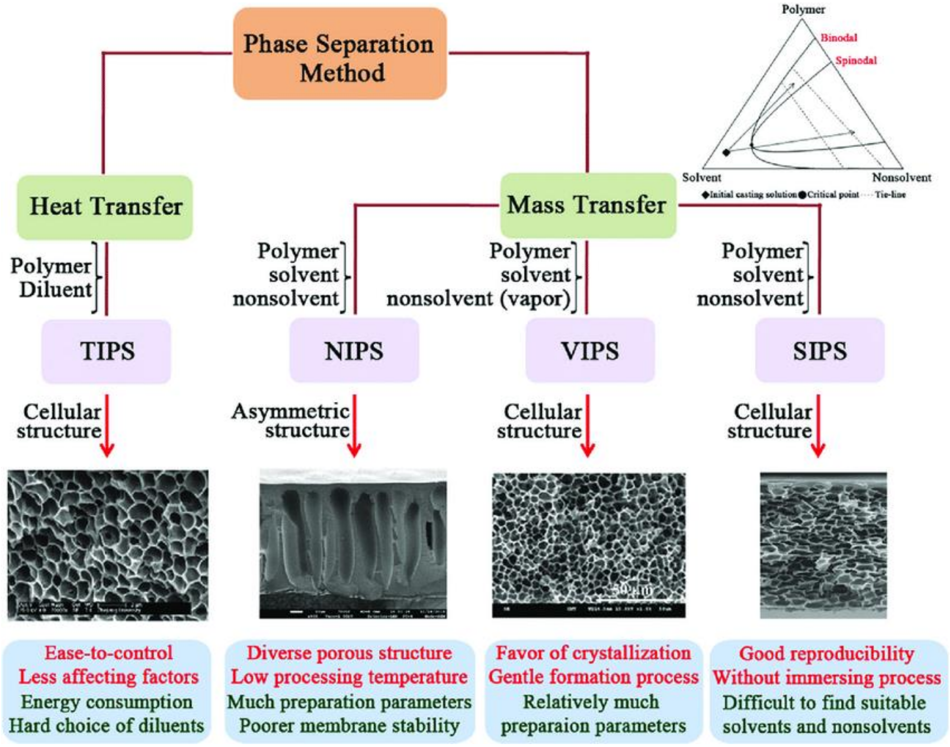

Figure 1.3. Comparison of different phase separation methods. Reproduced with permission from Royal Society of Chemistry [6].

A combination of these methods can also induce film precipitation, such as water vapor absorption followed by an immersion precipitation process [11]. These methods are compared in **Figure 1.3** in terms of components required, membrane morphology, and advantages and disadvantages. Different techniques have different phase separation mechanisms, which leads to various pore structures such as cellular, finger-like, and sponge-like pores [6]. Of all the above techniques, NIPS is the most popular membrane formation technique as it permits the formation of different membrane morphologies using a wide variety of polymers [21,30]. The following section provides more information about the immersion precipitation process.

1.3.1.1 Theoretical approach of nonsolvent-induced phase separation

In the NIPS technique, a polymer-solvent solution (casting solution) is cast as a thin film on a support (e.g., a glass plate) and immersed in a nonsolvent bath. After immersion, the solvent diffuses into the coagulation bath, and the nonsolvent diffuses into the cast film. Over time, the exchange of solvent and nonsolvent leads to thermodynamic instability, resulting in demixing and forming a solid polymeric film with an asymmetric structure. A schematic illustration of the solvent-nonsolvent exchange process is shown in **Figure 1.4A.** The phase separation process can be explained based on two perspectives [12,31]:

1. Thermodynamic perspective: A thermodynamically stable dope solution is prepared by dissolving the polymer in a solvent. It is then immersed in a nonsolvent bath, creating a thermodynamically unstable environment for the dope solution. For the mixing of two or more components, the free energy of mixing is expressed as [29]:

$$\Delta G_{mix} = \Delta H_{mix} - T\Delta S_{mix} \qquad 1.1$$

where ΔG_{mix} is the Gibbs free energy of mixing, ΔH_{mix} and ΔS_{mix} are the enthalpy and entropy of mixing, respectively. For spontaneous mixing (polymer/solvent), the free energy of mixing is negative ($\Delta G_{mix} < 0$). Phase separation occurs when the free energy of mixing becomes positive. Unlike low molecular weight solvents, polymers contribute less to the entropy of mixing, indicating that the enthalpy of mixing mostly determines the solubility of the polymer in a polymer/solvent system [29]. To evaluate the enthalpy of mixing, Hildebrand developed the following solubility parameter approach.

$$\Delta H_{mix} = V^{mix}\phi_1\phi_2(\delta_1 - \delta_2)^2 \qquad 1.2$$

$$\delta = \left[\frac{\Delta H_V - RT}{V}\right]^{1/2} = [CED]^{1/2} \quad 1.3$$

Where V^{mix} is the molar volume of the mixture, ϕ_1 and ϕ_2 are volume fractions of components, while δ_1 and δ_2 are the solubility parameters of the components. Since the negative value of ΔG_{mix} is obtained when ΔH_{mix} approaches zero, components with close values of solubility parameters are likely miscible. The solubility parameter of a component is defined to be the square root of cohesive energy density, which accounts for the strength of interactions between molecules per unit volume [32,33]. It is possible to find ΔH_V and δ, by vaporizing the substance. However, for polymers, δ is estimated commonly by swelling tests since polymers cannot be evaporated. The test consists of immersing the polymer into several solvents, and the solubility parameter of the solvent that swells the polymer most is taken to be the closest value to the solubility parameter of the polymer [29]. Hansen divided solubility parameters into three parameters, which quantitatively represent different aspects of bonding: the polar (atomic) bonding (δ_P), the permanent dipole-permanent dipole (molecular) bonding (δ_D), and the hydrogen (molecular) bonding (δ_H). The total parameter, δ, is then calculated as follows [32,33]:

$$\delta^2 = \delta_D^2 + \delta_P^2 + \delta_H^2 \quad 1.4$$

The solubility parameters are typically expressed in $MPa^{½}$ units. The smaller the difference between two polymers δ, the higher the likelihood of compatibility between them. When the δ values of two components are similar, it suggests that their solubility parameters are closely matched, making them more likely to form a compatible blend or solution. The Hansen solubility parameters (HSP) distance between two molecules, conventionally called R_a, can also be utilized to assess the similarity between two molecules as follows:

$$R_a^2 = 4(\delta_{D1}-\delta_{D2})^2 + (\delta_{P1}-\delta_{P2})^2 + (\delta_{H1}-\delta_{H2})^2 \quad 1.5$$

The numerical coefficient of 4 preceding the term is determined based on experimental data. Additionally, another parameter, denoted as R_o or the radius of the solubility sphere, is experimentally assessed for individual components. R_o sets a threshold for the distance of solubility parameters, beyond which interactions between components are considered to have low affinity. The relative energy difference (RED) is calculated by dividing the R_a value by the R_o value of the solute.

$$\mathrm{RED} = R_a/R_o \tag{1.6}$$

The RED value below one suggests a strong affinity between components, whereas rising RED values signify diminishing affinity (**Figure 1.4B**). The boundary condition is specified at 1.0, where substance compatibility becomes uncertain. The solubility parameter approach can simplify the implementation of the phase inversion process by assisting in the selection of suitable solvent and nonsolvent combinations for the polymer.

The nonsolvent-induced phase separation process can be elucidated using a ternary phase diagram, an approach initially introduced by Strathmann et al. [34], as depicted in **Figure 1.4C**. It is important to note that this figure only approximates the overall system and does not illustrate the variation in precipitation paths at different locations within the membrane.

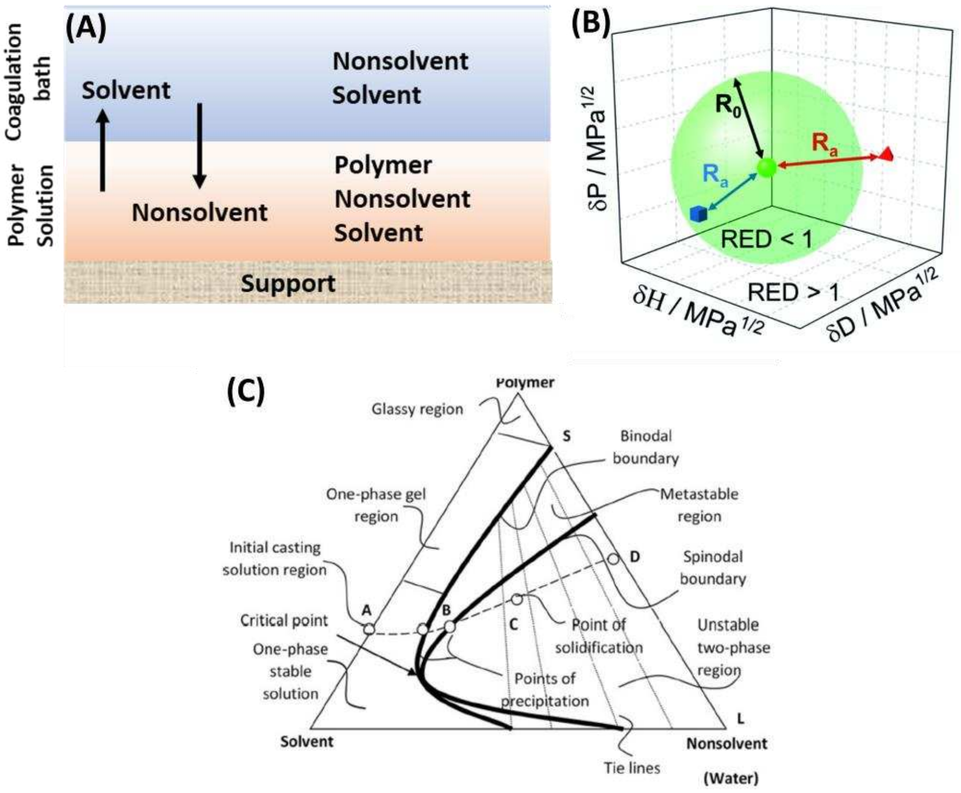

Figure 1.4. A) Exchange of solvent-nonsolvent during phase separation, (B) Hansen sphere to determine compatibility between two components, (C) schematic representation of the ternary phase diagram describing the formation of phase separation membranes. Reproduced with permission from Elsevier [29,31,35].

The phase behavior of the polymer/solvent/nonsolvent system in **Figure 1.4C** is described below [11,31]:

- The vertices of the triangle denote the pure components (polymer, solvent, and nonsolvent). Any point located within the triangle comprises all three components.
- Within the triangle, there exist two regions:
  - A one-phase region where all components are fully miscible.
  - A two-phase region where the system segregates into two phases: 1) polymer-rich phase and 2) polymer-poor phase.
- Throughout the membrane formation process, the composition evolves from point A (representing the initial casting solution) to point D (indicating the final membrane composition). The polymer composition undergoes a transition from the one-phase region to the two-phase region along the trajectory ABC.
- Point B signifies the concentration at which the polymer initially precipitates. Progressing along the line BCD involves a loss of solvent and a gain of nonsolvent (usually water), resulting in an increase in polymer concentration and viscosity. At point C, the viscosity becomes sufficiently high to regard the precipitated polymer as solid. Beyond this solidification point, the mobility of polymer chains or bulk is impeded.
- At point D, a state of equilibrium is reached with two phases. One phase, denoted by point S, constitutes the polymer-rich matrix, while the other phase, represented by point L, forms the pores in the membrane. The specific location of point D along the S-L line determines the overall porosity of the membrane.
- The phase separation of the polymer solution can occur via two distinct pathways: binodal demixing and spinodal decomposition. In the case of binodal demixing, if the polymer solution reaches the metastable region, phase separation takes place through a nucleation and growth mechanism. Conversely, spinodal decomposition involves the polymer solution traversing both the bi- and spinodal regions, ultimately settling in the thermodynamically unstable region. This process results in the formation of two co-continuous phases that can subsequently transform into nuclei.

Additionally, the precipitation rate and path differ across various locations within the membrane. For example, precipitation is swift at the top surface, leading to a deceleration in the rate of solvent-nonsolvent exchange as it progresses toward the bottom surface of the film.

2. Kinetic perspective: The kinetic aspect is connected to the mass transfer (solvent out and nonsolvent into the casting solution) among all components throughout the precipitation process [36]. In this context, the membrane structure is influenced by the precipitation rate. There is a widely recognized consensus that parameters affecting precipitation kinetics, such as viscosity, and thermodynamics, such as solvent-nonsolvent and solvent-polymer interactions, play a significant role in shaping the ultimate membrane structure.

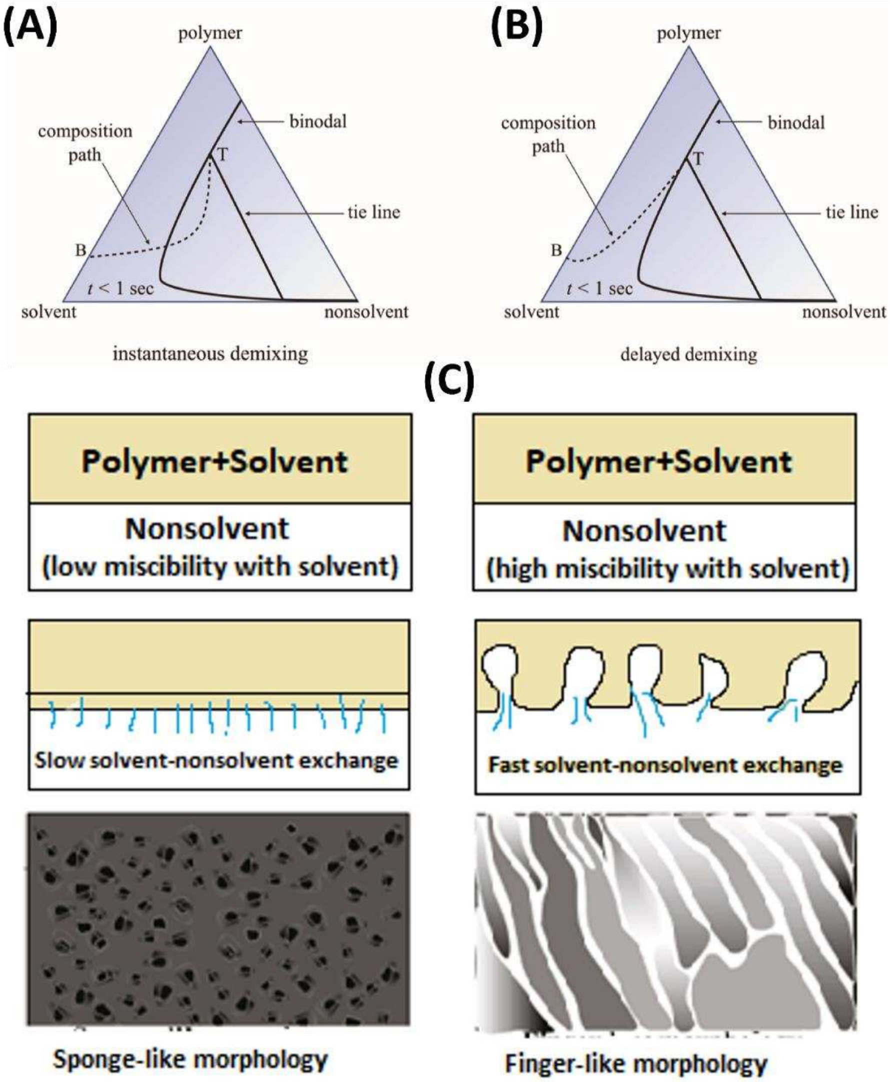

Figure 1.5. Composition path of a cast film after immersion (t<1sec): A) instantaneous demixing and B) delayed demixing; T and B represent the top and bottom of the film; C) Membrane morphologies at instantaneous and delayed demixing. Reproduced with permission from American Chemical Society [30].

Liquid-liquid demixing occurs when the polymer film comes into contact with the nonsolvent. Depending on the exchange rate, two distinct demixing types can be identified. The phase separation process can involve either an instantaneous or delayed demixing pathway, as illustrated in **Figures 1.5A and 1.5B** [36]. Instantaneous demixing occurs when liquid-liquid demixing initiates immediately after immersion in the nonsolvent bath. In contrast, delayed demixing takes place when the demixing process begins only after a significant period, signifying the penetration of more nonsolvent into the film. As depicted in **Figure 1.5A**, the overall composition surpasses the binodal boundary at $t < 1$ sec, resulting in an immediate demixing following immersion in a nonsolvent bath. Conversely, in delayed demixing (**Figure 1.5B**), overall compositions persist within the one-phase region after immersion in the nonsolvent bath and only traverse the binodal line after a more prolonged period. In the case of instantaneous demixing, there is a rapid exchange between solvent and nonsolvent, typically leading to a relatively porous upper layer with macrovoids (finger-like pores) in the sublayer. This step usually involves the abrupt intrusion of nonsolvent, promoting macrovoid formation through the local instability of the interfacial tension between the polymer solution and water [9]. In contrast, in delayed demixing, the exchange between solvent and nonsolvent occurs at a slower rate, typically leading to the formation of a dense upper layer with a sponge-like sublayer. The membrane morphology resulting from both the demixing processes, both instantaneous and delayed, is shown schematically in **Figure 1.5C**.

1.3.1.2 Factors affecting membrane formation

Several fabrication parameters can significantly influence the phase separation process and membrane morphology. Some crucial parameters are polymer types, molecular weight and concentration of polymers, types of solvent and nonsolvent, composition of coagulation bath, temperature, humidity, and modifier. A brief description of these parameters is provided below:

The selection of the polymer is vital as it impacts the thermal and chemical stability of the membrane, as well as its charge and hydrophilicity. Additionally, in the case of a nonporous membrane, the solubility and diffusivity are directly influenced by the chosen polymer [30]. Typically, amorphous polymers with high molecular weights and toughness are preferred for membrane fabrication. Conversely, crystalline or rigid glassy polymers are generally unfavored because membranes formed from these materials tend to be too brittle [11]. Furthermore, the molecular weight of the polymer can impact the resulting membrane morphology. High molecular weight polymers exhibit greater viscosity compared to low molecular weight ones. Considering the kinetics involved, the viscosity of the casting solution influences the inter-diffusion rate between solvent and nonsolvent. A highly viscous solution tends to have slower inter-diffusion, often leading to delayed demixing.

The polymer concentration is another crucial parameter influencing membrane morphology, mechanical characteristics, and the flux through the membrane. Increasing the polymer concentration in the casting solution leads to a higher concentration at the nonsolvent interface. Consequently, the volume fraction of the polymer increases, resulting in membranes with lower porosity and reduced flux. In fact, beyond a specific polymer concentration, water flux can be reduced to zero, even in the presence of a porous sublayer in the membrane [30].

Selecting a solvent plays a crucial role in determining the resulting membrane morphology. The solvent and nonsolvent must be miscible, and the polymer should readily dissolve in the chosen solvent. When there is strong miscibility between the solvent and nonsolvent, instantaneous demixing occurs; conversely, weak mutual affinity leads to delayed demixing [30,37].

Additionally, the membrane structure can be controlled by introducing a solvent into the precipitation medium. However, [30]. A delay in the demixing process due to a decline in nonsolvent activity and the diffusion rate into the polymer film leads to a denser structure or a decrease in polymer concentration at the film interface, resulting in a more open structure. Temperature is another significant factor that influences membrane morphology [30]. It directly affects the viscosity of the casting solution, resulting in a change in the exchange rate of solvent-nonsolvent during phase inversion.

Adding modifiers in the casting solution can significantly change the membrane's structural parameters, like porosity, thickness, and tensile strength. Including a co-solvent, a salt, or polymer additives are effective modifiers [38,39]. Adding an organic or inorganic component can induce changes in pore structure, transforming it from a finger-like to a sponge-like configuration or vice versa. Additionally, this modification can enhance pore interconnectivity, increase hydrophilicity, and improve permeability [21]. Some of the commonly used additives are pluronic F-127, polyvinylpyrrolidone (PVP), polyethylene glycol (PEO), LiCl, water, alcohols, propanoic acid, and surfactants [21,30,38].

Overall, an appropriate adjustment of one or a combination of the interdependent parameters allows for control of membrane morphology and structure.

1.3.2 Electrospinning

Electrospinning has advanced as a potent technology for producing membranes composed of fibers ranging from nano- to micrometer scales, resulting in distinctive membrane characteristics attributed to the exceptionally high surface-to-volume ratio and increased membrane porosity [40]. This versatility is broadened by various materials that can undergo electrospinning, encompassing biomaterials, and synthetic polymers. The ease of use and ability to scale up electrospinning make it attractive for producing nanofibers with tailored properties to meet diverse application needs.

1.3.2.1 Working principle

Electrospinning encompasses an electrohydrodynamic process in which a liquid droplet undergoes electrification to create a jet, followed by stretching and elongation to produce fibers [41]. As depicted in **Figure 1.6**, the basic electrospinning setup is relatively straightforward, allowing accessibility in nearly every laboratory. The primary components consist of a high-voltage power supply, a syringe pump, a spinneret (typically a hypodermic needle with a blunt tip), and a conductive collector. The power supply can be either direct current (DC) or alternating current (AC). In the electrospinning process, the liquid is expelled from the spinneret, forming a pendant droplet due to surface tension. Upon electrification, electrostatic repulsion among surface charges of the same sign causes the droplet to deform into a Taylor cone, releasing a charged jet. Initially extending in a straight line, the jet undergoes vigorous whipping motions due to bending instabilities. As the jet is stretched into finer diameters, it rapidly solidifies, resulting in the deposition of solid fibers on a grounded collector. Overall, the electrospinning procedure can be segmented into four sequential stages [42]: (i) electrification of the liquid droplet and creation of the Taylor cone or cone-shaped jet; (ii) elongation of the charged jet along a linear trajectory; (iii) narrowing of the jet under the influence of an electric field and the development of electrical bending instability, commonly referred to as whipping instability; and (iv) solidification and gathering of the jet as solid fibers on a grounded collector.

1.3.2.2 Processing parameters

The selection of solvent is likely the most critical factor in electrospinning, as only a limited range of solvents and compositions can effectively dissolve specific polymers and facilitate fiber formation through electrospinning [40]. However, many polymers are typically challenging to dissolve, necessitating solvents with strong solvation properties. These solvents often tend to be toxic (such as halogenated solvents), challenging to recycle, and have a significant environmental impact (e.g., ionic liquids). Consequently, the choice of solvent significantly influences the environmental impact, safety, and overall sustainability of the ES process.

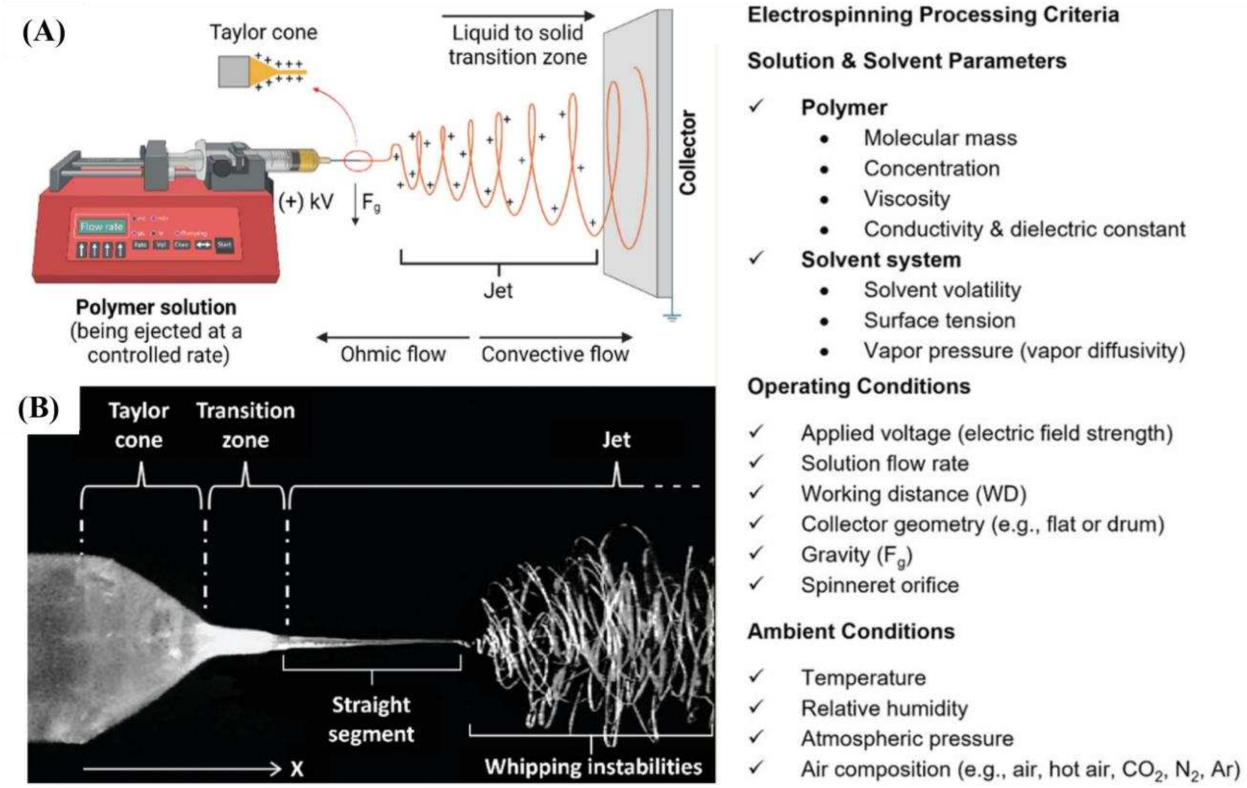

Figure 1.6. Electrospinning principle and process parameters: a) schematic illustration of the electrospinning concept, b) Rapid-capture image providing the formation of the Taylor cone, showcasing the linear section of the polymer jet, succeeded by the region where the jet undergoes whipping motion [43].

Numerous parameters are crucial and require careful consideration during electrospinning (**Figure 1.6**) [43]. Solution parameters include polymer concentration, molecular weight, solvent volatility, solution viscosity, surface tension, and solution conductivity. When it comes to electrospinning parameters, it is crucial to adjust the electric field strength, electrostatic potential, flow rate, and the distance between the spinneret and the collector in coordination with the properties of the polymer solution. Lastly, ambient parameters include the temperature, humidity, and the type of atmosphere. More information on how these parameters affect the electrospun fibers can be found in detail in other literature [43,44].

1.4 Current challenges and potential solutions for sustainable polymeric membrane fabrication

Membrane technology has become an integral aspect of our everyday existence. The rapid advancement of this technology has given rise to a pressing challenge — the unsustainable disposal of used membranes. Moreover, some aspects of the membrane manufacturing process are not entirely sustainable. For instance, the involvement of fossil-based polymers and a large amount of toxic organic solvents in membrane fabrication create a severe risk to health and the environment [45]. In the past decades, the membrane market has been dominated mainly by petroleum-based nonbiodegradable polymers. Most membranes are prepared from fossil-based polymers such as polysulfone [14], polyacrylonitrile [15], polyamide-imide [16], and polyvinylidene fluoride [17]. Although these polymeric membranes are extensively used in different applications such as wastewater treatment, desalination, gas separation, biomedical, pharmaceutical, food, and beverage industries, the negative impacts of these polymers on the environment cannot be neglected [46]. They are usually nonrenewable and difficult to degrade. They can generate microplastics that adversely affect living organisms and the environment. A prior study has highlighted that approximately 12% of all polymers undergo incineration post-use, leading to the release of CO_2, while 80% find their way into landfills, eventually contributing to ocean pollution [47]. Consequently, there is a compelling need to innovate and produce membranes that follow a sustainable lifecycle, both derived from bio-based sources and capable of biodegradation from their production to their end-of-life stage. Some promising strategies to improve the sustainability of membrane technology, considering the cradle-to-grave approach guided by the twelve principles of green chemistry, are schematically represented in **Figure 1.7**. Over the coming few decades, the chemical sectors are expected to gradually transform into fully sustainable and environment-friendly processes. Five strategies are proposed to improve sustainability in the membrane manufacturing phase [5]. The first way is to replace the nonbiodegradable fossil-based polymers entirely or partially with renewable bio-based polymers. Bio-based or biodegradable polymers have promising potential to substitute conventional fossil-based polymers due to their biodegradable nature, biocompatibility, versatility, low carbon footprint, low toxicity, and social acceptance [5,45]. Second, traditional solvents should be replaced with greener alternatives. The third way is to treat the wastewater, mainly containing organic solvents and polymers, generated during membrane fabrication. The annual wastewater generation worldwide from the membrane manufacturing process is estimated to be over 50 billion liters, of which only 31% is somehow treated nowadays [48].

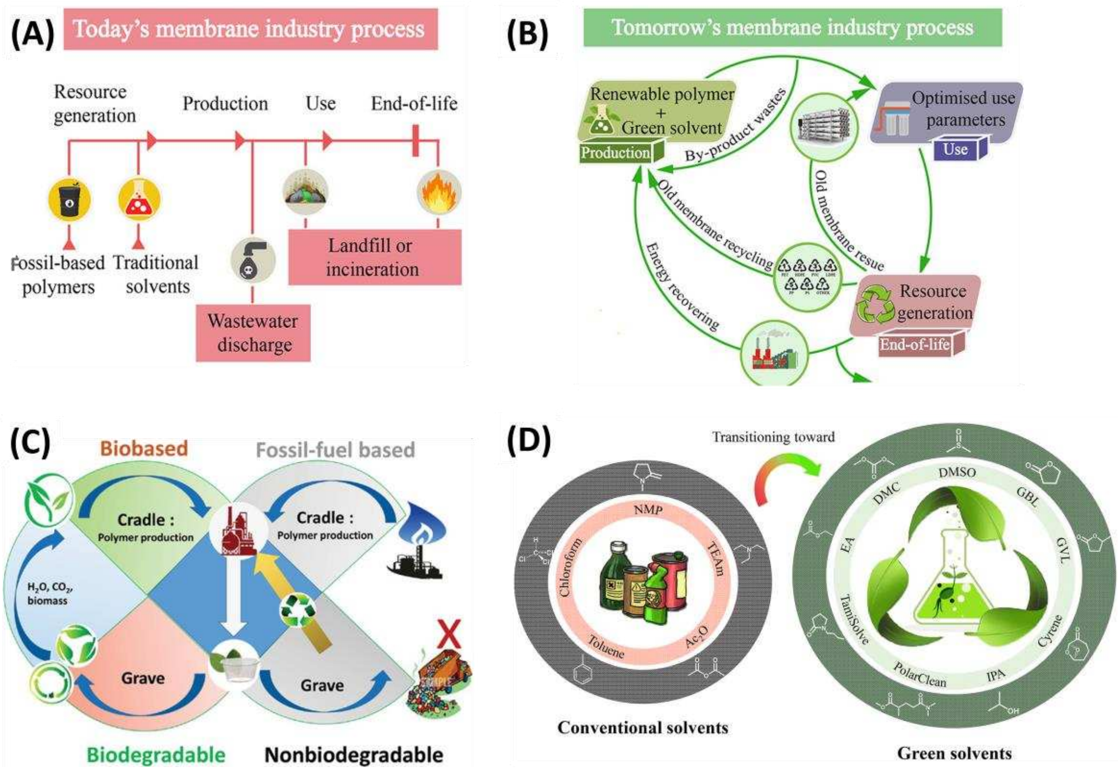

Figure 1.7. Strategies to improve the sustainability in membrane technologyfrom fabrication to end-of-life management: (A,B) characteristics of today's and tomorrow's membrane industry process, reproduced with permission from American Chemical Society [5], (C,D), promising approaches to improve the sustainability in membrane technology by replacing fossil-based polymer and toxic solvents, reproduced with permission from Royal Society of Chemistry [49].

The fourth strategy could be reducing membrane fabrication steps, resulting in less use of toxic solvents and reduced energy consumption and cost. Finally, room temperature should be considered for casting solution preparation to reduce energy consumption.

1.4.1 Replacement of fossil-based non-degradable polymers

Biodegradability is the key feature that needs to be considered to open a new horizon into a sustainable membrane separation technology, shifting the reliance on fossil-based polymers to bio-based polymers. Bio-based polymers can eliminate many environmental problems related to fossil-based nondegradable polymers. Therefore, the development of bio-based polymers for membrane fabrication has gained more attention in recent years. There is a key difference between bio-based and biodegradable polymers [50]. Not all bio-based polymers are biodegradable, and not all biodegradable polymers are bio-based. Bio-based polymers, usually obtained from renewable resources, can be biodegradable (e.g., polyhydroxyalkanoate (PHA)) or nondegradable (e.g., bio-polyamide). Therefore, a polymer can be considered a biopolymer if it is obtained from bio-based or renewable resources with biodegradability potential. Biodegradable polymers primarily undergo degradation through physical decomposition and biological degradation [51].

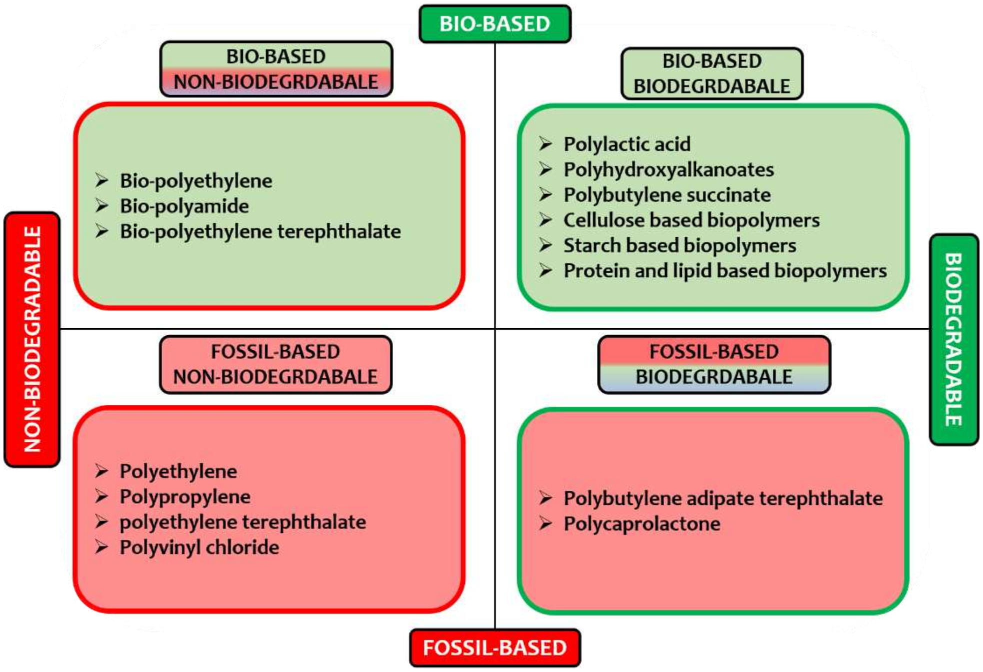

Figure 1.8. A schematic illustration of the interrelationship between bio-based and fossil-based polymers in terms of biodegradability.

While physical decomposition (e.g., oxidation, photodegradation, and hydrolysis) may lead to polymer degradation partially or completely, a complete degradation occurs by the action of microorganisms in the biological process, generating molecules like carbon dioxide, water, nitrogen, and biomass [52]. A schematic illustration of bio-based and fossil-based polymers is shown in **Figure 1.8**. Bio-based polymers can be obtained from three different renewable sources [53,54]:

1. Plant or vegetable-based polymers (e.g., cellulose, starch, alginate, lignin)
2. Animal-based polymers (e.g., chitin and chitosan, collagen and sericin)
3. Bacterial fermentation (e.g., polylactic acid, polybutylene succinate, polyhydroxyalkanoates)

Biodegradable materials have attracted significant attention in different applications, such as food packaging, water treatment, drug delivery, wound healing, and membrane manufacturing [55,56]. Considering biopolymers as membrane materials, they have been used for different membrane-based applications, such as microfiltration, ultrafiltration, nanofiltration, pervaporation, gas separation, and tissue engineering [54]. Although bio-based materials are of great interest, extensive applications of these materials as a replacement for petrochemical-based materials in the membrane industry are still challenging due to some inherent limitations, such as poor processability, low thermal and mechanical properties, low melting point, and poor moisture and gas barrier [57]. Despite these challenges, bio-based materials have a promising future as an alternative to fossil-based materials.

1.4.2 Solvent selection criteria for greener alternatives

The membrane fabrication steps involve the use of harmful solvents during the membrane fabrication process, such as dimethylformamide (DMF) [18], dimethylacetamide (DMAc) [19], and N-methyl-pyrrolidone (NMP) [20]. Adopting greener alternatives is essential in response to the environmental and health risks linked with conventional solvents. One popular strategy gaining attention involves using non-toxic green solvents to replace toxic organic solvents completely [58–60]. Several factors must be considered when choosing a proper alternate solvent for the phase inversion process (**Figure 1.9A**). A thermodynamically stable dope solution needs to be prepared for this process; therefore, the chosen solvent should be a good solvent to solvate polymer at ambient temperature. Moreover, the morphology and properties of the membrane alter with the properties of the solvent, such as viscosity, density, and polarity [61–63]. A recent review of the progress on improving sustainable membrane fabrication is discussed in detail elsewhere [12,58]. The choice of a solvent has a significant role in final membrane properties**.** Solvent power or solvency describes the interaction of the solvents with the polymers. The higher the solvent power, the higher the solubility of polymers [38,63]. The varying solvent power of different solvents leads to differences in phase separation rates, ultimately impacting the resultant membrane structure and performance. For example, for polyethersulfone (PES) polymer, NMP has stronger solvent power than DMSO [39]. Therefore, the kinetics of phase separation (which typically depends on the polymer-solvent and solvent-nonsolvent affinity) will differ for both cases and eventually form membranes with different structures. The coagulation value, indicating the amount of nonsolvent needed to add to the polymer solution for phase inversion to occur, is also a representation of thermodynamic stability [37]. This value has a significant effect on the membrane morphology. For example, PES with PolarClean solvent produced a porous structure due to its low coagulation value (i.e., instantaneous demixing occurs), whereas cellulose acetate (CA) in PolarClean produced nonporous structures due to a higher coagulation value (i.e., delayed demixing occurs) [21]. Moreover, the choice of solvent and its effect on membrane structure also depend on the compatibility of nonsolvent and solvent in terms of their miscibility, polarity, boiling point, viscosity, and molecular weight [25,37,64]. For instance, a higher boiling point solvent allows the dissolving of many fluoropolymers and polysulfones [39,64].

The solution viscosity also influences membrane morphology. A reduction in solution viscosity enhances the mutual diffusion rate between solvent and nonsolvent, leading to a more porous (finger-like) structure [39,65]. Systems with a less solvent-nonsolvent affinity are more prone to delayed demixing than those with a higher solvent-nonsolvent affinity. Again, highly polar solvents, i.e., those with a high affinity with water, require less nonsolvent to induce phase inversion. For instance, when DMSO (having polar sulfoxide group) is used as a solvent, it leads to a rapid phase inversion compared to NMP [39]. While choosing an alternative green substitute for toxic solvents, it is crucial to consider the parameters mentioned above.

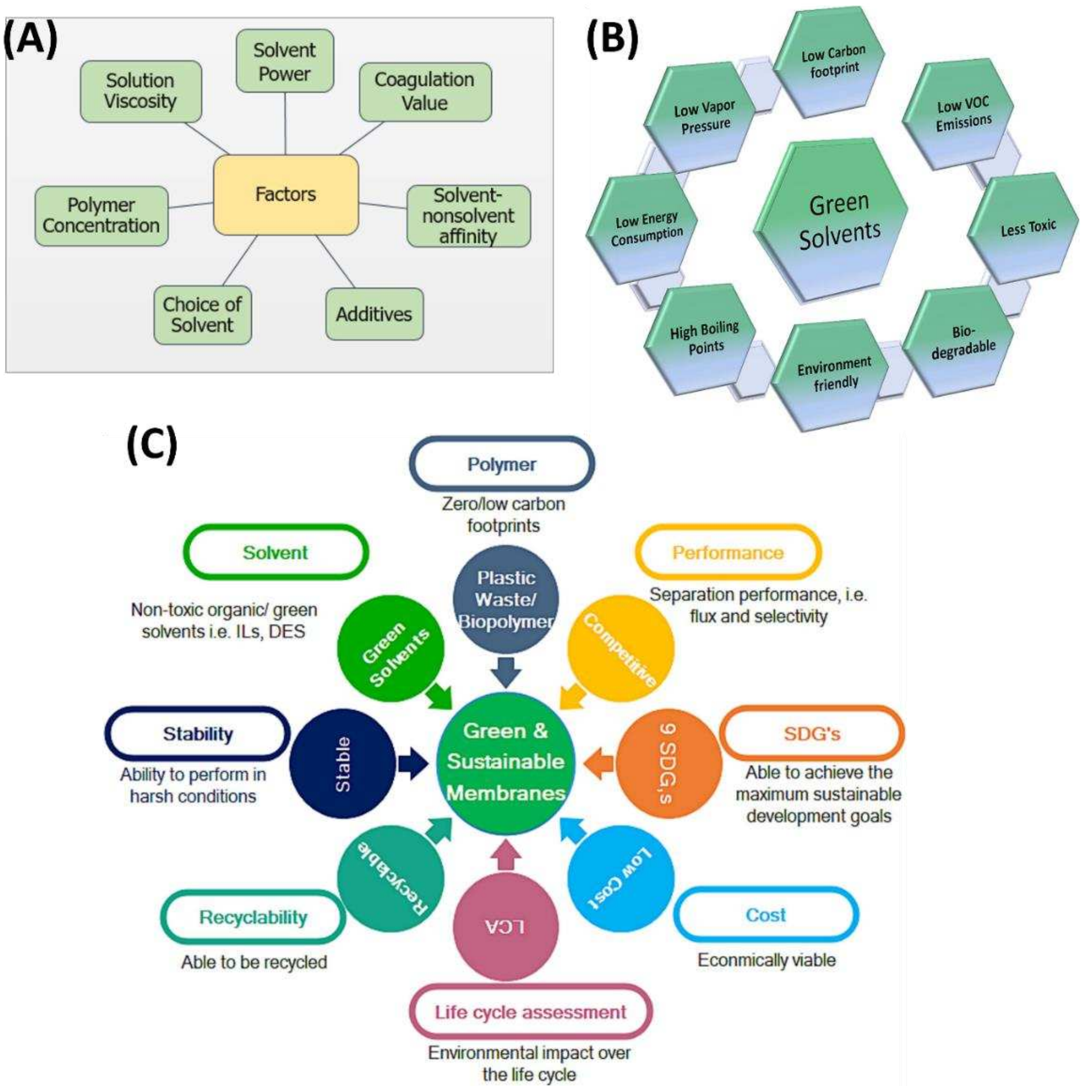

Figure 1.9. (A) Considerations of parameters for solvent selection, (B) properties and advantages of green solvent, reproduced with permission from Elsevier [66] and (C) green and sustainable membrane for the circular economy, reproduced with permission from Elsevier [66].

1.4.3 Greener alternatives to toxic solvents

Extensive research has been conducted to improve membrane sustainability using greener alternative solvents (**Table 1.1**). **Figure 1.9B** illustrates the advantages of employing environmentally friendly solvents. Marino et al. employed a green and eco-friendly solvent, methyl-5-(dimethylamino)−2-methyl-5-oxopentanoate (PolarClean), for PES membrane preparation by coupling VIPS-NIPS method and successfully applied in ultrafiltration and nanofiltration applications [38]. PolarClean has high solvent power, high boiling point, excellent miscibility with water, and excellent toxicological and eco-toxicological profile such as inherently biodegradable, not irritant, not mutagenic, and not skin sensitizing which makes it a better alternative green solvent for membrane preparation. Its solubility parameters are close to those of commonly used toxic solvents such as NMP, DMF, and DMAc, indicating that PolarClean can substitute conventional toxic solvents. Moreover, it may reduce the carbon footprint since it can be produced from the byproduct of Polyamide 6,6 synthesis [38]. Later, Wang and coworkers also used this solvent for polysulfone (PSF), PES, and cellulose acetate (CA) membrane formation using NIPS method [21]. Their findings demonstrated that this solvent exhibits suitable properties comparable to conventional toxic solvents and is compatible with traditional polymers. Another alternative bio-based solvent, dihydrolevoglucosenone (Cyrene^{TM}), was employed by Marino et al. for the first time for PES and PVDF membrane formation by the VIPS-NIPS method [25]. The absence of any pore-forming agent or additives in this process and the use of bio-based nontoxic solvents allow it to produce membranes sustainably for water treatment application. This bio-based solvent (synthesized from cellulose and levoglucosenone intermediate) is a dipolar aprotic solvent with high stability towards oxidation, and its polarity is similar to that of conventional solvents.

Moreover, it has good water miscibility, a high boiling point, and good compatibility with conventional polymers. Marino's group also showed that DMSO EVOL^{TM} can be used as a greener alternative to toxic NMP for PES membrane preparation [39]. The obtained membrane resulted in higher pore size, thickness, and water permeability than the membrane prepared using NMP as a solvent. DMSO is a biologically harmless water-soluble organic solvent that can easily be derived from the renewable process stream in industrial paper production or extracted from lignin and the binding substances of trees [67]. It also has a high boiling point and good compatibility with polymers. DMSO EVOL^{TM} used in this work was a re-engineered version of DMSO (pleasant-smelling) with an unaltered solvency as DMSO. Recently, Russo et al. employed dimethyl isobromide (DMI) as a green solvent for preparing PVDF and PES-based membranes using the VIPS-NIPS method [64]. DMI is a non-toxic sugar-based solvent (derived from D-sorbitol). It is cheaper than Cyrene, which is also a sugar-based solvent. Furthermore, it has a high boiling point and good polymer solubility (PES and PVDF). Gronwald and Weber employed another green solvent, N-dimethyl lactamide (AGNIQUE AMD 3L), to prepare a PES membrane suitable for ultrafiltration applications [65]. They proposed this solvent as the only efficient solvent for the PES UF membrane preparation, which fully complies with the green chemistry principles.

AGNIQUE AMD 3L is a bio-based protic solvent based on lactic acid produced by microbial fermentation using starchy substrates.

Table 1.1. A brief overview of the literature on sustainable membrane preparation utilizing biodegradable polymers and nontoxic solvents

Polymer	Solvent	Fabrication method	Application	Comment	Ref.
PES	PolarClean	Phase separation	UF, MF	Nontoxic solvent and fossil-based nonbiodegradable polymer	[68]
PES	AGNIQUE AMD 3L	Phase separation	UF	Nontoxic solvent and fossil-based nonbiodegradable polymer	[69]
PLA/PBS	DCM/DMF	Electrospinning	MF	Toxic solvent and biodegradable polymer	[70]
PCL/Chitosan	Formic acid/Acetic acid	Electrospinning	MF	Slightly toxic solvent and biodegradable polymer	[71]
PVDF	TamiSolve® NxG	Phase separation	UF, MF	Nontoxic solvent and fossil-based nonbiodegradable polymer	[72]
PES	[EMIM]DDEP	Phase separation	UF	Nontoxic solvent and fossil-based nonbiodegradable polymer	[73]
PSF	Rhodiasolv PolarClean	Phase separation	UF, NF	Nontoxic solvent and fossil-based nonbiodegradable polymer	[74]
PES	Cyrene™	Phase separation	MF, UF	Nontoxic solvent and fossil-based nonbiodegradable polymer	[25]
PES	DMSO EVOL™	Phase separation	MF	Nontoxic solvent and fossil-based nonbiodegradable polymer	[39]
PVDF	Dimethyl Sulfoxide	Electrospinning	MF	Nontoxic solvent and fossil-based nonbiodegradable polymer	[75]
PLA	NMP	Phase separation	UF	Toxic solvent and biodegradable polymer	[76]
Cellulose acetate	Methyl lactate	Phase separation	UF	Nontoxic solvent and biodegradable polymer	[77]
PHBHV	Cyrene	Phase separation	Pervaporation	Nontoxic solvent and biodegradable polymer	[78]
Cellulose	([EMIM]OAc)	Phase separation	UF, NF	Nontoxic solvent and biodegradable polymer	[79]

The solvent's biodegradability, high boiling point, toxicological profile, and good water miscibility make it a promising greener alternative to conventional toxic solvents in terms of sustainability. Ionic liquids, a relatively new class of chemicals, have attracted many applications as an alternative to conventional organic solvents [63]. They are more environment-friendly than typical toxic solvents but are not usually employed in membrane fabrication methods because polymers such as polyetherimide (PEI) and polyacrylonitrile (PAN) hardly dissolve in ionic liquids [80,81]. For example, Kim et al. proposed a new route for membrane preparation based on the dissolution of PES membrane in 1-ethyl-3-methylimidazolium dimethylphosphate ([EMIM]DEP) without the addition of organic or volatile solvent [9]. The synthesis of this ionic liquid involves non-hazardous chemicals, making the process environment-friendly and healthier than conventional membrane preparation methods. The water permeance of the resultant membrane showed two times higher permeance than in NMP, six times higher permeance than DMAc, and 20-fold higher permeance than in DMF. Moreover, this ionic liquid can be recycled and recovered using simple steps based on evaporation [9]. Another promising ionic liquid, 1-ethyl-3-methylimidazolium acetate ([EMIM]OAc), is used in many studies for membrane preparation by phase inversion [81–83]. This ionic liquid has low toxicity and good dissolving power for cellulose. This also can be recycled and recovered using evaporation steps [9,84]. However, the structure and performance of the resultant membranes, while using ionic liquids as a solvent, showed considerable differences from the membrane prepared from commonly used solvents. This difference was attributed to ionic liquids' higher viscosity than conventional solvents [9,84].

1.4.4 Aqueous phase separation approach

Although some of the solvents explained above are non-toxic, some limitations still exist, such as cost, the requirement for an additional step in solvent synthesis, and challenges in recovering certain solvents. Very recently, some research showed that water can be used as a solvent to prepare polyelectrolyte (PE)-based free-standing membranes [59,85–87]. Water is mostly abundant and does not require any additional step of solvent preparation. PEs are water-soluble polymers with ionizable groups in their repeating units. They dissociate into either positively or negatively charged polymeric chains (i.e., polycation and polyanion, respectively) in ionizing solvents such as water and polar organic solvents. In an uncharged state, the oppositely charged counterions maintain the electroneutrality of the repeating unit [88]. Based on the charge density, PEs can be divided into two types: strong polyelectrolyte and weak polyelectrolyte. Strong PEs are permanently charged over a wide pH range; thus, their polymeric conformations cannot be modulated upon changing the pH. Conversely, the dissociation constant (pKa) of weak PEs is in the range ∽2-10, meaning that they dissociate partially over the intermediate pH range. Therefore, [89,90]. Polyelectrolytes (PEs) are of interest in scientific research due to their large potential in advanced technology, biomedical applications, and molecular biology [90].

Polyelectrolyte complexation refers to the phase separation between aqueous solutions of two oppositely charged polyelectrolytes, which form an insoluble complex after mixing together, resulting in a dense phase, either coacervate (liquid-like) or precipitate (solid-like) [91]. Research on polyelectrolyte complexes (PECs) gained attention after Bungenberg de Jong and coworkers came up with the idea of PEC in the early 1930s who showed complex coacervate formation by the interaction of natural PEs in aqueous media [92]. However, extensive research on PEC started when Michaels and co-workers presented their work on the formation and properties of stoichiometric complexes of poly(4-vinyl benzyl-trimethylammonium chloride) and poly(sodium styrene sulfonate) [93]. Since then, the fascinating potential of PECs in different fields has spurred the growing interest until now. Much research has focused on understanding the formation and behavior of PECs at various conditions, such as temperature, pH, ionic strength, solvent type, composition, and concentration. When two oppositely charged PEs mix together, they can form PEC spontaneously. **Figure 1.10** represents the PEC formation mechanism. During this process, two oppositely charged PEs interact with each other by electrostatic interaction. Nevertheless, hydrogen bonding and hydrophobic interactions also have additional influence [94]. On the other hand, small counterions are not restricted to the PE chain and are released to the solution. As they are more random in solution rather than in the vicinity of PE backbones, there is an increase in entropy in the system, which favors the PEC formation [94,95]. Besides, when two oppositely charged PEs are mixed together, their charge can be compensated intrinsically or extrinsically. Intrinsic charge compensation is defined as the compensation of the charge of adsorbed polyions by the oppositely charged adsorbed polyions. On the contrary, when the charge is compensated by the counterions, it is defined as extrinsic charge compensation [96].

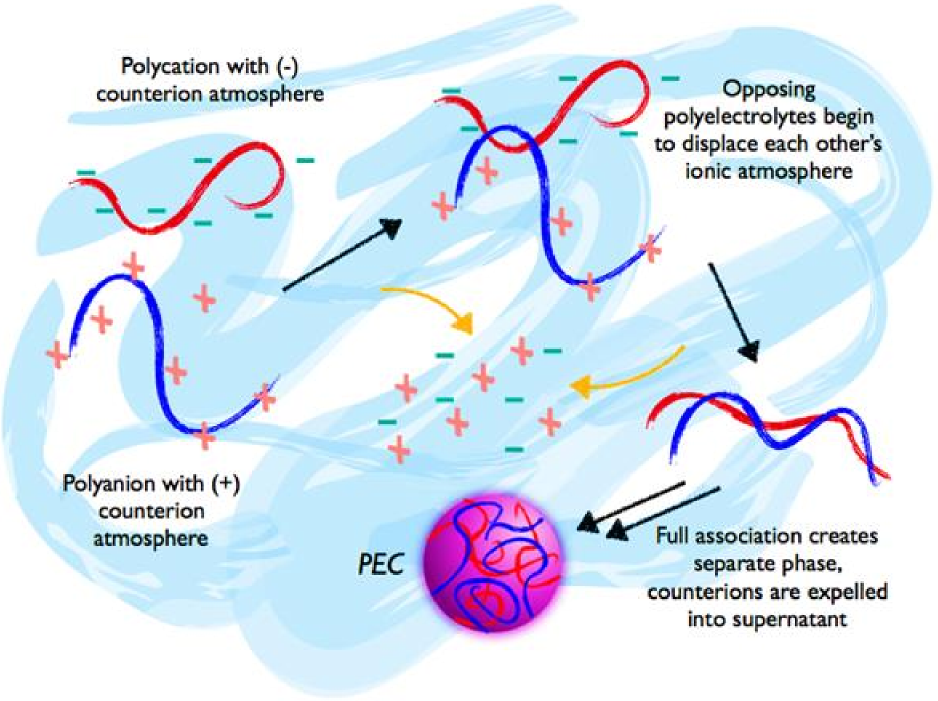

Figure 1.10. Polyelectrolyte complexation mechanism [97]

Conventional methods like solvent evaporation (**Figure 1.11A**) and nonsolvent-induced phase separation (NIPS) (**Figure 1.11B**) enable the preparation of free-standing membranes from a single polymer (PE). However, developing free-standing polyelectrolyte complex (PEC) membranes required new techniques such as interfacial complexation (**Figure 1.11D**), PEC deposition (**Figure 1.11E**), and multicasting (**Figure 1.11F**) [98]. In interfacial complexation, a PE film is submerged in a bath containing PEs with opposite charges. The multicasting method involves either casting, drying, and recasting a PEC dispersion or casting a PE solution followed by an oppositely charged PE solution. The PEC deposition method mixes dilute solutions of oppositely charged PEs to create a dispersion, which is then cast, and the solvent (typically water) is evaporated to form the film, or the dispersion is filtered to obtain the membrane. These methods often take place in aqueous media, aligning with sustainability goals, but face challenges like nonuniform ionic cross-linking, lack of scalability, lengthy evaporation times, and poor control over membrane structure. Recent advancements, such as Krishna B et al.'s hot-pressing method (pressing a PEC agglomerate at a certain temperature) (**Figure 1.11H**), have mitigated these issues [99].

Recently, de Vos introduced a water-based approach to preparing PEC membranes, known as the aqueous phase separation (APS) approach, which combines NIPS' versatility with the benefits of

PE membranes. This process involves adjusting pH to control PE solubility for single polymer membranes (**Figure 1.11C**) and using pH- or salinity-switch methods for PEC membranes (**Figure 1.11G**), enhancing sustainability and scalability. Significant attention has been paid to fabricating PEC membranes using the APS approach. For example, Sadman et al. showed that polyelectrolyte complex membrane can be prepared from anionic PSS cationic poly(N-ethyl-4vinylpyridinium) (QVP-C2) using a salt-mediated aqueous phase separation process [59]. Here, only water was used as a solvent, and the salt concentration was used to trigger the phase separation. Durmaz et al. also reported that membranes can be prepared from anionic PSS and cationic PDADMAC by salinity change-induced APS process [100]. Baig et al. reported that the solution pH can also trigger aqueous phase separation [60]. They prepared membranes from PSS and PAH. Recently, Willot et al. and Nielen et al. also reported that membranes can be prepared from pH-responsive polymers using the APS process [85,86]. They used water and green acetic acid to prepare the membrane. Membranes prepared from the APS and NIPS show similar phase separation mechanisms, and the membrane structure can be controlled with different parameters. Since the APS process requires no toxic solvents (only water), it can be considered significantly more sustainable and greener than the conventional method. However, the main drawback of this process is that this process is only applicable to membrane preparation from water-soluble polymers. A brief summary of some aqueous phase separation membranes reported so far in the literature is provided in **Table 1.2**.

Green and sustainable membranes represent a key technology for advancing the circular economy and achieving sustainable development goals (**Figure 1.9C**) [66]. They align with circular growth principles, particularly in areas such as water treatment, filtration, energy production, and material separation. The sustainable development of membranes, achieved by utilizing biopolymers or waste valorization, is crucial in reducing natural resource consumption. This approach aligns with the circular economy's objective of maximizing resource utilization. Moreover, membranes prepared from low carbon footprints (using green solvents) prioritize resource conservation and minimize waste generation. Overall, using biodegradable materials and non-toxic solvents enhances human health and environmental well-being and plays a pivotal role in fostering a greener and more sustainable membrane manufacturing industry. However, the shift towards environmentally friendly solvents that align with regulations poses various challenges that require careful consideration, especially concerning their performance and competitive pricing.

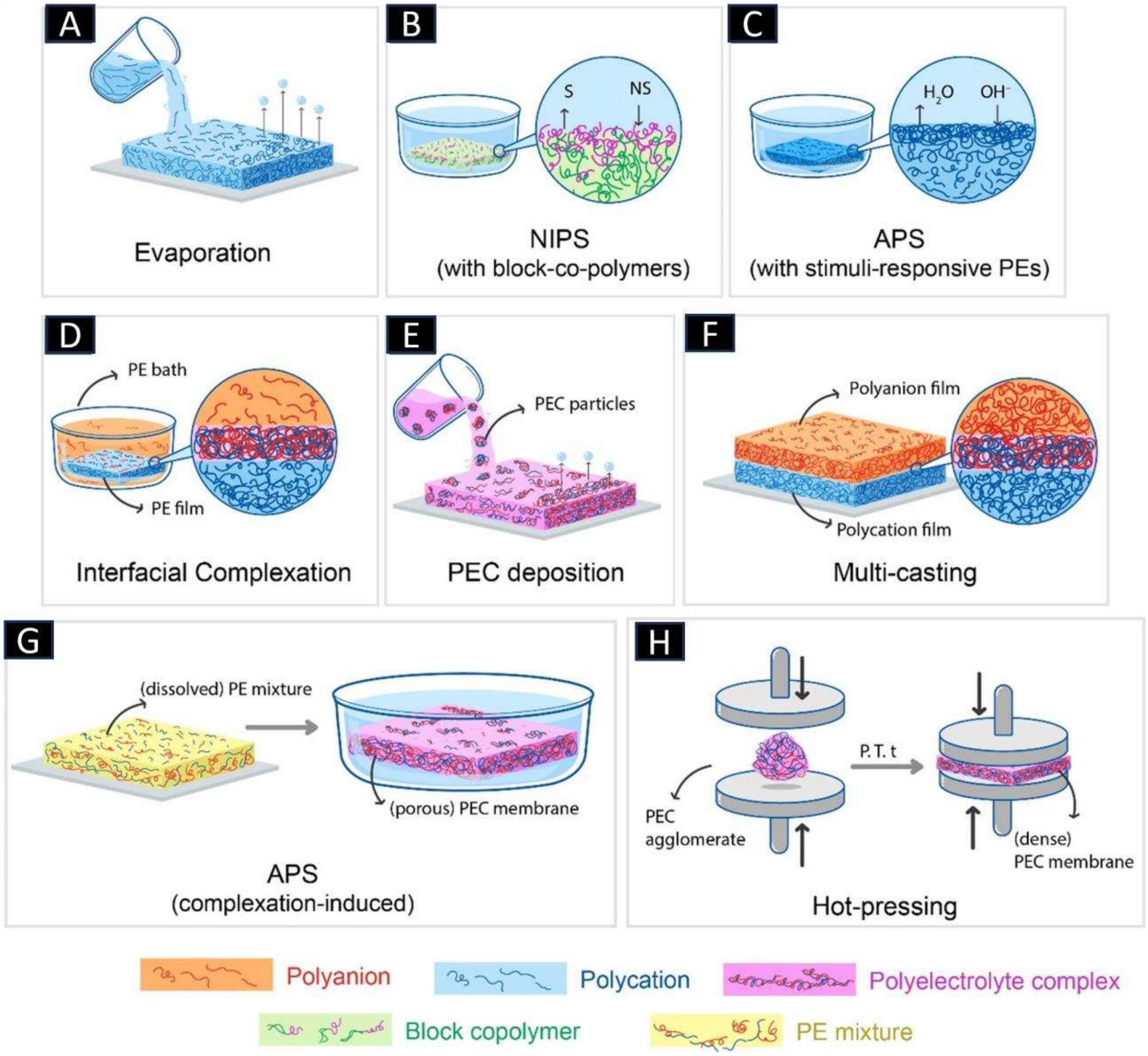

Figure 1.11. Illustrations of methods for preparing PE and PEC free-standing membranes: (A) solvent evaporation, (B) membrane formation from block copolymers via the NIPS technique, (C) membrane preparation with stimuli-responsive PEs via APS, (D) interfacial complexation between two oppositely charged PEs, (E) PEC deposition by removing water from PEC dispersion, (F) multicasting, where each layer can be formed from any PE or PEC solution, (G) membrane formation via complexation-induced APS, and (H) preparation of dense membrane by hot-pressing [98].

Table 1.2. Summary of some literature studies on aqueous phase separation membranes

Polymer	Solvent	Fabrication method	Application	Performance	Limitation	Ref.
q-PVP-PSS	Water	Precipitation followed by redissolution casting	UF	PWP 95-375 LMHbar^{-1}, >95% rejection of 100 nm Polystyrene particles	Multiple steps, time-consuming, less control parameters	[101]
PVP	Acetic acid/HCl	pH shift-induced APS	MF, NF	MF: PWP (250-950 LMHbar^{-1}), >97% oil droplet rejection, NF: PWP (2.2 LMHbar^{-1}, 94% calcein retention)	Poor stability and mechanical properties	[102]
PSS/PAH	High pH water	pH shift-induced APS	MF, UF, NF	MF: PWP (3200 LMHbar^{-1}), >99% oil droplet rejection, UF: PWP (12.5 LMHbar^{-1} , 98% BSA retention, NF: PWP (2 LMHbar^{-1}), >80% micropollutant retention))	Harsh condition, low PWP for NF and UF	[60,103]
PAA/PDADMAC	Water/H_2SO_4	pH shift-induced APS	MF	MF: PWP (1000 LMHbar^{-1}), >90% oil droplet retention	Low stability, harsh condition	[104]
PSS/PEI	Water	pH shift-induced APS	MF, NF	MF: PWP (65-130 LMHbar^{-1}), >99% oil droplet retention, NF: PWP (1.7-4 LMHbar-1), >97% $MgCl_2$ retention	Low pure water permeability, fossil-based polymer	[105]
PSS/PDADMAC	High salinity solution	Salinity gradient-induced APS	NF	NF: PWP (0.1-1 LMHbar^{-1}), >80% $MgSO_4$ retention	Low water permeability, limited control parameters	[100]
PSS/PDADMAC	High salinity solution	Salinity gradient-induced APS	UF	NF: PWP (20 LMHbar^{-1}), low salt retention	Low salt rejection, limited control parameters	[100]
PSS/PDADMAC	High salinity solution	Salinity gradient-induced APS	UF, NF	UF: PWP (6 LMHbar^{-1}), NF: PWP (0.1-0.2 LMHbar^{-1}), >90% $MgCl_2$ retention	Very low pure water permeability, limited control parameters	[106]
Chitosan	Acetic acid or base LiOH, KOH, Urea solution	APS	UF	UF: PWP (100-110 LMHbar^{-1}), >99% 100 nm PS particles retention	Poor stability	[107]

1.5 Perspective of biopolymers in membrane fabrication

Bio-sourced and biodegradable polymers are gaining prominence as alternatives to conventional synthetic materials. The perspective of biopolymers in membrane fabrication holds great promise for sustainable and eco-friendly advancements in materials science. From water treatment to biomedical applications and sustainable packaging, the versatility of biopolymers opens up new possibilities for addressing global challenges while promoting a greener future. Continued research and technological advancements in this field are essential to unlock the full potential of biopolymers in membrane-based technologies.

One key advantage of biopolymers is their eco-friendly origin and biodegradability, as they are sourced from renewable biomass. This stands in stark contrast to traditional non-degradable membrane materials, often derived from non-renewable petrochemical sources. Moreover, the use of biopolymers aligns with the principles of sustainability and circular economy, reducing dependence on finite resources and minimizing environmental impact.

The majority of biodegradable polymers used in membrane fabrication can be made from biobased and petro-based materials, such as cellulose acetate (CA), lignin, sodium alginate (SA), polylactic acid (PLA), polyhydroxyalkanoate (PHA), polybutylene succinate (PBS), polycaprolactone (PCL, and poly-(butylene adipate-co-terephthalate) (PBAT) [108]. Biopolymers offer a versatile platform for tailoring membrane properties. By manipulating the molecular structure and composition, researchers can fine-tune parameters such as permeability, selectivity, and mechanical strength. This tunability allows for the customization of membranes to suit specific applications, making biopolymers an attractive choice for a wide range of membrane-based technologies. In water treatment, biopolymer-based membranes have demonstrated comparable efficiency in separating contaminants and purifying water. Some examples of biopolymer usage in membrane fabrication have been discussed in brief below:

Cellulose acetate (CA): CA membranes have been extensively used on an industrial scale since the first asymmetric CA membrane was developed with high flux and high salt rejection by Loeb and Sourirajan [109]. They were initially used for desalination and ultrafiltration applications; later, they were used in pervaporation and gas separation applications [77,110]. CA is likely the ideal bio-based material for membrane fabrication owing to its several advantages, such as low cost, biodegradability, hydrophilicity, and facile synthesis [111]. However, the major disadvantages of the CA membranes are high fouling tendency, low flux, low oxidation, chemical resistance, and narrow operating ranges at different temperatures and pH. Most membranes also suffer from bacterial growth on the membrane surface, reducing membrane performance and service life. Several modifications on CA membranes have been reported to offset these issues, such as chemical grafting, surface modification, and plasma methods. Additive blending, for instance, the addition of pore formers and nanoparticles to the CA membrane, has also been investigated to improve the antifouling property as well as the performance of the CA membrane. Kalyani et al. blended sodium alginate and hydroxyethylcellulose to prepare a pervaporation membrane using phase inversion to separate *t*-butanol/water mixtures. After cross-linking with phosphoric acid, this membrane exhibited a selectivity of 3327 and a water flux of 0.2 $kgm^{-2}h^{-1}$ [112]. Ying Ee et al. recently used the electrospraying technique to coat the CA ultrafiltration membrane with octahedral UiO66-NH_2 nanocrystals and cellulose nanocrystals for desalination application [113]. The electrospray-coated CA membrane showed excellent resistance to biofouling, high water/salt permselectivity with almost double water permeability coefficient of 0.24 $Lm^{-2}h^{-1}bar^{-1,}$ and retention efficiency over 94% for brackish water desalination. Goetz et al. prepared cellulose acetate membrane via an electrospinning approach [114]. CA, acetic acid, and acetone were used to prepare the dope solution for electrospinning. The membrane surface was coated with chitin nanocrystals via filtration and drying to tailor the surface characteristics. The chitin coating resulted in a superhydrophilic membrane with a contact angle of 0°, whereas uncoated CA mats had a contact angle of 132°. This CA mat coated with 5% chitin nanocrystals also showed a 131% increase in mechanical strength and a 340% increase in stiffness. Moreover, biofouling and biofilm formation were also significantly reduced due to chitin nanocrystals' antibacterial and antifungal properties.

Bacterial cellulose (BC): BC is another cellulose-based material with high mechanical strength, hydrophilicity, and biodegradability. Due to its properties, it can be a promising material for membrane fabrication. Xi et al. prepared a bacterial cellulose-based underwater superoleophobic ultrafiltration membrane with nano-sized pores suitable for nanoparticles and nanoemulsions separation with sizes below 100 nm in an aqueous solution [115].

Lignin: Lignin is considered the second most abundant but underutilized biopolymer. It is primarily produced from the pulp and paper industry. Almost 50-70 million tons of lignin is derived annually from wood. However, only 1-2% of the produced lignin is utilized as a value-added product, while the majority is incinerated for energy generation [116]. The lignosulfonate molecule contains many aromatic rings and phenylpropane units containing hydroxyl and sulfonic groups [117]. These groups act as active centers for lignin modification and utilization. When added as a blend or composite, the interaction between lignin and polymers includes strong dipole-dipole interaction, ion-dipole interaction, Lewis acid-base interaction and charge transfer complexation, etc [118]. Lignin possesses excellent physical and chemical properties, such as biodegradability, high carbon content, thermal stability, and UV absorption properties [119]. The high phenolic and methoxy hydroxyl groups provide lignin with excellent antimicrobial and antioxidant properties. Due to the presence of many functional groups in the lignin structures, lignin derivatives can be used to modify the membrane properties when added as an additive. For example, Shamaei et al. modified the selective layer of TFC forward osmosis (FO) membranes using different concentrations of hydrophilic sulfonated kraft lignin (SKL) (1, 3, and 5 wt%) [120]. The modified TFC-FO membrane with 5 wt% of SKL provided a 2-fold enhancement in water flux compared to the pristine membrane. Moreover, it exhibited excellent antifouling performance and enhanced wettability compared to the unmodified membrane.

Sodium alginate (SA): SA is a hydrophilic anionic polysaccharide with a low price and good degradability [121,122]. It is easy to be crosslinked due to the presence of abundant carboxyl and hydroxyl groups. It is considered a promising material for different applications, such as dehydration of organics, oil/water separation, dye adsorption, and wound healing applications, due to its excellent resistance to organic solvents, solubility in water, biocompatibility, biodegradability, low toxicity, and good film forming properties [123–125]. Starch-based polymers have been used mostly as an additive for membrane fabrication. For instance, Ambre et al. prepared a mixed matrix nanofiltration membrane using hyperbranched graphene oxide-starch as an additive to improve the permeability and rejection efficiency [126]. Starch was also used in combination with polyvinyl alcohol (PVA) to prepare a hydrogel nanofiber membrane using an electrospinning technique to improve the water flux and separation efficiency [127].

Polylactic acid (PLA): PLA is a kind of aliphatic polyester obtained from biodegradable resources [46]. Generally, PLA is described as a semi-crystalline polymeric material with melting temperature (T_m) in the 170-180°C range and glass transition temperature (T_g) around 55-59°C.

The main issues with PLA polymer are its brittleness and low thermal stability, but different strategies, i.e., plasticizing, using it in combination with other polymers, or using some fillers, can help in increasing its applicability [51]. Zhang et al. synthesized PLA hollow-fiber membrane with improved hydrophilicity through a phase inversion process tailored by mixing some additives, i.e., PVP-K30 (polyvinylpyrrolidone K30) and Tween-80 [128]. The membrane showed high rejection of colloidal ferric hydroxide (98.5%), good permeance recovery (86.8%), pollution resistivity, and excellent antifouling behavior.

Polyhydroxyalkanoates (PHA): PHA is another highly promising biopolymer made by various Gram-positive and Gram-negative bacteria through fermentation using different carbon sources [129,130]. Because of their plastic-like characteristics and biodegradable nature, PHAs have the potential to serve as alternatives to non-biodegradable materials like poly(ethylene) (PE) and poly (propylene) (PP). The most known PHA polymers generated by microbes are polyhydroxy butyrate (PHB) and poly(3-hydroxybutyrate-co-3-hydroxyvalerate) PHBHV. PHAs have strong hydrolytic and UV resistance and sink in water, which helps speed up soil anaerobic decomposition. Additionally, they exhibit piezoelectric behavior. Their melting temperature is in the range of 40 to 180°C, while glass transition temperature falls between 50 to 4°C. Tomietto et al. fabricated biobased PHBHV membranes through phase inversion induced by evaporation, and these membranes were tested for microfiltration (MF) applications [131]. The results demonstrated pure water permeabilities exceeding 200 $Lm^{-2}h^{-1}bar^{-1}$, coupled with an impressive bacteria rejection rate of 99.95%.

Polybutylene Succinate (PBS): PBS is a promising aliphatic polyester with high chemical and thermal resistance, flexibility, low degradation rate, and affordable cost [46]. Butanediol and succinic acid, both of which can be found in bio-based renewable resources, were polymerized to prepare this semi-crystalline biopolymer. Its glass transition temperature and melting point range from 45 to -10°C and 90 to 120°C, respectively [51]. Its mechanical characteristics are comparable to PE and PP's, and its processibility is much better than that of other biopolymers like PLA. Bang et al. produced a nanofibrous membrane based on PBS, exhibiting impressive oil adsorption capacity (ranging from 18.7 g/g to 38 g/g) and high separation efficiency for water and oil mixtures (99.4–99.98%) and emulsions (98.1–99.5%) compared to conventional nanofibers made from organic polymers [132]. Importantly, in terms of disposal after use, this biodegradable nanofibrous membrane demonstrated the ability to return to nature through hydrolysis and biodegradation processes.

Ecoflex®: PBAT, predominantly derived from fossil sources, is commercially known as Ecoflex®, produced by BASF (Germany). Ecoflex® F Blend C1200 shares properties akin to LDPE due to its elevated molecular weight and long-chain branched molecular structure [133]. Ampawan et al. developed a PLA/PBAT-based membrane using a nonsolvent-induced phase separation process [134]. They blended PLA with PBAT and incorporated functionalized cellulose microfibers from empty fruit bunch (EFB), modified with maleic anhydride (MEFB). In a dynamic adsorption process, the PLA/PBAT-MEFB membrane exhibited a higher pure water flux (1214 $Lm^{-2}h^{-1}$) than the PLA/PBAT membrane (371 $Lm^{-2}h^{-1}$). Notably, the PLA/PBAT-MEFB membrane demonstrated superior performance in removing 97.2% of MB (Methylene Blue), while the PLA/PBAT membrane removed only 58.7%.

Overall, the above-mentioned biopolymer-based membranes not only address water scarcity challenges but also contribute to the development of sustainable water treatment solutions. Despite their numerous advantages, the widespread adoption of biopolymers in membrane fabrication remains challenging. Issues such as scalability, cost-effectiveness, and long-term durability must be addressed to ensure the commercial viability of biopolymer-based membranes. Lastly, finding compatible, non-toxic solvents for biopolymers that do not compromise membrane performance adds another layer of difficulty to their widespread adoption. Researchers and industry stakeholders are actively exploring innovative processing techniques and improving the understanding of the structural characteristics of biopolymers to overcome these challenges.

1.6 Research objectives

Membrane technology has become an integral aspect of our everyday existence. However, its rapid development has led to significant challenges, particularly the unsustainable disposal of used membranes. Additionally, certain aspects of membrane fabrication are not fully sustainable. For example, using fossil-based, non-biodegradable polymers and substantial amounts of toxic organic solvents in the manufacturing process poses serious health and environmental risks. The objective of this research was to explore innovative strategies to enhance the sustainability of the membrane fabrication process. This goal was achieved through several steps: replacing the conventional toxic solvents with greener alternatives, introducing two tuning parameters to enhance the performance of APS membranes, and employing environmentally friendly solvents and biodegradable polymers as promising replacements for fossil-based non-biodegradable membrane materials. These steps were performed to promote sustainability in the membrane fabrication process.

In order to achieve this research purpose, the following research initiatives were undertaken:

1. ***Preparation of organic solvent-free polyelectrolyte complex membrane and investigation of the effect of two tuning parameters to enhance the performance of APS membrane*****:** The first part of the research focused on developing high-performance polyelectrolyte complex (PEC) membranes using a toxic organic-solvent-free approach known as aqueous phase separation (APS). Two main methods, salinity change-induced APS and pH shift-induced APS, have been explored so far for APS membrane preparation. Salinity-gradient APS membranes exhibit robust stability in organic solvents, high salt rejection, and charge reversal capabilities, yet they face challenges with morphology control and low water flux. Conversely, pH shift-induced APS relies on PE charging behaviors at varying pH levels in the casting and coagulation solutions. This method allows for versatile combinations of strong and weak PEs to tailor microfiltration to nanofiltration membranes, but it requires extremely low pH solutions for complexation, limiting scalability. Recent advancements in mild pH-shift APS using PSS and PEI show promise but struggle with low pure water permeabilities. Therefore, there is still room to improve the APS membrane performance. Among the different combinations of PEs, the PSS-PEI combination could be the best choice due to the mild pH requirement and higher ionic crosslinking density. Like NIPS, the APS process showed excellent control over membrane pore size and performance. There are also some similarities in the key tuning parameters. For NIPS, it is well known that casting solution temperature significantly affects the thermodynamic and kinetics aspects of phase separation, which in turn significantly affects the structure and separation performance of membranes. However, the influence of this parameter was not investigated for any APS membrane formation. Besides casting solution temperature, the monomer mixing ratio could also affect the membrane morphology and performance. Therefore, introducing new tuning parameters—monomer mixing ratio and casting solution temperature—aims to optimize PSS/PEI APS membrane morphology and performance.

2. ***Developing a green and biodegradable high-performance electrospun membrane*****:** The previous work focused on the fabrication of polyelectrolyte complex membranes based on a water-based phase separation approach, which reduces toxic solvents. However, to achieve complete sustainability, non-biodegradable polymers must be replaced with biodegradable alternatives in membrane fabrication. Thus, the subsequent phase of this research focused on substituting non-biodegradable polymers with bio-based materials and employing eco-friendly solvents. Bio-based membranes produced with green solvents offer significant advantages in water purification but face challenges such as membrane fouling and structural stability over time. This study focused on utilizing the electrospinning technique to develop an environmentally friendly and biodegradable electrospun membrane by blending biodegradable polycaprolactone (PCL) with biobased sulfonated kraft lignin (SKL). SKL, sourced from a local pulp mill, was used in its untreated form to preserve its environmentally benign properties. Membrane researchers recognize that transitioning away from toxic solvents in membrane production processes poses a significant challenge. The selection of a suitable benign solvent for preparing PCL/SKL electrospun membranes was crucial to avoid secondary pollution and align with sustainable practices. The research also delved into understanding how varying levels of hydrophilic SKL content influence the morphology, mechanical properties, and wettability of the resulting PCL-based electrospun membranes. This pioneering study marks the initial exploration of the potential of green PCL/SKL electrospun membranes for applications in wastewater treatment.

3. ***Developing environmentally friendly membranes through a sustainable phase inversion approach*****:** The growing energy crisis and environmental pollution issues have made eco-friendly transformation in the membrane industry essential. Consequently, there is increasing interest in using bio-based and biodegradable polymers for sustainable membrane fabrication. Alongside this, the exploration of new environmentally friendly solvents has become significant due to the rising focus on sustainable and green chemistry. Transitioning from traditional solvents to eco-friendly alternatives depends on both their availability and compatibility with the specific polymers used in membrane production. This part of the research explores the use of biodegradable PCL, low-cost biobased SKL and a compatible green solvent in membrane fabrication via nonsolvent-induced phase separation. This study is the first to examine the potential of SKL and PCL as compatible materials for fabricating high-performance, environmentally friendly phase inversion membranes, employing acetic acid as a green solvent. The proposed approach not only ensures simplicity and scalability but also promotes sustainability in membrane fabrication.

1.7 Thesis structure

The current thesis is prepared in a paper-based format. Chapters 2, 3, and 4 were based on the published journal papers.

Chapter 1 introduces the research background and literature review, highlights research gaps, challenges, and potential solutions to research problems, and finally provides the research questions and objectives.

Chapter 2 presents an organic solvent-free aqueous phase separation process as a sustainable alternative for membrane fabrication. It introduces the monomer mixing ratio and casting solution temperature as new tuning parameters for preparing APS-based membranes. The chapter also provides a detailed investigation into how these parameters affect membrane morphology and performance.

Chapter 3 introduces a simple and eco-friendly method to fabricate biodegradable electrospun membranes by blending polycaprolactone with sulfonated kraft lignin in acetic acid using the electrospinning technique. This study highlights a novel functionality of the PCL/SKL blend, demonstrating its capability to fabricate superhydrophilic electrospun membranes with excellent anti-oil fouling properties. The study details the impact of SKL content on membrane morphology, mechanical properties, and wettability, as well as their stability, reusability, and biodegradability.

Chapter 4 uses the NIPS method to explore the potential of sulfonated kraft lignin as an environmentally friendly additive in producing biodegradable PCL membranes. This approach enhances environmental sustainability by employing a benign solvent (acetic acid) to prevent secondary pollution. The proposed approach in this study ensures simplicity, scalability, and sustainability in the membrane fabrication process. Additionally, this chapter provides a thorough characterization and performance analysis of the prepared membranes.

Finally, Chapter 5 summarizes the key findings of the research presented in this dissertation. This chapter offers insights into future research directions in sustainable and green membrane fabrication processes.

Chapter 2

Organic solvent-free polyelectrolyte complex membrane preparation: Effect of monomer mixing ratio and casting solution temperature*

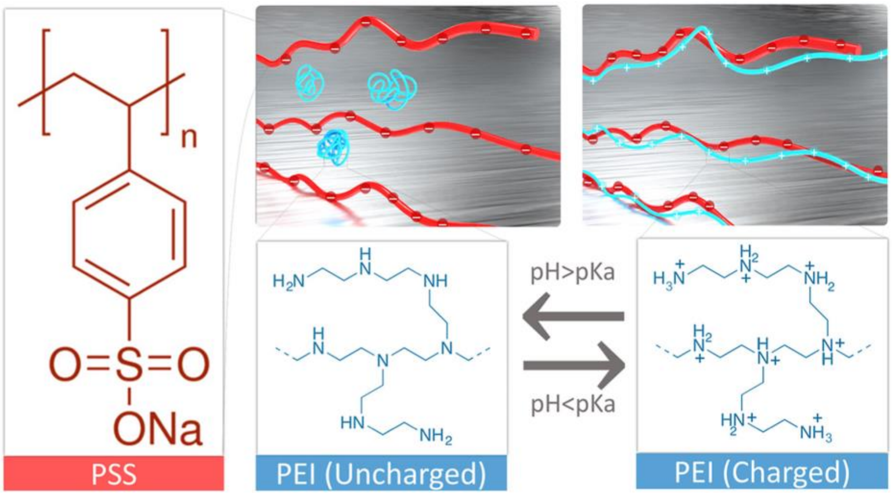

---

* Published as: **Md.M.H. Mizan,** M. Rastgar, S.A. Aktij, A. Asad, P. Karami, A. Rahimpour, Mohtada Sadrzadeh, Organic solvent-free polyelectrolyte complex membrane preparation: Effect of monomer mixing ratio and casting solution temperature, Published in Journal of Membrane Science, 2023, 668, 121197.

2.1 Introduction

Membrane-based technology has been used in a wide range of applications, including water and wastewater treatment [135], controlled drug delivery [136], food and dairy [137], pharmaceutical removal [138], and gas separation applications [139]. Most commercial polymeric membranes are prepared using phase separation techniques, mainly nonsolvent-induced phase separation (NIPS). One of the significant drawbacks of NIPS is the use of toxic organic solvents such as dimethylformamide (DMF), N-methyl pyrrolidone (NMP), and dimethyl acetamide (DMAc), which are harmful to human health and the environment [21]. Recently, the European Union has added these solvents to the restriction list through Registration, Evaluation, Authorisation, and Restriction of Chemicals (REACH) legislation [22–24]. The adverse effect of these toxic solvents led the researchers to look for alternative nontoxic, nonhazardous, and greener solvents for membrane fabrication [63,72,140,141]. Very recently, a complete water-based approach has been proposed for polymeric membrane fabrication, known as aqueous phase separation (APS) [142]. It eliminates the use of toxic organic solvents. In replacement, water is used as both solvent and nonsolvent mediums. Therefore, a particular class of water-soluble polymers, known as polyelectrolytes, is used in this novel technique. Polyelectrolytes (PEs) are polymers with ionizable groups in their repeating units [88]. Their dissociation in ionizing solvents, such as water and polar organic solvents (DMSO), determines the charge density in the polymeric chains [143]. Based on the charge density, PEs can be of two types: strong polyelectrolytes and weak polyelectrolytes [89,90]. Strong PEs are permanently charged over a wide pH range. Conversely, weak PEs dissociate partially over the intermediate pH range depending on their acid dissociation constant (pKa). Therefore, the pH of the polymer solution can be used to control its solubility and charge.

Two methods have been utilized so far to prepare APS membranes, i.e., “salinity change-induced APS” and “pH shift-induced APS’ [59,60,100,144]. In the former method, homogeneous casting solutions are prepared using two oppositely charged PEs at a high salt concentration. High salt concentration prevents the complexation between PEs by charge screening. It is then immersed in a low salt concentration at which complexation occurs, resulting in a water-insoluble solid film [100]. The membranes prepared using this method exhibited excellent stability in organic solvent (e.g., 2-propanol), high salt rejection, and charge reversal behavior [59,145,146]. However, limited control over membrane morphology and low water flux (~0.1-1 LMH/bar) are the major downsides of these salinity-based APS membranes. On the other hand, the pH shift-induced method involves either a single pH-responsive PE [26, 29] or a mixture of two oppositely charged PEs [60]. This method relies on the charging and uncharging behaviors of the PEs at different pH of the dope solution and coagulation bath. First, the casting solutions are prepared at a pH where one of the PEs is charged and the other is uncharged so that no interaction occurs between them. Afterward, this cast film is immersed in a nonsolvent at a pH where both the PEs are charged. Hence, complexation occurs between the PEs, resulting in the formation of a water-insoluble polyelectrolyte complex (PEC) membrane.

Many combinations of strong and weak PEs can be utilized to prepare microfiltration to nanofiltration membranes via pH shift-induced APS. Baig et al. reported two combinations of PEs to prepare different kinds of microfiltration and nanofiltration membranes [60,105]. One of them is the mixture of strong polyanion poly (sodium 4-styrene sulfonate) (PSS) and weak polycation poly (allylamine hydrochloride) (PAH). They prepared the casting solution at a high pH (~pH 14) where PSS is charged but PAH is uncharged, thus preventing the complexation. Then, the cast film was immersed in a low pH (~pH 1) solution, which charged the PAH, resulting in complexation and controlled precipitation, thus forming an insoluble PEC membrane [60]. Later, they systematically studied the influence of different tuning parameters, such as casting solution composition and coagulation bath composition, on preparing nanofiltration, ultrafiltration, and microfiltration membranes [103]. They reported that the difference in pH between the casting solution and coagulation bath acted as a driving force for H^+ diffusion into the solution; a rapid exchange of H^+ ions resulted in faster precipitation. However, the need for solutions with extremely low pH for complexation could limit its large-scale production. Recently, Baig et al. reported another combination of PEs (PSS and branched PEI (Polyethyleneimine)) that required mild pH conditions (~pH 12 to ~pH 4) for APS membrane preparation [105]. Although they reported decent salt and oil retentions in this work, pure water permeabilities were low for NF (~1.7 LMH/bar) and MF (~130 LMH/bar) membranes. Therefore, there is still room to improve the APS membrane performance with these monomers. PSS-PEI combination in this regard could be the best choice due to the mild pH requirement and higher ionic crosslinking density compared to PSS-PAH [147] and PAA-PDADMAC (Polyacrylic acid-Poly (diallyldimethyl ammonium chloride)) [104].

Like NIPS, the APS process showed excellent control over membrane pore size and performance. There are also some similarities in the key tuning parameters, such as casting solution and coagulation bath compositions. For NIPS, it is well known that casting solution temperature has a significant effect on the thermodynamic and kinetics aspects of phase separation [148–152], which in turn significantly affects the structure and separation performance of membranes. However, the influence of these parameters has not yet been investigated for any APS membrane formation. Previous studies on APS membranes, particularly PSS-PEI membranes, showed low pure water permeabilities, which need to be improved by fine-tuning the key parameters. Besides casting solution temperature, the monomer mixing ratio could also enhance the water flux. It was reported for PSS-PAH and PSS-PDADMAC systems that the monomer mixing ratio significantly affects the final membrane morphology, pure water permeability, and surface charge [103,146].

Given the gaps and drawbacks of APS membranes, the present work focused on improving the performance of the PSS-PEI membrane prepared via an organic solvent-free APS process. We systematically investigated the effect of monomer mixing ratio and casting solution temperature on PSS-PEI membrane formation. We will demonstrate how monomer mixing ratios control the final membrane morphology and improve the water flux. Moreover, casting solution temperatures were varied to investigate their effects on final membrane morphology and pure water permeability. The findings of this work will contribute to developing high-performance organic solvent-free NF and UF membranes simply by tuning the casting solution temperature and monomer mixing ratio.

2.2 Experimental

2.2.1 Materials

PSS (average M_w. 1000 kDa, powder form) and Branched PEI (average M_w. 25 kDa, 100 wt%) were purchased from Sigma Aldrich and used as polyanion and polycation, respectively. Glacial acetic acid (ReagentPlus, ≥99.0%), sodium acetate (anhydrous, ReagentPlus, ≥99.0%), glutaraldehyde (GA, 25 wt% in water), glycerol solution (83.5-89.5%), polyethylene glycol (PEG) with different molecular weights (200, 400, 600, 1500, 2000, 6000, 10000, 20000 and 35000 $gmol^{-1}$), humic acid (HA), n-hexadecane and salts such as magnesium sulfate ($MgSO_4$, >99.5%), magnesium chloride hexahydrate ($MgCl_2.6H_20$, ≥99%), sodium chloride (NaCl, >99.5%) and sodium sulfate (Na_2SO_4, 99%) were purchased from Sigma Aldrich. Bovine Serum Albumin (BSA) was purchased from ChemCruz. Phosphate buffer saline (PBS) of pH 7.4 was kindly provided by the Biochemistry lab of the National Research Council (NRC), Canada. Deionized water (18.2 M cm^{-1}, Milli-Q, Millipore) was used to prepare the casting solution and the coagulation bath. All the chemicals were used without further purification.

2.2.2 Membrane preparation

2.2.2.1 Casting solution preparation

The casting solutions were prepared in two steps. The first step consists of preparing two individual solutions of PSS and PEI. In this step, pure PSS was dissolved in deionized water to obtain a 25 wt% aqueous solution of PSS (pH of ~8). Likewise, a 25 wt% aqueous solution of PEI was prepared by diluting pure PEI with deionized water (pH of ~12). Then, both solutions were continuously stirred to make them homogeneous. In the next step, two polyelectrolyte solutions were mixed at different monomer molar mixing ratios, ranging from 1:1.65 to 1:1.80, to prepare 25 wt% casting solutions. The pH of all the casting solutions was ~12 (**Figure A.S1**). The molecular weights of the monomers (PSS ~206.19 Da and PEI ~43.04 Da per ethylenimine unit) were used to calculate the desired molar mixing ratio. The casting solutions were then stirred until they became homogeneous. The composition of the casting solution is shown in **Table 2.1**. Casting solutions with other monomer ratios, such as 1:1, 1:1.50, and 1:1.60, were also prepared; however, these resulted in either a soft gel-like material or a very dense membrane with low water flux. Moreover, the monomer mixing ratio above 1:1.80 resulted in an irregular top surface. All the casting solutions were left unstirred overnight until they became bubble-free.

Table 2.1. Composition of casting solution prepared at different monomer ratios

Monomer Ratio (PSS:PEI)	PSS (wt%)	PEI (wt%)	Water (wt%)
1:1.65	18.62	6.38	75
1:1.70	18.45	6.55	75
1:1.75	18.30	6.70	75
1:1.80	18.16	6.84	75

2.2.2.2 Casting

The PSS-PEI casting solutions, prepared at different monomer mixing ratios, were cast on a plexiglass plate and then spread over the plate using a micrometer film applicator (Gardo, Pompano Beach, FL, USA) with a clearance gap of 500 µm. An automatic film applicator (TQC Sheen, AB3120, The Netherlands) was used to adjust the casting speed at 10 mm/s. The plexiglass plate is then immersed in a 0.5 M acetate buffer bath at pH 4. The buffer bath was prepared at room temperature by adding a specific amount of acetic acid and sodium acetate. Compared to other pH and acetate buffer concentrations, PSS-PEI membranes prepared at 0.5M acetate buffer bath at pH 4 exhibited relatively better water permeability and mechanical strength performance, as reported in the literature [105]. In addition, Glutaraldehyde (GA) was added to the buffer bath to densify the membrane structure and improve the mechanical strength. GA reacts with the primary amine groups of PEI under aqueous conditions and forms an imine bond via the Schiff base reaction [153,154]. The effect of GA on APS membranes has already been elaborately studied by Baig et al. for the PSS-PEI and PSS-PAH aqueous phase separation membranes [60,105]. Based on their study, a 0.01 wt% concentration of GA was chosen to keep its concentration as low as possible since it is toxic at higher concentrations. The cast films precipitated in less than 30 seconds after immersion. After five hours, they were removed from the buffer bath and stored in deionized water for further characterization and performance tests. To evaluate the effect of casting solution temperature, the homogeneous casting solution was heated to the desired temperature (40 and 60°C) without stirring using a hot plate for about 15 min. The plexiglass plate was also heated to adjust the casting solution temperature. The heated casting solutions were then cast and immersed immediately in the buffer bath. After five hours, the precipitated films were removed from the acetate buffer bath and stored in deionized water for further use.

2.2.3 Membrane characterization

2.2.3.1 Evaluation of the viscosity of the casting solutions

The viscosity of the casting solution was measured using a rotational rheometer (Malvern Kinexus Lab+) at three different temperatures, namely at 25, 40, and 60°C. The sample solutions were loaded between two plates and waited until stabilization at the desired temperature. The dynamic viscosities were recorded as a function of shear rate (0.1-100 s^{-1}).

2.2.3.2 Evaluation of the surface potential of the membranes

The zeta potential of the membranes was evaluated with a Surpass^{TM} 3 Electrokinetic analyzer (Anton Paar, Graz, Austria). The zeta potential values were measured over the pH range of 4-9 using a 1 mM KCl solution. Sodium hydroxide and Hydrochloric acid were used to adjust the pH to desired values.

2.2.3.3 Evaluation of the chemical compositions of the membranes

The chemical nature of the fabricated membranes was determined using attenuated total reflectance-Fourier transform infrared (ATR-FTIR). The infrared spectra were measured at room temperature using Agilent Technologies, Cary 600 series. All samples were scanned thirty times over the wavelength range of 400-4000 cm^{-1} and with a resolution of 4 cm^{-1}.

2.2.3.4 Evaluation of the surface topography of the membranes

The surface morphology and cross-sectional structure of the fabricated membranes were examined by a field emission scanning electron microscope (FESEM, Zeiss Sigma 300 VP) at the acceleration voltage of 10 kV. Before SEM analysis, all the membrane samples were immersed in 20 wt% glycerol solution, followed by drying in a fume hood to prevent pore collapse. For cross-section SEM imaging, the samples were first immersed in liquid nitrogen and then fractured carefully. Afterward, all the SEM samples were kept in a vacuum oven at 30 °C overnight. Before imaging, all the membrane samples were sputter-coated with gold (~10 nm). ImageJ software was used to determine the average thickness of the membranes. The surface topography of the fabricated membranes was evaluated using atomic force microscopy (AFM, Bruker Dimension Icon, USA). All the AFM measurements were executed in tapping mode at a scan rate of 1.0 Hz under ambient temperature and humidity over a 10 µm × 10 µm surface area of the samples. Nanoscope analysis software V.1.40 was used to analyze the AFM data and to calculate the surface roughness parameters.

2.2.3.5 Evaluation of the surface wettability of the membranes

The surface wettability of the membranes was evaluated by contact angle analysis. The analysis was carried out by sessile drop method using a contact angle analyzer (Kruss DSA 100 Gmbh Germany) with a 2 µL droplet of DI water in air. The droplet of water was deposited on the membrane surface using a micro syringe. At least three droplets were placed on the surface for each sample, and average contact angles were measured.

2.2.3.6 Evaluation of the permeation performance of the membranes

Membrane filtration was conducted using a dead-end setup (Amicon, UFSC05001). The effective membrane area was 13.4 cm^2. Compressed nitrogen gas was used to apply the desired pressure. Each membrane was compacted until a steady flux was reached at 10 psi and 40 psi for UF and NF membranes, respectively. The permeate weight was recorded with a weighing balance (ME4002, Mettler Toledo, USA) at regular time intervals. Pure water flux (*J*) was then determined using the following equation:

$$J\ (Lm^{-2}h^{-1}) = \frac{M(kg)}{\rho(kgL^{-1})A(m^2)\Delta t(h)} \tag{2.1}$$

where M is the mass of the permeate, ρ is the density of water, A is the effective membrane area, and Δt is the measurement time. The permeability (*P*) was calculated from the slope of the constant flux versus transmembrane pressure as follows:

$$P\ (Lm^{-2}h^{-1}bar^{-1}) = \frac{J\ (Lm^{-2}h^{-1})}{TMP\ (bar)} \tag{2.2}$$

where TMP is the transmembrane pressure, defined as the pressure difference between the feed and permeate sides.

2.2.3.7 Evaluation of the molecular weight cut-off of the membranes

The molecular weight cut-off (MWCO) of the fabricated membranes was evaluated using dilute aqueous solutions (250 ppm) of PEG having different molecular weights, ranging from 0.2-35 kDa. Before each experiment in a dead-end cell, all the NF-type membranes were pre-compacted at 40 psi to reach a steady state of pure water flux. Similarly, membrane pre-compaction was done at 10 psi for UF membranes to achieve a stable pure water flux. Afterward, MWCO measurements were conducted starting from the lowest MW of the PEG solution. Different MW of PEG solutions were filtered through the dead-end cell, and samples from feed, permeate, and retentate solutions were collected for the total organic carbon (TOC) analysis using a total organic carbon analyzer (TOC-L CPH, Shimadzu, Japan). During the filtration, the PEG solution inside the cell was continuously stirred to minimize the concentration polarization. Before replacing different MW of PEG solution, membrane surfaces were washed by stirring with deionized water for 20 min at 200 rpm. The MWCO is defined as the minimum molecular weight of a solute at which the membrane retains 90 % of the solute. The TOC retention results were calculated using **Eq. 2.4** were plotted against the molecular weights of PEGs and extrapolated to 90% retention to determine the MWCO of each sample. MWCO values (in Da) were used to determine the average pore size of the membranes (d_p in nm) using the following equation [155]:

$$d_p = 0.09(MWCO)^{0.44} \tag{2.3}$$

2.3.8 Evaluation of the separation performance of the membranes

The nanofiltration performance of the membrane was evaluated by different monovalent and divalent salt retention tests in the dead-end cell. Approximately 40 ml of 5 mM aqueous solution of NaCl, $NaSO_4$, $MgSO_4$, and $MgCl_2.6H_20$ were used as the feed and filtered through the cell at 40 psi. Salt solutions were stirred continuously to minimize the concentration polarization during the experiment. The feed, permeate, and retentate samples were collected and tested for conductivity using a Fisher Scientific AR50 ion conductivity meter. Separate calibration curves were first generated using the known concertation of salt solutions. The salt concentration in the feed, permeate, and retentate was then evaluated by analyzing their conductivities. The salt retention (*R*) was then calculated using **Eq. 2.4**.

$$R(\%) = \left(1 - \frac{C_P}{(C_F + C_R)/2}\right) \times 100 \tag{2.4}$$

Where C_F, C_p, and C_R are the feed, permeate, and retentate concentrations, respectively. Since the feed concentration constantly changes in the dead-end cell, an average of C_F and C_R was considered for retention calculation.

The ultrafiltration performance of the membranes was investigated using protein (BSA) and a model organic matter (HA) retention test. An aqueous solution of BSA was prepared by dissolving 100 ppm of BSA in 1× phosphate buffer saline (PBS) of pH 7.4. The solution pH was then adjusted at 7.0 using 0.1 M hydrochloric acid (HCl). BSA is negatively charged at this pH [156]. Next, the BSA solution was filtered through the membranes in a dead-end cell at 10 psi. The concentration of BSA in feed, permeate, and retentate was analyzed using a total organic carbon analyzer (TOC-L CPH, Shimadzu, Japan), and retention was calculated using **Eq. 2.4**. A 100 ppm of HA was prepared by dissolving in 0.1 M sodium hydroxide, followed by the pH adjustment to 7.0 with 1 M HCl. Humic acid is negatively charged at this pH [157]. The as-prepared HA solution was then filtered through the membranes in a dead-end cell at 10 psi, and permeate sample was collected. The HA concentration in the feed, permeate, and retentate was evaluated from their absorbance at the wavelength of 254 nm using a UV–Vis spectrophotometer (Thermo Electron Corporation, model: Genesys 10- S). The HA retention was then determined using **Eq. 2.4.** The flux J_1 while filtering the BSA and HA solution was recorded and used to find the flux decline rate (FDR) based on the following equation:

$$FDR = (1 - \frac{J_1}{J}) \times 100 \tag{2.5}$$

After filtering BSA and HA solution, membrane is washed and filtered with pure water again. This pure water flux (J_2) was recorded and used to determine the flux recovery rate (FRR) of the membrane using the following equation:

$$FRR = (J_2/J) \times 100 \tag{2.6}$$

2.3 Result and Discussion

In this work, PSS-PEI complex membranes were prepared using a pH shift-induced APS approach at varying casting solution temperatures and monomer molar mixing ratios. The effect of the PSS-PEI monomer molar mixing ratio and casting solution temperature on the membrane structure and performance are discussed in the following sections.

2.3.1 Effect of monomer molar mixing ratio

The casting solutions were prepared at different PSS and PEI monomer mixing ratios, varying from 1:1.65 to 1:1.80. These homogeneous solutions had a pH of ~12, which is higher than the pKa of primary (4.5), secondary (6.7) and tertiary amines (11.6) of branched PEI [158,159]. At such pH in the casting solution, branched PEI remained at a deprotonated (uncharged) state; hence no complexation between PSS and PEI was observed. After immersing the cast film in a bath containing 0.01 wt% GA and 0.5 M acetate buffer bath at pH 4, the branched PEI is fully charged. Hence, pH-induced complexation occurred between PSS and PEI immediately after immersing in an acetate buffer bath, resulting in a water-insoluble solid film. The fabrication process is shown schematically in **Figure 2.1**.

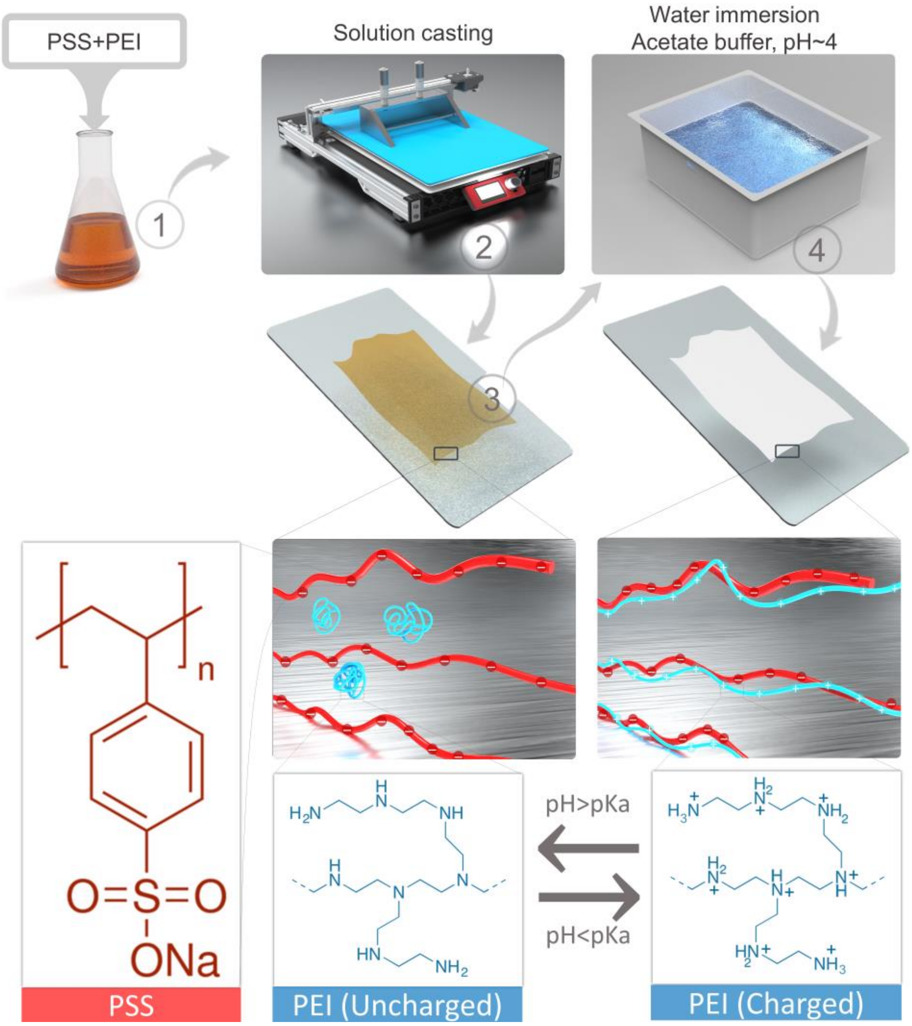

Figure 2.1. A schematic illustration and mechanism of the membrane fabrication process. (1) Dissolution of PSS/PEI with different mixing ratios in water, (2) casting of the polymeric solution through a film applicator, (3) immersing of the cast solution in an acetate buffer bath for phase inversion, and (4) washing of the solidified membrane with DI water. As can be seen, the low pH of the acetate buffer solution bath promotes protonation along branched PEI chains where the electrostatic forces between negative PSS and positive PEI cause complexation in the cast membrane film.

The surface and cross-section morphology of these membranes were evaluated using SEM analyses. **Figure 2.2** shows the SEM images of the membranes prepared at different monomer ratios. All the membranes were asymmetric in structure, having a dense top layer with a finger-like substructure. Baig et al. also observed a similar membrane structure for a 1:2 ratio of PSS and PEI [105]. The rapid precipitation due to the large driving force (pH~12 to pH~4) was attributed to the formation of the finger-like substructure of these membranes. There is no clear observation of defects on the top surface of the membranes even at ×30,000 magnification. Membranes prepared above the 1:1.75 ratio of PSS-PEI formed patterned surfaces, as seen from the photograph in **Figure A.S1**. The higher degree of branching in the presence of excess PEI can be the reason for this patterned surface formation. It was reported in the literature that the precipitation process slows down in the presence of excess charge [103]. Therefore, another possible reason for this patterned morphology can be the branched-chain rearrangement during the slower precipitation process. This morphology is a new finding for PSS-PEI membranes, which was not observed in the previous studies at varying monomer ratios.

The surface topography images of the membranes at different monomer ratios are shown in **Figure 2.3**. The arithmetic average roughness (*Ra*) and root mean square average roughness (*Rq*) are shown in **Table 2.2**. Membrane surface roughness increased from ~6 nm to ~12 nm when the monomer ratio of PSS-PEI changed from 1:1.65 to 1:1.80. This trend can be attributed to the excess amount of PEI, generating more heterogeneous morphology [160,161]. The higher content of PEI in the casting solution resulted in positively charged membranes, as seen in **Figure 2.4A.** Zeta potential tests indicated that surface charge increased from ~7 mV to ~21 mV at pH 6 with the changes in the PSS-PEI monomer ratio (**Table 2.2**). This increase in zeta potential suggests a lower number of ion pairs per carbon atom in the PEC membranes at a higher monomer ratio [147]. Hence, at a 1:1.65 monomer ratio, a relatively compact membrane is expected due to a lower excess charge and higher ionic crosslinking.

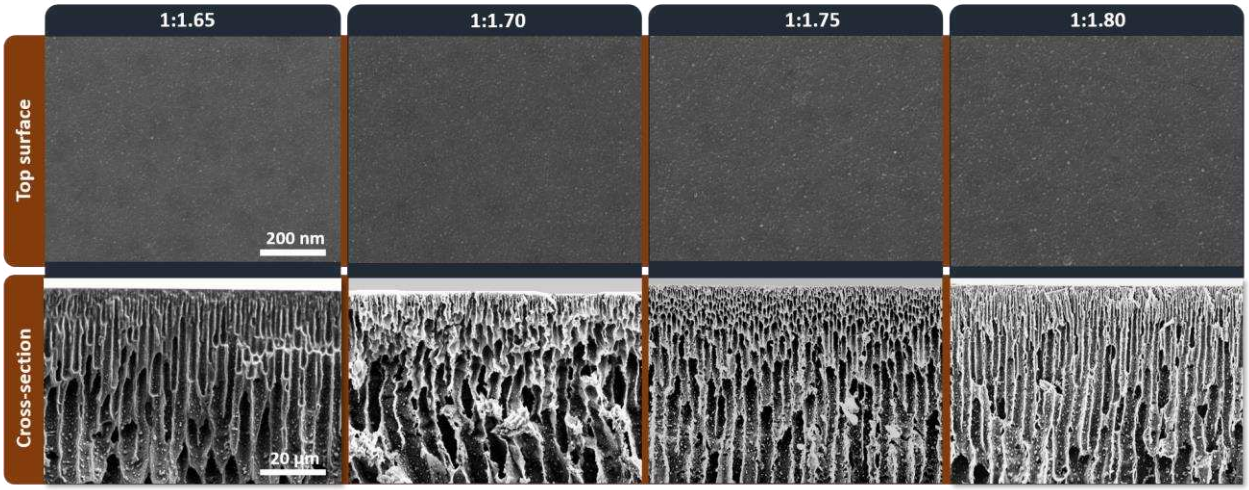

Figure 2.2. Top surface and top cross-section SEM images of PSS-PEI membranes at different monomer ratios. Top surface images were taken at ×30000 magnification.

In contrast, a more swollen and open structure is expected with higher excess charges [146,162]. This hypothesis agrees with the experimental observation, as a more swollen and pattern-like surface was formed at a PSS-PEI monomer ratio of 1:1.80. Therefore, the change in roughness is mainly due to the more compact structure at a lower monomer ratio compared to the more swollen structure at a higher monomer ratio of PSS-PEI. The excess charges due to the excess PEI and the increased surface area due to the patterned and rougher surface could synergistically improve the membrane performance.

The water contact angle of the membranes is shown in **Table 2.2**. It can be seen that the contact angle did not change significantly, it reduced slightly from 42° to 40° with the change in monomer mixing ratio, likely due to the excess amine group on the membrane surface.

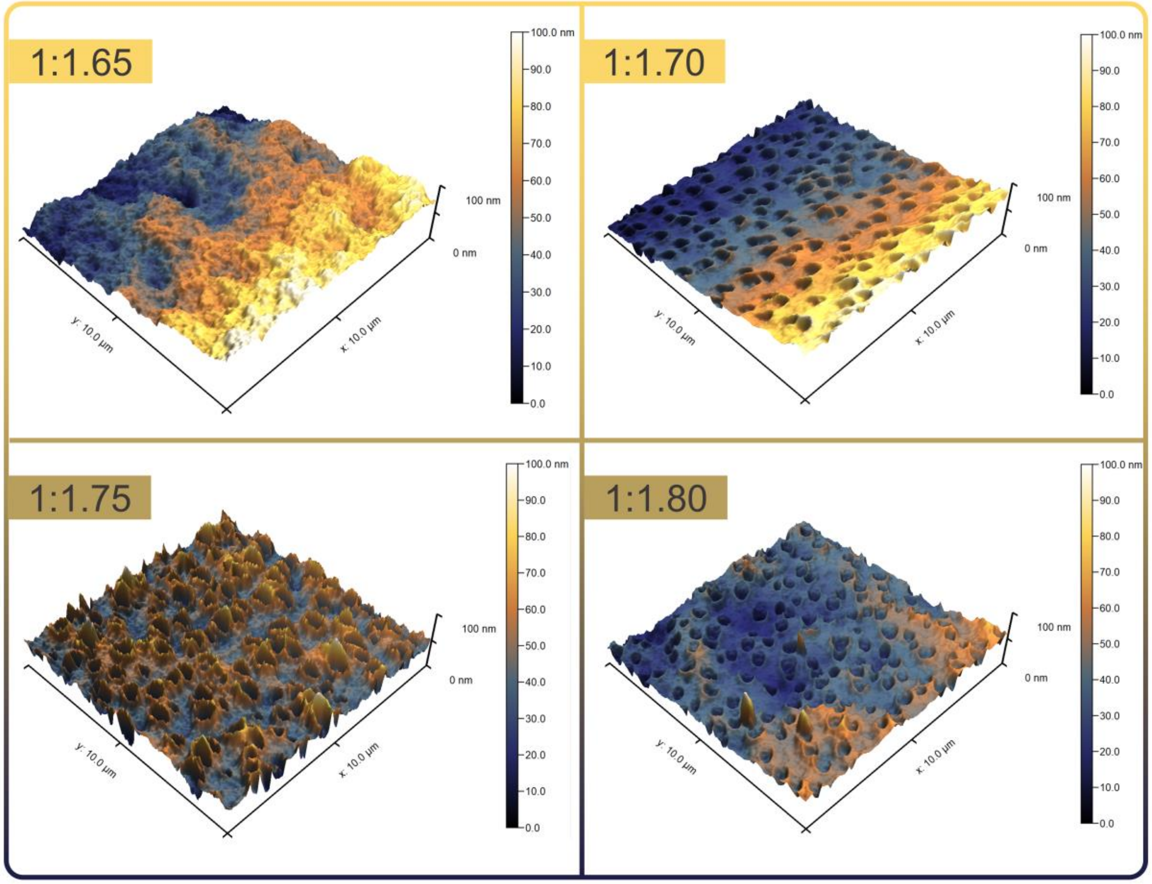

Figure 2.3. AFM topographic images and surface roughness values of the membranes were prepared at different monomer mixing ratios of PSS and PEI.

Table 2.2. Surface roughness parameters, zeta potential, and contact angle values of the membranes at different monomer mixing ratios of PSS and PEI. All values are reported from at least three different measurements from different samples.

Monomer mixing ratio (PSS:PEI)	Ra (nm)	Rq (nm)	Contact angle (°)	Zeta potential at pH 6 (mV)
1:1.65	6 ± 1.3	8 ± 1.5	42.2 ± 1.0	7.8 ± 1.0
1:1.70	9 ± 1.0	12 ± 1.0	41.5 ± 0.7	11.4 ± 1.0
1:1.75	10 ± 1.0	14 ± 1.5	42.0 ± 0.5	13.2 ± 1.2
1:1.80	12 ± 1.0	16 ± 1.5	40.4 ± 0.8	20.6 ± 1.5

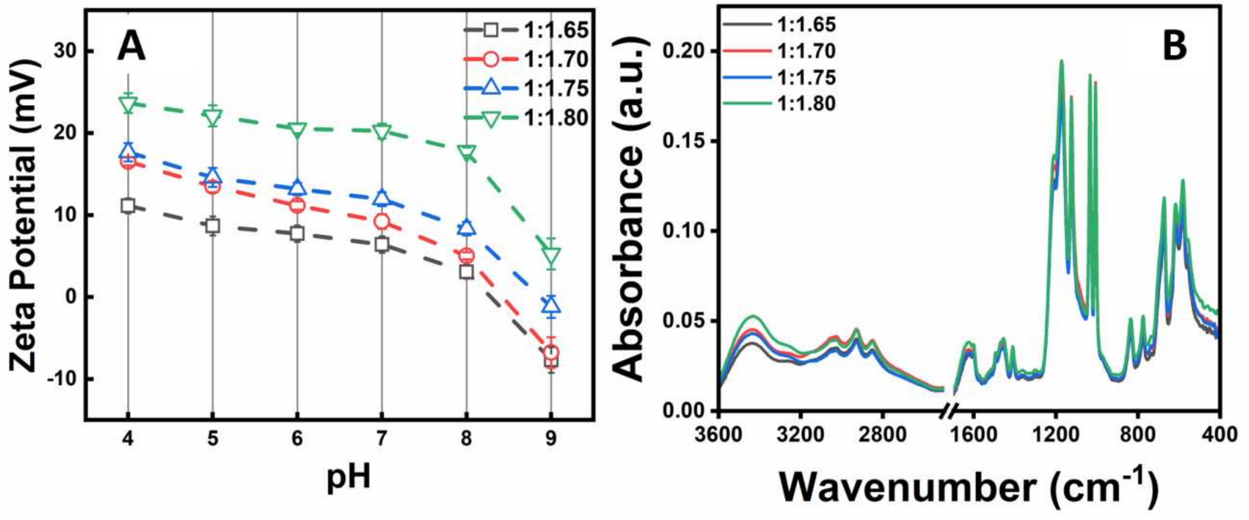

Figure 2.4. Effect of PSS-PEI monomer ratio on (A) surface zeta potential and (B) FTIR spectrums of the resultant membranes. The zeta potential values are reported from at least three different measurements from different samples.

The information about the chemical composition of the membranes was obtained using FTIR analysis, as shown in **Figure 2.4B**. There are no significant changes in the FTIR spectrum for different monomer ratio membranes, which is expected since all of them were prepared using the same recipe except for a change in monomer ratio. All spectra exhibited characteristic peaks at 3400 cm^{-1} (N-H stretch), 2975 cm^{-1} (C-H stretch), 1167 cm^{-1} (C-N stretch), and 678 cm^{-1} (N-H wag). The peak at 1660 cm^{-1} represented the imine bond formed from the Schiff-base reaction between GA and the primary amine of PEI [154]. Two peaks at 1006 and 1035 cm^{-1} are ascribed to the sulfonate moieties of PSS [163].

Figure 2.5A shows the effect of monomer mixing ratios on pure water permeability (PWP) values. Membranes prepared at 1:1.65 and 1:1.70 showed relatively less permeability, i.e., ~4.5 and ~8 $LMHbar^{-1}$, respectively, compared to membranes prepared at 1:1.75 and 1:1.80 ratio, i.e., ~39 and ~199 $LMHbar^{-1}$, respectively. **Figure A.S2** shows the change in pure water permeability with time. The sharp increase in permeability can be attributed to the more open structure and higher surface area of membranes at a higher monomer ratio. As shown in **Figure 2.4A,** surface charges increase with the increase in monomer ratios. The excess charge results in a more swollen and open membrane structure, resulting in more water pathways through the membrane and enhanced PWP [146]. Moreover, membranes with higher surface charges can attract more water molecules, increasing the water flux through the membrane [146,164,165].

Another apparent reason for the increasing trend in permeability is the change in the pore sizes of the membranes with a monomer ratio. MWCO of the membranes was evaluated to determine the average pore sizes and the potential application of these membranes. **Figure A.S4** presents the molecular sieving curves of the membranes. The MWCO was calculated at 90% retention of PEG solutes. It shows that MWCO varies with the monomer ratio, i.e., ~214 Da and ~294 Da for 1:1.65 and 1:1.70, respectively, which are ideal for nanofiltration (NF) applications (200-1000 Da) [11]. Therefore, these membranes would be suitable for water softening by retaining hydrated divalent and multivalent cations [166] and removing small organic molecules in pharmaceutical wastewater [167]. On the other hand, MWCO was ~10100 Da for the ratio of 1:1.75, which is in the range of ultrafiltration (UF) applications (1-1000 kDa) [168]. The average pores size of the membranes was calculated using **Eq. 2.3** and presented in **Figure 2.5B**. The average pore sizes were 0.95, 1.10, and 5.20 nm for 1:1.65, 1:1.70, and 1:1.75 membranes, respectively. The larger pore size usually resulted in an enhancement in permeate flux [169], which was also in line with the membrane performance observed from the PWP values in **Figure 2.5A**. The pore size enlargement can be attributed to less ionic crosslinks and more branched chains of PEI at a higher monomer ratio [170]. It was reported in the literature that PECs that are closer to the stoichiometric ratio of PEs have more ionic crosslinks resulting in a more compact (i.e., denser) structure [171]. Therefore, with a higher concentration of PEI, such as for PSS-PEI monomer ratios of 1:1.75 and 1:1.80, less ionic crosslinks can be expected, resulting in a less compact structure on the surface (i.e., larger pores). The operation pH range of the PSS-PEI APS membrane was determined by the pH stability test of the membrane. The membranes prepared at 1:1.70 were immersed in different pH aqueous solutions, i.e., pH 1, pH 4, pH 8 and pH 10, for seven days and then tested to evaluate their performance. The pH stability experiment showed that pure water permeability remained the same for the membranes treated at pH 1, 4 and 8 (**Figure A.S2**). However, the pH 10 treated membrane showed instability, probably due to the APS membrane's decomplexation (PEI becomes uncharged at this pH). Therefore, pH 1 to 8 is the operating range for this developed membrane. This finding agrees with the previous APS membrane study [105].

The nanofiltration performance of the membranes prepared at different monomer mixing ratios was evaluated based on retention tests of four types of salt, consisting of monovalent and divalent anions and cations. **Figure 2.5C** shows the salt retention performance of membranes formed at 1:1.65 and 1:1.70 monomer ratios. Since all the membranes have an excess amount of PEI, positive surface charges are expected, which was confirmed by their zeta potential values (**Figure 2.4A**).

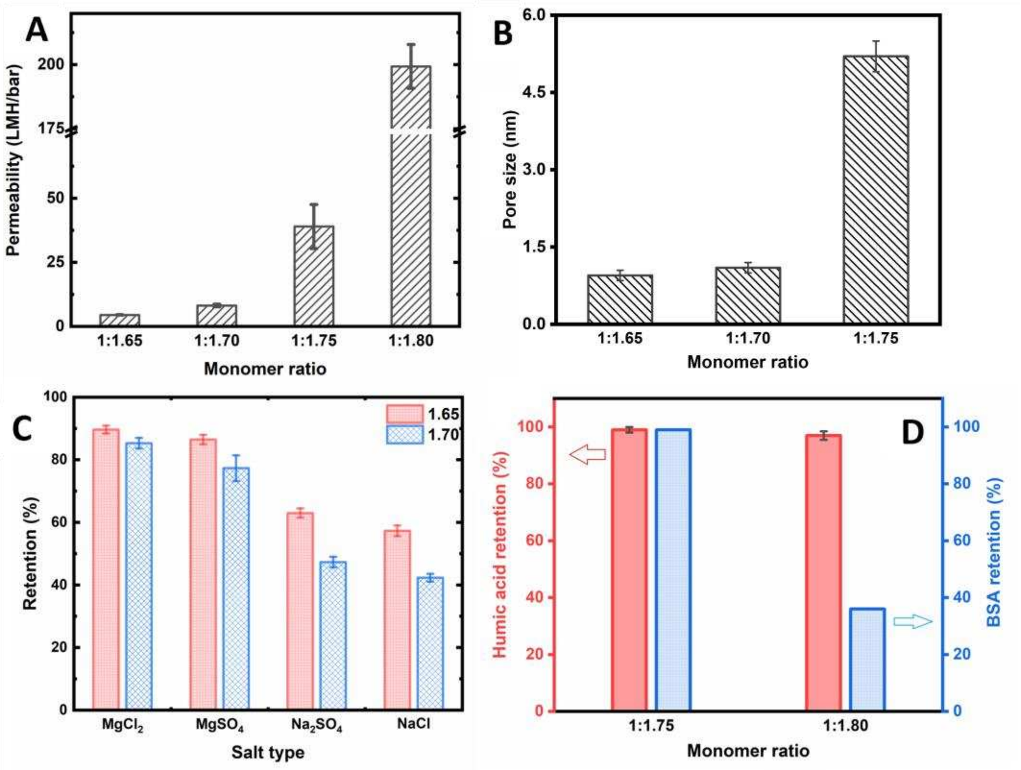

Figure 2.5. (A) Pure water permeability, (B) pore size, (C) salt retention, and (D) humic acid and BSA retention of membranes at different monomer mixing ratios. All permeability and retention values are from at least three different measurements from different samples.

The salt retention data shows that all membranes retain divalent cations (i.e., $MgCl_2$ and $MgSO_4$) more than monovalent cations (i.e., NaCl and Na_2SO_4), signifying the influence of species charge on separation performance. This separation phenomenon can be explained based on the Donnan exclusion mechanism. According to this mechanism, membranes with an excess charge repel the ions of the same charge and vice versa [162,172]. In contrast, size exclusion (also known as the sieving effect), dielectric exclusion, and steric hindrance can also determine the salt retention performance [173,174]. As can be seen from **Figure 2.5C** that NaCl salt retained less than Na_2SO_4, revealing that salt separation occurred due to the size exclusion effect. These findings are in agreement with the salt separation performance of PSS-PEI APS membranes reported by Baig et al. [105]. For 1:1.65 monomer ratio, salt retention was following the order of $MgCl_2$ (~90%) > $MgSO_4$ (~86%) > Na_2SO_4 (~64%) >NaCl (~57%). Similarly, 1:1.70 ratio membranes followed the order of $MgCl_2$ (~85%) > $MgSO_4$ (~77%) > Na_2SO_4 (~47%) >NaCl (~42%). The lower salt retention in the 1:1.70 than 1:1.65 membrane can be due to the larger pore size and less dense structure of the 1:1.70 membrane, allowing slightly more salt passage through the membrane. According to the salt retention performance, it can be said that these membranes function based on both the size exclusion and Donnan exclusion mechanism.

The separation performance of ultrafiltration membranes was evaluated based on the retention test of BSA as model protein (average hydrodynamic diameter ~8.6 nm [175]) and HA as model natural organic matter (average hydrodynamic diameter ~10.6 nm). The average hydrodynamic diameter of Sigma Aldrich HA was estimated from the literature [176–179]. **Figure 2.5D** shows the BSA and HA retention values of two different monomer ratio membranes. At a 1:1.75 ratio, membranes showed 100% retention of BSA and HA, which was expected since the average pore size of this membrane (~5.20 nm) is less than the average size of BSA and HA. In contrast, the membrane formed at a 1:1.80 ratio showed retention of ~98% for HA and ~36% for BSA. This implies that the average pore size of this membrane is within the range of ~8.6 nm to ~10.6 nm. According to the BSA and HA retention performance, membranes prepared at monomer ratios 1:1.75 and 1:1.80 can be good candidates for protein and natural organic matter removal applications. The only drawback of these membranes is that they are positively charged, which is less advantageous for antifouling behavior than the negatively charged membranes. As can also be seen from **Figure A.S3,** the FDR values of the membranes are significant (40-64%) and also FRR values are low (55-70%), indicating a high fouling tendency of these membranes during filtering negatively charged foulant. Therefore, some surface modifications can be done in future studies for getting better antifouling properties of these membranes. Overall, this section indicates that nanofiltration and ultrafiltration membranes can be prepared just by a small change in the monomer mixing ratio.

2.3.2 Effect of casting solution temperature

To evaluate the effect of casting solution temperature, homogeneous casting solutions (at 1:1.70 PSS-PEI monomer mixing ratio) were heated to 40°C and 60°C before casting and immersing into an acetate buffer bath. PSS-PEI membrane (1:1.70 at room temperature (25°C)) was used as the control membrane. **Figure 2.6** shows the top surface and cross-section SEM images of the membranes prepared at three different casting solution temperatures, i.e., 25, 40, and 60°C. No significant difference is observed among the membrane structures; all membranes have asymmetric structures consisting of a thin top layer and a finger-like substructure. No visible defects were seen on the top surfaces of the membranes. The finger-like morphology suggested that phase separation occurred mainly due to the instantaneous onset of the demixing process since the rapid demixing process usually resulted in finger-like structures [180].

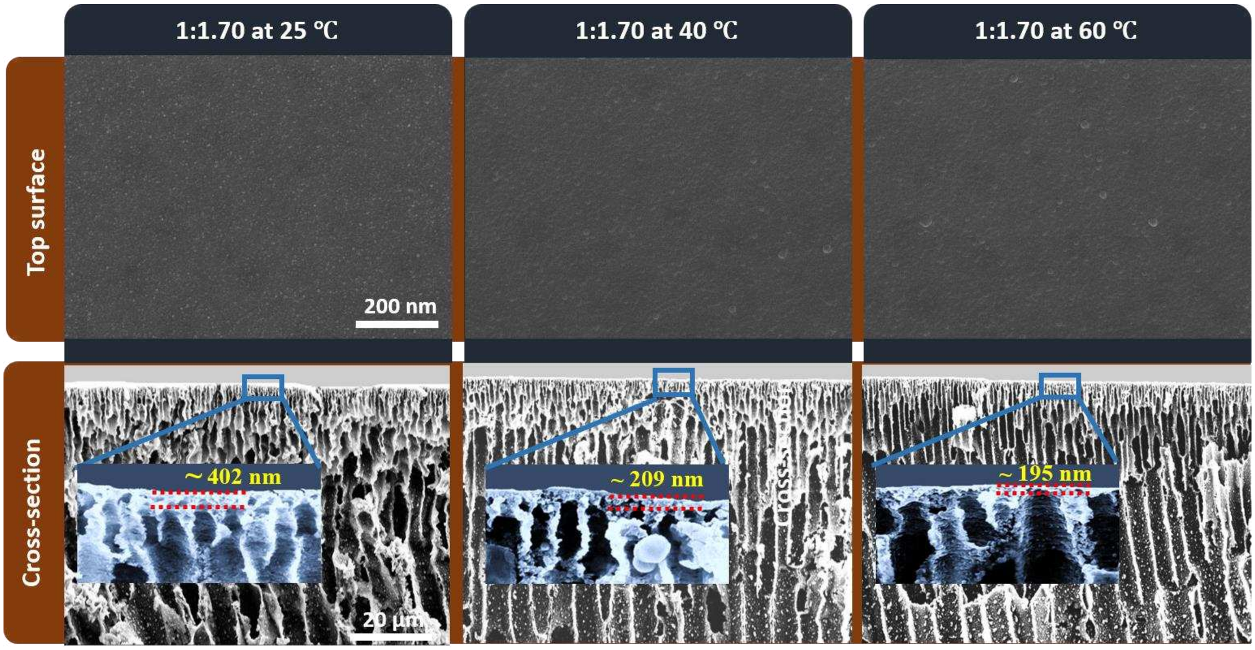

Figure 2.6. Top surface and top cross-section SEM images of PSS-PEI membranes (1:1.70 monomer ratio) at different casting solution temperatures: 25°C, 40°C, and 60°C. Top surface images were taken at ×30000 magnification. A zoomed cross-section with the skin layer is also shown in the inset.

The effect of casting solution temperature on final membrane morphology is evident on the skin layer. A closer look at the top layer reveals that the skin layer becomes thinner with the increase in casting solution temperature (as shown in the inset of **Figure 2.6**). This change in the skin layer can be attributed to the change in viscosity of the dope solution at different temperatures, as shown in **Figure 2.7A**. Shear viscosity at zero shear rate was measured as 2.3, 1.4, and 1.1 Pa.s for casting solution at 25, 40, and 60°C, respectively. The change in shear viscosity with shear rate is presented in **Figure A.S5**. Temperature induces some segmental motion in a glassy polymer (e.g., T_g of PSS is ~228°C [181]). In contrast, a higher degree of polymeric chains mobility is expected at a temperature above the glass transition temperature (T_g) (e.g., T_g of branched PEI is -53°C [182]) since it provides sufficient thermal energy to overcome the rotational restrictions and the interactions between chains [183], resulting in reduced viscosity at higher temperatures [184,185].

Moreover, polymeric chains become more extended with increasing temperature resulting in reduced thickness [149,183], as was also evident from the total thickness of the membranes shown in **Figure 2.7B**. The reduction in skin layer thickness with temperature can be explained by the phase inversion kinetics. It is well known that viscosity significantly affects the solvent-nonsolvent diffusion rate, i.e., low viscosity facilitates solvent-nonsolvent exchange rate and fastens the top layer solidification [183,186]. Therefore, the onset of precipitation is faster for the membranes prepared at high temperatures (low viscosity) compared to the low-temperature dope solution (high viscosity), resulting in a relatively thinner top layer. These observations on the effect of casting solution temperature and viscosity on the membrane morphology are consistent with the previous studies [148,149,187,188].

The AFM images and surface roughness values of the membranes are shown in **Figure A.S6** and **Table 2.3**. It can be seen that surfaces become slightly smoother with the increase in dope solution temperature. This smoothening of the surface can be ascribed to the lower casting solution viscosity at a higher temperature, which is in line with the previous studies on the effect of solution viscosity on PVDF membranes [189,190].

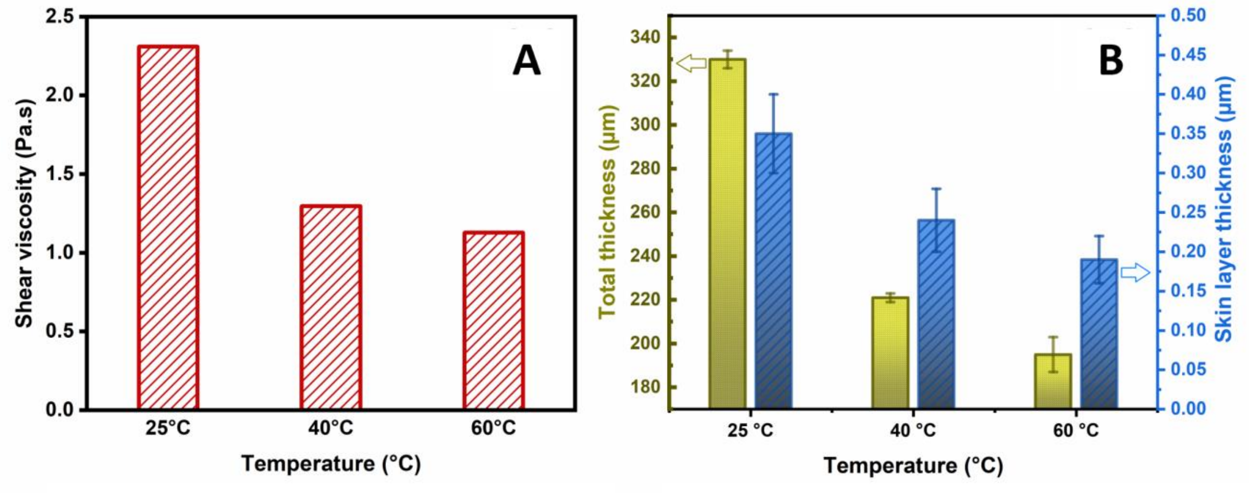

Figure 2.7. Effect of casting solution temperature on (A) viscosity at zero shear rate and (B) total and skin layer thickness of membranes. PSS-PEI at a ratio of 1:1.70 was used for preparing the casting solution. All values are reported from at least three different measurements from different samples.

Zeta potential measurement reveals that the temperature of the casting solution does not significantly affect the surface charge of the membranes (as shown in **Figure A.S7**). As expected, all the membranes were positively charged (~11 mV) due to excess positively charged PEI in the casting solution. Moreover, casting solution temperature does not show any change in the chemical composition of the membranes, as was evident from the similar FTIR spectra of the membranes (**Figure A.S7**). The water contact angle of the membranes prepared at different casting solution temperatures is shown in **Table 2.3 and in Figure A.S8**. It can be seen that the contact angles were almost similar (~41°) for all the membranes.

Table 2.3. Surface roughness parameters, Zeta potential, and contact angle values of the membranes at different casting solution temperatures. All values are reported from at least three different measurements.

Casting solution temperature	Ra (nm)	Rq (nm)	Contact angle (°)	Zeta potential at pH 6 (mV)
25°C	9 ± 1.0	12 ± 1.0	41.5 ± 0.7	7.8 ± 1.0
40°C	5 ± 1.0	6 ± 1.5	40.6 ± 0.5	8.7 ± 1.0
60°C	6 ± 1.0	7 ± 1.0	41.1 ± 1.0	8.1 ± 1.1

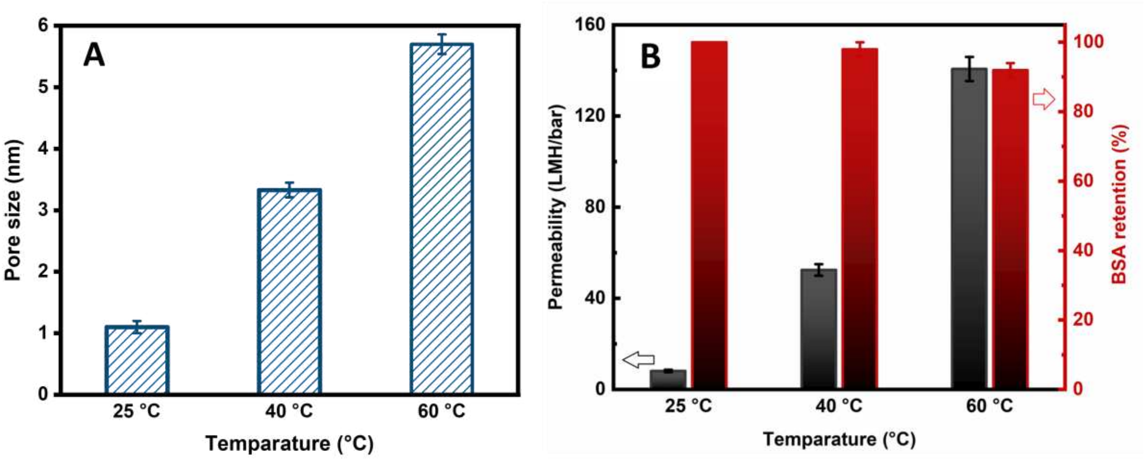

Figure 2.8. Effect of casting solution temperature on (A) average pore size of membranes and (B) water permeability and BSA retention. PSS-PEI at a ratio of 1:1.70 was used for preparing the casting solution. All permeability and retention values are from at least three different measurements from different samples.

To determine the pore size and application range of these membranes, MWCO was evaluated by a molecular sieving curve (**Figure A.S4**). Based on the different molecular weights of the PEG solute retention test, MWCO was measured as ~3662 and ~12437 Da for 1:1.70 (40°C) and 1:1.70 (60°C) membranes, respectively, which are in the ultrafiltration range (1-1000 kDa) [168]. The previous section showed that the 1:1.70 monomer ratio of PSS-PEI at room temperature (25°C) resulted in a nanofiltration membrane (MWCO of ~294 Da). The MWCO data suggests that ultrafiltration and nanofiltration type membranes can be fabricated simply by tuning the casting solution temperature. MWCO values were further used to determine the average pore size of the membranes based on **Eq. 2.3** and presented in **Figure 2.8A**. The average pore size was calculated as 1.1, 3.3, and 5.7 nm for membranes prepared at casting solution temperatures of 25, 40, and 60°C, respectively. As can be seen, the average pore size is enlarged with the increase in temperature of the casting solution. These changes in pore size with casting solution temperature can be ascribed to the phase separation kinetics. It is well known that the viscosity of the casting solution largely affects the phase separation kinetics, resulting in different membrane morphologies[60]. For example, the low viscosity of the casting solution usually fastens the solvent-nonsolvent exchange rate, resulting in more porous structures [148,191]. Therefore, the pore enlargement of membranes with higher casting solution temperatures is due to the relatively faster demixing process than the lower casting solution temperature. **Figure 2.8B** shows the pure water permeability and BSA retention results of membranes at different casting solution temperatures. PWP increased sharply with the increasing temperature in casting solutions. PWP for membranes at 25, 40, and 60°C casting solution temperature was measured as ~8, 53, and 140 LMH/bar, respectively. The permeability change with time is shown in **Figure A.S2**. The considerably higher PWP of membranes at higher casting solution temperatures can be ascribed to the thinner skin layer (**Figure 2.7B**) and larger pore size of the membranes (**Figure 2.8A**). The ultrafiltration performance of the membranes was evaluated by the BSA retention test. As can be seen from **Figure 2.8B**, BSA retention was ~100%, 98%, and 90% for membranes prepared at casting solution temperatures of 25, 40, and 60°C, respectively. The BSA (hydrodynamic diameter ~8.6 nm) retention results are in accordance with the average pore size of the membranes (as shown in **Figure 2.8** , which means that BSA retention is mainly based on the size exclusion mechanism. This section demonstrated that casting solution temperature could be used as a crucial parameter to control the membrane morphology and prepare a high-performance membrane for ultrafiltration applications. Overall, the above results indicate that monomer mixing ratio and casting solution temperature can be considered two new parameters for aqueous phase separation membranes. Just by tuning these parameters, nanofiltration and ultrafiltration membranes can be prepared with good control over membrane pore size and performance.

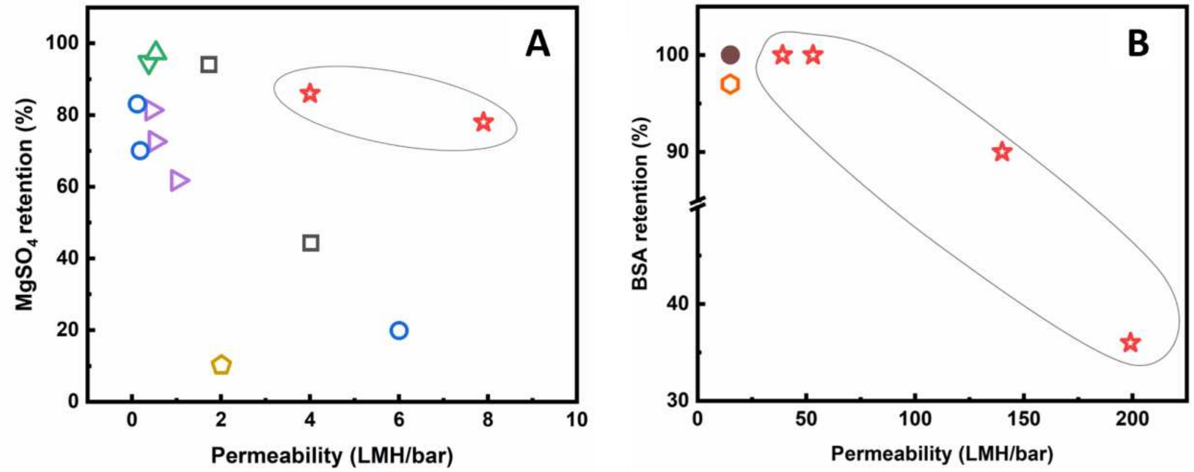

Figure 2.9. Comparison of (A) $MgSO_4$ retention versus permeability and (B) BSA retention versus permeability of different membranes prepared via water-based aqueous phase separation. This work showed better performance compared to the other literature. (▲ [192], ▽ [147], ○ [106], ▷ [193], ⬠ [60], □ [105], ● [104], ⬡ [103], ☆ [This work])

Moreover, in terms of pure water flux and separation performance, this work outweighs the performance of previously reported work, as shown in **Figure 2.9**. Therefore, the findings of this work will contribute to developing high-performance NF and UF-type APS membranes simply via tuning the casting solution temperature and monomer mixing ratio.

2.4 Conclusion

Analogous to NIPS, many tuning parameters significantly affect the structure and performance of membranes prepared via the organic solvent-free APS process. In this work, we systematically studied the influence of monomer mixing ratio and casting solution temperature on pH shift-induced PSS-PEI membranes. The results suggest that nanofiltration and ultrafiltration type membranes can be prepared by controlling the monomer mixing ratio. The excess PEI content in the casting solution largely affected the membrane morphology, as was evident from the change in average pore size, surface roughness, and surface charge. Nanofiltration membranes were obtained at monomer mixing ratios of 1:1.65 and 1:1.70, having an MWCO of ~214 Da and ~294 Da, respectively. On the other hand, ultrafiltration membranes were obtained at higher PSS-PEI monomer ratios, having MWCO in the range of ~10-50 kDa. The increase in permeability from ~4.5 and ~8 LMHbar^{-1} (for 1:1.65 and 1:70 monomer ratio) to ~39 and ~199 LMHbar^{-1} (for 1:1.75 and 1:80 monomer ratio) was attributed to the synergistic effect of excess charges and enlarged pore sizes at higher monomer ratios. For NF membranes (1:1.65 and 1:70 ratio), the salt retention tests showed higher divalent salt retention than monovalent salts as follows: $MgCl_2$ > $MgSO_4$ > Na_2SO_4 >NaCl. This result indicates that the separation performance is based on the size and Donnan exclusion mechanisms. All the UF membranes (1:1.75 and 1:80 ratio) showed excellent protein and natural organic matter retention. Membranes prepared above a 1:1.75 monomer ratio exhibited pattern-like surfaces, which was an interesting finding from this work. Future studies will be devoted to understanding the mechanism behind this pattern formation and the variation of pattern types with different ratios. In this study, casting solution temperature was also found as a crucial tuning parameter to control the phase separation kinetics. The viscosity of the casting solution decreased with temperature, resulting in a faster precipitation process. The rapid demixing resulted in larger pore size and thinner skin layer of the membranes prepared at higher casting solution temperatures, i.e., 40 and 60°C. MWCO was measured as ~3662 and ~12437 Da for 1:1.70 (40°C) and 1:1.70 (60°C) membranes. PWP values showed a sharp increase from ~8 and

~140 LMH/bar with the change in temperature from 25 to 60°C. This drastic change in PWP was due to the combined effect of the thinner skin layer and the larger pore size of the membranes. High PWP with good BSA retention, ~100%, 98 %, and 90% for membranes prepared at casting solution temperatures of 25, 40, and 60°C, respectively, suggests that these membranes have a high potential to be used for ultrafiltration applications. The only drawback of these membranes is that they are positively charged, which is less advantageous for antifouling behavior than the negatively charged membranes. Therefore, some surface modifications can be done in future studies to improve the antifouling properties. Future work will also focus on improving the mechanical strength using nanofillers as additives. Overall, this work demonstrated that casting solution temperature and monomer mixing ratio could be used as new tuning parameters for high-performance PSS-PEI membrane fabrication with excellent control over membrane structure and performance.

Chapter 3

"Biomass to membrane": Sulfonated Kraft Lignin/PCL superhydrophilic electrospun membrane for gravity-driven oil-in-water emulsion separation*

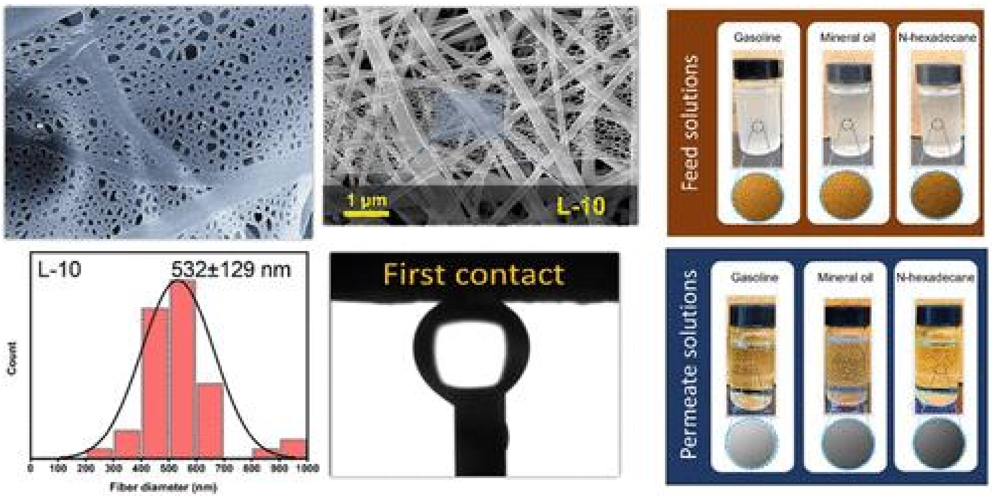

---

[*] Published as: **Md.M.H. Mizan**, P. M. Gurave, M. Rastgar, A. Rahimpour, R.K. Srivastava, Mohtada Sadrzadeh, "Biomass to Membrane": Sulfonated Kraft Lignin/PCL Superhydrophilic Electrospun Membrane for Gravity-Driven Oil-in-Water Emulsion Separation, Published in ACS Applied Material & Interfaces, 2023, 15, 35, 41961-41976.

3.1 Introduction

The effective and urgent treatment of oily wastewater, primarily discharged from the petrochemical, textile, metallurgical, and food industries, along with frequent oil spill accidents, has become imperative due to its detrimental effects on the environment and aquatic species [194,195]. Oily wastewater can typically exist in the form of immiscible oil/water mixtures or oil/water emulsions. Because of different polarity natures, the separation of immiscible oil from water solutions is relatively simple. However, it is difficult to break apart oil/water emulsions due to their small particle size (almost smaller than 20 µm), which are stabilized by surfactants [194,195]. The conventional approaches for the treatment of oil-contaminated wastewater include chemical (e.g., electrocoagulation and demulsification) [196,197], biological (e.g., biodegradation) [198], and physical methods (e.g., skimming, air flotation, and centrifugation) [199–201]. As a drawback, these methods often have low efficiency, particularly for separating emulsified oil-water mixtures [202]. They also suffer from complex operational processes, high energy costs, and the risk of causing secondary contamination. Therefore, there is an ongoing demand to develop more efficient, cost-effective, and environmentally friendly separation techniques for oily wastewater treatment.

Advanced membrane separation processes have recently demonstrated high efficiency in oily wastewater treatment, accompanied by the absence of secondary pollution production and low operational costs [203]. Among the various membrane fabrication methods, electrospinning is considered as a simple and efficient method for preparing nanofibrous membranes with controllable chemical composition, porosity, and morphology [204]. Electrospun membranes can effectively treat oil/water mixtures with high permeability and low energy consumption owing to their prominent features such as high surface-to-volume ratio and porosity, interconnected pore structures, and excellent modifiability. Despite these advantages, the fouling and poor recyclability of traditional electrospun membranes are significant obstacles that limit their widespread use in separating emulsified oil from water [195]. Therefore, it is crucial to develop advanced electrospun membranes exhibiting exceptional selectivity, superior chemical and physical stabilities, and excellent antifouling properties.

To date, extensive research has been reported in the literature about the fabrication of electrospun membranes with special wetting properties, such as superhydrophobicity or superoleophilicity [205,206]. Membranes with superhydrophobic or superoleophilic properties usually have a high affinity towards hydrophobic oil macromolecules. However, these oil-removing membranes demonstrate a high tendency towards severe fouling due to their inherent oleophilic characteristics, resulting in poor separation efficiency and shortened service life [207]. In contrast, superhydrophilic and underwater superoleophobic membranes are becoming increasingly popular in oily wastewater treatment. Furthermore, it is widely believed that membranes with higher hydrophilicity exhibit enhanced antifouling performance in oil/water separation processes. In this regard, many studies aimed to attain both hydrophilicity and stability in electrospun membranes by utilizing different post-processing surface modification techniques, such as plasma treatment [208], layer-by-layer assembly [209], spraying[210], and surface grafting [211]. Although these methods often improve the surface wetting characteristics, they require an additional post-modification process which unlikely increases the cost and processing time of membrane production [203]. Moreover, the complicated modification procedures and low stability of the added new functionalities impede the widespread implementation of these methods on a large-scale application. Blending hydrophilic functional polymeric additives with a polymer matrix during electrospinning is a one-step, convenient, and attractive alternative to improve the hydrophilicity of the membrane [206]. In addition to its simplicity, it usually enables easy modification of the surface energy or the addition of specific functional groups onto the fiber surface.

Despite the great interest in using electrospun membranes for oily wastewater treatment, the unsustainable disposal of these membranes has become an inevitable and crucial issue. The membrane fabrication typically employs fossil-based nonbiodegradable polymers (e.g., polysulfones [14], polyacrylonitrile [15], polyvinylidene fluoride [17]) and toxic solvents (e.g., dimethylformamide [18], dimethylacetamide [19], N-methyl-pyrrolidone [20]), which may cause serious harm to the human health and environment. Consequently, there is an increasing interest in using bioderived and biodegradable polymers to fabricate environmentally friendly electrospun membranes. A variety of biodegradable polymers were utilized to prepare nanofibrous membranes for oil/water separation, including cellulose [212], polylactide acid (PLA) [213], polybutylene succinate (PBS) [132] and polycaprolactone (PCL) [214]. Among these, PCL, an aliphatic polyester, has been widely utilized in different applications, such as tissue engineering, drug delivery, and water treatment, due to its excellent mechanical properties, biocompatibility, biodegradability, and processing advantages [203,215]. However, the relatively higher prices of PCL compared to conventional polymers limit their large-scale application. A facile strategy to overcome this problem is to blend them with inexpensive fillers. To date, most of the studies focus on improving the hydrophobicity of the PCL membrane by blending hydrophobic functional additives [214]. The addition of inexpensive additives can also decline its overall price. However, severe fouling due to pore blockage by oil droplets poses a significant challenge for the superhydrophobic PCL electrospun membranes [206]. Thus, improving the hydrophilicity of the PCL electrospun membranes is necessary to address the fouling problem. Lignin, an abundant biodegradable polymer, can be a promising hydrophilic additive to prepare hydrophilic PCL/lignin membranes owing to its favorable characteristics, such as the presence of hydrophilic carboxyl and hydroxyl groups, unique mechanical properties, biocompatibility, and cost efficiency [216]. The phenolic hydroxyl groups of lignin may also form intermolecular hydrogen bonds with the electronegative groups of PCL, which can increase the structural stability of the PCL/lignin composite [217]. Lignin is produced/extracted at a large scale as a waste coproduct in the wood pulping and lignocellulosic biorefinery industries [216]. Therefore, a blend of lignin and PCL will not only improve the functional and mechanical properties of the PCL electrospun membrane but also facilitate lignin valorization.

In the present study, we investigated the potential of sulfonated kraft lignin (SKL) as a promising bio-based additive for providing superhydrophilicity and underwater superoleophobicity in electrospun membranes based on PCL. The SKL was obtained from a local pulp mill and used without further chemical treatment to maintain its environmentally friendly nature. The use of acetic acid as a benign solvent for preparing the PCL/SKL electrospun membrane ensured the avoidance of secondary pollution and contributed to the overall green approach [218–220]. The influence of the hydrophilic SKL content on the morphology, mechanical properties, and wettability of the prepared electrospun membranes was studied in detail. Additionally, we systematically studied the anti-oil adhesion properties and separation efficiency of oil/water emulsion using gravity-driven filtration, which provides a cost-effective advantage for the separation of oily wastewater without the need for external energy sources or complex equipment.

Furthermore, we examined the effect of SKL on the stability, reusability, and biodegradability of the electrospun membranes. Overall, this study highlights a novel functionality of the PCL/SKL blend, demonstrating its capability for fabricating superhydrophilic electrospun membranes with excellent anti-oil fouling properties.

3.2 Experimental

3.2.1 Materials

Sulfonated kraft lignin (SKL) was kindly provided by West Fraser Mills Ltd, Canada, and was used without any further purification. Polycaprolactone (PCL, M_n = 80,000 gmol^{-1}), glacial acetic acid (ReagentPlus, ≥ 99.0%), n-butanol, n-hexadecane, mineral oil, and Tween 80 were purchased from Sigma Aldrich. Gasoline oil was purchased from Scepter Canada Inc., Canada.

3.2.2 Membrane fabrication

The PCL concentration in the dope solution was optimized to obtain a smooth and bead-free fiber surface. In this regard, PCL at concentrations varying from 10 to 25 wt% was first dissolved in glacial acetic acid (AA) and stirred overnight at 40°C to obtain a homogeneous solution. The solution was kept at room temperature for 2 h before carrying out the electrospinning operation with optimized parameters (**Table B.S1**). After finding an optimized PCL concentration (15 wt%), the electrospun dope solutions with different PCL/SKL compositions were prepared, as shown in **Table 3.1**.

Table 3.1. Details of the electrospun membrane composition and electrospinning operation parameters

Membrane	PCL (wt%)	Lignin (wt%)	AA (wt%)	Solution viscosity (Pa.s)	Electrospinning parameter		
					Voltage (kV)	Distance (cm)	Flowrate (mL/h)
L-0	15	0	85	2.38 ± 0.04	18	18	1
L-1	15	1	84	2.73 ± 0.11	18	18	1
L-5	15	5	80	3.74 ± 0.17	18	18	1
L-10	15	10	75	5.37 ± 0.16	18	18	1

In the first step, SKL was dissolved in AA and ultrasonicated for 30 min. Then, PCL was added to the solution and stirred overnight at 40°C to obtain a homogeneous solution. After resting the prepared homogeneous solution for 2 h at room temperature, 3 ml of dope solution was poured into a 5 ml plastic syringe equipped with a 20 G stainless steel needle. The syringe was mounted on a bench-top electrospinning machine (AME Energy Co. Ltd., China), and electrospinning was performed with optimized parameters. The electrospun fibers were collected on a drum covered by aluminum foil at 140 rpm. The collected nanofibrous membranes were then dried in a vacuum oven overnight at 35°C before further experiments. The obtained membranes were named L-0, L-1, L-5, and L-10. A schematic illustration of the electrospinning process and the digital images of the prepared electrospun membranes are shown in **Figure 3.1**. Importantly, it should be noted that we varied SKL concentration up to 10 wt% because we noticed the presence of undissolved SKL when the SKL solution in AA was further increased (**Figure B.S1**).

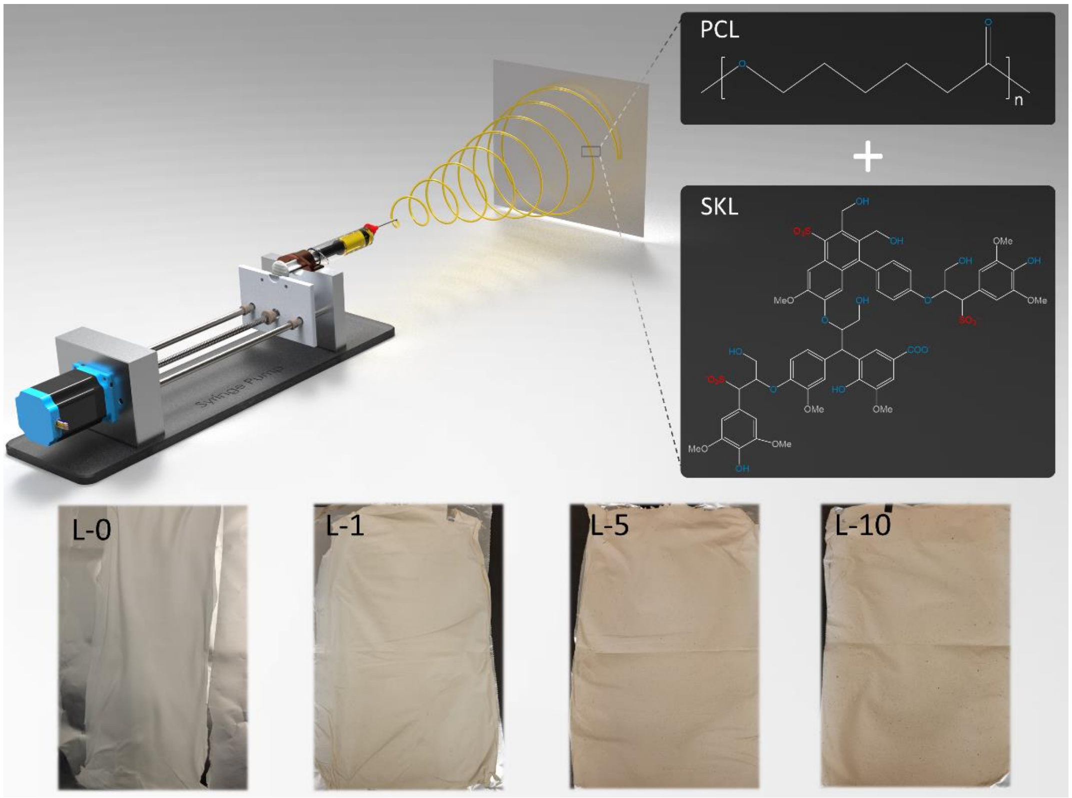

Figure 3.1. A schematic illustration of the electrospinning process and fabricated PCL/SKL electrospun membranes at various SKL concentrations: L-0 (0 wt%), L-1 (1 wt%), L-5 (5 wt%), and L-10 (10 wt%).

3.2.3 Membrane Characterization

3.2.3.1 Measurement of the viscosity of the casting solutions

The viscosity of the casting solution was evaluated using a rotational rheometer (Malvern Kinexus Lab+) at room temperature. The sample solutions were placed between two plates and waited until stabilized at the desired temperature. The dynamic viscosities were recorded at zero s^{-1} shear rate.

3.2.3.2 Evaluation of the membrane's surface potential

The SurpassTM 3 Electrokinetic analyzer (Anton Paar, Graz, Austria) was used to assess the zeta potential of the membranes. A 1 mM KCl solution was used to measure the zeta potential values of the membranes across a pH range of 3 to 9. Sodium hydroxide and Hydrochloric acid were used to adjust pH values. All values are reported from at least three different measurements from different samples.

3.2.3.3 Assessment of the membrane's chemical compositions

The chemical composition of the fabricated membranes was determined using Attenuated total reflectance-Fourier transform infrared (ATR-FTIR). The infrared spectra were obtained at room temperature using Agilent Technologies, Cary 600 series. Each sample was scanned 30 times within the wavelength range of 400-4000 cm^{-1} at a resolution of 4 cm^{-1}.

3.2.3.4 Evaluation of the surface topography, porosity and pore size of the membranes

The surface morphology of the fabricated membranes was analyzed using a field emission scanning electron microscope (FESEM, Zeiss Sigma 300 VP) with an acceleration voltage of 10 kV. Before SEM analysis, all the samples were kept overnight in a vacuum oven at 30 °C. The ImageJ software was utilized to measure the diameter of the fibers, and an average diameter was calculated based on measurements of 50 fibers. The same SEM equipment was used to analyze the composition of the nanofiber membrane, using energy-dispersive X-ray spectroscopy (EDS) mode at an operating voltage of 10 kV.

The porosity of the electrospun membrane was evaluated by the n-butanol uptake test. The porosity (ε) was calculated using the following equation:

$$\varepsilon\,(\%) = \frac{\frac{M_{BuOH}}{\rho_{BuOH}}}{(M_{BuOH}/\rho_{BuOH})+(M_m/\rho_p)} \times 100\% \qquad (3.1)$$

where M_m and M_{BuOH} represent the mass of the dry electrospun membrane and absorbed n-butanol, while ρ_p and ρ_{BuOH} are the densities of used polymers and n-butanol, respectively. The density of the polymer (ρ_p) was obtained from the following equation:

$$\frac{1}{\rho_p} = \frac{\phi_{skl}}{\rho_{skl}} + \frac{\phi_{PCL}}{\rho_{PCL}} \tag{3.2}$$

where ρ_{skl} and ρ_{PCL} are the densities of SKL (1.3 g/cm^3) and PCL (1.145 g/cm^3), respectively and ϕ_{skl} and ϕ_{skl} are the weight fraction of SKL and PCL, respectively.

The average pore size (*r*) of the electrospun membrane was calculated using the following equation: [221]

$$r = \frac{\sqrt{\pi}}{4}\left(\frac{\pi}{2\ \log\left(\frac{1}{\varepsilon}\right)} - 1\right) d \tag{3.3}$$

where *d* and *ε* represent the fiber diameter and porosity of the electrospun membrane, respectively.

3.2.3.5 Evaluation of the surface wettability of the membranes

The surface wettability of the membranes was evaluated by contact angle analysis using a contact angle analyzer (Kruss GmbH, Hamburg, Germany). The apparent water contact angle (WCA) was measured by placing a 6 µL water droplet on a membrane surface attached to a glass slide. The underwater oil contact angle (UWOCA) was measured by the captive bubble method with the same device. Small membrane samples were affixed to a 2 cm wide plastic holder with a double-sided tape and, subsequently, facing downward inside an optically sensitive quartz cuvette filled with deionized water. A syringe with J shape needle was used to make a 6 µL oil droplet (n-hexadecane, mineral oil, and gasoline oil) and placed the droplet on the membrane surface. For each sample, a minimum of three droplets were deposited onto the surface, and the resulting contact angles were measured and averaged.

3.2.3.6 Evaluation of the mechanical and thermal properties of the membranes

The mechanical properties of the electrospun membranes were assessed using a tensile testing instrument (ElectroForce 3200 Series III, Bose corporation). To prevent stress concentration and breakage during testing, each nanofibrous membrane sample was cut into a rectangle with dimensions of 5 cm by 1 cm and held in place with a paper holder at its end. The samples were pre-conditioned under specific temperature (25 °C) and humidity (25%) conditions. Tensile testing was carried out using a 250 g load cell and a 30 mm gauge length, with a crosshead speed of 0.01 mm/min. The average results of three samples were recorded for each membrane.

Thermal analysis of electrospun membranes was conducted by dynamic scanning calorimetry (DSC) with a TA Instruments model Q200. Samples weighing less than 5mg were subjected to scanning with a heating rate of 10 °C/min, ranging from 25 to 250 °C. All measurements were performed under the N_2 atmosphere**.**

3.2.3.7 Evaluation of leaching phenomenon of the SKL-modified electrospun membrane

To assess the SKL stability in the electrospun membrane, we conducted a leaching test on the SKL-modified membrane (L-10). A 220 mg sample of the membrane (10cm × 10cm) was placed in a beaker containing deionized (DI) water and stirred continuously for 21 days. At the end of each week, a 25 ml sample of the solution from the beaker was collected and stored for further testing. Subsequently, the beaker was emptied and replaced with fresh DI water. To assess the leaching behavior, we performed Inductively Coupled Plasma-Optical Emission Spectroscopy (ICP-OES) analysis on three samples collected at weekly intervals.

3.2.4 Membrane separation performance

3.2.4.1 Pure water filtration test

Electrospun membrane filtration experiments were conducted using a dead-end filtration setup (Amicon, UFSC05001) under no applied transmembrane pressure. The effective surface area was 13.4 cm^2. The permeate weight was automatically recorded with a weighing balance (ME4002, Mettler Toledo, USA) at a time interval of 15 s. The pure water flux (*J*) was then determined using:

$$J\ (L \cdot m^{-2} \cdot h^{-1}) = \frac{M(kg)}{\rho(kgL^{-1})A(m^2)\Delta t(h)} \tag{3.4}$$

where *M* is the mass of the permeate, ρ is the density of water, *A* is the effective membrane area, and Δt is the collection time. All values are reported from at least three different measurements from different samples.

3.2.4.2 Oil/water emulsion separation test

The oil-in-water emulsions were prepared by mixing 20 mg of Tween 80 surfactant with 1000 ml of distilled water until a clear solution was obtained. After that, 500 mg of oil was added and blended with a homogenizer (Homogenizer 150, Fisherband, Canada) for 4 min. The size of the oil droplet in the emulsion was determined using the dynamic light scattering (DLS, ALV/CGS-3 Goniometer) technique. Three oil-in-water emulsions (n-hexadecane, mineral oil, and gasoline oil) were used for further emulsion separation experiments. The oil/water emulsion separation performance of the membranes was evaluated using the following procedure: (1) pure water filtration test (J) was initially conducted for 10 minutes, (2) it was then replaced with oil/water emulsion, and the emulsion filtration test (J_1) was carried out for 10 minutes, (3) membrane was then washed with pure water for 2 minutes, (4) membrane was filtered with pure water again for 10 minutes and flux (J_2) was recorded. This procedure was considered as one cycle. The oil/water emulsion filtration test was repeated for three consecutive cycles. The flux decline rate (FDR) and flux recovery ratio (FRR) were determined using the following equations:

$$FDR = (1 - \frac{J_1}{J}) \times 100 \tag{3.5}$$

$$FRR = (\frac{J_2}{J}) \times 100 \tag{3.6}$$

The retentate and permeate samples were collected at the end of the oil/water emulsion filtration experiments. These samples were then tested using a UV-Vis spectrophotometer (Thermo Fisher Scientific GENESYS^{TM} 10) and the oil rejection efficiency (R) was calculated using: [146]

$$R(\%) = \left(1 - \frac{C_P}{(C_F + C_R)/2}\right) \times 100 \tag{3.7}$$

where C_F, C_p, and C_R are the feed, permeate, and retentate concentrations, respectively. An average of C_F and C_R was used to calculate the oil retention in the dead-end cell since the feed concentration constantly changes. The feed represents the solution in the dead-end cell before the filtration test. On the other hand, retentate refers to the solution that remains after the test. This approach considers the varying concentrations of the feed in the cell and provides a more accurate estimation of the rejection test. All values are reported from at least three different measurements from different samples.

3.3 Results and discussion

3.3.1 Electrospun membrane morphology and surface chemical composition

Polymer concentration has a significant impact on the nanofiber geometry and its microstructure. In order to obtain a smooth and uniform nanofibrous structure, a minimum polymer concentration (i.e., critical concentration) is required to attain sufficient chain entanglement that promotes the transition from electrospraying to electrospinning [42]. Below the critical concentration, the weak interactions between polymer chains cannot surpass the Rayleigh instability; thus, the jet fragmented into droplets, resulting in tiny particles or beads formation instead of uniform and stable fibers. This process is known as electrospraying. At a concentration above the critical concentration, the enhanced chain entanglements overcome the Rayleigh instability and thus result in continuous fiber formation. The polymer concentration also affects the viscosity of the solution. Generally, lowering the solution viscosity favors thinner fiber formation and vice versa. However, too high concentrations increase the viscoelastic forces, making it difficult to eject the solution from the spinneret. Therefore, polymer concentration must be optimized to obtain bead-free and continuous nanofibers in the resultant electrospun membranes. In this regard, the PCL concentration was optimized to get stable and uniform fibers. **Figure B.S2** shows the optical images of the electrospun membranes obtained from 10 to 25 wt% PCL solutions. At 10 wt% of PCL solution, only tiny droplets rather than continuous fibrous structures were observed, which could be due to the electrospraying effect at the very low viscosity of the dope solution. However, dope solutions with 15, 20, and 25 wt% PCL resulted in continuous fibrous structures. Among them, only 15 wt% PCL showed uniform and randomly oriented bead-free fiber formation, whereas 20 and 25 wt% PCL resulted in very few fibers. The less fiber formation at high concentrations can be ascribed to the high cohesiveness of the solution leading to difficulties in solution ejection from the spinneret. Based on the above results, 15 wt% PCL was chosen as the optimum dope solution concentration to prepare electrospun membranes for this work.

The influence of SKL content on the morphology of the PCL electrospun membranes was investigated using SEM analysis. **Figure 3.2** depicts the SEM images of as-spun nanofibrous membranes at various SKL concentrations (0-10 wt%). All the samples exhibited smooth, bead-free, and randomly distributed structures under optimized electrospinning conditions. The morphology suggested that the SKL was evenly distributed within the PCL matrix. Moreover, conjunctive structures among the adjacent fibers were observed in all the samples, which could be formed due to the incomplete evaporation of solvent [18,222]. The formation of such adhesion structures made the resultant electrospun membranes dimensionally stable, which is beneficial for the mechanical stability of the electrospun membranes. While membranes prepared from neat PCL showed few network structures, more fibrous networks were observed with increased SKL concentration in the precursor solution, indicating good compatibility between SKL and PCL. The hydrogen bonding between the hydroxyl groups of SKL and the carbonyl groups of PCL could also improve the compatibility between the two polymers [217]. Additionally, the membranes appeared darker brown with increasing SKL content in the dope solution, thus confirming the existence of SKL in the resultant electrospun membranes (**Figure 3.1**).

Interestingly, the L-10 electrospun membrane made from 10 wt% of SKL exhibited "fishnet-like nano webs" composed of nanowires with small pore sizes (**Figure 3.2**). The formation of the nanonet structure can be explained based on the mechanism proposed by Ding et al., where they attributed this nanoweb formation to the fast phase separation of charged droplets moving at high speed from the capillary tip to the collector [223]. It is proven that the charge density of the spinning solution affects the ejection modes of the Taylor cone [224,225]. A cylindrical jet is formed if the charge density surpasses the jet threshold, while a higher charge density above the droplet threshold forms spherical droplets. As the concentration of SKL increases, the charge density also rises due to the increase in negative functional groups, causing the ejection of spherical charged droplets. When these droplets travel from the needle tip to the collector, they get distorted and expand into a thin film in the air due to comprehensive forces acting on them. This thin film is then split into two-dimensional nanonet due to the fast solvent evaporation and rapid phase separation between polymer and solvent. The presence of this nanonet structure in the electrospun membrane can significantly improve the separation efficiency and structural stability. It is worth mentioning that the formation of the nanonet structure was observed once the concentration of SKL exceeded 5 wt% in the dope solution. For example, SKL concentration of 7 wt% in the PCL/SKL dope solution resulted in the formation of nanonets, as shown in **Figure B.S1**.

The elemental composition of the L-10 electrospun membrane was analyzed using EDS, as shown in **Figure 3.2 and Figure B.S3.** The elemental mapping shows the distribution of carbon, oxygen, and sulfur elements in the L-10 electrospun membrane. It is well known that the nanofibrous membrane made of PCL has solely carbon and oxygen elements [203]. Therefore, the even distribution of sulfur, as observed in elemental mapping, confirmed the presence of SKL in the electrospun membrane. The excellent compatibility and uniform distribution of SKL in the PCL matrix was further confirmed using DSC analysis, as shown in **Figure B.S4**. The results indicate a shift in the melting temperature of the PCL electrospun membrane from 57 °C to 59.5 °C upon introducing SKL into the PCL matrix. This slight increase in the melting point can be attributed to the formation of hydrogen bonds between the carbonyl groups of PCL and the phenolic hydroxyl groups of SKL [226,227].

The distribution of fiber diameters of electrospun membranes prepared at different SKL concentrations is also provided in **Figure 3.2**. The average diameter of the fibers increased from approximately 397 nanometers to about 532 nanometers as the SKL concentration increased from 0 wt% to 10 wt%, which can be ascribed to the increasing viscosity of the dope solution with a higher SKL concentration (**Table 3.1**). This observation is in line with the study of Kai et al. where they reported an increase in the fiber diameter of electrospun membranes made from PCL/lignin copolymers [228]. This trend was attributed to the strong viscoelastic forces in the viscous solution, which impeded the axial stretching of the jet, thus leading to a thicker fiber formation. The porosity and pore size of electrospun membranes plays a crucial role in determining their water flux and separation efficiency. **Table 3.2** provides the porosity and pore size values of all the electrospun membranes. All of the fabricated electrospun membranes showed very high porosity (>87%), which was ascribed to the randomly oriented nanofibers with diameters ranging from ~397 to ~532 nm. The pore size values indicate that the incorporation of SKL into the PCL matrix increased the pore size of the electrospun membranes. Specifically, the neat PCL membrane exhibited the smallest pore size, measuring approximately 2.27 μm, while the SKL-modified membrane (L-10) had the largest pore size, measuring approximately 3.84 μm. This enlargement in pore size can be attributed to the widening of the inter-fiber space, which occurs as the fiber diameter increases. These findings align with previous research, which also observed a direct relationship between an increase in fiber diameter and the enlargement of pore size in electrospun membranes [229].

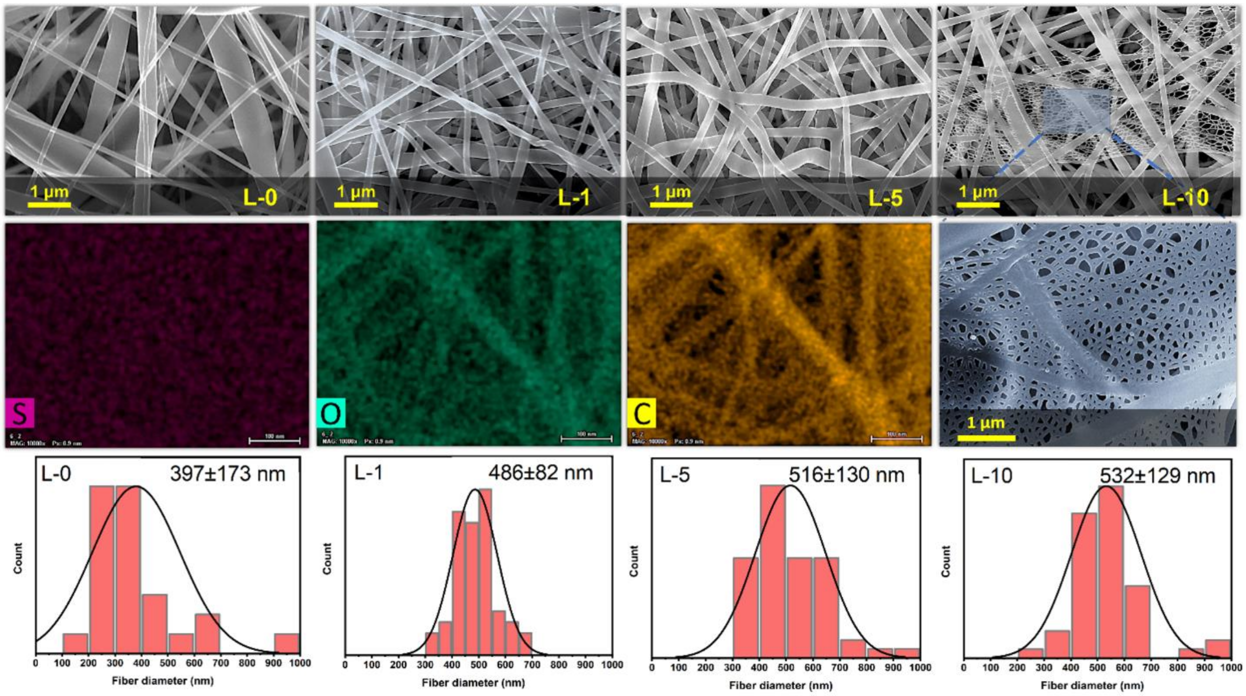

Figure 3.2. SEM images of fabricated PCL/SKL electrospun membranes at various SKL concentrations: L-0 (0 wt%), L-1 (1 wt%), L-5 (5 wt%), L-10 (10 wt%); A magnified image of the nanonet structure in L-10 electrospun membrane is also shown along with the corresponding S, O, and C elemental mapping images; the last row represents the fiber diameter distribution of L-0, L-1, L-5 and L-10 membranes.

The chemical composition of the electrospun membranes was analyzed through ATR-FTIR analysis. **Figure 3.3A** shows the FTIR spectra of different electrospun membranes (L-0, L-1, L-5, and L-10). SKL-containing membranes (L-1, L-5, L-10) exhibited the same main peaks as the pristine PCL membrane (L-0). L-0 membrane showed characteristic peaks at 1150, 1725, and 2940 cm^{-1}, corresponding to the C-O-C stretching, C=O stretching vibration of aliphatic ester, and CH_2 stretching vibration, respectively [217,230]. However, SKL-modified membranes showed some differences in the spectra, especially in the region between 3000 and 3500 cm^{-1} and 1480 and 1700 cm^{-1}, as shown in **Figure 3.3A**. The appearance of a broad peak at 3450 cm^{-1} corresponds to the O-H stretching vibration of SKL composition, and its intensity increased with the increasing SKL content [231].

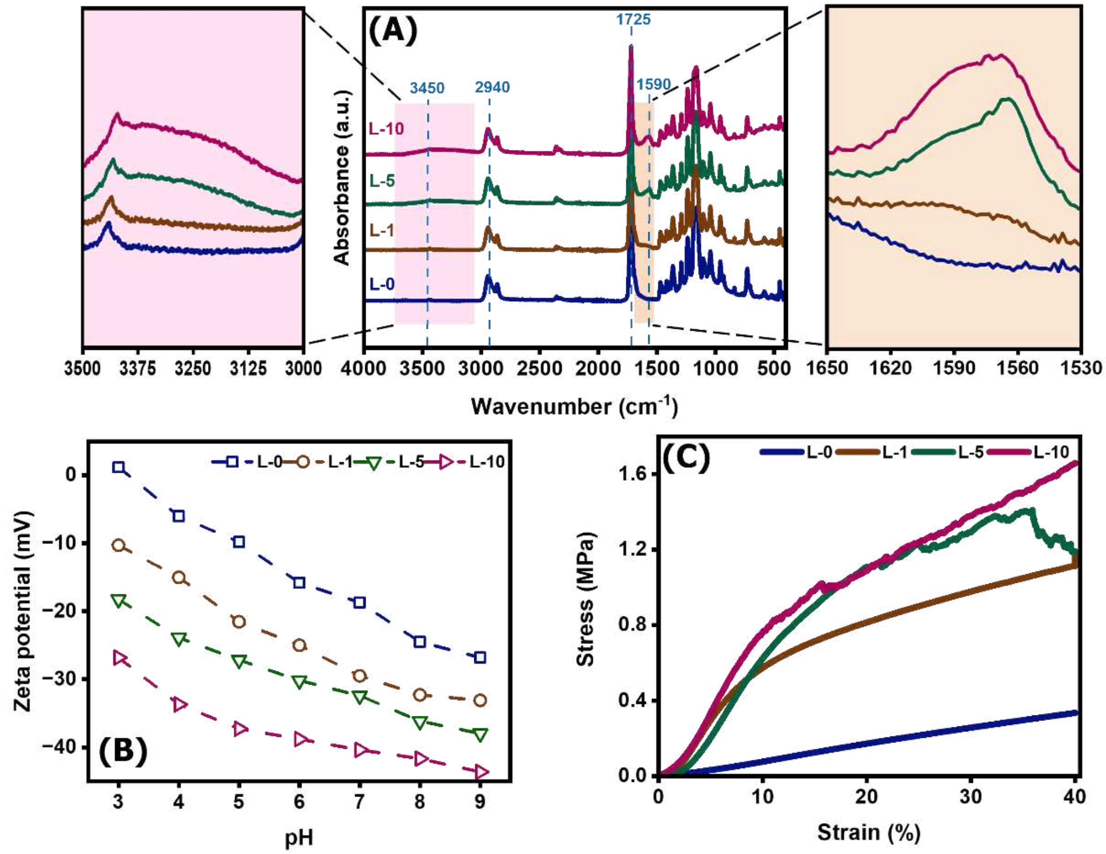

Figure 3.3. (A) ATR-FTIR spectra of PCL/SKL electrospun membranes (L-0, L-1, L-5, and L-10); magnified FTIR spectra between 3000 and 3500 cm^{-1} and between 1530 and 1650 cm^{-1} are also provided, (B) Effect of SKL content on the surface charge of the electrospun membranes at different pH (i.e., pH 3-9), and (C) stress-strain curves for different PCL/SKL electrospun membranes.

Moreover, it shifted slightly to the lower wavenumbers, indicating hydrogen bonding interaction between PCL and SKL. Similar behavior was also observed for PLA/lignin composite [231,232], where a shift to the lower wavenumbers was reported due to hydrogen bonds between hydroxyl groups of lignin and carbonyl groups of PLA. Another band also emerged at 1590 cm^{-1} for SKL-containing membranes, which is ascribed to the aromatic C=C stretching of lignin [120,217]. As the SKL content in the dope solution increased, the intensity of this band also increased, indicating a higher amount of lignin in the resultant membranes.

3.3.2 Surface potential and mechanical properties of the electrospun membranes

Table 3.2 provides the zeta potential of the prepared electrospun membranes at pH 7. The surface charges of the membranes in the pH range of 3 to 9 are also provided in **Figure 3.3B.** As can be seen, the surface charge continued to decrease with the increase in SKL content in the membrane. A similar trend was observed across the entire pH range.

Table 3.2. Zeta potential, Young's modulus, porosity, and pore size of the fabricated electrospun membranes.

Sample	Zeta potential at pH 7 (mV)	Young Modulus (MPa)	Porosity (%)	Pore Size (μm)
L-0	-21.7 ± 1.2	1.03 ± 0.11	87.4 ± 0.8	2.27 ± 0.9
L-1	-29.5 ± 1.2	4.50 ± 0.09	88.3 ± 0.4	3.02 ± 0.5
L-5	-32.4 ± 1.4	5.39 ± 0.14	88.9 ± 0.3	3.39 ± 0.8
L-10	-40.4 ± 1.3	6.96 ± 0.17	89.8 ± 0.4	3.84 ± 0.4

Since SKL contains abundant negatively charged functional groups, as observed from FTIR spectra, a decreasing trend in zeta potential can be expected. This phenomenon also provides a piece of further evidence of the successful incorporation of SKL into the PCL nanofiber matrix. The influence of SKL content on the mechanical properties of the fabricated electrospun membranes was evaluated using tensile testing analysis. Young's modulus was calculated from the slope of stress-strain curves in the elastic deformation region, as shown in **Figure 3.3C** and reported in **Table 3.2**. The neat PCL exhibited the lowest mechanical properties with a modulus of ~1.03 MPa, which could be due to its soft and elastic nature [228]. In contrast, the SKL-modified electrospun membranes showed significantly improved modulus of the membranes. For example, the maximum modulus (~6.96 MPa) was obtained for the L-10 membrane. The stiffness and chain rigidity of SKL, along with its uniform distribution within PCL, could be the reason for this significant improvement in mechanical properties [217]. In addition, the structural strength of the membrane could potentially be enhanced by the reinforcing effect via hydrogen bonding [233]. The enhancement in mechanical properties suggests that SKL is an effective and compatible filler to improve the mechanical strength of PCL nanofibers. The compatibility between PCL and SKL based on Hansen solubility parameter was further discussed in **Table B.S2**.

3.3.3 Electrospun membrane wettability

Earlier research suggests that the oil/water emulsion separation efficiency of the membrane is notably impacted by surface wettability [205,206]. In this work, the wettability of the fabricated membranes was evaluated by water contact angle (WCA) and underwater oil contact angle (UWOCA) measurements (**Figure 3.4**). **Figure B.S5A** demonstrates that the neat PCL (L-0) membrane had a WCA of ~133°. The high WCA suggested that the L-0 membrane had a very low affinity toward the water, which was predictable as the PCL polymer is inherently hydrophobic [234]. However, after modification with SKL, the resultant electrospun membranes demonstrated superhydrophilicity with WCA of ~0°. **Figure B.S5B**, which displays the dynamic WCA, provides insight into the degree of hydrophilicity in the SKL-modified membranes. This data demonstrates a clear correlation between the amount of SKL in the electrospun membrane and its water absorption rate. Evidently, the water absorption rate increased with the increasing SKL concentration. The above-mentioned wettability characteristics of the SKL-modified membranes can be attributed to two factors: 1) surface functionality and 2) surface geometry. It is well known that the wettability of the membrane surface highly depends on the surface functional groups. Therefore, introducing SKL with many hydrophilic functional groups, such as hydroxyl and carboxyl groups, onto the surface surely enhanced the hydrophilicity of the membrane. Moreover, surface roughness can also affect the wettability of prepared electrospun membranes. It is worth noting that we attempted to quantify the roughness of the SKL-modified electrospun membranes using atomic force microscopy (AFM). However, we could not obtain roughness measurements with AFM because the roughness exceeded the limitations of the AFM instrument. However, previous studies reported that large fiber diameters and high porosity of membranes usually result in a rougher surface [235,236]. Therefore, an increase in surface roughness was expected in the SKL-modified membrane due to the larger fiber diameter and slightly higher porosity resulting from the incorporation of SKL. This increase in roughness could also enhance the hydrophilicity of the membranes according to the Wenzel relation, [237] given as:

$$cos\theta^{*} = rcos\theta \tag{3.7}$$

where θ^{*} is the apparent contact angle, θ is the intrinsic contact angle, and r is the surface roughness. Since r is always greater than unity for electrospun membranes, an increase in roughness amplifies the surface wettability in the Wenzel state. In other words, the hydrophilicity increases with the roughness of the hydrophilic surface.

The UWOCA is commonly employed to evaluate the oil-fouling propensity of the membranes. A higher UWOCA is preferable as it implies that the membrane will have a lower tendency to attract oils, which leads to a stronger ability to resist oil fouling. This, in turn, leads to a lower flux decline and a higher flux recovery ratio during oil/water emulsion filtration operations. Three different oils, namely mineral oil, n-hexadecane, and gasoline, were used in this work to measure the UWOCA. As anticipated, the L-0 membrane displayed superoleophilicity (with a UWOCA angle of 0°) because of its hydrophobic nature (**Figure 3.4 and Figure B.S5C**). However, the SKL-modified membranes exhibited a notable increase in UWOCA. The UWOCA values for the L-1 membrane were 141°, 143°, and 144° for mineral oil, gasoline, and n-hexadecane oils, respectively. By incorporating additional SKL into the membrane, the UWOCA was further enhanced, as demonstrated by the OCA measurements for L-5 membranes (>147°). A similar trend was also observed for the L-10 membrane. It showed complete repellence towards all types of oil (Gasoline, n-hexadecane, and mineral oil). The dynamic underwater mineral oil adhesion behavior of the L-10 membrane is demonstrated in **Figure 3.4**. As can be seen, the mineral oil droplet was brought into contact with the membrane surface, squeezed to facilitate interaction between oil and membrane surface, and removed from the surface. The oil droplet did not adhere to the membrane surface, indicating the superoleophobic nature of the membrane. The superoleophobicity of the SKL-modified membrane (L-10) can be ascribed to the surface micro-nano structure and the corresponding Cassie-Baxter state at the solid/water/oil interfaces. When hydrophilic nanonet-nanofibrous membranes are submerged in water, the water gets trapped in the gaps of the rough fibrous structures, forming a solid/liquid/oil three-phase interface (Cassie-Baxter state). The formation of the nanonet structure on the electrospun membrane (as shown in **Figure 3.2**), has several effects on the membrane's surface. Firstly, it introduces surface heterogeneity, which can enhance the surface roughness of the membrane. This increased roughness can, in turn, lead to an improvement in the hydrophilicity of the membrane, as predicted by the Cassie-Baxter model [238]. Similar observations on the improvement of wettability by nanonets were also reported in previous studies [225,239,240].

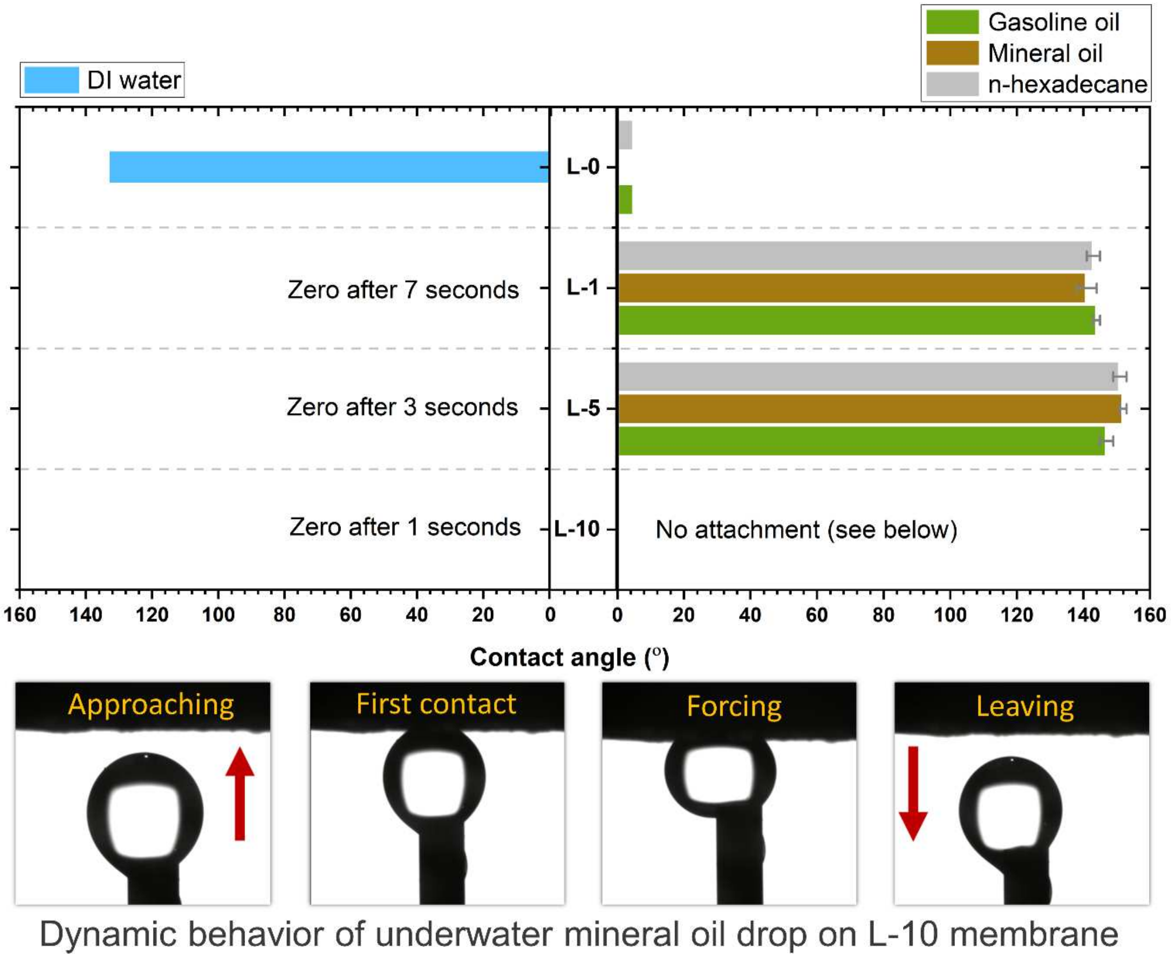

Figure 3.4. Water contact angle and underwater oil contact angle of L-0, L-1, L-5, and L-10 electrospun membranes (Images of WCA and UWOCA of these membranes are shown in **Figure B.S5**); The L-10 membrane did not show any attachment to the mineral oil droplets as can be seen from the dynamic underwater mineral oil adhesion behavior (L-10 membrane showed similar behavior with n-hexadecane and gasoline oil).

In the Cassie-Baxter state, the contact angle (θ^*) could be determined using the following equation: [238]

$$cos\theta^* = f(rcos\theta + 1) - 1 \tag{3-8}$$

where r is the surface roughness, f *is* the area fraction of solid/liquid interface, and θ is the intrinsic contact angle. When the hydrophilic membrane was kept underwater, the water molecules tended to trap inside the membrane pores, forming a thin hydrated layer over the surface [241]. This fully-wetted composite interface consisting of the membrane surface and hydrated layer reduced the area fraction of the solid/oil interface (*f*) and thus led to an increase in OCA (θ^*) to superoleophobicity according to eq. 3.8.

In recent years, there has been much interest in using superhydrophilic and underwater superoleophobic membranes with an OCA greater than 150° and a WCA less than 5° for oil/water separation [237]. These membranes strongly attract water molecules and exhibit excellent anti-oil fouling properties. According to the contact angle results obtained in this study, the L-5 and L-10 electrospun membranes appeared as promising options for achieving high oil/water separation efficiency and improved resistance to oil fouling.

3.3.4 Oil-in-water emulsion separation performance

The pure water fluxes of all electrospun membranes are presented in **Figure 3.5A**. The neat PCL membrane exhibited no water flux under gravity, as can be anticipated due to its hydrophobic nature. However, the SKL-modified electrospun membranes showed significant improvement in flux. The obtained water fluxes for the L-1, L-5, and L-10 membranes were ~ 626, ~841, and ~890 LMH, respectively. Such a significant enhancement in water flux can be attributed to the enhanced hydrophilicity, highly porous structure (>88%) and an enlargement in the pore size (**Table 3.2**) of the SKL-modified electrospun membranes. The oil-in-water emulsion separation ability of the SKL-modified membranes (L-1, L-5, and L-10) was evaluated using a series of experiments following the protocol provided in **section 3.2.4.2**. The variation of flux with time for three different oil/water emulsions is presented in **Figure 3.5(B-D)**. The flux reduced rapidly for each cycle when substituting water with oil/water emulsion across all the membranes. Nonetheless, a simple cleansing with pure water restored the flux almost entirely. The corresponding FDR and FRR values were calculated using **eq. 3.4** and **3.5** are provided in **Figure 3.5(E-F)**. The L-1 membrane exhibited the highest FDR of 54-82% for different oil-in-water emulsions, whereas L-10 showed the lowest FDR in the 46-79% range. This is due to the difference in the degree of hydrophilicity in L-1 and L-10 membranes. Since the L-1 membrane had low underwater oleophobicity (as shown in **Figure 3.4 and Figure B.S5**) compared to the L-10 membrane, some tiny oil droplets could adhere to the surface, resulting in pore blockage and severe flux decline. On the other hand, the L-10 membrane exhibited underwater superoleophobicity as demonstrated in the contact angle analyses; therefore, very low oil adhesion and, hence, low water flux decline was expected. However, a sharp decrease in flux was observed during the emulsion separation test, resulting in a high FDR. This rapid flux decline can be explained by the mechanism proposed by Asad et al. and Ge et al. [18,242]. According to their hypothesis, the higher flux through the membrane led to an intensified concentration polarization, causing the oil concentration to rise in the vicinity of the membrane surface. Since the emulsion was stabilized through the surfactant, oil droplets hardly aggregated, forming an oil filter cake layer on the membrane surface. This layer could potentially improve the separation efficiency to some extent by preventing small oil droplets from passing through. However, the cake layer could also block the membrane surface pores, leading to a sharp decline in water flux. A variation in permeation fluxes was observed for each electrospun membrane while filtrating different oil/water emulsions (**Figure 3.5(B-D)**). For example, the L-10 membrane showed permeation fluxes of 170 to 480 LMH for n-hexadecane, gasoline, and mineral oil emulsions. This can be ascribed to the variations in physical characteristics and the size and amount of oil droplets in the emulsion [18,20]. It is noteworthy that, except for the L-1 membrane, all of the SKL-modified membranes could recover almost all of their initial water flux after simple washing with water (**Figure 3.5F**). The high FRR values of the L-5 and L-10 membranes (~97-99%) could be ascribed to the excellent anti-oil-fouling properties of the membranes, which resulted from the underwater superoleophobicity of the membranes. As a result, the oil cake layer could be easily removed from the surface by rinsing it with water, allowing water flux to be restored. On the other hand, the inadequate hydration capacity of the L-1 membrane (as also proved by UWOCA results) led to severe oil fouling that caused significantly low FRR values ranging from approximately 72% to 86%.

The oil droplet size distribution in different emulsions is shown in **Figure 3.6A**. The size of the oil droplets was obtained in the range of 1.0 to 4.0 μm. The emulsion separation efficiency of the SKL-incorporated membranes was evaluated by measuring the oil rejection using **eq. 3.6**. While L-1 membrane showed very low oil rejection (~67-75%), L-5 and L-10 membranes exhibited very high separation efficiency in the range of ~96 to 99%, as demonstrated in **Figure 3.6B**. The results of the separation efficiency are consistent with the observations made during contact angle analysis. It is noteworthy that the L-10 electrospun membrane exhibited the highest water flux and separation efficiency. The enhanced water flux of the L-10 membrane can be attributed to its improved hydrophilicity and larger pore size. On the other hand, the highest separation flux is likely the result of the combined effect of the membrane's nanonet structures with narrow internal holes and the rapid formation of a hydration layer on its hydrophilic surface.

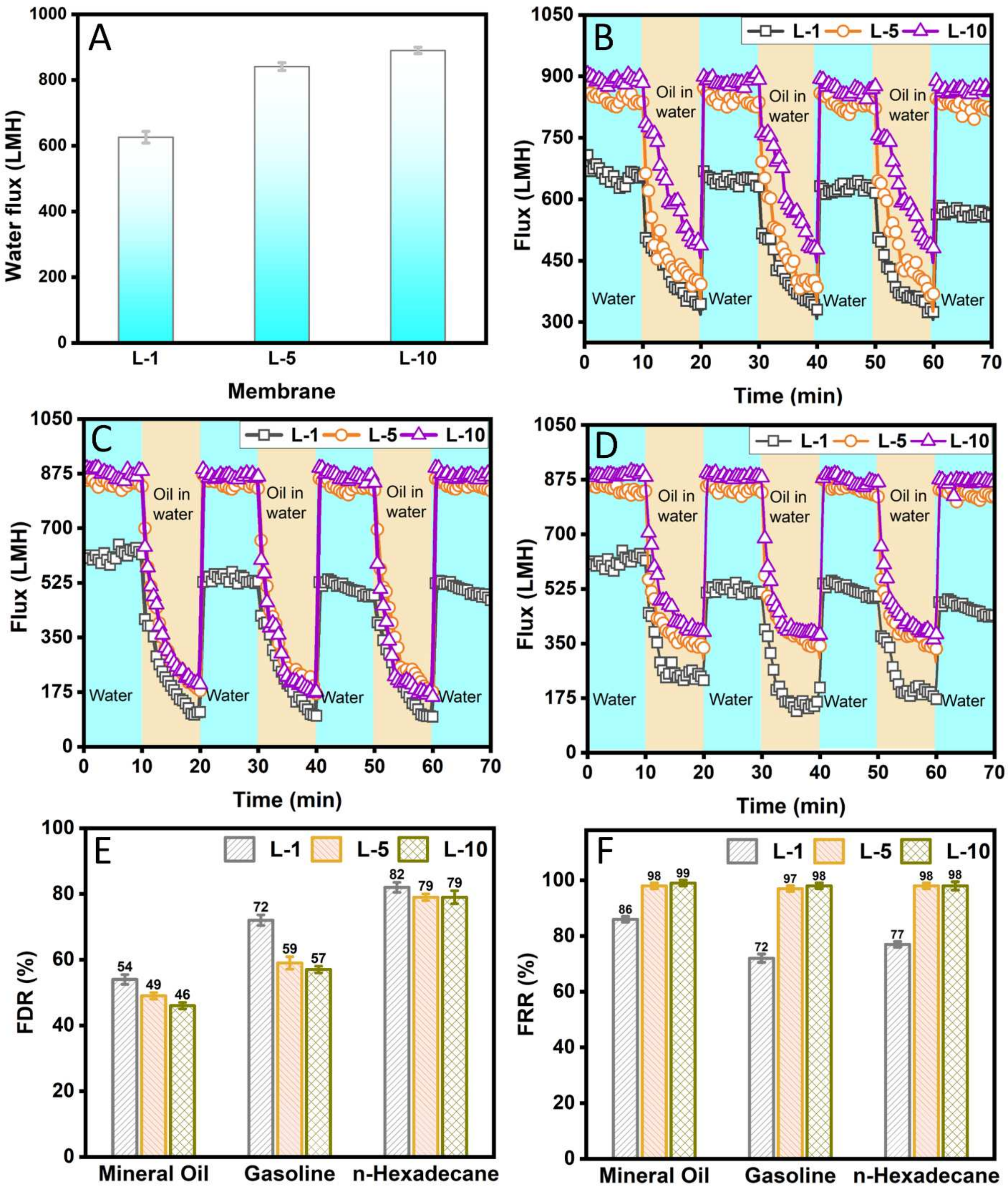

Figure 3.5. Pure water flux of L-1, L-5, and L-10 membranes (A), variation of permeate water flux vs. time during filtration of (B) mineral oil in water, (C) n-hexadecane in water, (D) gasoline oil in water emulsions. (E) and (F) show the flux decline rate (FDR) and flux recovery ratio (FRR) of SKL-modified electrospun membranes after filtration of mineral oil, gasoline, and n-hexadecane in water emulsions.

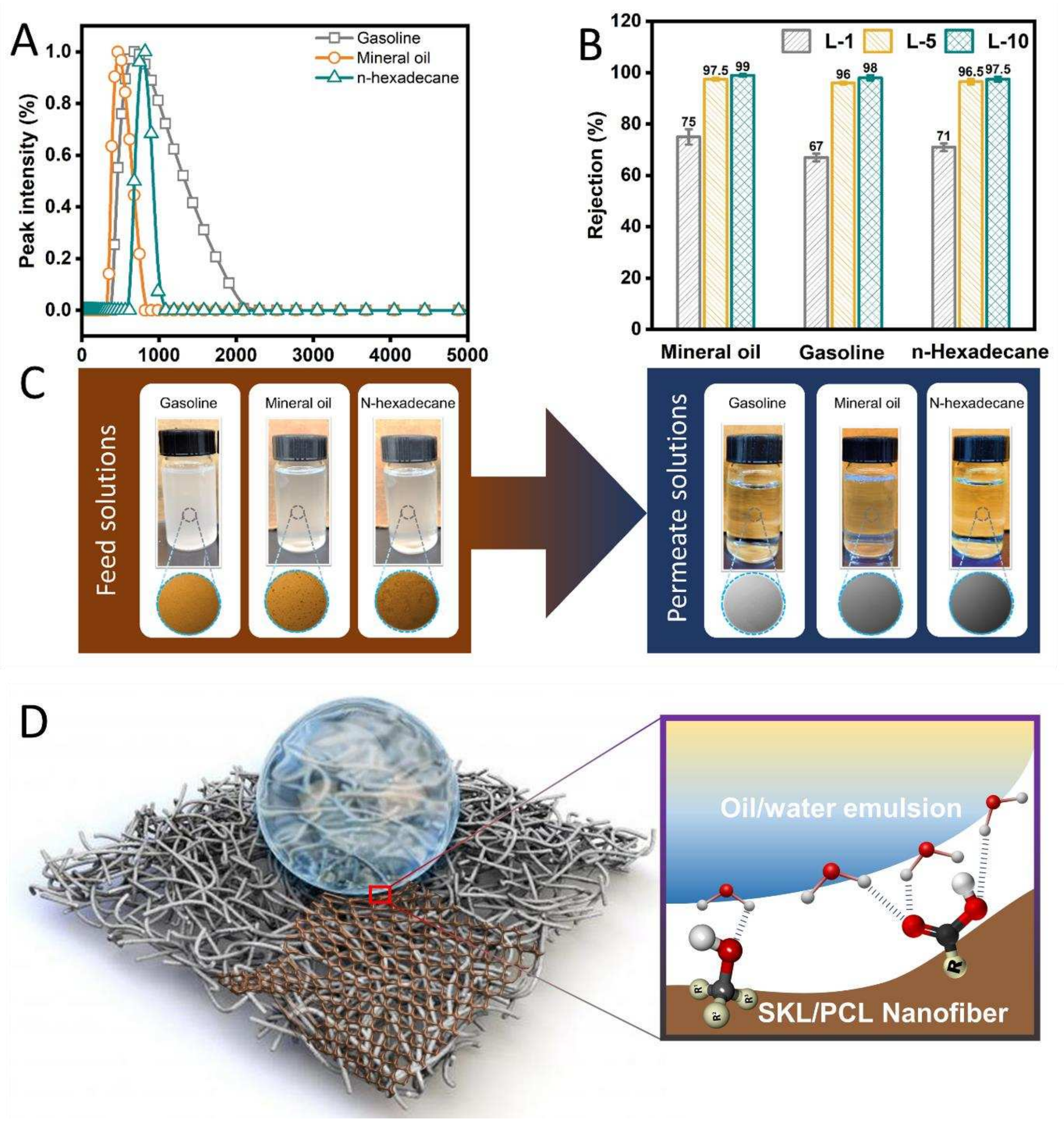

Figure 3.6. (A) Size distribution of oil droplets in different oil in water emulsion, (B) mineral oil, gasoline, and n-hexadecane oil rejection efficiency of different SKL-modified membranes under gravity, (C) digital and optical microscopy images of the emulsion and permeate samples from L-10 membrane, and (D) schematic showing the oil/water emulsion separation mechanism of the SKL-modified membrane.

The digital and optical images of the oil-in-water emulsion and the permeate solutions after treatment by the L-10 membrane are presented in **Figure 3.6C**. The milky and translucent feed emulsions were effectively separated into clear and transparent permeates. The optical microscope images of the emulsion clearly showed the presence of oil droplets, while no oil droplets were detected in the permeate solution, confirming the high oil/water separation efficiency of the membranes.

3.3.5 Separation mechanism

A plausible mechanism for high emulsion separation efficiency and excellent anti-oil-fouling properties of the SKL-modified membranes can be attributed to the superhydrophilic and underwater superoleophobic nature of the membranes [243]. A schematic representation of the oil/water emulsion separation mechanism is illustrated in **Figure 3.6D**. It is well known that membranes with high underwater oil contact angles and less water contact angles usually have more hydration capacity [244]. The contact angle analysis confirmed that SKL-incorporated membranes had higher UWOCA and lower WCA than neat PCL electrospun membranes. Therefore, when the modified membranes came in contact with the oil/water emulsion, water could be easily attracted to the polar hydroxyl and carboxylic groups of SKL through hydrogen bonding interaction, resulting in a robust hydration layer formation on the surface [245]. The presence of polar functional groups on the membrane surface increased the surface energy, which, in turn, improved the affinity of the membrane surface toward water [20]. Moreover, the strongly bound water molecules increased the mass transfer resistance of oil droplets, thus preventing direct contact between the membrane surface and oil droplets. The higher the hydration ability, the higher the ant-oil-fouling performance of the membranes. This suggests that the SKL-modified membranes would be highly effective in preventing oil fouling, which is also supported by their FRR and oil rejection values. Moreover, the selective water permeation through the membranes can be explained by the estimation of intrusion pressure based on the simplified Young-Laplace equation [18,224]:

$$\Delta P_c = -\frac{2\gamma cos\theta_a}{r} \tag{3.9}$$

where ΔP_c is the liquid intrusion pressure, γ is the surface tension of water in the air, or interface tension between oil and water, θ_a is the liquid contact angle, and r is the equivalent pore radius of the membrane. Upon contact with the modified membrane surface, the water instantly wets the surface, resulting in a contact angle of less than 90°, as evident from **Figure B.S5**. This causes a negative intrusion pressure ($\Delta P_c < 0$), which facilitates easy water permeation through the membrane even under gravity. It should be noted that incorporating SKL content in the membranes resulted in larger pore sizes (**Table 3.2**), yet there was an increase in oil rejection efficiency (**Figure 3.6B**). The hydrophilic nature of the SKL-modified membranes can explain this contradictory phenomenon. When oil droplets come into contact with the membrane surface in water, a hydrated layer already formed on the hydrophilic membrane surface prevents the direct contact of oil with the fibers. This results in a UWOCA greater than 90° (as depicted in **Figure 3.4**). The high UWOCA leads to a positive intrusion pressure ($\Delta P_c > 0$), indicating a high oil-repellent characteristic of the membrane. The higher the hydration ability, the higher the oil repellency. Therefore, it can be concluded that the hydrophilicity of the SKL-modified membrane surface (i.e., hydration layer) mostly controls the separation efficiency.

3.3.6 Electrospun membrane reusability, stability, and biodegradability

The recyclability of the PCL/lignin electrospun membrane was further investigated by cyclic mineral oil in the water emulsion separation experiment. **Figure 3.7A** shows the flux and separation performance of the L-10 membrane during each cycle test. As explained before, the water flux decline occurred during the emulsion separation due to the enhanced concentration polarization of oil droplets on the membrane surface. However, water flux was recovered after a simple water flushing. After 10 cycle tests, the membrane retained a high flux recovery ratio (~98%) and excellent separation efficiency (~98%), indicating excellent anti-oil-fouling properties of the membrane. Furthermore, as evident from **Figure B.S6**, the hydrophilicity of the membrane remained unchanged even after being used multiple times. Moreover, no significant changes in the nanofiber morphology were observed from the SEM analysis (**Figure B.S8**), indicating the robust reusability of the as-spun SKL-incorporated electrospun membrane.

The stability of the electrospun membrane was also investigated by immersing the L-10 membrane at different pH conditions (i.e., pH 1, 5, 10, and 12) for 72 h under severe stirring. The digital image of the immersed membrane samples before and after the pH stability test is shown in **Figure B.S7**. After the test, it was discovered that all the membranes, except for the pH 12 membrane, exhibited significant stability. In addition, no color change in the solutions was observed after the stability test. However, the membrane sample exposed to pH 12 was very fragile and exhibited some leaching of the SKL from the membranes, resulting in a change in solution color from transparent to brownish. The wettability and SEM analyses (**Figure B.S7 and Figure B.S8)** confirm that the membrane retained its hydrophilicity and stability even after undergoing a pH change from 1 to 10. This suggests that the membrane has maintained its structural stability and functionality even under harsh conditions, making it a promising electrospun membrane for oily wastewater treatment.

To further assess the stability of SKL within the electrospun membrane, we performed a leaching test specifically on the SKL-modified membrane (L-10). This analysis aimed to identify any presence of sulfur content in the solution, which would represent the leaching of SKL from the membrane. The ICP-OES results in **Table B.S3** demonstrate a very low leaching rate (0.0023 mg/m^2.h) during the first week. This can be attributed to the small amount of loosely attached SKL on the surface of the membrane. Interestingly, there was nearly no leaching observed in the subsequent weeks. These findings provide clear evidence that SKL exhibits high stability within the PCL matrix, primarily due to its excellent compatibility with the host polymer.

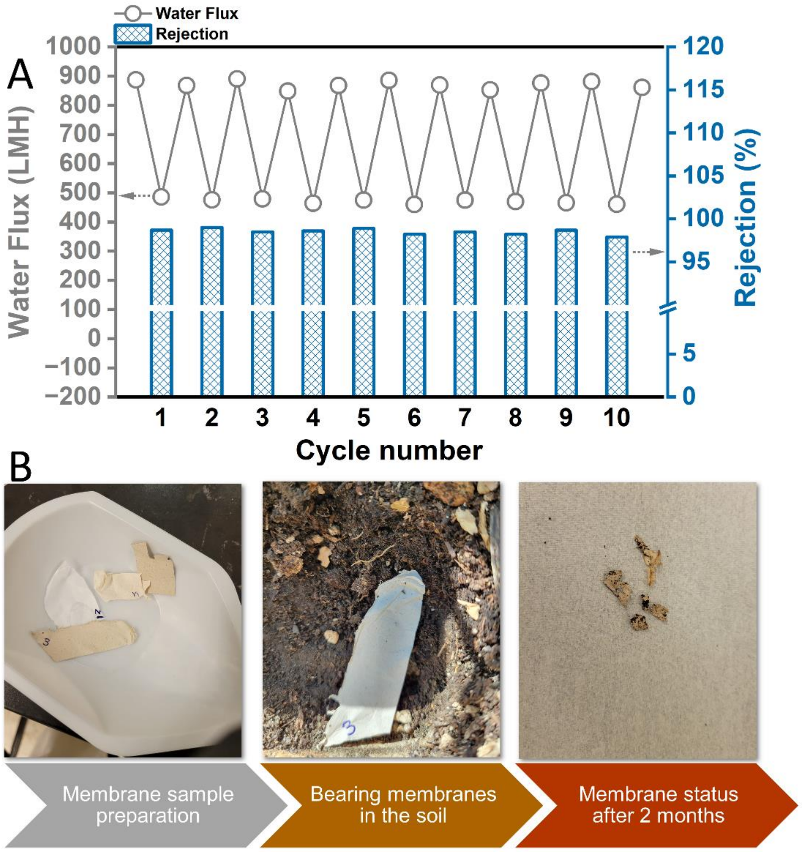

Figure 3.7. (A) The cyclic mineral oil in water emulsion separation performance of L-10 electrospun membrane under gravity, (B) Visual photographs of SKL-modified membranes before burial test and after 2 months of soil burial test.

The biodegradability of the prepared SKL-modified electrospun membrane was evaluated by burying the membrane sample in the soil under ambient conditions for 2 months, as shown in **Figure 3.7B**. After the burial test, only some pieces of the SKL-modified membranes were obtained, indicating a high degradation of the membrane in the soil. To better understand the biodegradation of the membranes, the morphological changes in the samples were evaluated using SEM analysis before and after the burial test. The changes in the nanofibrous structures after the test are evident from the SEM images, as shown in **Figure B.S9**. The fibrous structures collapsed, softened, and merged after the burial test. Moreover, no nanonet structures were observed after the biodegradability test. These interesting results confirm the biodegradability of the SKL-modified electrospun membranes.

To gain a better understanding of the impact of SKL on the degradation rate of the electrospun membrane, a soil burial test was also performed for both neat PCL and SKL-modified electrospun membranes (L-10) for one month. The weight of the membranes was measured at 10-day intervals, and the changes in membrane weight recorded during the test are presented in **Figure B.S10**. It is evident that the degradation rate of the SKL-modified electrospun membrane was faster than the neat PCL electrospun membrane. At the end of the test, the SKL-modified membrane showed almost 61% degradation, while neat PCL exhibited ~30% degradation. Previous studies have indicated that PCL has a low degradation rate due to its high crystalline nature and hydrophobicity [246]. However, blending PCL with a suitable biodegradable polymer can improve the degradation rate. Studies have shown that increasing porosity and introducing hydrophilic components can enhance biodegradation [247,248]. Therefore, the accelerated degradation rate observed in the electrospun membrane modified with SKL, as compared to the neat PCL electrospun membrane, can be attributed to two factors. Firstly, the increased membrane porosity (as reported in **Table 3.2**) contributes to a larger surface area available for degradation processes. Secondly, the enhanced hydrophilicity of the SKL-modified membrane (as shown in **Figure 3.4**), promotes greater interaction with water molecules, facilitating hydrolytic degradation processes.

Since biodegradation in the soil is a complex phenomenon and can be influenced by several factors concurrently, such as enzyme types, reaction kinetics, membrane hydrophilicity, porosity, and available surface area [228,248], future work can be focused on investigating the biodegradation behavior of these membranes in a certain time interval in different degradation conditions.

Long-term oil/water emulsion filtration experiment: The long-term oil/water emulsion separation experiment under gravity was performed using the optimum SKL-modified electrospun membrane (L-10). The change of flux over time and the separation efficiency of the L-10 membrane are shown in **Figure 3.8(A-D)**. The results indicate an immediate decline in flux during the initial few minutes, consistent with the observations from the short-cycle filtration experiments presented in **Figure 3.5**. Subsequently, there was a gradual and continuous decrease in flux over the next 50 minutes. After the long-term (60 minutes) filtration, the emulsion flux was 125, 320, and 420 LMH for n-hexadecane, gasoline, and mineral oil in water emulsion, respectively. The FDR varied from 52% to 85% for different oils in water emulsion. However, the flux was almost completely restored (FRR >97.5%) after a simple rinse with pure water, which can be attributed to the excellent anti-oil fouling properties and superhydrophilicity of the SKL-modified electrospun membrane. These findings demonstrate the long-term stability and robustness of the SKL-modified electrospun membrane in oil/water emulsion filtration applications, highlighting its potential for efficient and sustainable separation processes. The rapid flux decline in gravity-driven oil/water emulsion experiments was previously observed in other studies [241,249]. The state-of-the-art oil/water emulsion separation membranes suffer greatly from fouling and permeability decline. While many studies have focused on developing superwetting membranes with excellent antifouling properties, most of them have utilized intermittent or discontinuous operation modes for short durations (e.g., 10-30 minutes). The observed flux decline in these studies ranged from 60% to 92% [241,249]. In fact, no literature reported a long-term (e.g., more than 1hr) oil/water emulsion separation performance using gravity-driven dead-end filtration mode [206]. Therefore, it is evident that a decline in permeability is expected when separating oil/water emulsions for extended durations in gravity-driven filtration mode. As a proof of concept, we performed a mineral oil/water emulsion filtration test using the L-10 membrane for 7 hrs (**Figure B.S11**). As discussed before, the flux decline, which limits the continuous long-term filtration, is mainly due to the formation of an oil filter cake layer over the membrane surface [241,249]. In most of the studies on water-removing membranes, it was reported that the oil filter cake layer performs the predominant role in permeate flux decline. In cases where the membrane possesses strong antifouling properties, the cake layer can be effectively removed through a simple rinsing or flushing with water. Although the flux declines rapidly in this gravity-driven filtration, this system is energy-efficient due to its gravity-driven nature. In comparing gravity-driven filtration with other technologies, the decreased energy consumption or complete absence of external energy has often been mentioned as an advantage [250]. However, it should be noted that the decreased energy consumption in gravity-driven membrane filtration comes at the expense of flux.

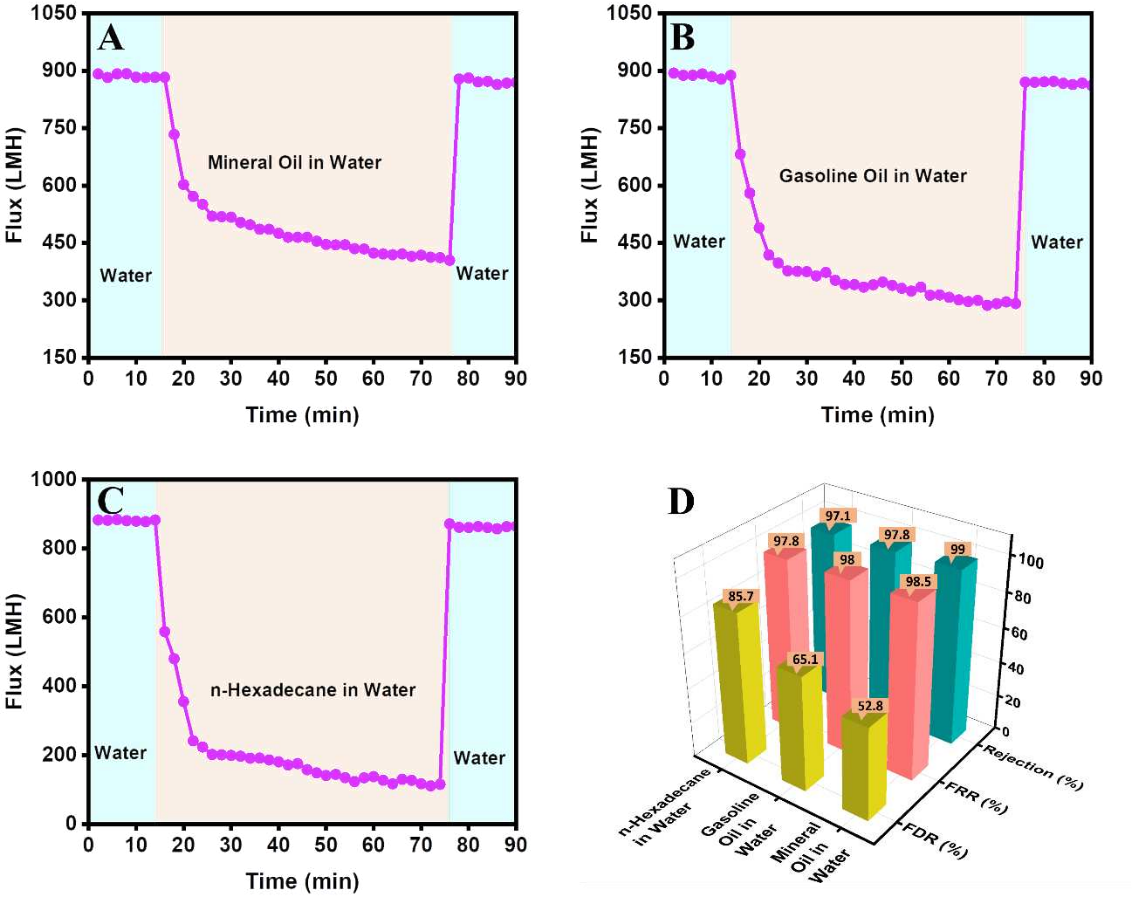

Figure 3.8. Long-term oil/water emulsion separation experiments using L-10 electrospun membrane: (A) mineral oil in water, (B) gasoline oil in water, (C) n-hexadecane in water, and (D) FDR, FRR and oil rejection values.

Table B.S4 compares the oil/water emulsion separation efficiency between some recently reported hydrophilic membranes and the electrospun membranes prepared in this study. The results indicate that the SKL-modified electrospun membranes exhibited comparable oil/water separation efficiency and anti-oil-fouling performance. However, most membranes studied so far were either prepared from nonbiodegradable fossil-based sources or required toxic solvents. Conversely, the membranes in this study were prepared to utilize entirely biobased and biodegradable polymers, and the solvent employed was environmentally friendly and non-toxic. Therefore, the electrospun membrane developed in this study could be a promising green solution for separating oily wastewater.

3.4 Conclusion

In this work, we successfully fabricated a biobased and biodegradable electrospun nanofibrous membrane for oily wastewater treatment by simply blending PCL with a waste byproduct of SKL. The influence of SKL content on the surface morphology, chemical composition, and mechanical properties was investigated using SEM, FTIR, and tensile testing analyses. Adding SKL to the precursor solution resulted in a thicker fiber formation with nanonet-like structures. We also observed that the addition of SKL made the electrospun membrane more negatively charged (from ~ -21 to -40 mV) due to the enrichment of hydrophilic functional groups, such as -OH and -COOH, on the surface. Additionally, the findings from the tensile testing analysis suggest that SKL played a significant role in enhancing the structural strength of the electrospun membrane, which was attributed to its inherent chain rigidity and the intermolecular hydrogen bonding interaction between phenolic hydroxyl groups of SKL and carbonyl groups of PCL. The wettability results indicated that as-spun PCL nanofibrous membranes were hydrophobic (WCA ~133°), whereas it transformed into a superhydrophilic and underwater superoleophobic membrane (WCA ~0° and UWCA >147°) simply by adding SKL in the dope solution without any additional post-treatment. Furthermore, the SKL-modified membranes (L-5 and L-10) demonstrated excellent pure water flux of 800-900 LMH and an emulsion flux of 170-480 LMH during the gravity-driven filtration of three surfactant-stabilized oil-in-water emulsions, namely mineral oil/water, gasoline/water, and n-hexadecane/water emulsions. In addition, these membranes exhibited superior anti-oil-fouling performance with excellent separation efficiency (97-99%) and high FRR (>98%). Furthermore, the SKL-modified electrospun membrane showed excellent reusability and maintained structural stability and wettability for a wide pH range. The absence of any leaching phenomenon observed in the SKL-modified membrane further demonstrates its exceptional stability within the electrospun membranes. Therefore, we conclude that the hydrophilic SKL content in the PCL electrospun membranes endowed them with superhydrophilicity and excellent structural stability.

Chapter 4

Green Polycaprolactone/Sulfonated Kraft Lignin Phase Inversion Membrane for Dye/Salt Separation*

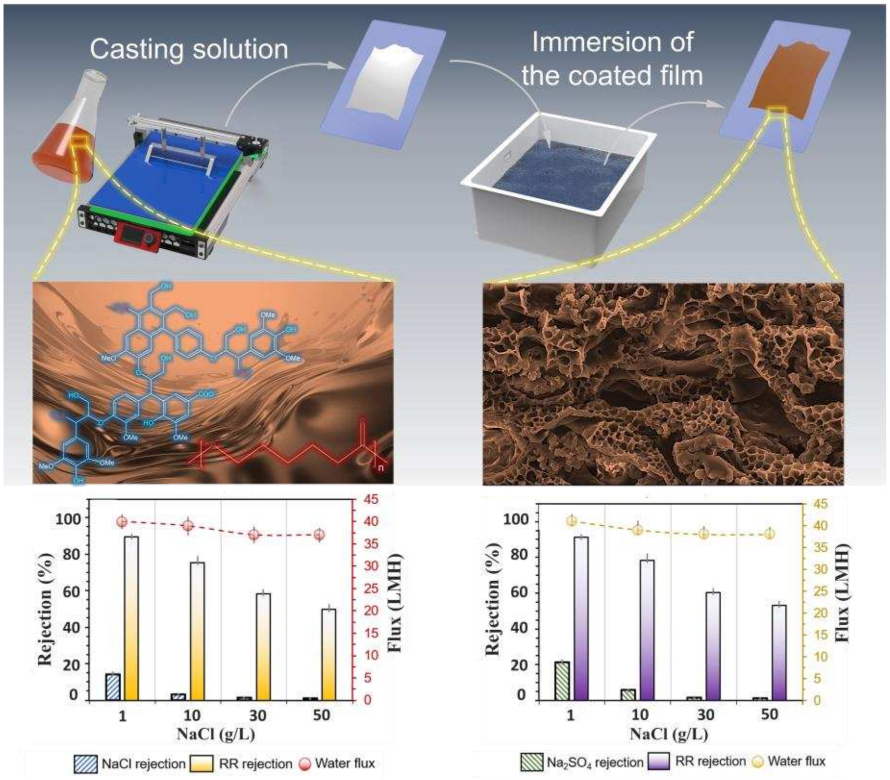

---

*Published as: **Md.M.H. Mizan**, M. Rastgar, H. Sultana, Mohtada Sadrzadeh, Green polycaprolactone/sulfonated kraft lignin phase inversion membrane for dye/salt separation, Published in Journal of Membrane Science, 2024, 702, 122806.

4.1 Introduction

Dyes have widespread applications in various industries, including textiles, leather, cosmetics, packaging, pharmaceuticals, paper, and plastics, resulting in substantial production of dye-contaminated wastewater [251–253]. The textile industry, in particular, is a significant contributor to water pollution, accounting for up to 20% of industrial wastewater emissions worldwide [27]. The release of non-biodegradable and light-absorbing dyes into water bodies is frequently accompanied by inorganic salts (e.g., NaCl and Na_2SO_4), thereby intensifying the challenges associated with their effective filtration [254–256]. The unregulated disposal of dye wastewater without appropriate treatment contaminates underground resources, threatening aquatic ecosystems and human health [257–259]. Hence, it is crucial to adopt efficient wastewater treatment technology, promote clean water recovery, and shift towards sustainable practices within the textile and dyeing industry [260]. So far, a range of biological (e.g., microbial degradation) [261], physical (e.g., adsorption) [262], and chemical (e.g., coagulation and chemical oxidation) [263] methods have been explored for the treatment of dye-containing wastewater. However, these conventional methods suffer from low separation efficiency, resource wastage, and the production of secondary pollution due to the addition of new chemicals [251,264]. In response to these challenges, membrane-based separation technology is suggested as a viable and competitive alternative for wastewater treatment in the textile industry due to its simplicity, low cost, minimal energy requirement, and high separation efficiency [257,259].

Specifically, a nanofiltration (NF) membrane with a molecular weight cut-off of 200-1000 Da is considered an optimal choice for treating dye effluent from textile wastewater, primarily because of its low operating pressure, high water flux, and effective removal of dye molecules [256,265]. NF membranes typically feature a dense selective layer that effectively rejects dyes. However, limitations arise as they also exclude divalent ions and most monovalent ions due to size exclusion and electrostatic interaction, leading to an increased transmembrane osmotic pressure difference and necessitating higher pressure or energy for separation [252,254,264]. Therefore, ongoing research aims to develop separation membranes with exceptional dye rejection and high salt permeation. An effective strategy involves controlling the pore size and adding surface charge, as observed in loose nanofiltration (LNF) or tight ultrafiltration (TUF) membranes. These membranes have slightly larger pores for efficient salt permeation without compromising dye rejection, enabling efficient fractionation of dye/salt mixtures. To date, various methods, like nonsolvent-induced phase inversion (NIPS) [266], layer-by-layer (LBL) assembly [267], surface coating 19, and interfacial polymerization [269], have been employed alongside the incorporation of nanofillers and surface modifiers to fabricate and enhance the performance of LNF and TUF membranes. For example, Sun et al. fabricated LNF membranes using lignin as raw material and dopamine as a surface modifier via LBL assembly on a polysulfone support [267]. The optimum membrane exhibited high water permeability (~65 LMH/bar), dye rejection (>96%), and salt permeation (>85%) with a flux recovery ratio (FRR) of ~80%. Recently, Liu et al. prepared a self-healing TUF membrane by the NIPS method, using a blend of 2-acrylamido-2-methyl-1-propanesulfonicacid-polyaniline (AMPS-PANI) and polyethersulfone [260]. The prepared membrane showed high pure water flux (~95.3 LMH) and dye rejection (~97.3% for methyl blue and ~98.8% for Congo red), low NaCl salt rejection (~7.2%) with high FRR (~90.6%). Cheng et al. prepared a polyester-amide LNF membrane via an interfacial polymerization technique that achieved over 98% dye rejection and >90% NaCl permeation [269]. While these studies have showcased notable enhancements in the separation of dye and salt mixtures, several challenges still exist, such as nanomaterial aggregation, inadequate polymer matrix and filler compatibility, complicated synthesis and fabrication processes, back-flushing issue, and high fouling tendency, hindering the large-scale applications of LNF and TUF membranes for textile wastewater treatment [259,265,268].

Moreover, the fabrication steps of these membranes primarily relied on fossil-based polymers (e.g., polysulfone [14], polyacrylonitrile [15], polyamide-imide [16], and polyvinylidene fluoride [17]) and toxic organic solvents (e.g., dimethylformamide (DMF) [18], dimethylacetamide (DMAc) [19], and N-methyl-pyrrolidone (NMP) [20]), raising environmental concerns due to their toxicity, poor degradability at the end of their life cycle and potential for secondary pollution during recycling. Given the rising energy crisis and environmental pollution issues, the eco-friendly transformation of this engineering sector has become crucial. Therefore, there is a growing interest in using bio-based polymers as raw materials to improve sustainability in membrane fabrication. From water treatment to biomedical applications and sustainable packaging, the versatility of biopolymers opens up new possibilities for addressing global challenges while promoting a greener future [108,270]. Biodegradable membranes naturally decompose and reintegrate into the environment without posing risks, decreasing pollution in ecosystems, minimizing waste, and reducing the environmental impact of disposal. Additionally, with the increasing interest in sustainable and green chemistry, new environmentally friendly solvents (e.g., CyreneTM [25], dimethyl isosorbide [26], and sulfolane [27]) are explored for membrane fabrication. However, the shift from traditional solvents to more eco-friendly alternatives depends not only on the accessibility of these options but also on the compatibility between the selected green solvents and the particular polymers employed in membrane fabrication [5].

Various biodegradable polymers, including cellulose [212], polylactic acid (PLA) [213], polybutylene succinate (PBS) [132], and polycaprolactone (PCL) [214], have been employed in membrane fabrication. For example, cellulose acetate (CA) membranes have been widely employed in industrial applications ever since Loeb and Sourirajan pioneered the development of the first asymmetric CA membrane [109]. CA stands out as an ideal candidate for bio-based membrane fabrication due to its numerous advantages, including affordability, biodegradability, hydrophilicity, and facile synthesis. [111]. However, high fouling propensity, low flux, poor chemical resistance, and narrow operational ranges across varying temperatures and pH levels are the major disadvantages of the CA membranes [108]. Moreover, cellulose-based membranes are susceptible to bacterial growth on their surfaces, leading to compromised membrane performance and reduced service life. To address these challenges, various modifications to CA membranes have been reported, including chemical grafting, surface modification, and plasma techniques [271]. Zhang et al. synthesized PLA-based hollow fiber membrane with improved hydrophilicity through a phase inversion process tailored by the mixing of some additives, i.e., PVP-K30 (polyvinylpyrrolidone K30) and Tween-80 [128]. The resultant membrane showed high rejection of colloidal ferric hydroxide (98.5%) and high permeance recovery (86.8%). Recently, Bang et al. produced a nanofibrous membrane based on PBS, exhibiting impressive oil adsorption capacity (ranging from 18.7 g/g to 38.5 g/g) and high separation efficiency for water and oil mixtures (99.4–99.98%) and emulsions (98.1–99.5%) compared to conventional nanofibers made from organic polymers [132]. Among different biopolymers, PCL, an aliphatic polyester, stands out for its mechanical strength, biocompatibility, biodegradability, and ease of processing, making it versatile in applications like tissue engineering, drug delivery, and water treatment [203,215]. However, its relatively higher cost than conventional polymers hinders widespread use. To address this, a simple approach involves combining PCL with cost-effective biobased fillers, which reduces the overall cost while enhancing structural properties. In this regard, lignin emerges as a renewable and low-cost additive to prepare PCL/lignin membrane, given its advantageous features like hydrophilic functional groups, biocompatibility, and cost-effectiveness [216]. In the wood pulping and lignocellulosic biorefinery industries, lignin is obtained on a large scale as a waste byproduct. Our group recently successfully fabricated a biodegradable PCL/lignin electrospun membrane for oil/water emulsion separation, using environmentally friendly acetic acid as the solvent [272]. Importantly, we demonstrated that the combination of PCL and lignin not only improves permeation properties but also facilitates the effective utilization of lignin resources.

To date, very few articles in the literature detail the fabrication of phase inversion membranes using PCL specifically for wastewater treatment applications. For instance, Manholi et al. conducted a study examining the effect of six different solvents on PCL-based microfiltration membranes fabricated via the NIPS method [273]. Their study primarily focused on solvents' effect on precipitation kinetics and thermodynamics of phase inversion. Mruthunjayappa et al. reported a biodegradable PCL/cellulose acetate-based ultrafiltration membrane fabricated via the NIPS method [274]. Their optimum membrane exhibited high water flux (~53.3 LMH) and excellent dye rejection (>88%) with superior antifouling properties (FRR>88%). Although they succeeded in forming a PCL-based biodegradable membrane with enhanced separation performance, using a toxic solvent (i.e., N, N-dimethylformamide) in the fabrication process raises concerns about the sustainability of the membrane production.

In this study, we explored the potential of sulfonated kraft lignin (SKL) as an environmentally friendly additive in producing biodegradable PCL membranes using the NIPS method. To maintain an eco-friendly approach, we employed acetic acid (AA) as a benign solvent in the PCL/SKL TUF membrane fabrication, ensuring that secondary pollution is prevented and overall environmental friendliness is reinforced. To understand the modality of the two phases, we initially investigated the influence of SKL content within the PCL matrix using a range of characterization techniques, including contact angle, SEM, EDS, FTIR, XPS, zeta potential, DSC and AFM. Subsequently, we evaluated the filtration performance of the fabricated membrane by using single-component solutions, specifically dyes and salts, to determine its suitability for the selective separation of these components. Furthermore, we filtered dye/salt mixtures to assess separation performance at varying salt concentrations and provide insights into the underlying mechanism. Additionally, we evaluated the antifouling performance and long-term stability of the optimum membrane. To the best of authors' knowledge, this study explored for the first time the potential of the SKL and PCL as compatible materials for fabricating high-performance environmentally friendly phase inversion membranes, employing acetic acid as a green solvent. The proposed fabrication approach not only ensures simplicity and scalability but also promotes sustainability throughout the membrane production process.

4.2 Materials and Methodology

4.2.1 Materials

Sulfonated kraft lignin (SKL, molecular weight 5000-8000 Da) was kindly supplied by West Fraser Mills Ltd, Canada, and was utilized as-is without further purification. Polycaprolactone (PCL, molecular weight 80,000 g/mol), glacial acetic acid (AA, ReagentPlus grade, ≥99.0% purity), humic acid (HA), bovine serum albumin (BSA) along with reactive red 120 (RR, 1469.9 Da), reactive black 5 (RB, 991.8 Da), methyl orange (MO, 327.3 Da), methylene blue (319.85 Da) and rhodamine B (479.01 Da) were purchased from Sigma Aldrich. The chemical structures of the dyes are provided in **Figure C.S1**. The inorganic salts, namely, sodium sulfate, magnesium sulfate, sodium chloride, magnesium chloride, and potassium chloride, were obtained from Fisher Scientific. No further purification was carried out on any of the chemicals before their usage.

4.2.2 Membrane fabrication

The PCL/SKL membranes were fabricated using a nonsolvent-induced phase separation (NIPS) method. Various combinations of PCL and SKL were used to prepare the casting solution, as shown in **Table 4.1**. The composition of PCL was kept fixed at 15 wt.%. In the first step, a specific quantity of SKL was dissolved in glacial acetic acid and ultrasonically sonicated for 30 min. Then, PCL was added to the solution, and the mixture was stirred continuously at 40°C for an entire night to achieve a homogeneous solution. The resulting homogeneous solutions were then allowed to settle for 1 h at room temperature to remove any trapped air bubbles. The casting solution was subsequently cast on a nonwoven polyester fabric attached to a glass plate. A micrometer film applicator (Gardo, Pompano Beach, FL, USA) (gap thickness:150 μm) was employed to spread the solution evenly over the nonwoven fabric. The casting speed at 10 mm/s was adjusted using an automatic film applicator (TQC Sheen, AB3120, The Netherlands). Following the casting process, the glass plate was promptly placed into a nonsolvent (water) bath, resulting in the precipitation of a solid film in less than 1 min. The solidified film was kept in the bath for 1 h to complete the phase separation. After that, the membrane was removed from the coagulation bath and stored in deionized water for further characterization and performance tests.

Table 4.1. Details of PCL/SKL phase inversion membrane composition

Membrane	PCL (wt.%)	SKL (wt.%)	AA (wt.%)
M1	15	7	78
M2	15	8	77
M3	15	9	76
M4	15	10	75

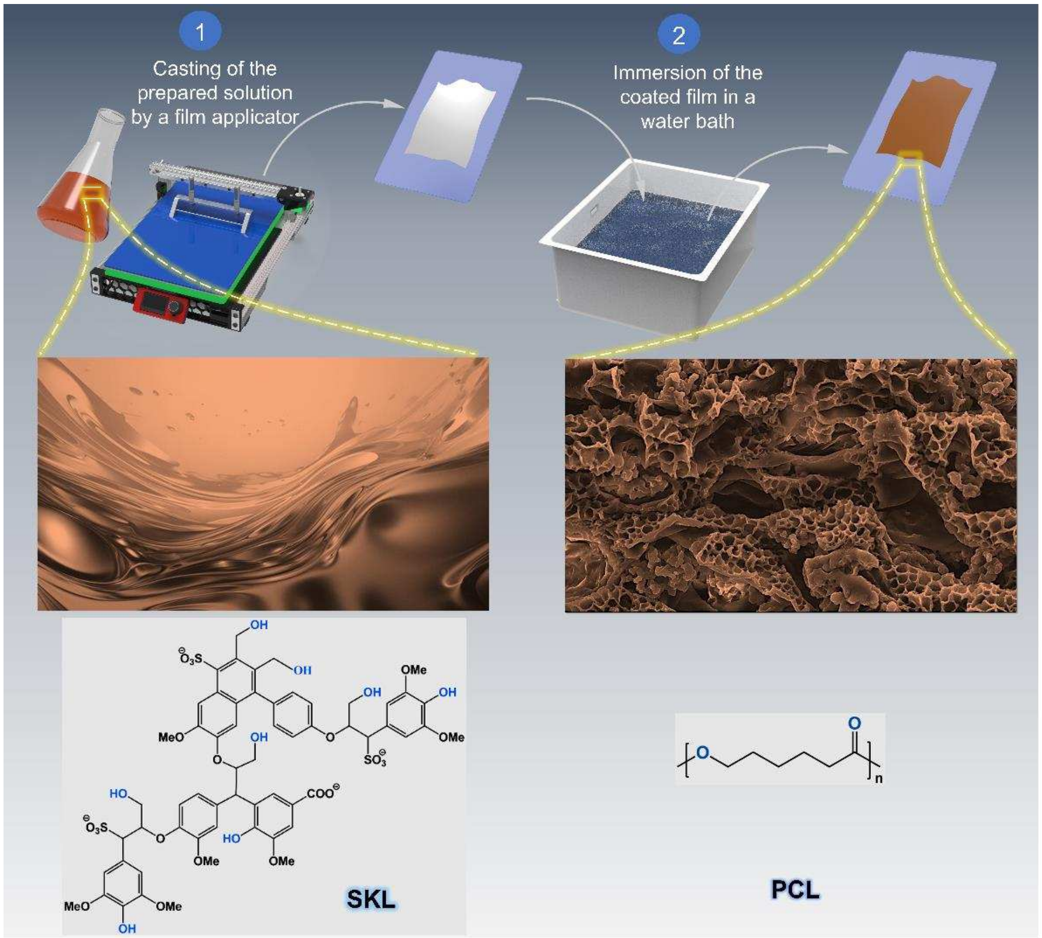

Figure 4.1. A schematic representation of the membrane fabrication process.

The membrane fabrication steps are schematically presented in **Figure 4.1**. It is important to mention that we varied the SKL concentration within the range of 7 to 10 wt.% due to specific observations. While fabricating the neat PCL membrane (0 wt.% SKL) and PCL/SKL membrane with SKL concentrations below 7 wt.%, we observed no flux through the resultant membrane at the operating pressure of 40 psi. The absence of flux can be ascribed to the pronounced hydrophobic characteristics of the PCL membrane. This observation indicates that SKL concentrations below 7 wt.% were insufficient to modify the wettability of the PCL membrane significantly. Conversely, when we attempted to increase the SKL concentration in the AA solvent over 10 wt.%, we observed undissolved SKL in the solution.

4.2.3 Characterization of membranes

4.2.3.1 Assessment of surface topography of the membranes

The top surface morphology and cross-sectional structure of the fabricated membranes were analyzed using a field emission scanning electron microscope (FESEM, Zeiss Sigma 300 VP) at 10 kV acceleration voltage. For cross-section SEM imaging, the samples were frozen in liquid nitrogen and carefully fractured. Afterward, all SEM samples were placed in a vacuum oven at 30°C overnight. Before imaging, a layer of gold was sputter-coated onto all membrane samples. The elemental composition of the prepared membrane was also measured with the same SEM equipment using energy-dispersive X-ray spectroscopy (EDS) mode at an operating voltage of 10 kV. The surface topography of the membranes was assessed using atomic force microscopy (AFM, Bruker Dimension Icon, USA). All AFM measurements were conducted in tapping mode with a scan rate of 1.0 Hz, at ambient temperature and humidity, covering a 10 μm × 10 μm surface area of the samples. The Gwyddion software was employed to analyze the AFM data and determine surface roughness parameters.

4.2.3.2 Evaluation of chemical composition and surface potential of membranes

Attenuated total reflectance-Fourier transform infrared (ATR-FTIR) was used to evaluate the chemical composition of the fabricated membranes. Infrared spectra were acquired at room temperature using Agilent Technologies, Cary 600 series instrument. Each sample underwent 30 scans over a wavelength range of 400-4000 cm^{-1} with a resolution of 4 cm^{-1}. Chemical bonds and elemental composition (O, C, and S) of the PCL/SKL membranes were also assessed with a Kratos AXIS ULTRA XPS equipped with a monochromatic Al Kα X-ray source. To collect information on the thickness from 1 to 10 nm of the surface layer, high-resolution scans of 0.1 eV with a range of 0-1100 eV were conducted. The zeta potential of the membranes was determined using the SurpassTM 3 electrokinetic analyzer from (Anton Paar, Graz, Austria). The zeta potential values were measured over a pH range of 3 to 9 using a 1 mM KCl solution. To adjust the pH values, sodium hydroxide and hydrochloric acid were used. All values are reported from at least three different measurements from different samples.

4.2.3.3 Evaluation of the contact angle of membranes

Contact angle analysis was performed to assess the surface wettability of the membranes using a contact angle analyzer from Kruss GmbH in Hamburg, Germany. The apparent water contact angle (WCA) was determined by depositing a 2 μL water droplet on a membrane surface affixed to a glass slide. At least three droplets were placed on each sample's surface, and the resulting contact angles were measured and then averaged.

The Wenzel equation was employed to find the relationship between surface roughness and the wettability of the membrane, as depicted by the following equation [237,275,276]:

$$cos\theta^{*} = rcos\theta \tag{4.1}$$

where θ and θ^{*} are the intrinsic and apparent contact angles, respectively, and r represents the surface roughness. Moreover, the correlation between surface roughness, hydrophilicity and interfacial free energy was determined using modified Young-Dupre equation [120]:

$$-\Delta G_{sl} = \sigma_{lv}\left(1 + \frac{cos\theta_{s}}{r}\right) \tag{4.2}$$

where ΔG_{sl}, σ_{lv}, θ_{s}, and r refers to the solid-liquid interfacial free energy, liquid surface tension, apparent static contact angle, and surface roughness ratio, respectively. The surface roughness ratio is measured from the ratio of the actual area to the projected surface area.

4.2.4 Membrane separation performance

4.2.4.1 Pure water filtration test

A pure water filtration test was conducted with a lab-scale cross-flow filtration setup. The filtrations were performed under an operating pressure of 40 psi with a flow rate of 3 LPM (liters per min). The feed solution was maintained at room temperature using a circulating water bath. During the filtration, the permeate was collected in a beaker, and its weight was automatically recorded using a weighing balance (ME4002, Mettler Toledo, USA) at 30-second intervals. The pure water flux (J_w) was then calculated using this data.

$$J_w(Lm^{-2}h^{-1}) = \frac{m\ (kg)}{A_m\ (m^2)\rho(kgL^{-1})\Delta t(h)} \tag{4.3}$$

where m is the weight difference of collected permeate between each time interval, A_m denotes the effective membrane surface area, ρ represents the density of water, and Δt is the collection time. All values are reported from at least three different measurements from different samples.

4.2.4.2 Dye/Salt separation test

Three different anionic dyes (MO, RB, and RR) and four inorganic salts (NaCl, Na_2SO_4, $MgCl_2$, and $MgSO_4$) were used to evaluate the prepared membrane's dye and salt separation performance. The operating conditions were the same as those used for the pure water filtration test. In the first stage, membrane separation performance for single dyes and single salts was tested. In the next step, dye/salt mixtures at different salt concentrations were used as the feed solution to investigate the dye/salt selectivity of the membrane. For the first scenario, single salts and single dyes with a concentration of 1 g/L and 0.1 g/L were filtered separately through the membrane using a cross-flow setup. For the second scenario, the same equipment and procedures were used to assess the dye/salt mixture separation performance of the membrane. In this case, dye/salt mixtures were prepared by mixing 0.1 g/L RR dye solution with varying concentrations (1 to 50 g/L) of inorganic salts, specifically NaCl and Na_2SO_4. In each case, the water flux was measured using **eq. 4.3**, and the rejection (R) was calculated using the following equation:

$$R\ (\%) = (1 - \frac{C_p}{C_f}) \times 100 \tag{4.4}$$

where C_f and C_p are the solute concentrations in the feed and permeate, respectively. For inorganic salts, the feed and permeate concentrations were evaluated using the Fischer scientific AR50 ion conductivity meter. The dye solutions' concentration in the feed and permeate sides were assessed using a UV–Vis spectrophotometer (Agilent 8453). For each case, separate calibration curves were first generated using the known salt or dye solution concentration. All filtration tests were repeated at least three times to confirm the repeatability.

4.2.4.3 Evaluation of the MWCO of membrane

To determine the molecular weight cut-off (MWCO) of the membrane, a series of experiments were carried out using PEG solutions at a concentration of 250 ppm, with varying molecular weights ranging from 0.2 to 35 kDa. The MWCO measurements were conducted using a cross-flow filtration setup, commencing from the filtration of the lowest molecular weight of PEG. The collected permeate and feed solution concentrations were analyzed using a total organic carbon analyzer (TOC-L CPH, Shimadzu, Japan). The stokes diameter (d_p) of the PEG solute can be calculated from the molecular weight (MW) of the PEG solute, using **eq. 4.5** [269]. MWCO of membrane refers to the minimum molecular weight of PEG solute at R = 90%. A probability density function, as expressed in **eq. 4.6**, can be used to plot PEG rejection vs Stokes diameter to determine the pore size distribution of the membrane [257,277].

$$d_p = 33.46 \times 10^{-12} \times MW^{0.557} \tag{4.5}$$

$$\frac{dR(d_p)}{dd_p} = \frac{1}{d_p ln\sigma_p \sqrt{2\pi}} \exp\left[-\frac{(lnd_p - ln\mu_p)^2}{2(ln\sigma_p)^2}\right] \tag{4.6}$$

where μ_p is the mean effective pore size at PEG solute rejection of R = 50%, and σ_p represents the geometric standard deviation calculated from the ratio of Stokes diameter at R = 84.13% over that at R = 50%.

4.2.4.4 Antifouling performance and stability test of membrane

The antifouling performance of the membrane was analyzed using humic acid (0.1 g/L), BSA (0.1 g/L), and dye/salt mixture (RR/Na_2SO_4) with a concentration of 0.1 g/L of dye and 1 g/L of salt, respectively. The antifouling test was carried out in two cycles, each lasting 5 hrs. At the outset of each experiment, the initial water flux (J_w) was set to ~43 LMH, achieved by adjusting the operating pressure while maintaining a concentrate flow rate of 3 LPM. After obtaining a steady flux, the deionized (DI) water was replaced with foulant solutions and filtered for 4 hrs. The change in flux (J_1) with time while filtering foulant solutions was continuously recorded. Following each cycle, the membrane was thoroughly cleaned with deionized (DI) water to remove any remaining foulants. Next, the DI water was filtered again, and the water flux after cleaning (J_2) was recorded. The antifouling ability of the membrane was then assessed using four fouling properties, namely flux decline rate (FDR), flux recovery ratio (FRR), reversible fouling ratio (R_r), and irreversible fouling ratio (R_{ir}), which were calculated using **eq. 4.7-4.10** as an index of antifouling performance.

$$FDR(\%) = (1 - \frac{J_1}{J_w}) \times 100 \tag{4.7}$$

$$FRR\ (\%) = \frac{J_2}{J_w} \times 100 \tag{4.8}$$

$$R_r(\%) = (\frac{J_2 - J_1)}{J_w}) \times 100 \tag{4.9}$$

$$R_{ir}(\%) = (1 - \frac{J_2}{J_w}) \times 100 \tag{4.10}$$

The stability of the membrane at different pH conditions was also evaluated. To assess the pH stability, three pieces of the optimum membrane were immersed in pH 3, 6, and 9 for one day and then tested for RR/Na_2SO_4 (0.1 g/L and 1 g/L, respectively) mixture separation performance. The water flux and rejection were calculated using **eq. 4.3 and 4.4**. The dye/salt mixture (RR (0.1 g/L)/Na_2SO_4 (1 g/L)) separation performance was also performed for three consecutive days (6 h/day) to investigate the long-term separation performance of the PCL/SKL membrane. The permeate was collected every 2 hrs, and daily average rejection rates were reported in the study. Thermal analysis of the PCL/SKL membrane was carried out to check the thermal stability using dynamic scanning calorimetry (DSC) with a TA Instruments model Q200. Samples (weighing less than 5 mg) underwent scanning with a heating rate of 10 °C/min. These measurements were conducted under N_2 atmosphere.

4.2.4.5 Effect of ionic strength on separation performance of membrane

The ionic strength of an aqueous solution can significantly impact membrane separation performance. To evaluate the effect of the ionic strength of the solution, varying concentrations of salts (ranging from 1 to 50 g/L) were introduced into the dye solution. The ionic strength (I, in mol/L) was determined using the following equation:

$$I = \frac{1}{2} \sum Z_i^2 C_i \tag{4.11}$$

where C_i is the salt concentration (mol/L), and Z_i represents the valency of salt ions. To delve deeper into the impact of salt concentration on the surface charge density of the membrane, we calculated the surface charge density (σ_d, C/m^2) of the membrane using the equations as follows [277–279]:

$$\sigma_d = \frac{\varepsilon\zeta}{\lambda} \tag{4.12}$$

$$\lambda = \sqrt{(\frac{\varepsilon K_B T}{2N_A e^2 I})} \tag{4.13}$$

where λ, ε, and ζ stand for the Debye length (m), the absolute permittivity of the medium (C^2/Nm^2) and zeta potential (V), respectively. Additionally, K_B denotes the Boltzmann's constant (1.38×10^{-38} J/K), while e, N_A, and T represent the elementary charge (1.6×10^{-19} C), Avogadro's number (6.023×10^{23} mol^{-1}), and absolute temperature (K), respectively. Furthermore, the Freundlich adsorption isotherm (**eq. 4.14**) [280,281] was employed to establish a relationship between the surface charge density and the ionic concentration.

$$\ln \sigma_d = \ln a + b \ln C \tag{4.14}$$

where *C* denotes the salt concentration (mol/L), and the parameters (*a* and *b*) depend on the salt nature.

4.3 Results and Discussion

We fabricated biodegradable TUF membranes by combining a biobased hydrophilic additive (SKL) with a biodegradable hydrophobic polymer (PCL) through the NIPS method. The polymers were dissolved in a green solvent (AA) during the membrane fabrication to promote sustainability. The following sections will explore the impact of low-cost hydrophilic additive (SKL) on the membrane structure and performance.

4.3.1 Membrane morphology and chemical composition of membrane

The influence of hydrophilic SKL content on the morphology of the PCL/SKL membranes was evaluated using FESEM analysis. **Figure 4.2** shows the top surface and cross-section of the fabricated PCL/SKL membranes using different SKL concentrations. All the membranes had very dense top surfaces, with no visible pores or defects, even at ×40,000 magnifications. **Figure C.S2** provides the whole cross-section of the prepared membranes with and without the polyester support. The membranes exhibited an asymmetric structure, featuring a sponge-like substructure with a few macrovoids beneath the thin and dense top layer. No significant variations in cross-sections were observed among the membranes fabricated at different SKL concentrations. The sponge-like cross-section with a very dense top surface suggests delayed demixing during the phase separation process [282]. This phenomenon is often associated with slow precipitation kinetics, typically leading to the formation of tight membranes [283]. The interconnected sponge-like substructure with a dense upper layer can provide better mechanical strength, stability, and selectivity compared to finger-like morphologies [284,285]. The observed morphology in the PCL/SKL phase inversion membrane aligns with findings from previous work done by Gervand et al [286]. They reported a sponge-like morphological structure with a dense top surface in PCL/MXene nanofiltration membrane prepared through the NIPS method using NMP as a solvent. The delayed precipitation in the present work can be attributed to two factors: the heat of mixing of solvent and nonsolvent and the compatibility between polymer and solvent. It is generally known that instantaneous phase separation is favorable when the heat of mixing is exothermic, while endothermic heat of mixing leads to delayed phase separation [287–289]. In the case of an AA/water system, the heat of mixing is endothermic over a wide range of concentrations [290,291]. This is because the energy required to break the individual associated complexes is larger than the energy liberated in forming the mixed complexes (acetic acid monomers and dimers associate with water molecules). The polymer and solvent compatibility can also influence the precipitation kinetics during the phase inversion process. One commonly used method to assess polymer-solvent compatibility is based on the Hansen solubility parameters. A smaller difference in solubility parameters between the polymer and the solvent indicates a high compatibility, leading to a delayed phase separation and a sponge-like morphology in the membranes [273,287]. **Table C.S1** provides the solubility parameters for PCL, SKL, and AA. The theoretical calculations revealed a very small difference in the interaction parameters between the polymers and the AA solvent. This further supports the slower precipitation rate during the phase separation of the fabricated membranes, ultimately resulting in an asymmetric membrane with a spongy sublayer. However, some studies reported different morphologies in PCL-based phase inversion membranes. Mruthunjayappa et al. prepared photoactive PCL/CA ultrafiltration membranes using dichloromethane (DCM) and DMF as solvents [274]. The prepared membranes exhibited porous surfaces with finger-like substructures.

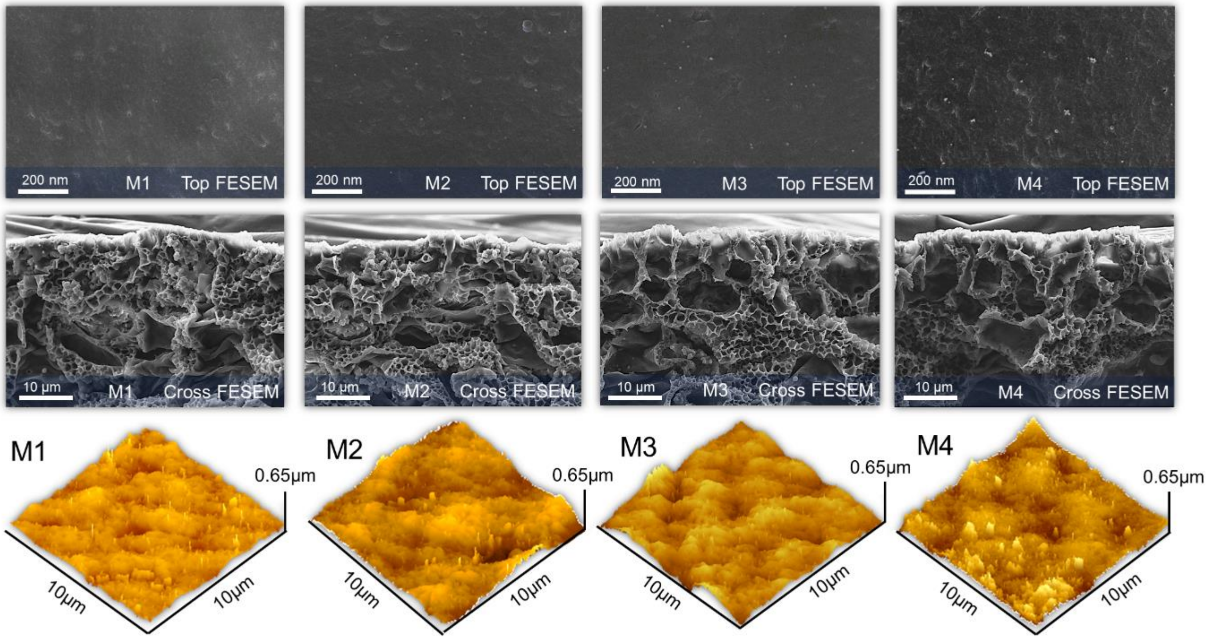

Figure 4.2. FESEM and AFM images of the fabricated PCL/SKL phase inversion membranes at different SKL concentrations: M1 (7 wt.%), M2 (8 wt.%), M3 (9 wt.%) and M4 (10 wt.%). The top and second rows show the top surface and cross-section FESEM images, while the last row presents AFM images of the membranes.

In another study, Manholi et al. reported the effect of six different solvents on porous PCL-based phase inversion membranes [273]. They observed that varying the solvent types could impact the phase separation kinetics, shifting the membrane morphology from a finger-like structure to a spongy one. They concluded that a finger-like morphology was favored when solvents such as DMF, NMP, and triethyl phosphate (TEP) were employed. This was attributed to the exothermic heat of mixing of DMF/water, NMP/water, and TEP/water system and the higher value of solvent-polymer interaction parameter (5-7.5 MPa$^{1/2}$). In contrast, a sponge-like morphology was formed while using solvents like tetrahydrofuran (THF), acetone, and 1,4-dioxane, possibly due to their endothermic heat of mixing with water and lower value of polymer-solvent interaction parameter (1-4 MPa$^{1/2}$). Hence, it can be inferred that the discrepancies in the morphologies observed in the existing literature are likely due to differences in the phase separation behavior induced by the various solvent types. This, in turn, affects the interaction parameters and the miscibility between solvent and nonsolvent during the fabrication process.

To assess the presence of SKL in the PCL matrix, the elemental composition of the PCL/SKL membrane (M3) was analyzed using EDS, as shown in **Figure C.S2**. According to the EDS analysis, the fabricated PCL/SKL membrane contains carbon (74%), oxygen (21%), sodium (0.28%), and sulfur (4.22%) elements. PCL is commonly recognized as a polymer composed solely of carbon and oxygen elements [203]. Further analysis of elemental composition was conducted using XPS analysis (**Figure C.S3**). The survey spectra revealed the presence of carbon (at 285 eV), sodium (1072 eV), oxygen (532 eV), and sulfur (at 165 eV) in the SKL-modified membrane (M3) [292]. The identification of sulfur through XPS analysis validates the presence of SKL within the modified membrane, a component not found in the pure PCL membrane. Based on our previous study, elemental sodium and sulfur in the SKL originate from the ionic functional groups (e.g., sodium carboxylate and sodium sulfate) [293]. The surface morphology of the membranes was further characterized through AFM analysis (**Figure 4.2**). The surface average roughness (Ra) and root-mean-square roughness (Rq) values are presented in **Table 4.2**. The roughness values exhibited significant variations as the SKL content was increased in the PCL matrix. The membrane with the lowest SKL content (7 wt.%) showed the least roughness (~29 nm), while the highest roughness (~43.5 nm) was observed in the membrane with the maximum concentration of SKL (10 wt.%). The observed increasing trend in surface roughness with increasing SKL content can be related to the chemical composition and molecular structure inconsistency in PCL/SKL membranes. SKL is a complex 3D dimensional structure comprising aliphatic and aromatic groups in its backbone, while PCL is a linear aliphatic semicrystalline polyester [294,295]. Such a mixture likely creates surface voids, impacting surface roughness. The increased roughness leads to a higher specific surface area of the membrane, which, in turn, favors an increase in water permeability. The FTIR analysis was also carried out to determine the chemical composition of the fabricated PCL/SKL membranes. **Figure 4.3A** illustrates the FTIR spectra of various PCL membranes modified with SKL (M1, M2, M3, and M4). A pure PCL membrane typically displays characteristic peaks at 1150, 1725, and 2940 cm^{-1} (**Figure C.S3**), corresponding to the stretching vibration of C-O-C, C=O in aliphatic ester, and CH_2 stretching vibration [272]. All PCL/SKL membranes (M1-M4) exhibited characteristic peaks similar to the neat PCL membrane except the peaks at 3000-3500 cm^{-1}. The appearance of a broad peak at 3450 cm^{-1} is associated with the O-H stretching vibration of the SKL components, which include phenols and aliphatic alcohols [272,293].

Table 4.2. Average surface roughness (Ra), root mean square roughness (Rq), roughness ratio (r), and solid-liquid interfacial free energy (ΔG_{sl}) values of the PCL/SKL membranes.

Membrane	R_a, nm	R_q, nm	r	ΔG_{sl}, mJ/m^2
M1	28.93	37.49	1.09	-91.5
M2	36.23	46.55	1.11	-104.5
M3	40.17	52.69	1.16	-106.6
M4	43.48	57.88	1.31	-100.8

As highlighted in **Figure 4.3A**, the intensity of this band exhibited a rising trend from M1 to M4, indicating an increasing quantity of SKL content in the resultant membrane. Additionally, FTIR spectra shifted slightly towards lower wavenumbers, suggesting potential hydrogen bonding interaction between PCL and SKL. Previous studies reported a similar trend in the PLA/lignin composite [231,232] and the PCL/SKL electrospun membrane [272]. In both cases, a shift towards lower wavenumbers was attributed to hydrogen bond formation between the hydroxyl groups of lignin and the carbonyl groups of PLA/PCL. Two additional bands at 620 and 1110 cm^{-1} can be attributed to the S=O and S-O stretching of sulfonate groups, respectively [120,293]. The peak at 1590 cm^{-1} can be ascribed to the stretching vibrations of aromatic C=C bonds in SKL and C=O stretching of carboxylate groups [120,217]. The intensity of this peak showed an upward trend, indicating a higher quantity of SKL in the resultant membranes. In summary, all membranes modified with SKL displayed characteristic peaks corresponding to phenols, aliphatic alcohols, carboxylates, and sulfonate functional groups. These functional groups can enhance the hydrophilicity of the resulting membranes and contribute to the antifouling properties of the PCL/SKL membranes.

4.3.2 Surface charge and wettability of membrane

The surface charge of a membrane is a critical parameter to evaluate its separation properties, particularly when dealing with the separation of charged dyes and salts. The zeta potential values of the PCL/SKL membranes at varied pH (pH 3-9) are shown in **Figure 4.3B**. It can be seen that all membranes possess negative surface potential within the entire studied pH range. The surface charge became slightly more negative with the increase in SKL content in the PCL matrix (e.g.,

(-40 mV (M1) to -45 mV (M3) at pH 7). The observed negatively charged surfaces in the membrane can be attributed to the ionization of the surface functional groups, such as carboxylates and sulfonates, originating from the SKL molecular structure. The negatively charged surfaces could contribute to the efficient separation of negatively charged solutes and anionic dyes due to the electrostatic repulsion effect [277].

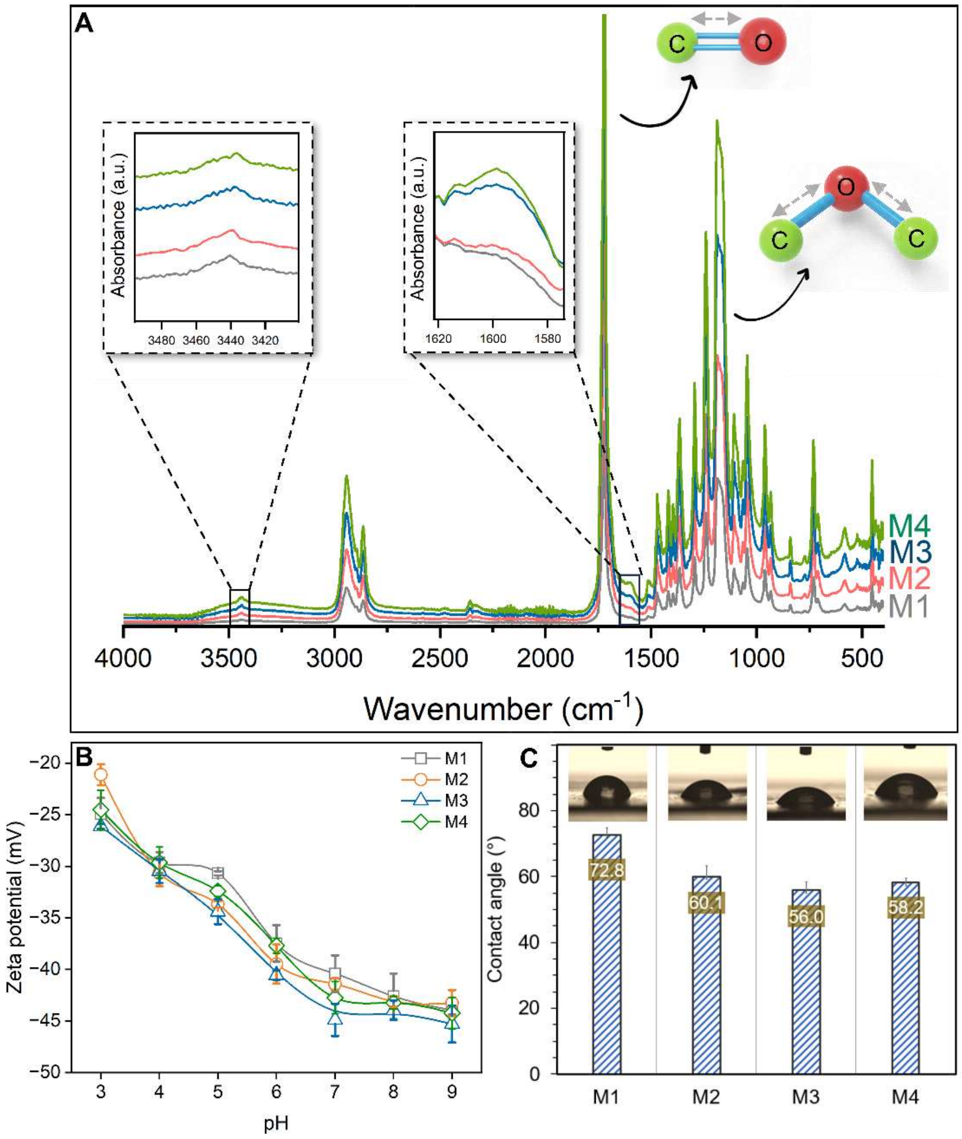

Figure 4.3. (A) ATR-FTIR spectra of PCL/SKL phase inversion membranes (M1, M2, M3, and M4); magnified FTIR spectra within the range of 3000 to 3500 cm^{-1} and 1480 to 1700 cm^{-1} are also included, (B) the surface charge of the PCL/SKL membranes at different pH (i.e., pH 3-9), and (C) water contact angle values for different PCL/SKL phase inversion membranes.

The wettability of the PCL/SKL membranes was assessed by water contact angle (WCA) analysis. **Figure 4.3C** shows that the obtained WCA values are ~72°, ~60°, ~56°, and ~58° for M1, M2, M3, and M4 membranes, respectively, implying that the PCL/SKL membranes become more hydrophilic with increased SKL content in the PCL matrix. Previous studies on pure PCL-based phase inversion membranes reported high water contact angles (>80°) of the membranes due to the inherent hydrophobic nature of PCL [273,274]. The enhanced hydrophilicity in SKL-modified membrane can be attributed to the presence of abundant hydrophilic functional groups such as hydroxyl and carboxyl groups on the membrane surface [272]. Surface geometry could also affect the wettability of the PCL/SKL membranes. The increased surface roughness (**Table 4.2**) may contribute to the enhanced hydrophilicity of the SKL-modified membranes according to Wenzel equation (**eq. 4.1**). The surface free energy, an important parameter to determine the wettability of the membrane, also relies on the surface roughness and contact angle according to the modified Young-Dupre equation (**eq. 4.2**). A higher absolute value of interfacial free energy is preferred for an enhanced wettability of the membrane surface. As can be seen from **Table 4.2**, the ΔG_{sl} value increased from ~91 mJ/m^2 for M1 to ~106 mJ/m^2 for M3 membrane, suggesting an improved wettability that can enhance antifouling properties. Therefore, it can be concluded that the quantity of SKL content within the PCL matrix significantly impacts the surface free energy and, consequently, the wettability of the membranes. It is worth mentioning that the deviation in contact angle and surface free energy values for the M4 membrane compared to the M3 membrane, which goes against the observed trend, may be attributed to the lower-than-expected SKL content in the PCL matrix (M4). Some SKL leaching was observed in the coagulation bath during the PCL/SKL membrane fabrication at the highest SKL concentration (M4, 10 wt.%), which could cause these discrepancies.

4.3.3 Membrane performance on separating single salts and dyes

Figure 4.4A shows the pure water flux of the PCL/SKL membranes. All SKL-modified membranes showed reasonable flux at 40 psi except for M1, which showed zero flux, likely due to its low hydrophilicity. As shown in **Figure 4.3C**, M1 had the highest contact angle (~73°) among the SKL-modified membranes. M2 and M3 exhibited an increasing trend in water flux with increased SKL content. M2 had a minimum water flux of ~32 LMH, while M3 showed a maximum water flux of ~45 LMH. The water flux of M4 was lower than that of M3, approximately 37 LMH, with a large error bar. This can be ascribed to the leaching of SKL in the coagulation bath at high concentrations (10 wt.%), reducing the SKL loading and causing inconsistency in membrane fabrication. The lower hydrophilicity of M4 compared to M3, as depicted in **Figure 4.3C**, supports this result.

To assess the potential of the PCL/SKL membranes for dye separation, three different anionic dyes (RR, RB, and MO) were filtered, and the dye rejection results are presented in **Figure 4.4B**. For the high molecular weight (MW) dyes (RR and RB, with the MW of 1469.9 Da and 991.8 Da, respectively), the rejection percentage of all membranes (M2-M4) was higher than 93%. In contrast, the smallest dye molecule, MO (MW: 327.3 Da), demonstrated the lowest rejection rate, ranging from 49 to 53%. The observed dye separation phenomenon can be attributed to the synergistic combination of electrostatic repulsion and size-sieving effect [27]. Among the SKL-modified membranes, M3 demonstrated the highest water flux and rejection rate for all dyes; therefore, it is considered for further studies. The MWCO, as described in section 2.4.3, was used to determine the pore size of the optimum PCL/SKL membrane (M3). **Figure 4.4C** illustrates the molecular weight sieving curve and pore size distribution of the M3 membrane. The average pore size and distribution were determined using the probability density function of PEG rejection and its corresponding Stokes diameter (**eqs. 4.5 and 4.6**). The results revealed that M3 possessed a molecular weight cut-off (MWCO) of 8.69 kDa and a mean pore size of 2.46 nm. Additionally, the pore size distribution curve indicated a broad distribution of pores ranging from 1 to 10 nm within this membrane.

Figure 4.4D shows the single salt rejection performance of the optimum SKL-modified membrane (M3). The membrane showed a high salt permeation, with the order of salt rejection as follows: Na_2SO_4 (~25%) > $MgSO_4$ (~11.5%) > NaCl (~11.1%) > $MgCl_2$ (~8%). As can be seen, salt retention for divalent anion (Na_2SO_4 and $MgSO_4$) was higher than monovalent anion (NaCl and $MgCl_2$). The observed salt rejection sequence can be explained based on the Donnan exclusion [220,267]. According to this mechanism, the repulsion between similarly charged monovalent ions and membrane surface is weaker than that of divalent ions. Therefore, the negatively charged M3 membrane rejected more divalent anions than monovalent anions.

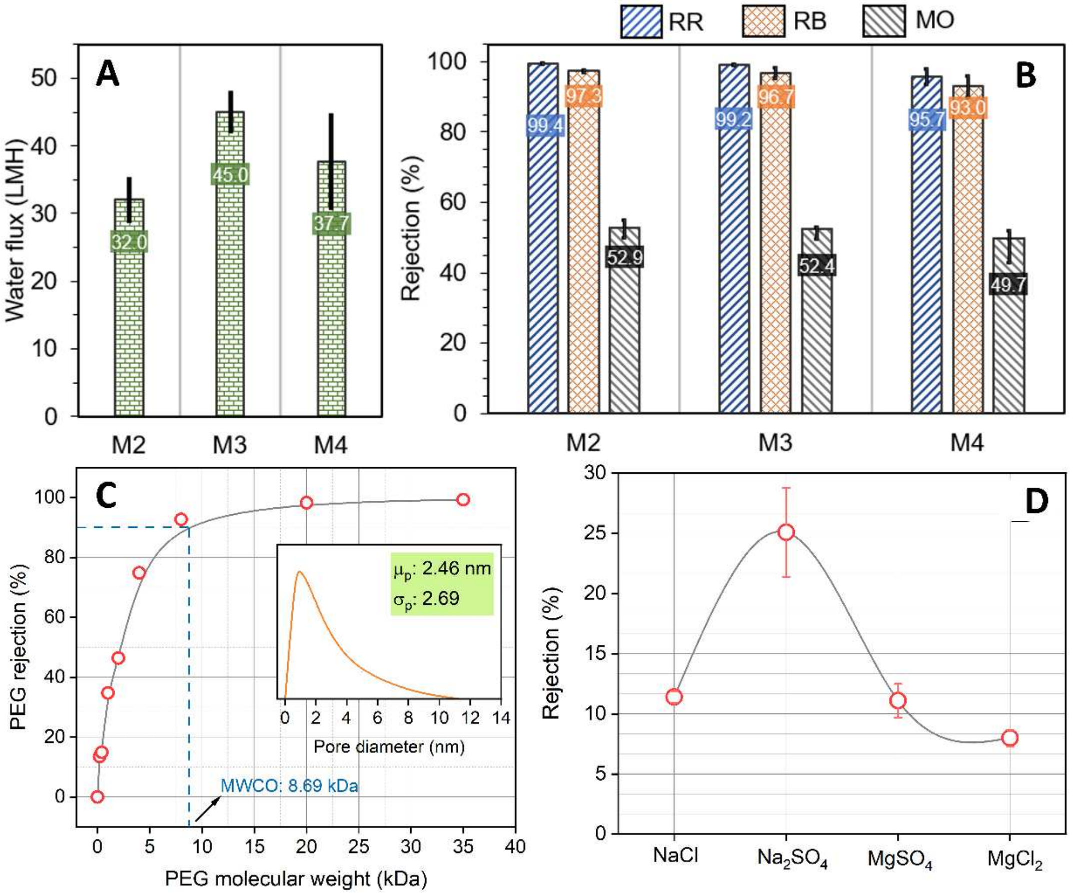

Figure 4.4. (A) pure water flux of membranes (M2, M3, and M4), (B) single anionic dye (RR, RB, and MO) rejection of PCL/SKL membranes, (C) MWCO sieving curve of M3 membrane; pore size distribution of the membrane is also included, and (D) single salt rejections of the optimum membrane (M3). All values are reported from at least three different measurements from different samples.

The effect of increasing salt (NaCl and Na_2SO_4) concentration on the salt rejection performance of the optimum membrane (M3) was also investigated. Previous studies have reported that increased salt concentration in the feed can substantially elevate the osmotic pressure of the solution, leading to a reduction in permeation flux in high-salinity dye wastewater [296]. However, as shown in **Figures 4.5A and 4.5B**, the M3 membrane experienced no significant flux decline at different concentrations of NaCl and Na_2SO_4. The flux remained within ± 3 LMH error margin of the average water flux (44 LMH). The consistent flux observed at high salt concentrations can be explained by the high salt permeation through the membrane, effectively minimizing the transmembrane osmotic pressure difference [255]. **Figure 4.5** also demonstrates a decline in salt rejection with the increasing salt concentration. The rejection rate reduced from ~21% to ~1% for

Na_2SO_4 and from ~12 to ~0.8% for NaCl by increasing the salt concentration from 1 to 50 g/L. This reduction in salt rejection is likely due to the suppressed Debye length and shielding of surface charge at high salt concentrations, leading to a weakened electrostatic repulsion effect between the membrane and charged ion species [264]. Overall, the combination of high dye rejection and salt permeation suggests a high potential for this SKL-modified membrane in the efficient fractionation of dye/salt mixtures.

4.3.4 Membrane performance on separating dye/salt mixture

Figures 4.5C and 4.5D illustrate the effect of salt concentration on the dye/salt mixture separation performance of the M3 membrane. In this test, RR dye concentration was fixed at 0.1 g/L, while NaCl and Na_2SO_4 concentrations varied between 1 and 50 g/L. At a low salt concentration of NaCl and Na_2SO_4 (i.e., 1g/L), the M3 membrane showed remarkable dye rejection (>90%) with high salt permeation (>80%), which suggested excellent dye/salt fractionation performance of the membrane. Although M3 had a high MWCO (8.69 kDa) and larger pore sizes (1-10 nm) than the feed solute size (RR, 1.47 kDa), the high dye rejection at the saltless and low salt concentration (1 g/L) can be attributed to the electrostatic repulsion effect between the anionic dye and negatively charged surface [257,269]. However, the dye removal efficiency gradually declined with increasing salt concentration. The RR dye rejection reduced from ~90 to ~49% and ~93 to ~53% by increasing the NaCl and Na_2SO_4 concentration from 1 to 50 g/L, respectively. The corresponding rejection of NaCl and Na_2SO_4 salts also reduced significantly from ~14% to ~1% and ~22% to ~1%, respectively, with no significant change in water flux. Increasing salt concentration can significantly compress the electrostatic double layer of the membrane surface and weaken the electrostatic repulsion between anionic dye and membrane surface by screening the membrane surface charge, resulting in less dye rejection and high salt permeation [265,277]. Notably, if the electrostatic repulsion effect were the only mechanism governing dye removal efficiency, the membrane would exhibit negligible dye rejection at a high salt concentration (50 g/L) due to an insufficient surface charge to repel anionic dyes at this concentration. Therefore, other factors like dye aggregation and steric hindrance can also impact the dye separation performance at different ionic strengths of the dye solution. It is reported in the literature that dye molecules can aggregate via π-π stacking interaction in aromatic rings, forming clusters of large molecular size due to a reduction in electrostatic repulsion between dye molecules at high ionic strength [264,267].

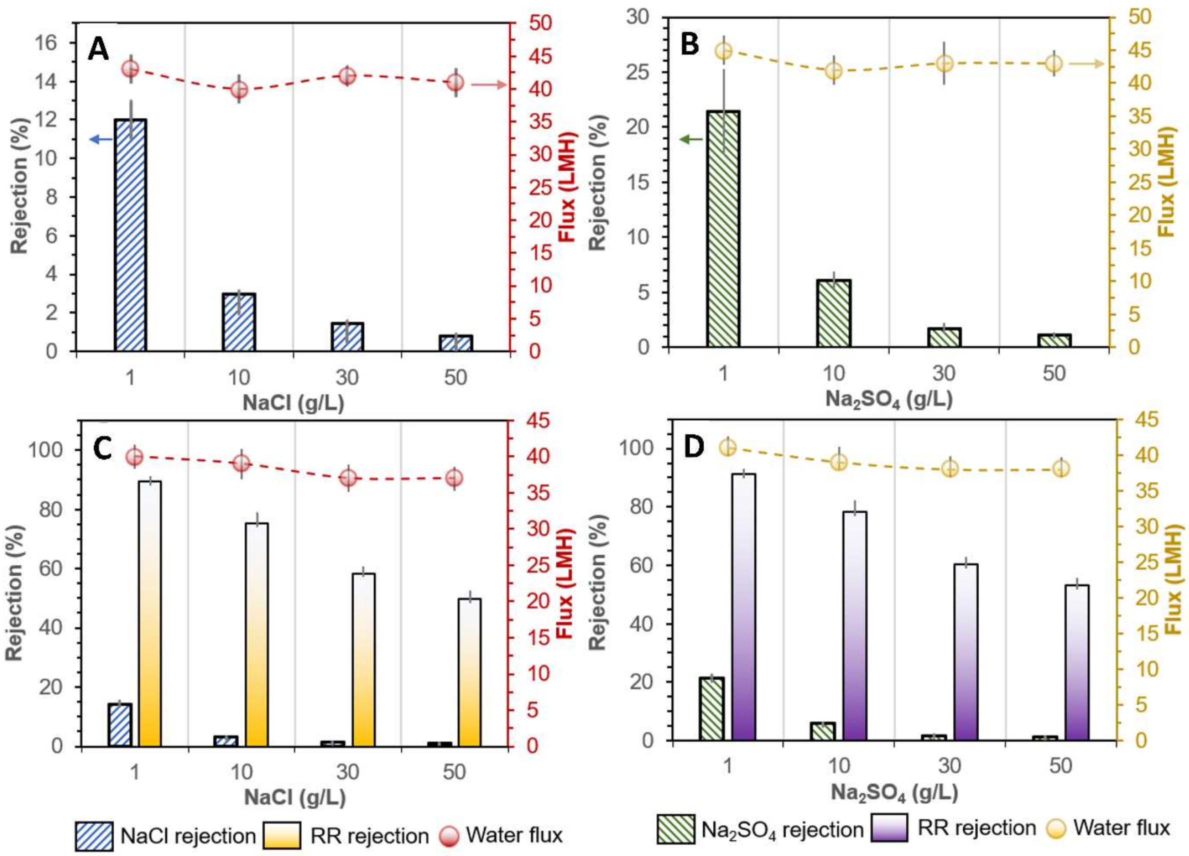

Figure 4.5. Salt rejection and water flux at increasing concentrations of (A) NaCl and (B) Na_2SO_4; Separation performance of M3 Membrane at different dye/salt mixtures were also provided: (C) RR/NaCl and (D) RR/ Na_2SO_4. In both mixtures, dye concentration was 0.1 g/L, and salt concentration was varied from 1 to 50 g/L. All values are reported from at least three different measurements from different samples.

This hypothesis is supported by the change in the maximum absorption peak of RR solution at different salt concentrations (**Figure C.S5**), aligning with the previous research, noting a peak shift due to dye aggregation [264,269].

The contribution rate of different factors (i.e., charge, steric hindrance, and molecular weight effect) in dye separation was further examined in the following section according to the method proposed by Hu et al. [277] **Figure 4.6A** demonstrates the rejection of three anionic dyes and neutral PEG solutes at different molecular weights. It can be observed that the rejection of RR (~99%), RB (~97%), and MO (~53%) was significantly higher than the rejection of neutral PEG molecules of similar molecular weight (1479, 991, and 327 Da), which was 38%, 29%, and 13%, respectively. This indicates that other than the molecular sieving effect, the electrostatic interaction (charge effect) between negatively charged membrane and anionic dyes played a role in achieving high dye rejection. Additionally, the presence of stereoscopic structures with multiple benzene rings in dyes, unlike the linear structure of PEG, suggests that steric hindrance could also contribute to the separation of dyes in conjunction with the charge effect. The contribution rate of these factors, as presented in **Figure 4.6B**, can be calculated from **Figure 4.6A**. The contribution rate of the molecular weight effect was calculated from the rejection value of PEG with the same MW as the dye molecules. For example, the rejection of neutral PEG at 327 Da (equivalent MW as MO) was 13.5%, whereas the rejection of MO was 52.7%. Subsequently, the contribution rate was calculated, with 25.7% attributed to the molecular weight effect (dividing the MO rejection by the PEG rejection) and 74.3% to the charge and steric hindrance (subtracting the contribution rate of the molecular weight effect from 100%). It can be seen from **Figure 4.6B** that the contribution rate of molecular weight increased from 25.7% to 38.4%, while steric hindrance and charge effect contribution rate decreased from 74.3% to 61.6% with the increase in dye MW from 327 Da (MO) to 1479 Da (RR). The contribution rate reveals that the rejection of different dyes at saltless conditions can be attributed to the combined effect of charge, steric hindrance, and molecular weight. However, when salt is present in the dye solution, the impact of these factors on dye separation may vary due to changes in membrane surface charge resulting from changes in ionic strength.

To explore the effect of salt concentration on membrane charge, the zeta potential of the membrane (M3) was measured using different concentrations of KCl, as depicted in **Figure 4.6C**. It can be seen that the surface negative charge declined with the ionic strength due to the electrostatic shielding effect. Hence, the effect of electrostatic repulsion (charge effect) between membrane surface and anionic dyes is expected to reduce with increasing ionic strength, thereby leading to less rejection of dyes. This observation is further explored by measuring the surface charge density at various ionic strengths (**Table C.S2**) using **eq. 4.11-4.13**. The results reveal an increasing trend in surface charge density with ionic strength. The obtained charge density was plotted against the ionic strength using **eq. 4.14**, as shown in **Figure 4.6D**, which exhibited a linear relationship with a correlation coefficient of 0.98. This observation aligns well with the Freundlich adsorption isotherm, indicating that an increase in surface charge density results from the ion adsorption from the solution. As more ions accumulate with increasing ionic strength, more surface area will be covered, thus reducing the Debye length and membrane surface charge (**Figure 4.6E**). This aligns with the observed trend of dye rejection in **Figures 4.5C and 4.5D** at high salt concentrations.

According to Gouy-Chapman-Stern theory, the increase in salt concentration is anticipated to result in complete surface coverage with counterions, neutralizing the charged surfaces and collapsing the diffuse layer [297,298]. Therefore, no charge effect on dye separation is expected at high salt concentrations. However, estimating zeta potential at higher ionic strengths using theories modeling ions as point charges, such as the Gouy-Chapman-Stern theory, is unreliable due to ion hydration and spatial extension. Moreover, Zeta potential measurement by electrokinetic analyzers is constrained by relatively low ionic strength, typically below 0.1 M. To further explore the charge effect at high salt concentration, the zeta potential was measured indirectly at high ionic strength using the extrapolation method proposed by Coday et al. [298]. This method combines streaming potential measurements with theoretical modeling, allowing estimation of zeta potential at higher ionic strengths [298]. To estimate zeta potential, a 1:1 electrolyte (KCl) solution was used at varying concentrations (1-100 mM), and streaming potential measurements (**Table C.S2**) were carried out on the optimum membrane. The obtained streaming potential coefficient (dU/dP) was then plotted against the inverse square root of electrolyte conductivity ($k^{-1/2}$) on a log-log scale (**Figure C.S6**). It is worth noting that the electrolyte conductivity was verified to increase linearly with the ionic strength (0.001 to 1 M) (**Figure C.S6**). The inverse square root of conductivity was used since the Debye length equation (**eq. 4.13**) includes the inverse square root of ionic strength. The plot of (dU/dP) against ($k^{-1/2}$) enables extrapolation of the streaming potential coefficient to high ionic strength, which was then used to estimate the zeta potential using the Helmholtz-Smoluchowski equation [298]:

$$\zeta = \frac{dU}{dp}\frac{\eta}{\varepsilon}k \tag{4.15}$$

where $\frac{dU}{dp}$ is the streaming potential coefficient, η denotes the electrolyte viscosity, and k denotes electrolyte conductivity.

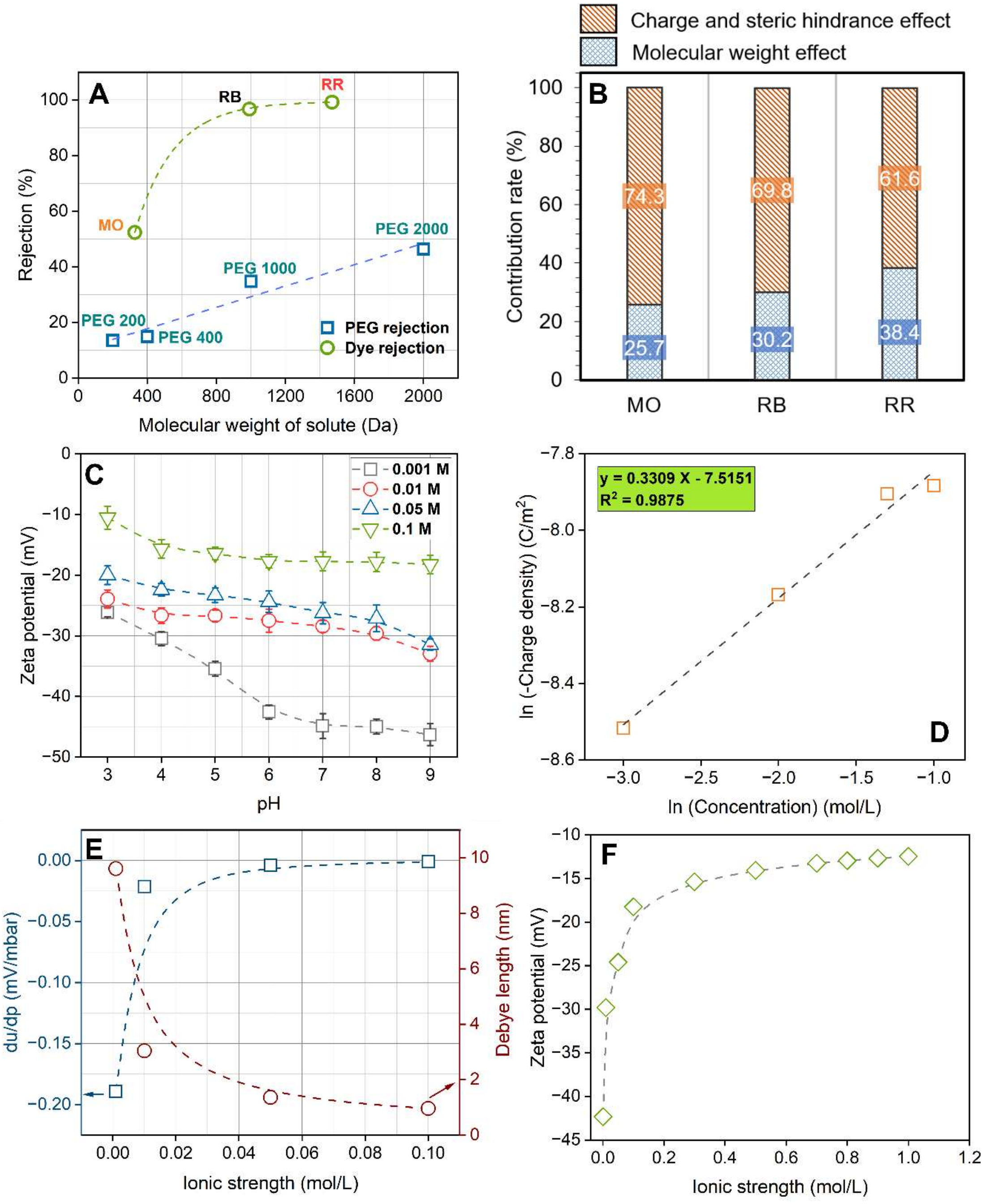

Figure 4.6. (A) Rejection of anionic dyes and equivalent MW PEG solutes, (B) contribution rate of different factors for dye separation, (C) zeta potential values at different pH (3-9) with increasing ionic strength (0.001-1 M KCl), (D) surface charge density and concentration relation, (E) change of streaming potential coefficient and Debye length with ionic strength, and (F) extrapolated zeta potential values at high ionic strength (0.001 to 1 M KCl).

Figure 4.6F shows the extrapolated zeta potential values at different ionic strengths (0.001 to 1 M). The zeta potential exhibited a sharp decrease at low concentrations (ranging from 0.001 to 0.1 M ionic strengths) and subsequently experienced a marginal reduction beyond the 0.2 M ionic strength values. Interestingly, it remained almost constant above 0.7-0.8 M, corresponding to a Debye length of 3.5-3.2 Angstrom, equivalent to the hydration radius of potassium ion (3.31 Angstrom). This indicates that the diffuse layer shrinkage is limited to the hydrated size of counterions. Therefore, complete charge neutralization will not occur even at a very high KCl, NaCl, or Na_2SO_4 concentration, which aligns with the zeta potential value (~-13 mV) obtained at high ionic strength (1M), as shown in **Figure 4.6F**. Hence, the charge effect, even though to a lesser extent, can still influence dye rejection at higher salt concentrations (10-50 g/L).

Based on the above observation, it can be concluded that the charge effect was the dominant factor for dye separation at low salt concentration, while its contribution rate reduced with increasing salt concentration but cannot be neglected completely. It is worth mentioning that while the developed PCL/SKL membrane demonstrated effective separation of dye/salt mixtures up to a salt concentration of 10 g/L, its efficiency was reduced at higher salt concentrations (50 g/L). Future work could focus on enhancing the dye/salt selectivity, particularly under highly saline conditions, without compromising water flux. This improvement might involve surface coating or introducing an additional bio-based additive to create a more tightly selective PCL/SKL membrane.

4.3.5 Antifouling performance stability of membrane

Figure 4.7 (A-F) presents the antifouling performance of the PCL/SKL membrane (M3) while filtering RR (0.1 g/L) / Na_2SO_4 (1 g/L) mixture, humic acid (0.1 g/L), and BSA (0.1 g/L) solutions. **Figure 4.7A** shows that the flux of the membrane reduced slightly in the first cycle, decreasing from ~43 LMH to ~40 LMH while using RR/Na_2SO_4 mixture as feed solution. However, the flux was restored after a simple rinsing with water, and a similar trend was observed in the second cycle. The corresponding fouling properties (**Figure 4.7D**) at the end of the fouling test exhibited impressive results with a high FRR (~99%), low FDR (~4.61%), R_r (~4%), and R_{ir} (<1%), indicating an excellent fouling resistance of PCL/SKL membrane toward dye solution. **Figure 4.7B** demonstrates the flux change with time while using humic acid as a feed solution. Like the dye/salt mixture, the flux initially decreased, followed by stabilization. Flux recovery was observed after hydraulic cleaning. The antifouling index (**Figure 4.7E**) also showed high FRR

(~98%) and very low FDR (~7%), R_r (~6%), and R_{ir} (~1%). The antifouling behaviour of the M3 membrane was further explored by filtering BSA solution (0.1 g/L) (**Figure 4.7C and 4.7F**). The membrane maintained its excellent antifouling performance with high FRR (~97%) and very low FDR (~8%), R_r (~6%), and R_{ir} (~3%). The SEM images of the membranes taken before and after the fouling tests (**Figure C.S7**) revealed no significant deposition of foulants, indicating the excellent antifouling performance of the membrane. The remarkable antifouling properties of the PCL/SKL membrane can be attributed to its negatively charged surface and excellent hydrophilicity. The excellent wettability of the membrane can be ascribed to the hydrophilic functional groups (e.g., hydroxyl and carboxyl groups) on the membrane surface (as illustrated in **Figure 4.3A**). The hydrophilic groups effectively attract water molecules, thus forming a hydration layer on the surface, preventing the adsorption of contaminants [257,260]. Moreover, the electrostatic repulsion between the negatively charged membrane surface (**Figure 4.3B**) and anionic foulants (dye and humic acid) restricts the attachment of foulants on the membrane surface, enhancing fouling resistance of the PCL/SKL membrane [269]. The negative charge of the membrane and its electrostatic repulsion effect towards anionic foulant was further explored by immersing the membrane in both anionic and cationic dye solutions. It can be observed from **Figure 4.7G** that positively charged dyes (Methylene Blue and Rhodamine B) were adsorbed on the membrane surface after its exposure to the cationic dye solution overnight. On the other hand, a clean membrane was obtained after exposing the membrane to an anionic dye (RR) solution overnight, indicating its negative charge on the surface and electrostatic repulsion effect towards anionic dyes.

The SKL-modified membrane also exhibited excellent stability in a wide pH range (pH 3-9). The membranes exposed to different pH conditions were tested to assess their separation performance, as shown in **Figure 4.7H**. The membrane flux and dye/salt rejection remained almost stable at all conditions, suggesting excellent PCL/SKL membrane stability in this pH range. **Figure 4.7I** shows the long-term dye/salt separation performance of the membrane. The result exhibited a slight reduction in flux from ~42 LMH (1st day) to ~38 LMH on the 2nd day, followed by stable flux on the third day. The flux decline was likely due to the compaction or dye solute built up during the long-term experiments. However, the membrane exhibited high dye rejection (>90%) and low salt rejection (<20%) during the test for three consecutive days.

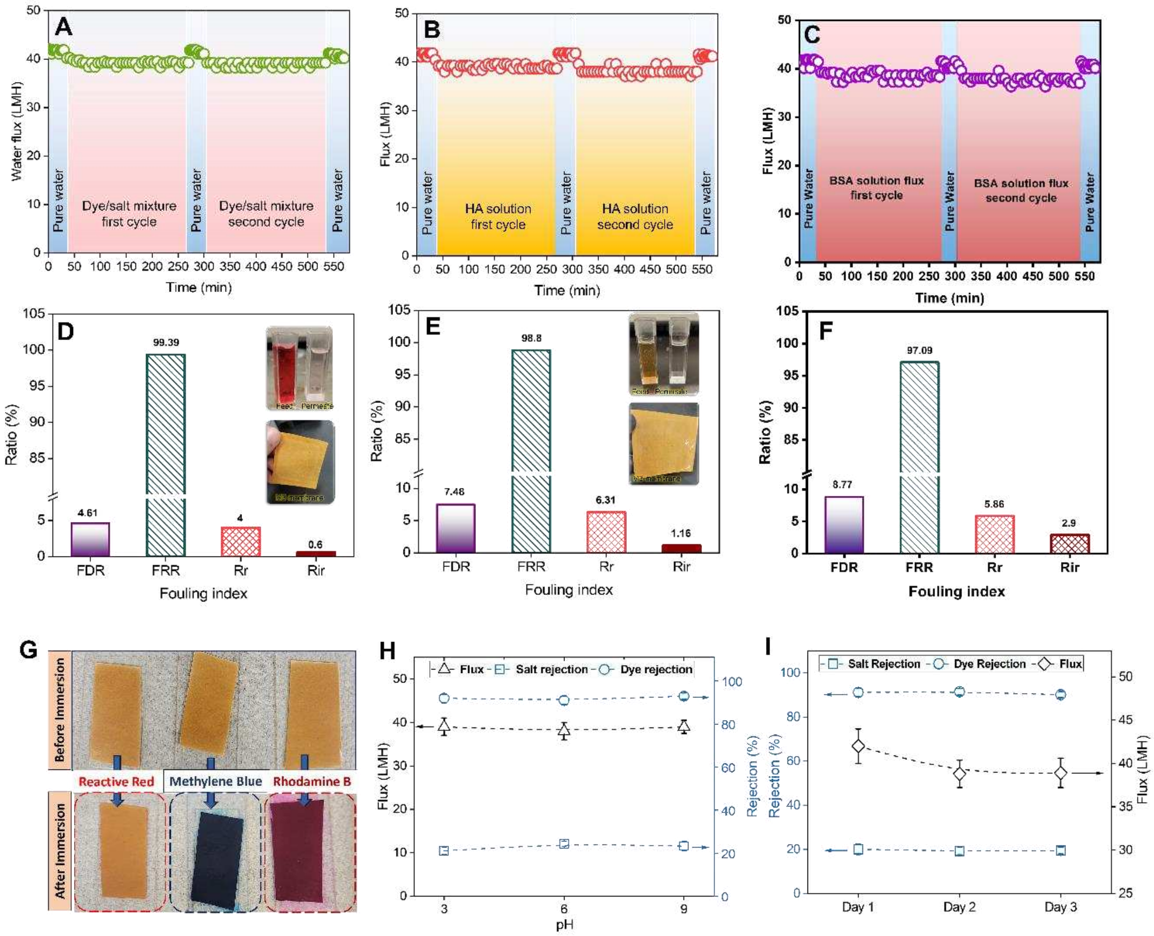

Figure 4.7. Antifouling performance and fouling properties of PCL/SKL membrane(M3): (A, D) RR (0.1 g/L)/Na_2SO_4 (1 g/L) mixture in the feed, (B, E) Humic acid (0.1 g/L) in the feed solution, (C, F) BSA (0.1 g/L) in the feed solution; (G) Dye adsorption behavior of M3 membrane after immersing the M3 membrane overnight in solutions containing cationic dyes (Methylene blue and Rhodamine B) and anionic dye (Reactive red); (H) RR (0.1 g/L)/Na_2SO_4 (1 g/L) separation performance of M3 membrane after immersing at different pH (pH 3, 6, and 9) for 1 day, and (I) shows the long-term performance of PCL/SKL (M3) membrane.

It is worth mentioning that SKL content in the PCL matrix had excellent stability. In our recent research on PCL/SKL membrane, we observed no leaching of the SKL content from the PCL matrix, with the SKL content being less than 10 wt% [272]. This excellent stability was attributed to the hydrogen bonding interaction and strong compatibility between PCL and SKL. Additionally, we demonstrated that the presence of hydrophilic SKL content accelerated the biodegradation rate of the PCL/SKL membrane [272]. The DSC analysis (**Figure C.S3**) showed that the prepared

PCL/SKL membrane has a melting point of around 60°C, indicating its suitability for wastewater treatment application at a temperature below this threshold.

Table 4.3. Dye/salt mixture separation performance of PCL/SKL membrane (M3) and other reported membranes in the literature.

Membrane	Dye/Salt mixture	PWP, LMH/bar	Rejection (Dye/Salt) %	Selectivity (R_{dye}/R_{salt})	Ref.
TA/GOQDs	MB/NaCl	11.7	97.6/17.2	5.7	[299]
AL/SL	CR/NaCl	63.1	96.3/15.4	6.3	[267]
PAI/PEI	MG/NaCl	18.5	95/11.3	8.4	[300]
PS-b-PEG	CR/NaCl	49.3	98.7/0.1	987	[301]
MoS_2-PSBMA/PES	RB/NaCl	18.05	98.2/1.1	89.2	[302]
HNTs-PIL/PES	RR/Na_2SO_4	7.75	85/3	28.3	[303]
sPPSU	Disperse Blue 1/Na_2SO_4	15	99.26/4.89	20.3	[27]
NF-SPEI	RR/NaCl	33.3	97/3.2	30.3	[304]
GO-PSBMA/PES	RR/ Na_2SO_4	11.98	97.2/10	9.72	[305]
PCL/SKL	RR/ Na_2SO_4	15.3	93.1/20 (1g/L) 53/1.1 (50 g/L)	4.65 (1g/L) 48.2 (50 g/L)	This work
	RR/NaCl		91.5/9.5 (1g/L) 51.1/1 (50 g/L)	9.63 (1g/L) 51.1 (50 g/L)	

* PWP (pure water permeability); GOQDs (Graphene oxide quantum dots); PAI (polyamide-imide); MoS_2-PSBMA (Molybdenum disulfide modified by zwitterionic 2-methacryloyloxy ethyl dimethyl (3-sulfopropyl)-ammonium) hydroxide sulfobetaine methacrylate); HNTs-PIL/PES (poly (ionic liquid) brush modified Hallosyte nanotube/PES); MG (Methyl Green); RB (Reactive Black); RR (Reactive Red); AL (Alkaline lignin); SL (Sodium lignin sulfonate); sPPSU (sulfonated polyphenylene sulfone); SPEI (Sulfonated polyethyleneimine); CR (Congo Red); PSBMA (poly(sulfobetaine methacrylate)).

Moreover, the PCL/SKL membrane prepared in the present study exhibited robust mechanical stability, primarily due to the nonwoven polyester fabric serving as a support. There were no instances of membrane detachment from the support observed before or after the experiments under both wet and dry conditions. The cross-section SEM image (**Figure C.S2 E, F**) also showed membrane formation inside the nonwoven polyester support, which favors strong attachment of the PCL/SKL membrane with the support. For further evaluation, we provided digital images of the membrane before and after bending and twisting the membrane (**Figure C.S8**), which confirms the excellent mechanical stability of the membrane as no cracks or detachments were observed. A supplementary video is also provided showing the mechanical robustness of the PCL/SKL membrane.

Table 4.3 compares the separation efficiency for dye/salt mixtures between the PCL/SKL (M3) membrane prepared in this study and membranes reported in previous research. The findings indicate that the SKL-modified phase inversion membrane shows comparable dye and salt separation performance, particularly at low salt concentrations. Although selectivity was improved at higher ionic strength, we observed relatively low dye rejection with increasing salt concentrations. It is worth mentioning that most membranes examined in prior studies were either prepared from non-biodegradable fossil-based materials or required toxic solvents. In contrast, the PCL/SKL membranes are exclusively derived from biobased and biodegradable polymers, and the solvent used was green and non-toxic. Future research could investigate potential modifications such as coatings or membrane crosslinking to enhance the dye removal efficiency under high salinity conditions. Hence, the green PCL/SKL membrane developed in this study with excellent antifouling properties holds promise as an eco-friendly solution for separating dye/salt separation. These membranes have significant potential to be used in nanofiltration (NF) or microfiltration (MF) applications by controlling process parameters and preparation techniques. For instance, adjusting the composition of PCL and SKL, adding pore formers, or applying surface modifications like interfacial polymerization can tailor membrane structure, improve performance, and broaden their application in NF or MF processes.

4.4 Conclusion

This study highlights a facile and scalable fabrication of a green and biodegradable phase inversion membrane for dye/salt separation by simply blending biodegradable PCL with the low-cost biobased additive SKL. We also employed acetic acid as an environmentally friendly and green alternative solvent to enhance the sustainability of the membrane fabrication process. A comprehensive analysis of the influence of hydrophilic SKL content on membrane structure and morphology was carried out using SEM, AFM, FTIR, WCA, and zeta potential analyses. We observed that adding hydrophilic SKL in the PCL matrix made the membrane more hydrophilic and rougher. Moreover, hydrophilic functional groups such as hydroxyl and carboxyl groups of SKL made the membrane surface more negative. The optimum PCL/SKL membrane, with an SKL concentration of 9 wt.% (M3), exhibited excellent water flux (~45 LMH) with impressive dye rejection (>98% for RR) and high salt permeation (>90% for NaCl) at low salt concentrations. However, the membrane showed a decline in RR dye rejection from ~90% to ~50% with increasing salt concentration (1-50 g/L). The corresponding permeation of NaCl and Na_2SO_4 salts also increased significantly from ~86% to ~99% and ~78% to ~99%, respectively. The dye rejection behavior of the M3 membrane at different salt concentrations was attributed to the combined effect of charge, steric hindrance, and molecular size. The M3 membrane exhibited excellent antifouling properties during dye and humic acid filtration with high FRR (>98%) and low FDR (< 7.5%). The PCL/SKL membrane also exhibited excellent stability and consistent separation performance over a long period. Overall, the green and biodegradable PCL/SKL membrane prepared in this study paved a new way toward sustainable membrane fabrication for wastewater treatment applications.

Chapter 5

Conclusion and Future Work

5.1 Summary of key findings

This comprehensive PhD research addresses the sustainability challenges in polymeric membrane fabrication, which often uses fossil-based polymers and toxic organic solvents, leading to significant environmental and health risks. It provides insights on using biodegradable materials and green solvents, characterization techniques, major challenges, and future trends for sustainable membrane production.

Pursuing the 12 green chemistry principles is a key objective in various research fields to reduce or eliminate hazardous and toxic materials in chemical reactions and applications. Membrane science and technology play a crucial role across many industries, yet they face challenges in aligning with green chemistry and sustainability goals. A significant issue is the widespread use of toxic solvents in polymeric membrane fabrication, which contradicts green chemistry principles. Thus, finding alternative, greener solvents to replace conventional ones has become a hot topic. Moreover, membrane production relies heavily on finite fossil resources, exacerbating resource depletion and environmental degradation. These fossil-based nonbiodegradable polymers present significant environmental challenges, as they do not degrade naturally, leading to persistent waste in landfills and oceans. Disposing of these membranes creates long-term ecological issues, as they can release microplastics and other contaminants. Overall, the reliance on nonbiodegradable polymers undermines sustainability efforts and necessitates a shift towards eco-friendly, biodegradable alternatives.

Five different strategies are proposed by the researchers to improve sustainability in the membrane manufacturing phase. First, nonbiodegradable fossil-based polymers should be replaced with renewable bio-based polymers, which are biodegradable, biocompatible, versatile, low in carbon footprint, and socially accepted. Second, greener alternatives to traditional, toxic solvents should be used. Third, wastewater containing organic solvents and polymers generated during fabrication should be treated. Fourth, fabrication steps should be reduced to decrease the use of toxic solvents, energy consumption, and costs. Finally, casting solutions should be prepared at room temperature to lower energy consumption further.

The first part of the PhD research showed a promising strategy to enhance the permeability of PSS/PEI membrane prepared by APS process. This work focused on eliminating the use of toxic solvents as well as enhancing the APS membrane performance. This study systematically investigated the influence of two parameters, i.e., monomer mixing ratio and casting solution temperature, on the performance of PSS-PEI membranes. By adjusting the monomer mixing ratio, both NF and UF membranes were prepared. NF membranes, with MWCO values of ~214 Da and ~294 Da, were achieved at monomer ratios of 1:1.65 and 1:1.70, respectively, while UF membranes with MWCO values between ~10-50 kDa were obtained at higher monomer ratios. Excess PEI in the casting solution significantly affected membrane morphology, altering pore size, surface roughness, and charge. Permeability increased with higher monomer ratios due to the synergistic effects of excess charges and larger pores. NF membranes demonstrated higher retention of divalent salts compared to monovalent salts, following the order: $MgCl_2$ > $MgSO_4$ > Na_2SO_4 > NaCl, indicating a separation mechanism based on size and Donnan exclusion. UF membranes exhibited excellent retention of proteins and natural organic matter, particularly those prepared with monomer ratios above 1:1.75, which displayed pattern-like surfaces. Casting solution temperature was another crucial factor, with higher temperatures (40°C and 60°C) leading to faster precipitation, larger pore sizes, and thinner skin layers. This resulted in a sharp increase in PWP from ~8 to ~140 LMH/bar as the temperature rose from 25°C to 60°C.

Although the previous research successfully reduces the usage of toxic solvents, the use of fossil-based nonbiodegradable polymers still remains a challenge. Exploring environmentally friendly, renewable, and cost-effective raw materials is crucial for sustainable membrane fabrication. Therefore, the second part of the PhD research was focused on preparing biodegradable membranes to promote sustainability in membrane fabrication. In this study, a biodegradable electrospun nanofibrous membrane was fabricated for oily wastewater treatment by blending PCL with a waste byproduct, SKL. The impact of SKL on the membrane's morphology, composition, and mechanical properties was analyzed using SEM, FTIR, and tensile testing. Adding SKL resulted in thicker fibers with nanonet-like structures and increased the membrane's negative surface charge due to hydrophilic anionic functional groups. The tensile strength of the membrane improved due to the rigidity of SKL and hydrogen bonding with PCL. The membrane's wettability changed from hydrophobic to superhydrophilic and underwater superoleophobic with SKL addition. SKL-modified membranes exhibited high water flux (800-900 LMH) and emulsion flux (170-480 LMH) in filtering various oil-in-water emulsions. They also demonstrated excellent anti-oil-fouling performance, with 97-99% separation efficiency and a flux recovery rate of over 98%. The membranes showed outstanding reusability, structural stability, and wettability across a wide pH range without leaching. This study concludes that incorporating SKL in PCL electrospun membranes provides superhydrophilicity and excellent structural stability, making them effective for oily wastewater treatment.

The final phase of the research built upon earlier findings that identified SKL and PCL as effective materials for preparing biodegradable membranes. This phase shifted focus to developing PCL/SKL-based membranes through a nonsolvent-induced phase separation process, in contrast to the electrospinning technique used in the previous research. This study introduced a scalable, eco-friendly method for preparing biodegradable PCL/SKL-based phase inversion membranes for dye/salt separation, using acetic acid as a green solvent to enhance sustainability in the fabrication process. Comprehensive analyses using SEM, AFM, FTIR, WCA, and zeta potential indicated that adding hydrophilic SKL to the PCL matrix increased the membrane's hydrophilicity and roughness, while also introducing more negative surface charges due to SKL's hydroxyl and carboxyl groups. The optimal membrane, with 9 wt.% SKL (M3), demonstrated impressive performance with a water flux of ~45 LMH, dye rejection of over 98% for RR, and high salt permeation (>90% for NaCl) at low salt concentrations. However, dye rejection decreased from ~90% to ~50% as salt concentration increased (1-50 g/L), while salt permeation for NaCl and Na_2SO_4 increased significantly. The membrane's dye rejection behavior was influenced by charge, steric hindrance, and molecular size. The M3 membrane also showed excellent antifouling properties during dye and humic acid filtration, with a high flux recovery ratio (FRR >98%) and low flux decline ratio (FDR <7.5%). The PCL/SKL membrane also exhibited stability and consistent performance over time. Overall, this green and biodegradable PCL/SKL membrane offers a sustainable solution for wastewater treatment applications.

5.2 Future work

Green and sustainable membranes are crucial for advancing the circular economy and achieving sustainable development goals. They align with circular growth principles in water treatment, filtration, energy production, and material separation. Developing advanced membrane materials with enhanced mechanical, thermal, and chemical stability and competitive or superior performance compared to conventional membranes is increasingly crucial from industrial and environmental perspectives. Natural components and materials in membrane technology offer significant advantages, including inherent biocompatibility and biodegradability, making them more environmentally friendly than conventional synthetic materials. Utilizing renewable biopolymers or waste valorization in sustainable membrane development reduces natural resource consumption and maximizes resource utilization, aligning with the circular economy's objectives. However, using biopolymers in membrane fabrication presents several challenges, including ensuring adequate mechanical strength and stability to match or exceed conventional materials. Additionally, the processing and scalability of biopolymer-based membranes can be complex and costly, requiring significant research and development. Lastly, finding compatible, non-toxic solvents for biopolymers that do not compromise membrane performance adds another layer of difficulty to their widespread adoption.

Membrane scientists are also aware that eliminating toxic solvents from membrane fabrication processes is a significant future challenge. The choice of solvent for membrane preparation depends on various factors. A crucial requirement for a diluent in phase inversion is its ability to dissolve the selected polymer at room temperature or at high temperatures. The type of solvent significantly affects the final membrane morphology and properties. However, transitioning to environmentally friendly solvents that meet regulatory standards poses challenges, particularly regarding their performance and competitive pricing. This shift requires careful consideration to balance sustainability with effectiveness and cost-efficiency.

Overall, using biodegradable materials and non-toxic solvents enhances human health and environmental well-being and is essential for fostering a greener and more sustainable membrane manufacturing industry. Researchers and industry stakeholders are actively exploring innovative processing techniques and improving the understanding of the structural characteristics of biopolymers to overcome the underlying challenges.

Key aspects of next-generation membrane technology include reduced toxicity, decreased environmental persistence, an intelligent platform, and alignment with the circular economy. Considering the recent technical advancements and ongoing challenges in sustainable membrane fabrication critically reviewed in this article, the following recommendations for future research are proposed:

1. The organic solvent-free aqueous phase separation (APS) process offers a sustainable alternative to the traditional nonsolvent-induced phase separation process yet faces challenges due to the use of fossil-based polyelectrolytes and the low water permeability of APS membranes.

Polyelectrolytes hold significant promise for creating next-generation membranes with advanced functionalities. The field is still evolving, and future research is expected to explore multifunctional polyelectrolyte membranes that combine properties like low fouling, easy cleaning, and specific selectivity. One inherent benefit of polyelectrolytes is their water solubility, which permits the formation of polyelectrolyte coatings and standalone membranes without requiring organic solvents. This advantage can be further leveraged by using biobased polyelectrolytes (PEs) in membrane separations. Although recent studies have explored monovalent anion selectivity and pervaporation using biodegradable PEs [306–308], such as chitosan derivatives, there is considerable potential to investigate PEs like pectin, alginic acid, and cellulose derivatives for membrane-based separations.

2. The use of petroleum-based polymers in membrane materials poses significant environmental concerns, while biobased polymers present a sustainable alternative. However, biopolymers face challenges such as poor mechanical properties, instability over long-term use, and high costs. Further research is essential to refine membrane preparation using biobased materials to achieve performance on par with or exceeding that of petroleum-based membranes. Biopolymers offer unique properties like high porosity, surface area, and sometimes comparable mechanical strength, making them suitable for various applications. Natural materials like cellulose, chitin, and silk fibroin in membrane technology offer excellent mechanical strength, biocompatibility, and biodegradability. Additionally, these materials can be functionalized and modified; for example, chitosan and lignin can be altered to provide antibacterial properties and enhanced selectivity for specific ions. Combining natural materials with carbon nanotubes, graphene, or metal nanoparticles further enhances their properties and functionality [308,309]. Additionally, cross-linking or plasma treatment techniques may be employed to improve the mechanical and functional properties of biopolymer-based membranes. The future of green or natural component-based membranes in water treatment and other applications appears promising, with ongoing research focused on improving performance and expanding their uses.

3. The utilization of green solvents to substitute current toxic ones is another important strategy to improve the sustainability of the membrane manufacturing process. However, environmental advantages alone most likely cannot enable the widespread adoption of green solvents, other factors related to its compatibility with polymers, performance, health, and cost should also be

taken into account. Ensuring that green solvents effectively dissolve and interact with the chosen polymers is crucial for achieving the desired membrane properties. Additionally, the impact of solvent on the final membrane's morphology, stability, and functionality needs thorough evaluation since it can significantly affect the thermodynamics and kinetics of the phase separation process. Balancing these factors requires careful evaluation to ensure that the chosen green solvent not only aligns with sustainability goals but also supports the practical requirements of membrane fabrication.

4. Exploring environmentally friendly, renewable, low-cost raw materials is vital for sustainable membrane fabrication. Future research should focus on developing scalable, biodegradable membranes using commercially available, low-cost biopolymers with excellent thermal and mechanical properties, such as PBAT and PLA. These biopolymers are promising due to their high production capacity, superior properties, and suitability for thin film preparation. Despite their successful use in various industries, including packaging and biomedical applications, the potential of PBAT and PLA in membrane technology remains underexplored. Further investigation is needed to fully understand and optimize their capabilities for membrane applications.

5.3 List of contributions

5.3.1 Journal papers

1. **Md.M.H. Mizan**, M. Rastgar, S.A. Aktij, A. Asad, P. Karami, A. Rahimpour, Mohtada Sadrzadeh, Organic solvent-free polyelectrolyte complex membrane preparation: Effect of monomer mixing ratio and casting solution temperature, Published in Journal of Membrane Science, 2023, 668, 121197.
2. **Md.M.H. Mizan**, P. M. Gurave, M. Rastgar, A. Rahimpour, R.K. Srivastava, Mohtada Sadrzadeh, "Biomass to Membrane": Sulfonated Kraft Lignin/PCL Superhydrophilic Electrospun Membrane for Gravity-Driven Oil-in-Water Emulsion Separation, Published in ACS Applied Material & Interfaces, 2023, 15, 35, 41961-41976.
3. **Md.M.H. Mizan**, M. Rastgar, H. Sultana, Mohtada Sadrzadeh, Green polycaprolactone/sulfonated kraft lignin phase inversion membrane for dye/salt separation, Published in Journal of Membrane Science, 2024, 702, 122806.

5.3.2 Book chapters

1. **Md.M.H. Mizan**, F.R. Omi, H. Sultana, Mohtada Sadrzadeh, Bio-sourced and biodegradable materials for membrane fabrication, (Chapter 7 in Green membrane technologies toward environmental sustainability), 2023, Elsevier.
2. **Md.M.H. Mizan**, F. Seyedpour, Mohtada Sadrzadeh, Exploring biomimetic membranes: applications and challenges, (Chapter 5 in Green membrane technologies toward environmental sustainability), 2023, Elsevier.

5.3.3 Conference presentations

1. **Md.M.H. Mizan,** Pooria Karami, Laleh Shamaei, Joao B.P. Soares, Mohtada Sadrzadeh, Fabrication of green membranes for water treatment, Canadian Chemical Engineering Conference (CCEC), 2022.
2. **Md.M.H. Mizan**, Mohtada Sadrzadeh, Organic solvent-free polyelectrolyte complex membrane preparation: Effect of monomer mixing ratio and casting solution temperature, American Chemical Society (ACS) Fall 2023, August 13-17, 2023, San Francisco, California, USA

References

[1] A. Giwa, S.W. Hasan, A. Yousuf, S. Chakraborty, D.J. Johnson, N. Hilal, Biomimetic membranes: A critical review of recent progress, Desalination 420 (2017) 403–424. https://doi.org/10.1016/j.desal.2017.06.025.

[2] G. Goel, C. Hélix-Nielsen, H.M. Upadhyaya, S. Goel, A bibliometric study on biomimetic and bioinspired membranes for water filtration, NPJ Clean Water 4 (2021). https://doi.org/10.1038/s41545-021-00131-4.

[3] P. Karami, B. Khorshidi, M. McGregor, J.T. Peichel, J.B.P. Soares, M. Sadrzadeh, Thermally stable thin film composite polymeric membranes for water treatment: A review, J Clean Prod 250 (2020). https://doi.org/10.1016/j.jclepro.2019.119447.

[4] E.W. Allen, Process water treatment in Canada's oil sands industry: II. A review of emerging technologies, Journal of Environmental Engineering and Science 7 (2008) 499–524. https://doi.org/10.1139/S08-020.

[5] W. Xie, T. Li, A. Tiraferri, E. Drioli, A. Figoli, J.C. Crittenden, B. Liu, Toward the Next Generation of Sustainable Membranes from Green Chemistry Principles, ACS Sustain Chem Eng 9 (2021) 50–75. https://doi.org/10.1021/acssuschemeng.0c07119.

[6] W. Lu, Z. Yuan, Y. Zhao, H.H. Zhang, H.H. Zhang, X. Li, Porous membranes in secondary battery technologies, Chem Soc Rev 46 (2017) 2199–2236. https://doi.org/10.1039/c6cs00823b.

[7] Y. Yang, Q. Zhang, S. Li, S. Zhang, Preparation and characterization of porous polyelectrolyte complex membranes for nanofiltration, RSC Adv 5 (2015) 3567–3573. https://doi.org/10.1039/c4ra13699c.

[8] K.-V. Peinemann, S. Pereira Nunes, L. Giorno, Membranes Technology Volume 3: Membranes for Food Applications, Wiley-VCH Verlag GmbH & Co. KGaA, Weinheim, Germany, 2010. https://doi.org/10.1002/9783527631384.

[9] D. Kim, O.R. Salazar, S.P. Nunes, Membrane manufacture for peptide separation, Green Chemistry 18 (2016) 5151–5159. https://doi.org/10.1039/c6gc01259k.

[10] T. Liu, Q.F. An, Q. Zhao, J.K. Wu, Y.H. Song, B.K. Zhu, C.J. Gao, Synergistic strengthening of polyelectrolyte complex membranes by functionalized carbon nanotubes and metal ions, Sci Rep 5 (2015) 1–7. https://doi.org/10.1038/srep07782.

[11] R.W. Baker, Membrane technology and applications, 3rdedition ed., John Wiley and Sons, Ltd, 2012.

[12] J.F. Kim, Recent Progress on Improving the Sustainability of Membrane Fabrication, Journal of Membrane Science & Research 6 (2020) 241–250. https://doi.org/10.22079/JMSR.2019.106501.1260.

[13] M. Razali, J.F. Kim, M. Attfield, P.M. Budd, E. Drioli, Y.M. Lee, G. Szekely, Sustainable wastewater treatment and recycling in membrane manufacturing, Green Chemistry 17 (2015) 5196–5205. https://doi.org/10.1039/c5gc01937k.

[14] M. Obaid, N.A.M. Barakat, O.A. Fadali, M. Motlak, A.A. Almajid, K.A. Khalil, Effective and reusable oil/water separation membranes based on modified polysulfone electrospun nanofiber mats, Chemical Engineering Journal 259 (2015) 449–456. https://doi.org/10.1016/j.cej.2014.07.095.

[15] Y. Cai, D. Chen, N. Li, Q. Xu, H. Li, J. He, J. Lu, Self-healing and superwettable nanofibrous membranes for efficient separation of oil-in-water emulsions, J Mater Chem A Mater 7 (2019) 1629–1637. https://doi.org/10.1039/c8ta10254f.

[16] N. Helali, L. Shamaei, M. Rastgar, M. Sadrzadeh, Development of layer-by-layer assembled polyamide-imide membranes for oil sands produced water treatment, Sci Rep 11 (2021) 8098. https://doi.org/10.1038/s41598-021-87601-4.

[17] A. Ahmadi, O. Qanati, M.S. Seyed Dorraji, M.H. Rasoulifard, V. Vatanpour, Investigation of antifouling performance a novel nanofibrous S-PVDF/PVDF and S-PVDF/PVDF/GO membranes against negatively charged oily foulants, J Memb Sci 536 (2017) 86–97. https://doi.org/10.1016/j.memsci.2017.04.056.

[18] J. Ge, D. Zong, Q. Jin, J. Yu, B. Ding, Biomimetic and Superwettable Nanofibrous Skins for Highly Efficient Separation of Oil-in-Water Emulsions, Adv Funct Mater 28 (2018) 1–10. https://doi.org/10.1002/adfm.201705051.

[19] H.P. Karki, L. Kafle, D.P. Ojha, J.H. Song, H.J. Kim, Cellulose/polyacrylonitrile electrospun composite fiber for effective separation of the surfactant-free oil-in-water mixture under a versatile condition, Sep Purif Technol 210 (2019) 913–919. https://doi.org/10.1016/j.seppur.2018.08.053.

[20] Y. Liang, S. Kim, E. Yang, H. Choi, Omni-Directional Protected Nanofiber Membranes by Surface Segregation of PDMS-Terminated Triblock Copolymer for High-Efficiency Oil/Water Emulsion Separation, ACS Appl Mater Interfaces 12 (2020) 25324–25333. https://doi.org/10.1021/acsami.0c05559.

[21] H.H. Wang, J.T. Jung, J.F. Kim, S. Kim, E. Drioli, Y.M. Lee, A novel green solvent alternative for polymeric membrane preparation via nonsolvent-induced phase separation (NIPS), J Memb Sci 574 (2019) 44–54. https://doi.org/10.1016/j.memsci.2018.12.051.

[22] 1-methyl-2-pyrrolidone - Substance Information – ECHA. https://echa.europa.eu/substance-information/-/substanceinfo/100.011.662 (accessed July 1, 2020).

[23] N,N-dimethylacetamide - Substance Information - ECHA. https://echa.europa.eu/substance-information/-/substanceinfo/100.004.389 (accessed July 1, 2020).

[24] N,N-dimethylformamide - Substance Information – ECHA. https://echa.europa.eu/substance-information/-/substanceinfo/100.000.617 (accessed July 1, 2020).

[25] T. Marino, F. Galiano, A. Molino, A. Figoli, New frontiers in sustainable membrane preparation: Cyrene^{TM} as green bioderived solvent, J Memb Sci 580 (2019) 224–234. https://doi.org/10.1016/j.memsci.2019.03.034.

[26] F. Russo, F. Galiano, F. Pedace, F. Aricò, A. Figoli, Dimethyl Isosorbide As a Green Solvent for Sustainable Ultrafiltration and Microfiltration Membrane Preparation, ACS Sustain Chem Eng 8 (2020) 659–668. https://doi.org/10.1021/acssuschemeng.9b06496.

[27] O. Setiawan, Z.G. Abdi, M. Weber, W.S. Hung, T.S. Chung, Employing sulfolane as a green solvent in the fabrication of nanofiltration membranes with excellent dye/salt separation performances for textile wastewater treatment, J Memb Sci 685 (2023). https://doi.org/10.1016/j.memsci.2023.121942.

[28] M. Mulder, MEMBRANE PREPARATION | Phase Inversion Membranes, in: Encyclopedia of Separation Science, 2000. https://doi.org/10.1016/b0-12-226770-2/05271-6.

[29] M. Mulder, Basic principles of membrane technology, Kluver Academic Publisher, Dordrecht, The Netherlands, 1996. https://doi.org/10.3917/spec.015.0003.

[30] G.R. Guillen, Y. Pan, M. Li, E.M.V. Hoek, Preparation and characterization of membranes formed by nonsolvent induced phase separation: A review, Ind Eng Chem Res 50 (2011) 3798–3817. https://doi.org/10.1021/ie101928r.

[31] M.K. Purkait, M.K. Sinha, P. Mondal, R. Singh, Introduction to Membranes, 2018. https://doi.org/10.1016/B978-0-12-813961-5.00001-2.

[32] Hansen Solubility Parameters, (n.d.). https://www.hansen-solubility.com/HSP-science/basics.php.

[33] C.M. Hansen, Polymer additives and solubility parameters, Prog Org Coat 51 (2004) 109–112. https://doi.org/10.1016/j.porgcoat.2004.05.003.

[34] H. Strathmann, P. Scheible, R.W. Baker, A rationale for the preparation of Loeb-Sourirajan-type cellulose acetate membranes, J Appl Polym Sci 15 (1971) 811–828. https://doi.org/10.1002/app.1971.070150404.

[35] S. Bapat, S.O. Kilian, H. Wiggers, D. Segets, Towards a framework for evaluating and reporting Hansen solubility parameters: applications to particle dispersions, Nanoscale Adv 3 (2021) 4400–4410. https://doi.org/10.1039/d1na00405k.

[36] A.K. Hołda, I.F.J. Vankelecom, Understanding and guiding the phase inversion process for synthesis of solvent resistant nanofiltration membranes, J Appl Polym Sci 132 (2015). https://doi.org/10.1002/app.42130.

[37] W. Xie, T. Li, C. Chen, H. Wu, S. Liang, H. Chang, B. Liu, E. Drioli, Q. Wang, J.C. Crittenden, Using the Green Solvent Dimethyl Sulfoxide to Replace Traditional Solvents Partly and Fabricating PVC/PVC-g-PEGMA Blended Ultrafiltration Membranes with High Permeability and Rejection, Ind Eng Chem Res 58 (2019) 6413–6423. https://doi.org/10.1021/acs.iecr.9b00370.

[38] T. Marino, E. Blasi, S. Tornaghi, E. Di Nicolò, A. Figoli, Polyethersulfone membranes prepared with Rhodiasolv®Polarclean as water soluble green solvent, J Memb Sci 549 (2018) 192–204. https://doi.org/10.1016/j.memsci.2017.12.007.

[39] T. Marino, F. Galiano, S. Simone, A. Figoli, DMSO EVOL^{TM} as novel non-toxic solvent for polyethersulfone membrane preparation, Environmental Science and Pollution Research 26 (2019) 14774–14785. https://doi.org/10.1007/s11356-018-3575-9.

[40] J. Avossa, G. Herwig, C. Toncelli, F. Itel, R.M. Rossi, Electrospinning based on benign solvents: current definitions, implications and strategies, Green Chemistry 24 (2022) 2347–2375. https://doi.org/10.1039/d1gc04252a.

[41] D. Ji, Y. Lin, X. Guo, B. Ramasubramanian, R. Wang, N. Radacsi, R. Jose, X. Qin, S. Ramakrishna, Electrospinning of nanofibres, Nature Reviews Methods Primers 4 (2024) 1. https://doi.org/10.1038/s43586-023-00278-z.

[42] J. Xue, T. Wu, Y. Dai, Y. Xia, Electrospinning and electrospun nanofibers: Methods, materials, and applications, Chem Rev 119 (2019) 5298–5415. https://doi.org/10.1021/acs.chemrev.8b00593.

[43] A. Keirouz, Z. Wang, V.S. Reddy, Z.K. Nagy, P. Vass, M. Buzgo, S. Ramakrishna, N. Radacsi, The History of Electrospinning: Past, Present, and Future Developments, Adv Mater Technol 8 (2023). https://doi.org/10.1002/admt.202201723.

[44] N.S.A. Halim, M.D.H. Wirzal, S.M. Hizam, M.R. Bilad, N.A.H.M. Nordin, N.S. Sambudi, Z.A. Putra, A.R.M. Yusoff, Recent Development on Electrospun Nanofiber Membrane for Produced Water Treatment: A review, J Environ Chem Eng 9 (2021). https://doi.org/10.1016/j.jece.2020.104613.

[45] S. Nanda, B.R. Patra, R. Patel, J. Bakos, A.K. Dalai, Innovations in applications and prospects of bioplastics and biopolymers: a review, Environ Chem Lett 20 (2022) 379–395. https://doi.org/10.1007/s10311-021-01334-4.

[46] S. Bandehali, H. Sanaeepur, A. Ebadi Amooghin, S. Shirazian, S. Ramakrishna, Biodegradable polymers for membrane separation, Sep Purif Technol 269 (2021) 118731. https://doi.org/10.1016/j.seppur.2021.118731.

[47] H.Y. Nguyen Thi, S. Kim, B.T. Duy Nguyen, D. Lim, S. Kumar, H. Lee, G. Szekely, J.F. Kim, Closing the Sustainable Life Cycle Loop of Membrane Technology via a Cellulose Biomass Platform, ACS Sustain Chem Eng 10 (2022) 2532–2544. https://doi.org/10.1021/acssuschemeng.1c08554.

[48] M. Razali, J.F. Kim, P.M. Budd, E. Drioli, Y.M. Lee, G. Szekely, Sustainable wastewater treatment and recycling in membrane manufacturing, Green Chemistry 17 (2015) 5196–5205. https://doi.org/10.1039/c5gc01937k.

[49] A. Mtibe, M.P. Motloung, J. Bandyopadhyay, S.S. Ray, Synthetic Biopolymers and Their Composites: Advantages and Limitations—An Overview, Macromol Rapid Commun 42 (2021) 2100130. https://doi.org/10.1002/MARC.202100130.

[50] K.C. Khulbe, T. Matsuura, Development of membranes from biobased materials and their applications, 2017. https://doi.org/10.1002/9781119441632.ch92.

[51] W.A. Wani, S. Pathan, S. Bose, The Journey of Alternative and Sustainable Substitutes for “Single-Use” Plastics, Adv Sustain Syst 5 (2021) 1–15. https://doi.org/10.1002/adsu.202100085.

[52] M. Van Der Zee, Analytical Methods for Monitoring Biodegradation Processes of Environmentally Degradable Polymers, in: Handbook of Biodegradable Polymers: Isolation, Synthesis, Characterization and Applications, Wiley-VCH, 2011: pp. 263–281. https://doi.org/10.1002/9783527635818.CH11.

[53] R.P. Babu, K.O. Connor, R. Seeram, Current progress on bio-based polymers and their future trends, Prog Biomater 2 (2013).

[54] R. Castro-Muñoz, J. González-Valdez, New trends in biopolymer-based membranes for pervaporation, Molecules 24 (2019) 1–17. https://doi.org/10.3390/molecules24193584.

[55] J. Baranwal, B. Barse, A. Fais, G.L. Delogu, A. Kumar, Biopolymer: A Sustainable Material for Food and Medical Applications, Polymers (Basel) 14 (2022) 1–22. https://doi.org/10.3390/polym14050983.

[56] F.B. Mamba, B.S. Mbuli, J. Ramontja, Recent advances in biopolymeric membranes towards the removal of emerging organic pollutants from water, Membranes (Basel) 11 (2021). https://doi.org/10.3390/membranes11110798.

[57] T. Mekonnen, P. Mussone, D. Bressler, Progress in bio-based plastics and plasticizing modifications, J Mater Chem A Mater 1 (2013) 13379–13398. https://doi.org/10.1039/c3ta12555f.

[58] S. Jiang, B.P. Ladewig, Green synthesis of polymeric membranes: Recent advances and future prospects, Curr Opin Green Sustain Chem 21 (2020) 1–8. https://doi.org/10.1016/j.cogsc.2019.07.002.

[59] K. Sadman, D.E. Delgado, Y. Won, Q. Wang, K.A. Gray, K.R. Shull, Versatile and High-Throughput Polyelectrolyte Complex Membranes via Phase Inversion, ACS Appl Mater Interfaces 11 (2019) 16018–16026. https://doi.org/10.1021/acsami.9b02115.

[60] M.I. Baig, E.N. Durmaz, J.D. Willott, W.M. de Vos, Sustainable Membrane Production through Polyelectrolyte Complexation Induced Aqueous Phase Separation, Adv Funct Mater 30 (2020). https://doi.org/10.1002/adfm.201907344.

[61] H.M. Fares, Q. Wang, M. Yang, J.B. Schlenoff, Swelling and Inflation in Polyelectrolyte Complexes, Macromolecules 52 (2019) 610–619. https://doi.org/10.1021/acs.macromol.8b01838.

[62] F. V. Adams, E.N. Nxumalo, R.W.M. Krause, E.M.V. Hoek, B.B. Mamba, The influence of solvent properties on the performance of polysulfone/β-cyclodextrin polyurethane mixed-matrix membranes, J Appl Polym Sci 130 (2013) 2005–2014. https://doi.org/10.1002/app.39378.

[63] A. Figoli, T. Marino, S. Simone, E. Di Nicolò, X.M. Li, T. He, S. Tornaghi, E. Drioli, Towards non-toxic solvents for membrane preparation: A review, Green Chemistry 16 (2014) 4034–4059. https://doi.org/10.1039/c4gc00613e.

[64] F. Russo, F. Galiano, F. Pedace, F. Aricò, A. Figoli, Dimethyl Isosorbide As a Green Solvent for Sustainable Ultrafiltration and Microfiltration Membrane Preparation, ACS Sustain Chem Eng 8 (2020) 659–668. https://doi.org/10.1021/acssuschemeng.9b06496.

[65] O. Gronwald, M. Weber, AGNIQUE AMD 3L as green solvent for polyethersulfone ultrafiltration membrane preparation, J Appl Polym Sci 48419 (2019) 1–12. https://doi.org/10.1002/app.48419.

[66] A. Naeem, B. Saeed, H. AlMohamadi, M. Lee, M.A. Gilani, R. Nawaz, A.L. Khan, M. Yasin, Sustainable and green membranes for chemical separations: A review, Sep Purif Technol (2024) 126271. https://doi.org/10.1016/j.seppur.2024.126271.

[67] N. Evenepoel, S. Wen, M. Tilahun Tsehaye, B. Van der Bruggen, Potential of DMSO as greener solvent for PES ultra- and nanofiltration membrane preparation, J Appl Polym Sci 135 (2018) 1–10. https://doi.org/10.1002/app.46494.

[68] T. Marino, E. Blasi, S. Tornaghi, E. Di Nicolò, A. Figoli, Polyethersulfone membranes prepared with Rhodiasolv®Polarclean as water soluble green solvent, J Memb Sci 549 (2018) 192–204. https://doi.org/10.1016/j.memsci.2017.12.007.

[69] O. Gronwald, M. Weber, AGNIQUE AMD 3L as green solvent for polyethersulfone ultrafiltration membrane preparation, J Appl Polym Sci 48419 (2019) 1–12. https://doi.org/10.1002/app.48419.

[70] T. Phaechamud, S. Chitrattha, Pore formation mechanism of porous poly(dl-lactic acid) matrix membrane, Materials Science and Engineering C 61 (2016) 744–752. https://doi.org/10.1016/j.msec.2016.01.014.

[71] H.N. Doan, P.P. Vo, A. Baggio, M. Negoro, K. Kinashi, Y. Fuse, W. Sakai, N. Tsutsumi, Environmentally Friendly Chitosan-Modified Polycaprolactone Nanofiber/Nanonet Membrane for Controllable Oil/Water Separation, ACS Appl Polym Mater 3 (2021) 3891–3901. https://doi.org/10.1021/acsapm.1c00463.

[72] T. Marino, F. Russo, A. Criscuoli, A. Figoli, TamiSolve® NxG as novel solvent for polymeric membrane preparation, J Memb Sci 542 (2017) 418–429. https://doi.org/10.1016/j.memsci.2017.08.038.

[73] D. Kim, O.R. Salazar, S.P. Nunes, Membrane manufacture for peptide separation, Green Chemistry 18 (2016) 5151–5159. https://doi.org/10.1039/c6gc01259k.

[74] H.H. Wang, J.T. Jung, J.F. Kim, S. Kim, E. Drioli, Y.M. Lee, A novel green solvent alternative for polymeric membrane preparation via nonsolvent-induced phase separation (NIPS), J Memb Sci 574 (2019) 44–54. https://doi.org/10.1016/j.memsci.2018.12.051.

[75] F. Russo, C. Ursino, E. Avruscio, G. Desiderio, A. Perrone, S. Santoro, F. Galiano, A. Figoli, Innovative Poly (Vinylidene Fluoride) (PVDF) Electrospun Nanofiber Membrane Preparation Using DMSO as a Low Toxicity Solvent, Membranes 2020, Vol. 10, Page 36 10 (2020) 36. https://doi.org/10.3390/MEMBRANES10030036.

[76] A. Moriya, T. Maruyama, Y. Ohmukai, T. Sotani, H. Matsuyama, Preparation of poly(lactic acid) hollow fiber membranes via phase separation methods, J Memb Sci 342 (2009) 307–312. https://doi.org/10.1016/j.memsci.2009.07.005.

[77] Y. Medina-Gonzalez, P. Aimar, J.F. Lahitte, J.C. Remigy, Towards green membranes: Preparation of cellulose acetate ultrafiltration membranes using methyl lactate as a biosolvent, International Journal of Sustainable Engineering 4 (2011) 75–83. https://doi.org/10.1080/19397038.2010.497230.

[78] P. Tomietto, F. Russo, F. Galiano, P. Loulergue, S. Salerno, L. Paugam, J.L. Audic, L. De Bartolo, A. Figoli, Sustainable fabrication and pervaporation application of bio-based membranes: Combining a polyhydroxyalkanoate (PHA) as biopolymer and Cyrene^{TM} as green solvent, J Memb Sci 643 (2022). https://doi.org/10.1016/j.memsci.2021.120061.

[79] E.N. Durmaz, P. Zeynep Çulfaz-Emecen, Cellulose-based membranes via phase inversion using [EMIM]OAc-DMSO mixtures as solvent, Chem Eng Sci 178 (2018) 93–103. https://doi.org/10.1016/j.ces.2017.12.020.

[80] D.Y. Xing, W.Y. Dong, T.S. Chung, Effects of different ionic liquids as green solvents on the formation and ultrafiltration performance of CA hollow fiber membranes, Ind Eng Chem Res 55 (2016) 7505–7513. https://doi.org/10.1021/acs.iecr.6b01603.

[81] D.Y. Xing, S.Y. Chan, T.S. Chung, The ionic liquid [EMIM]OAc as a solvent to fabricate stable polybenzimidazole membranes for organic solvent nanofiltration, Green Chemistry 16 (2014) 1383–1392. https://doi.org/10.1039/c3gc41634h.

[82] F.M. Sukma, P.Z. Culfaz-Emecen, Cellulose membranes for Organic Solvent Nanofiltration, 26th Annual Meeting of the North American Membrane Society, NAMS 2016 (2016) 228–230.

[83] A. Colburn, R.J. Vogler, A. Patel, M. Bezold, J. Craven, C. Liu, D. Bhattacharyya, Composite membranes derived from cellulose and lignin sulfonate for selective separations and antifouling aspects, Nanomaterials 9 (2019). https://doi.org/10.3390/nano9060867.

[84] D.Y. Xing, N. Peng, T.S. Chung, Formation of cellulose acetate membranes via phase inversion using ionic liquid, [BMIM]SCN, As the solvent, Ind Eng Chem Res 49 (2010) 8761–8769. https://doi.org/10.1021/ie1007085.

[85] J.D. Willott, W.M. Nielen, W.M. de Vos, Stimuli-Responsive Membranes through Sustainable Aqueous Phase Separation, ACS Appl Polym Mater 2 (2020) 659–667. https://doi.org/10.1021/acsapm.9b01006.

[86] W.M. Nielen, J.D. Willott, W.M. de Vos, Aqueous Phase Separation of Responsive Copolymers for Sustainable and Mechanically Stable Membranes, ACS Appl Polym Mater 2 (2020) 1702–1710. https://doi.org/10.1021/acsapm.0c00119.

[87] W.M. Nielen, J.D. Willott, Z.M. Esguerra, W.M. De Vos, Ion specific effects on aqueous phase separation of responsive copolymers for sustainable membranes, J Colloid Interface Sci 576 (2020) 186–194. https://doi.org/10.1016/j.jcis.2020.04.125.

[88] V.S. Meka, M.K.G. Sing, M.R. Pichika, S.R. Nali, V.R.M. Kolapalli, P. Kesharwani, A comprehensive review on polyelectrolyte complexes, Drug Discov Today 22 (2017) 1697–1706. https://doi.org/10.1016/j.drudis.2017.06.008.

[89] D. V. Pergushov, A.H.E. Müller, F.H. Schacher, Micellar interpolyelectrolyte complexes, Chem Soc Rev 41 (2012) 6888–6901. https://doi.org/10.1039/c2cs35135h.

[90] A. Sundaramurthy, Responsive polyelectrolyte multilayer nanofilms for drug delivery applications, Elsevier Ltd., 2018. https://doi.org/10.1016/b978-0-08-101997-9.00013-8.

[91] P.K. Jha, P.S. Desai, J. Li, R.G. Larson, pH and salt effects on the associative phase separation of oppositely charged polyelectrolytes, Polymers (Basel) 6 (2014) 1414–1436. https://doi.org/10.3390/polym6051414.

[92] H. Bungenberg de Jong, H. Kruyt, Coacervation (Partial miscibility in colloidal system), in: Koninklijke Nederlandse Akademie Van Wetenschappen, 1929: pp. 849–856.

[93] A.S. Michaels, R.G. Miekka, Polycation-polyanion complexes: Preparation and properties of poly-(vinylbenzyltrimethylammonium) poly-(styrenesulfonate), Journal of Physical Chemistry 65 (1961) 1765–1773. https://doi.org/10.1021/j100827a020.

[94] A.F. Thünemann, M. Müller, H. Dautzenberg, J.-F. Joanny, H. Löwen, Polyelectrolyte Complexes, Advance Polymer Science 166 (2004) 19–33. https://doi.org/10.1007/b11350.

[95] A.D. Kulkarni, Y.H. Vanjari, K.H. Sancheti, H.M. Patel, V.S. Belgamwar, S.J. Surana, C. V. Pardeshi, Polyelectrolyte complexes: mechanisms, critical experimental aspects, and applications, Artif Cells Nanomed Biotechnol 44 (2016) 1615–1625. https://doi.org/10.3109/21691401.2015.1129624.

[96] E. Guzmán, H. Ritacco, J.E.F. Rubio, R.G. Rubio, F. Ortega, Salt-induced changes in the growth of polyelectrolyte layers of poly(diallyl-dimethylammonium chloride) and poly(4-styrene sulfonate of sodium), Soft Matter 5 (2009) 2130–2142. https://doi.org/10.1039/b901193e.

[97] A. Herzog-Arbeitman, Polyelectrolyte Complexation: Entropy, Medicine, and the Beginning of Life, Reinvention: An International Journal of Undergraduate Research 12 (2019). https://doi.org/10.31273/REINVENTION.V12I2.338.

[98] E.N. Durmaz, S. Sahin, E. Virga, S. De Beer, L.C.P.M. De Smet, W.M. De Vos, Polyelectrolytes as Building Blocks for Next-Generation Membranes with Advanced Functionalities, ACS Appl Polym Mater 3 (2021) 4347–4374. https://doi.org/10.1021/ACSAPM.1C00654.

[99] A. Krishna B, S. Lindhoud, W.M. de Vos, Hot-pressed polyelectrolyte complexes as novel alkaline stable monovalent-ion selective anion exchange membranes, J Colloid Interface Sci 593 (2021) 11–20. https://doi.org/10.1016/J.JCIS.2021.02.077.

[100] E.N. Durmaz, M.I. Baig, J.D. Willott, W.M. de Vos, W.M. De Vos, W.M. de Vos, Polyelectrolyte Complex Membranes via Salinity Change Induced Aqueous Phase Separation, ACS Appl Polym Mater 2 (2020) 2612–2621. https://doi.org/10.1021/acsapm.0c00255.

[101] K. Sadman, D.E. Delgado, Y. Won, Q. Wang, K.A. Gray, K.R. Shull, Versatile and High-Throughput Polyelectrolyte Complex Membranes via Phase Inversion, ACS Appl Mater Interfaces 11 (2019) 16018–16026. https://doi.org/10.1021/acsami.9b02115.

[102] J.D. Willott, W.M. Nielen, W.M. de Vos, Stimuli-Responsive Membranes through Sustainable Aqueous Phase Separation, ACS Appl Polym Mater 2 (2020) 659–667. https://doi.org/10.1021/acsapm.9b01006.

[103] M.I. Baig, J.D. Willott, W.M. de Vos, Tuning the structure and performance of polyelectrolyte complexation based aqueous phase separation membranes, J Memb Sci 615 (2020) 118502. https://doi.org/10.1016/j.memsci.2020.118502.

[104] E.N. Durmaz, J.D. Willott, A. Fatima, W.M. de Vos, Weak polyanion and strong polycation complex based membranes: Linking aqueous phase separation to traditional membrane fabrication, Eur Polym J 139 (2020) 110015. https://doi.org/10.1016/j.eurpolymj.2020.110015.

[105] M.I. Baig, P. Putri, I. Sari, J. Li, J.D. Willott, W.M. De Vos, Sustainable Aqueous Phase Separation membranes prepared through mild pH shift induced polyelectrolyte complexation of PSS and PEI, J Memb Sci 625 (2021) 119114. https://doi.org/10.1016/j.memsci.2021.119114.

[106] J. Kamp, S. Emonds, J. Borowec, M.A. Restrepo Toro, M. Wessling, On the organic solvent free preparation of ultrafiltration and nanofiltration membranes using polyelectrolyte complexation in an all aqueous phase inversion process, J Memb Sci 618 (2021) 118632. https://doi.org/10.1016/j.memsci.2020.118632.

[107] G. Tu, S. Li, Y. Han, Z. Li, J. Liu, X. Liu, W. Li, Fabrication of chitosan membranes via aqueous phase separation: Comparing the use of acidic and alkaline dope solutions, J Memb Sci 646 (2022) 120256. https://doi.org/10.1016/J.MEMSCI.2022.120256.

[108] M.M.H. Mizan, F.R. Omi, H. Sultana, M. Sadrzadeh, Bio-sourced and biodegradable materials for membrane fabrication, Green Membrane Technologies towards Environmental Sustainability (2023) 169–208. https://doi.org/10.1016/B978-0-323-95165-4.00007-0.

[109] S. B. McCray, V.L. Vilker, K. Nobe, Reverse osmosis cellulose acetate membranes II. Dependence of transport properties on acetyl content, J Memb Sci 59 (1991) 317–330. https://doi.org/10.1016/S0376-7388(00)80820-0.

[110] M. Sivakumar, D.R. Mohan, R. Rangarajan, Studies on cellulose acetate-polysulfone ultrafiltration membranes: II. Effect of additive concentration, J Memb Sci 268 (2006) 208–219. https://doi.org/10.1016/j.memsci.2005.06.017.

[111] V. Vatanpour, A. Yuksekdag, M. Ağtaş, M. Mehrabi, E. Salehi, R. Castro-Muñoz, I. Koyuncu, Zeolitic imidazolate framework (ZIF-8) modified cellulose acetate NF membranes for potential water treatment application, Carbohydr Polym 299 (2023). https://doi.org/10.1016/j.carbpol.2022.120230.

[112] S. Kalyani, B. Smitha, S. Sridhar, A. Krishnaiah, Blend membranes of sodium alginate and hydroxyethylcellulose for pervaporation-based enrichment of t-butyl alcohol, Carbohydr Polym 64 (2006) 425–432. https://doi.org/10.1016/j.carbpol.2005.12.012.

[113] L.Y. Ee, R.P.W. Tan, S.F.Y. Li, Facile electrospray fabrication of ultralow biofouling cellulose acetate desalination membrane with nanocellulose/UiO66-NH2 fillers, J Memb Sci 666 (2022) 121200. https://doi.org/10.1016/j.memsci.2022.121200.

[114] L.A. Goetz, B. Jalvo, R. Rosal, A.P. Mathew, Superhydrophilic anti-fouling electrospun cellulose acetate membranes coated with chitin nanocrystals for water filtration, J Memb Sci 510 (2016) 238–248. https://doi.org/10.1016/j.memsci.2016.02.069.

[115] J. Xi, Y. Lou, Y. Chu, L. Meng, H. Wei, H. Dai, Z. Xu, H. Xiao, W. Wu, High-flux bacterial cellulose ultrafiltration membrane with controllable pore structure, Colloids Surf A Physicochem Eng Asp 656 (2023) 130428. https://doi.org/10.1016/j.colsurfa.2022.130428.

[116] T.M. Budnyak, A. Slabon, M.H. Sipponen, Lignin–Inorganic Interfaces: Chemistry and Applications from Adsorbents to Catalysts and Energy Storage Materials, ChemSusChem 13 (2020) 4344–4355. https://doi.org/10.1002/cssc.202000216.

[117] C. Wang, J. Zhang, C. Liu, X. Song, C. Zhang, Wood – inspired preparation of ligninsulfonate / trimesoylchloride nanofilm with a highly negatively charged surface for removing anionic dyes, Chemical Engineering Journal 412 (2021) 128609. https://doi.org/10.1016/j.cej.2021.128609.

[118] Y. Li, F. Li, Y. Yang, B. Ge, F. Meng, Research and application progress of lignin-based composite membrane, Journal of Polymer Engineering 41 (2021) 245–258. https://doi.org/10.1515/polyeng-2020-0268.

[119] M. Bustamante-Torres, B. Arcentales-Vera, S. Abad-Sojos, O. Torres-Constante, F. Ruiz-Rubio, Emilio Bucio, Lignin-Based Membrane for Dye Removal, in: S.S. Muthu, A. Khadir (Eds.), Membrane Based Methods for Dye Containing Wastewater Recent Advances, Springer, 2022: pp. 181–214.

[120] L. Shamaei, P. Karami, B. Khorshidi, R. Farnood, M. Sadrzadeh, Novel Lignin-Modified Forward Osmosis Membranes: Waste Materials for Wastewater Treatment, ACS Sustain Chem Eng 9 (2021) 15768–15779. https://doi.org/10.1021/acssuschemeng.1c03861.

[121] J. Shi, X. Liu, Y. Shang, S. Cao, Biomineralized polysaccharide alginate membrane for multi-responsive controlled drug delivery, J Memb Sci 352 (2010) 262–270. https://doi.org/10.1016/j.memsci.2010.02.026.

[122] F. Wang, H. Zhang, Y. Sun, S. Wang, L. Zhang, A. Wu, Y. Zhang, Superhydrophilic quaternized calcium alginate based aerogel membrane for oil-water separation and removal of bacteria and dyes, Int J Biol Macromol (2022). https://doi.org/10.1016/j.ijbiomac.2022.11.294.

[123] Y. Wang, Y. He, J. Yu, L. Zhang, S. Li, H. Li, Alginate-based nanofibrous membrane with robust photo-Fenton self-cleaning property for efficient crude oil/water emulsion separation, Sep Purif Technol 287 (2022). https://doi.org/10.1016/j.seppur.2022.120569.

[124] M. Ehsan, H. Razzaq, S. Razzaque, A. Bibi, A. Yaqub, Recent advances in sodium alginate-based membranes for dehydration of aqueous ethanol through pervaporation, Journal of Polymer Science 60 (2022) 2435–2453. https://doi.org/10.1002/pol.20220190.

[125] R. Vijitha, N.S. Reddy, K. Nagaraja, T.J. Sudha Vani, M.M. Hanafiah, K. Venkateswarlu, S.K. Lakkaboyana, K.S.V. Krishna Rao, K.M. Rao, Fabrication of polyelectrolyte membranes of pectin graft-copolymers with PVA and their composites with phosphomolybdic acid for drug delivery, toxic metal ion removal, and fuel cell applications, Membranes (Basel) 11 (2021). https://doi.org/10.3390/membranes11100792.

[126] J.P. Ambre, K.B. Dhopte, P.R. Nemade, V.H. Dalvi, High flux hyperbranched starch-graphene oxide piperazinamide composite nanofiltration membrane, J Environ Chem Eng 7 (2019). https://doi.org/10.1016/j.jece.2019.103300.

[127] E. Moradi, H. Ebrahimzadeh, Z. Mehrani, A.A. Asgharinezhad, The efficient removal of methylene blue from water samples using three-dimensional poly (vinyl alcohol)/starch nanofiber membrane as a green nanosorbent, Environmental Science and Pollution Research 26 (2019) 35071–35081. https://doi.org/10.1007/s11356-019-06400-7.

[128] J. Zhang, Y. Jiao, Y. Zhang, K. Wang, X. Sui, D. Song, E. Drioli, X. Cheng, Development of Hydrophilic Polylactic Acid Hollow-Fiber Membranes for Water Remediation, Ind Eng Chem Res (2022). https://doi.org/10.1021/acs.iecr.2c03100.

[129] F. Galiano, K. Briceño, T. Marino, A. Molino, K.V. Christensen, A. Figoli, Advances in biopolymer-based membrane preparation and applications, J Memb Sci 564 (2018) 562–586. https://doi.org/10.1016/j.memsci.2018.07.059.

[130] Z.A. Raza, S. Abid, I.M. Banat, Polyhydroxyalkanoates: Characteristics, production, recent developments and applications, Int Biodeterior Biodegradation 126 (2018) 45–56. https://doi.org/10.1016/j.ibiod.2017.10.001.

[131] P. Tomietto, P. Loulergue, L. Paugam, J.-L. Audic, Biobased polyhydroxyalkanoate (PHA) membranes: Structure/performances relationship, (2020). https://doi.org/10.1016/j.seppur.2020.117419.

[132] J. Bang, S. Park, S.-W. Hwang, J.-K. Oh, H. Yeo, H.-J. Jin, H.W. Kwak, Biodegradable and hydrophobic nanofibrous membranes produced by solution blow spinning for efficient oil/water separation, Chemosphere 312 (2023) 137240. https://doi.org/10.1016/j.chemosphere.2022.137240.

[133] M. Čolnik, M.K. Hrnčič, M. Škerget, Ž. Knez, Biodegradable polymers, current trends of research and their applications, a review, Chemical Industry and Chemical Engineering Quarterly 26 (2020) 401–418. https://doi.org/10.2298/CICEQ191210018C.

[134] S. Ampawan, N. Phreecha, S. Chantarak, W. Chinpa, Selective separation of dyes by green composite membrane based on polylactide with carboxylated cellulose microfiber from empty fruit bunch, Int J Biol Macromol 225 (2023) 1607–1619. https://doi.org/10.1016/j.ijbiomac.2022.11.218.

[135] E.O. Ezugbe, S. Rathilal, Membrane technologies in wastewater treatment: A review, Membranes (Basel) 10 (2020). https://doi.org/10.3390/membranes10050089.

[136] G. Jeon, S.Y. Yang, J.K. Kim, Functional nanoporous membranes for drug delivery, J Mater Chem 22 (2012) 14814–14834. https://doi.org/10.1039/c2jm32430j.

[137] A. Nazir, K. Khan, A. Maan, R. Zia, L. Giorno, K. Schroën, Membrane separation technology for the recovery of nutraceuticals from food industrial streams, Trends Food Sci Technol 86 (2019) 426–438. https://doi.org/10.1016/j.tifs.2019.02.049.

[138] P. Alfonso-Muniozguren, E.A. Serna-Galvis, M. Bussemaker, R.A. Torres-Palma, J. Lee, A review on pharmaceuticals removal from waters by single and combined biological, membrane filtration and ultrasound systems, Ultrason Sonochem 76 (2021) 105656. https://doi.org/10.1016/j.ultsonch.2021.105656.

[139] A.R. Kamble, C.M. Patel, Z.V.P. Murthy, A review on the recent advances in mixed matrix membranes for gas separation processes, Renewable and Sustainable Energy Reviews 145 (2021) 111062. https://doi.org/10.1016/j.rser.2021.111062.

[140] F. Prézélus, D. Chabni, L. Barna, C. Guigui, J.C. Remigy, A metrics-based approach to preparing sustainable membranes: Application to ultrafiltration, Green Chemistry 21 (2019) 4457–4469. https://doi.org/10.1039/c9gc01178a.

[141] F. Russo, F. Galiano, F. Pedace, F. Aricò, A. Figoli, Dimethyl Isosorbide As a Green Solvent for Sustainable Ultrafiltration and Microfiltration Membrane Preparation, ACS Sustain Chem Eng 8 (2020) 659–668. https://doi.org/10.1021/acssuschemeng.9b06496.

[142] Wiebe Matthijs de Vos, US20180318775 Aqueous phase separation method, 2018.

[143] W. Essafi, M.N. Spiteri, C. Williams, F. Boue, Hydrophobic polyelectrolytes in better polar solvent. structure and chain conformation as seen by SAXS and SANS, Macromolecules 42 (2009) 9568–9580. https://doi.org/10.1021/ma9003874.

[144] W.M. Nielen, J.D. Willott, W.M. de Vos, Aqueous Phase Separation of Responsive Copolymers for Sustainable and Mechanically Stable Membranes, ACS Appl Polym Mater 2 (2020) 1702–1710. https://doi.org/10.1021/acsapm.0c00119.

[145] J. Kamp, S. Emonds, J. Borowec, M.A. Restrepo Toro, M. Wessling, On the organic solvent free preparation of ultrafiltration and nanofiltration membranes using polyelectrolyte complexation in an all aqueous phase inversion process, J Memb Sci 618 (2021) 118632. https://doi.org/10.1016/j.memsci.2020.118632.

[146] E.N. Durmaz, J.D. Willott, M.M.H. Mizan, W.M. de Vos, Tuning the charge of polyelectrolyte complex membranes prepared via aqueous phase separation, Soft Matter 17 (2021) 9420–9427. https://doi.org/10.1039/d1sm01199e.

[147] M.I. Baig, J.D. Willott, W.M. De Vos, Enhancing the Separation Performance of Aqueous Phase Separation-Based Membranes through Polyelectrolyte Multilayer Coatings and Interfacial Polymerization, ACS Appl Polym Mater 3 (2021) 3560–3568. https://doi.org/10.1021/acsapm.1c00457.

[148] N.I.M. Nawi, M.R. Bilad, N.A.H.M. Nordin, M.O. Mavukkandy, Z.A. Putra, M.D.H. Wirzal, J. Jaafar, A.L. Khan, Exploiting the interplay between liquid-liquid demixing and crystallization of the PVDF membrane for membrane distillation, Int J Polym Sci 2018 (2018). https://doi.org/10.1155/2018/1525014.

[149] Z. Zhang, Q. An, Y. Ji, J. Qian, C. Gao, Effect of zero shear viscosity of the casting solution on the morphology and permeability of polysulfone membrane prepared via the phase-inversion process, Desalination 260 (2010) 43–50. https://doi.org/10.1016/j.desal.2010.05.002.

[150] I. Borisov, V. Vasilevsky, D. Matveev, A. Ovcharova, A. Volkov, V. Volkov, Effect of temperature exposition of casting solution on properties of polysulfone hollow fiber membranes, Fibers 7 (2019). https://doi.org/10.3390/?b7120110.

[151] D.T. Tran, J.P. Méricq, J. Mendret, S. Brosillon, C. Faur, Influence of preparation temperature on the properties and performance of composite pvdf-tio2 membranes, Membranes (Basel) 11 (2021). https://doi.org/10.3390/membranes11110876.

[152] E. Lasseuguette, L. Fielder-dunton, Q. Jian, M. Ferrari, The Effect of Solution Casting Temperature and Ultrasound Treatment on PEBAX MH-1657 / ZIF-8 Mixed Matrix Membranes Morphology and Performance, Membranes (Basel) 12 (2022) 584.

[153] F. Wang, J. Feng, C. Gao, Manipulating the properties of coacervated polyelectrolyte microcapsules by chemical crosslinking, Colloid Polym Sci 286 (2008) 951–957. https://doi.org/10.1007/s00396-008-1853-7.

[154] J.B. Lindén, M. Larsson, S. Kaur, W.M. Skinner, S.J. Miklavcic, T. Nann, I.M. Kempson, M. Nydén, Polyethyleneimine for copper absorption II: kinetics, selectivity and efficiency from seawater, RSC Adv 5 (2015) 51883–51890. https://doi.org/10.1039/c5ra08029k.

[155] M. Sadrzadeh, S. Bhattacharjee, Rational design of phase inversion membranes by tailoring thermodynamics and kinetics of casting solution using polymer additives, J Memb Sci 441 (2013) 31–44. https://doi.org/10.1016/j.memsci.2013.04.009.

[156] U. Böhme, U. Scheler, Effective charge of bovine serum albumin determined by electrophoresis NMR, Chem Phys Lett 435 (2007) 342–345. https://doi.org/10.1016/j.cplett.2006.12.068.

[157] S. Simelane, J.C. Ngila, L.N. Dlamini, The effect of humic acid on the stability and aggregation kinetics of WO3 nanoparticles, Particulate Science and Technology 35 (2017) 632–642. https://doi.org/10.1080/02726351.2017.1302536.

[158] A. Von Harpe, H. Petersen, Y. Li, T. Kissel, Characterization of commercially available and synthesized polyethylenimines for gene delivery, Journal of Controlled Release 69 (2000) 309–322. https://doi.org/10.1016/S0168-3659(00)00317-5.

[159] K.D. Demadis, M. Paspalaki, J. Theodorou, Controlled Release of Bis (phosphonate) Pharmaceuticals from Cationic Biodegradable Polymeric Matrices, Industrial and Engineering Chemistry Researchcal Research 50 (n.d.) 5873–5876.

[160] C. Li, D. Hu, L. Liu, L. Zhu, M. Xu, C. Wang, Y. Li, Positively charged loose nanofiltration membranes prepared by a green ionic cross-link method, J Mater Sci 57 (2022) 3067–3082. https://doi.org/10.1007/s10853-021-06857-3.

[161] H.K. Okoro, L. Ndlwana, M.I. Ikhile, T.G. Barnard, J.C. Ngila, Hyperbranched polyethylenimine-modified polyethersulfone (HPEI/PES) and nAg@HPEI/PES membranes with enhanced ultrafiltration, antibacterial, and antifouling properties, Heliyon 7 (2021) e07961. https://doi.org/10.1016/j.heliyon.2021.e07961.

[162] J. de Grooth, R. Oborný, J. Potreck, K. Nijmeijer, W.M. de Vos, The role of ionic strength and odd-even effects on the properties of polyelectrolyte multilayer nanofiltration membranes, J Memb Sci 475 (2015) 311–319. https://doi.org/10.1016/j.memsci.2014.10.044.

[163] H. Guo, Y. Ma, P. Sun, S. Cui, Z. Qin, Y. Liang, Self-cleaning and antifouling nanofiltration membranes - Superhydrophilic multilayered polyelectrolyte/CSH composite films towards rejection of dyes, RSC Adv 5 (2015) 63429–63438. https://doi.org/10.1039/c5ra11438a.

[164] H. Zhang, X. Quan, S. Chen, X. Fan, G. Wei, H. Yu, Combined Effects of Surface Charge and Pore Size on Co-Enhanced Permeability and Ion Selectivity through RGO-OCNT Nanofiltration Membranes, Environ Sci Technol 52 (2018) 4827–4834. https://doi.org/10.1021/acs.est.8b00515.

[165] M.J. Han, G.N.B. Baroña, B. Jung, Effect of surface charge on hydrophilically modified poly(vinylidene fluoride) membrane for microfiltration, Desalination 270 (2011) 76–83. https://doi.org/10.1016/j.desal.2010.11.024.

[166] A. Rahimpour, M. Jahanshahi, N. Mortazavian, S.S. Madaeni, Y. Mansourpanah, Preparation and characterization of asymmetric polyethersulfone and thin-film composite polyamide nanofiltration membranes for water softening, Appl Surf Sci 256 (2010) 1657–1663. https://doi.org/10.1016/j.apsusc.2009.09.089.

[167] *M.H. Sarrafzadeh A. Shahtalebi M. M. Montazer Rahmati, Application of nanolfiltration membrane in the separation of amoxicillin from pharmaceutical wastewater, Iranian J Environ Health Sci Eng 8 (2011) 109–116.

[168] S.F.E. Boerlage, M.D. Kennedy, M.R. Dickson, D.E.Y. El-Hodali, J.C. Schippers, The modified fouling index using ultrafiltration membranes (MFI-UF): Characterisation, filtration mechanisms and proposed reference membrane, J Memb Sci 197 (2002) 1–21. https://doi.org/10.1016/S0376-7388(01)00618-4.

[169] M. Zhu, Y. Mao, Large-pore-size membranes tuned by chemically vapor deposited nanocoatings for rapid and controlled desalination, RSC Adv 10 (2020) 40562–40568. https://doi.org/10.1039/d0ra07629e.

[170] Z. Zhenxin, T. Matsuura, Discussions on the formation mechanism of surface pores in reverse osmosis, ultrafiltration, and microfiltration membranes prepared by phase inversion process, J Colloid Interface Sci 147 (1991) 307–315. https://doi.org/10.1016/0021-9797(91)90162-2.

[171] Y. Chen, M. Yang, S.A. Shaheen, J.B. Schlenoff, Influence of Nonstoichiometry on the Viscoelastic Properties of a Polyelectrolyte Complex, Macromolecules 54 (2021) 7890–7899. https://doi.org/10.1021/acs.macromol.1c01154.

[172] D.M. Reurink, J.P. Haven, I. Achterhuis, S. Lindhoud, (Erik) H.D.W. Roesink, W.M. de Vos, Annealing of Polyelectrolyte Multilayers for Control over Ion Permeation, Adv Mater Interfaces 5 (2018). https://doi.org/10.1002/admi.201800651.

[173] L.Y. Ng, A.W. Mohammad, C.Y. Ng, A review on nanofiltration membrane fabrication and modification using polyelectrolytes: Effective ways to develop membrane selective barriers and rejection capability, Adv Colloid Interface Sci 197–198 (2013) 85–107. https://doi.org/10.1016/j.cis.2013.04.004.

[174] D. Vezzani, S. Bandini, Donnan equilibrium and dielectric exclusion for characterization of nanofiltration membranes, Desalination 149 (2002) 477–483. https://doi.org/10.1016/S0011-9164(02)00784-1.

[175] B. Jachimska, M. Wasilewska, Z. Adamczyk, Characterization of globular protein solutions by dynamic light scattering, electrophoretic mobility, and viscosity measurements, Langmuir 24 (2008) 6867–6872. https://doi.org/10.1021/la800548p.

[176] J.S. Kim, E.S.K. Chian, F.M. Saunders, E.M. Perdue, M.F. Giabbai, Characteristics of Humic Substances and Their Removal Behavior in Water Treatment, in: I.H. Suffet, P. MacCarthy (Eds.), Aquatic Humic Substances: Influence on Fate and Treatment of Pollutants, ACS, Washington, DC, 1989: pp. 473–497. https://doi.org/10.1021/ba-1988-0219.ch029.

[177] S. Hong, M. Elimelech, Chemical and physical aspects of natural organic matter (NOM) fouling of nanofiltration membranes, J Memb Sci 132 (1997) 159–181. https://doi.org/10.1016/S0376-7388(97)00060-4.

[178] A.R. Costa, M.N. De Pinho, Effect of membrane pore size and solution chemistry on the ultrafiltration of humic substances solutions, J Memb Sci 255 (2005) 49–56. https://doi.org/10.1016/j.memsci.2005.01.016.

[179] Á. de la Rubia, M. Rodríguez, D. Prats, pH, Ionic strength and flow velocity effects on the NOM filtration with TiO2/ZrO2 membranes, Sep Purif Technol 52 (2006) 325–331. https://doi.org/10.1016/j.seppur.2006.05.007.

[180] C.A. Smolders, A.J. Reuvers, R.M. Boom, I.M. Wienk, Microstructures in phase-inversion membranes. Part 1. Formation of macrovoids, J Memb Sci 73 (1992) 259–275. https://doi.org/10.1016/0376-7388(92)80134-6.

[181] P. Balding, R. Borrelli, R. Volkovinsky, P.S. Russo, Physical Properties of Sodium Poly(styrene sulfonate): Comparison to Incompletely Sulfonated Polystyrene, Macromolecules 55 (2022) 1747–1762. https://doi.org/10.1021/acs.macromol.1c01065.

[182] F. Román, P. Colomer, Y. Calventus, J.M. Hutchinson, Study of hyperbranched poly(ethyleneimine) polymers of different molecular weight and their interaction with epoxy resin, Materials 11 (2018) 1–26. https://doi.org/10.3390/ma11030410.

[183] M. Mulder, Basic principles of membrane technology, Kluver Academic Publisher, Dordrecht, The Netherlands, 1996. https://doi.org/10.3917/spec.015.0003.

[184] B. Al-Shammari, T. Al-Fariss, F. Al-Sewailm, R. Elleithy, The effect of polymer concentration and temperature on the rheological behavior of metallocene linear low density polyethylene (mLLDPE) solutions, Journal of King Saud University - Engineering Sciences 23 (2011) 9–14. https://doi.org/10.1016/j.jksues.2010.07.001.

[185] M.R. Hashmet, M. Onur, I.M. Tan, Empirical Correlations for Viscosity of Polyacrylamide Solutions with the Effects of Temperature and Shear Rate. II, J Dispers Sci Technol 35 (2014) 1685–1690. https://doi.org/10.1080/01932691.2013.873866.

[186] D.Y. Xing, N. Peng, T.S. Chung, Investigation of unique interactions between cellulose acetate and ionic liquid [EMIM]SCN, and their influences on hollow fiber ultrafiltration membranes, J Memb Sci 380 (2011) 87–97. https://doi.org/10.1016/j.memsci.2011.06.032.

[187] D.L. Kim, H. Vovusha, U. Schwingenschlögl, S.P. Nunes, Polyethersulfone flat sheet and hollow fiber membranes from solutions in ionic liquids, J Memb Sci 539 (2017) 161–171. https://doi.org/10.1016/j.memsci.2017.06.001.

[188] L.F. Liu, X.L. Gu, X. Xie, R.H. Li, C.Y. Yu, X.X. Song, C.J. Gao, Modification of PSf/SPSf blended porous support for improving the reverse osmosis performance of aromatic polyamide thin film composite membranes, Polymers (Basel) 10 (2018). https://doi.org/10.3390/polym10060686.

[189] N.T. Hassankiadeh, Z. Cui, J.H. Kim, D.W. Shin, A. Sanguineti, V. Arcella, Y.M. Lee, E. Drioli, PVDF hollow fiber membranes prepared from green diluent via thermally induced phase separation: Effect of PVDF molecular weight, J Memb Sci 471 (2014) 237–246. https://doi.org/10.1016/j.memsci.2014.07.060.

[190] I. Ali, O.A. Bamaga, L. Gzara, M. Bassyouni, M.H. Abdel-Aziz, M.F. Soliman, E. Drioli, M. Albeirutty, Assessment of blend PVDF membranes, and the effect of polymer concentration and blend composition, Membranes (Basel) 8 (2018). https://doi.org/10.3390/membranes8010013.

[191] C.A. Smolders, A.J. Reuvers, R.M. Boom, I.M. Wienk, Microstructures in phase-inversion membranes. Part 1. Formation of macrovoids, J Memb Sci 73 (1992) 259–275. https://doi.org/10.1016/0376-7388(92)80134-6.

[192] W.M. Nielen, J.D. Willott, W.M. de Vos, Aqueous Phase Separation of Responsive Copolymers for Sustainable and Mechanically Stable Membranes, ACS Appl Polym Mater 2 (2020) 1702–1710. https://doi.org/10.1021/acsapm.0c00119.

[193] E.N. Durmaz, M.I. Baig, J.D. Willott, W.M. De Vos, Polyelectrolyte Complex Membranes via Salinity Change Induced Aqueous Phase Separation, ACS Appl Polym Mater 2 (2020) 2612–2621. https://doi.org/10.1021/acsapm.0c00255.

[194] R. Su, S. Li, W. Wu, C. Song, G. Liu, Y. Yu, Recent progress in electrospun nanofibrous membranes for oil/water separation, Sep Purif Technol 256 (2021) 117790. https://doi.org/10.1016/j.seppur.2020.117790.

[195] C. Chen, D. Weng, A. Mahmood, S. Chen, J. Wang, Separation Mechanism and Construction of Surfaces with Special Wettability for Oil/Water Separation, ACS Appl Mater Interfaces 11 (2019) 11006–11027. https://doi.org/10.1021/acsami.9b01293.

[196] L. Shamaei, B. Khorshidi, B. Perdicakis, M. Sadrzadeh, Treatment of oil sands produced water using combined electrocoagulation and chemical coagulation techniques, Science of the Total Environment 645 (2018) 560–572. https://doi.org/10.1016/j.scitotenv.2018.06.387.

[197] R. Zolfaghari, A. Fakhru, L.C. Abdullah, S.S.E.H. Elnashaie, Demulsification techniques of water-in-oil and oil-in-water emulsions in petroleum industry, Sep Purif Technol 170 (2016) 377–407. https://doi.org/10.1016/j.seppur.2016.06.026.

[198] S.M. Ezzat, N.A. Ahmed, Short-Term Biodegradation of Crude Petroleum Oil in Water by Photostimulated Janibacter terrae Strain S1N1, ACS Omega 7 (2022) 13976–13984. https://doi.org/10.1021/acsomega.2c00460.

[199] W. Qi, Z. Yu, Y. Liu, Y. Li, Removal of emulsion oil from oilfield ASP wastewater by internal circulation flotation and kinetic models, Chem Eng Sci 91 (2013) 122–129. https://doi.org/10.1016/j.ces.2013.01.020.

[200] A. Abidli, Y. Huang, P. Cherukupally, Novel separator skimmer for oil spill cleanup and oily wastewater treatment : From conceptual system design to the first pilot-scale prototype development, Environ Technol Innov 18 (2020) 100598. https://doi.org/10.1016/j.eti.2019.100598.

[201] K.T. Klasson, P.A. Taylor, J.F.W. Jr, S.A. Jones, R.L. Cummins, S.A. Richardson, K.T. Klasson, P.A. Taylor, J.F.W. Jr, S.A. Jones, R.L. Cummins, S.A. Richardson, S.A. Jones, R.L. Cummins, S.A. Richardson, Modification of a Centrifugal Separator for In-Well Oil-Water Separation In-Well Oil-Water Separation, Sep Sci Technol 40 (2005) 453–462. https://doi.org/10.1081/SS-200042503.

[202] J.X. Wu, J. Zhang, Y.L. Kang, G. Wu, S.C. Chen, Y.Z. Wang, Reusable and Recyclable Superhydrophilic Electrospun Nanofibrous Membranes with in Situ Co-cross-linked Polymer-Chitin Nanowhisker

Network for Robust Oil-in-Water Emulsion Separation, ACS Sustain Chem Eng 6 (2018) 1753–1762. https://doi.org/10.1021/acssuschemeng.7b03102.

[203] F. Wang, K. Liu, Y. Xi, Z. Li, One-step electrospinning PCL/ph-LPSQ nanofibrous membrane with excellent self-cleaning and oil-water separation performance, Polymer (Guildf) 249 (2022) 124858. https://doi.org/10.1016/j.polymer.2022.124858.

[204] X. Yan, X. Xiao, C. Au, S. Mathur, L. Huang, Y. Wang, Z. Zhang, Z. Zhu, M.J. Kipper, J. Tang, J. Chen, Electrospinning nanofibers and nanomembranes for oil/water separation, J Mater Chem A Mater 9 (2021) 21659–21684. https://doi.org/10.1039/d1ta05873h.

[205] J. Wang, L. Wang, Superhydrophilic and underwater superoleophobic nanofibrous membrane for separation of oil/water emulsions, J Mater Res 35 (2020) 1504–1513. https://doi.org/10.1557/jmr.2020.137.

[206] I. Sadeghi, N. Govinna, P. Cebe, A. Asatekin, Superoleophilic, Mechanically Strong Electrospun Membranes for Fast and Efficient Gravity-Driven Oil/Water Separation, ACS Appl Polym Mater 1 (2019) 765–776. https://doi.org/10.1021/acsapm.8b00279.

[207] Z. Xue, S. Wang, L. Lin, L. Chen, M. Liu, L. Feng, L. Jiang, A Novel Superhydrophilic and Underwater Superoleophobic Hydrogel-Coated Mesh for Oil / Water Separation, Advanced Materials 23 (2011) 4270–4273. https://doi.org/10.1002/adma.201102616.

[208] D.M. Correia, C. Ribeiro, G. Botelho, J. Borges, C. Lopes, F. Vaz, S.A.C. Carabineiro, A. V. MacHado, S. Lanceros-Méndez, Superhydrophilic poly(l-lactic acid) electrospun membranes for biomedical applications obtained by argon and oxygen plasma treatment, Appl Surf Sci 371 (2016) 74–82. https://doi.org/10.1016/j.apsusc.2016.02.121.

[209] H. Wu, J. Shi, X. Ning, Y.Z. Long, J. Zheng, The High Flux of Superhydrophilic-Superhydrophobic Janus Membrane of cPVA-PVDF/PMMA/GO by Layer-By-Layer Electrospinning for High Efficiency Oil-Water Separation, Polymers (Basel) 14 (2022). https://doi.org/10.3390/polym14030621.

[210] J. Ge, J. Zhang, F. Wang, Z. Li, J. Yu, B. Ding, Superhydrophilic and underwater superoleophobic nanofibrous membrane with hierarchical structured skin for effective oil-in-water emulsion separation, J Mater Chem A Mater 5 (2017) 497–502. https://doi.org/10.1039/c6ta07652a.

[211] Y. Mei, C. Yao, K. Fan, X. Li, Surface modification of polyacrylonitrile nanofibrous membranes with superior antibacterial and easy-cleaning properties through hydrophilic flexible spacers, J Memb Sci 417–418 (2012) 20–27. https://doi.org/10.1016/j.memsci.2012.06.021.

[212] W. Ma, Q. Zhang, S.K. Samal, F. Wang, B. Gao, H. Pan, H. Xu, J. Yao, X. Zhan, S.C. De Smedt, C. Huang, Core-sheath structured electrospun nanofibrous membranes for oil-water separation, RSC Adv 6 (2016) 41861–41870. https://doi.org/10.1039/c6ra06224e.

[213] L. Liu, W. Yuan, A hierarchical functionalized biodegradable PLA electrospun nanofibrous membrane with superhydrophobicity and antibacterial properties for oil/water separation, New Journal of Chemistry 42 (2018) 17615–17624. https://doi.org/10.1039/C8NJ03112F.

[214] C.R. Reshmi, S.P. Sundaran, A. Juraij, S. Athiyanathil, Fabrication of superhydrophobic polycaprolactone/beeswax electrospun membranes for high-efficiency oil/water separation, RSC Adv 7 (2017) 2092–2102. https://doi.org/10.1039/c6ra26123j.

[215] M.A. Salami, F. Kaveian, M. Rafienia, S. Saber-Samandari, A. Khandan, M. Naeimi, Electrospun Polycaprolactone/lignin-based Nanocomposite as a Novel Tissue Scaffold for Biomedical Applications, J Med Signals Sens 7 (2017) 228–238. https://doi.org/10.4103/jmss.JMSS_11_17.

[216] S.J. Zhou, H.M. Wang, S.J. Xiong, J.M. Sun, Y.Y. Wang, S. Yu, Z. Sun, J.L. Wen, T.Q. Yuan, Technical Lignin Valorization in Biodegradable Polyester-Based Plastics (BPPs), ACS Sustain Chem Eng 9 (2021) 12017–12042. https://doi.org/10.1021/acssuschemeng.1c03705.

[217] D. Wang, J. Jang, K. Kim, J. Kim, C.B. Park, "tree to Bone": Lignin/Polycaprolactone Nanofibers for Hydroxyapatite Biomineralization, Biomacromolecules 20 (2019) 2684–2693. https://doi.org/10.1021/acs.biomac.9b00451.

[218] S. Bongiovanni Abel, L. Liverani, A.R. Boccaccini, G.A. Abraham, Effect of benign solvents composition on poly(ε-caprolactone) electrospun fiber properties, Mater Lett 245 (2019) 86–89. https://doi.org/10.1016/j.matlet.2019.02.107.

[219] M. Tobiszewski, J. Namieśnik, F. Pena-Pereira, Environmental risk-based ranking of solvents using the combination of a multimedia model and multi-criteria decision analysis, Green Chemistry 19 (2017) 1034–1042. https://doi.org/10.1039/c6gc03424a.

[220] M.M. Haque Mizan, M. Rastgar, S.A. Aktij, A. Asad, P. Karami, A. Rahimpour, M. Sadrzadeh, Organic solvent-free polyelectrolyte complex membrane preparation: Effect of monomer mixing ratio and casting solution temperature, J Memb Sci 668 (2023) 121197. https://doi.org/10.1016/j.memsci.2022.121197.

[221] W.W. Sampson, A multiplanar model for the pore radius distribution in isotropic near-planar stochastic fibre networks, J Mater Sci 38 (2003) 1617–1622. https://doi.org/10.1023/A:1023298820390.

[222] Y. Li, Z. Zhu, J. Yu, B. Ding, Carbon Nanotubes Enhanced Fluorinated Polyurethane Macroporous Membranes for Waterproof and Breathable Application, ACS Appl Mater Interfaces 7 (2015) 13538–13546. https://doi.org/10.1021/acsami.5b02848.

[223] B. Ding, C. Li, Y. Miyauchi, O. Kuwaki, S. Shiratori, Formation of novel 2D polymer nanowebs via electrospinning, Nanotechnology 17 (2006) 3685–3691. https://doi.org/10.1088/0957-4484/17/15/011.

[224] H.N. Doan, P.P. Vo, A. Baggio, M. Negoro, K. Kinashi, Y. Fuse, W. Sakai, N. Tsutsumi, Environmentally Friendly Chitosan-Modified Polycaprolactone Nanofiber/Nanonet Membrane for Controllable Oil/Water Separation, ACS Appl Polym Mater 3 (2021) 3891–3901. https://doi.org/10.1021/acsapm.1c00463.

[225] S. Zhang, H. Liu, N. Tang, J. Ge, J. Yu, B. Ding, Direct electronetting of high-performance membranes based on self-assembled 2D nanoarchitectured networks, Nat Commun 10 (2019) 1–11. https://doi.org/10.1038/s41467-019-09444-y.

[226] I. Spiridon, K. Leluk, A.M. Resmerita, R.N. Darie, Evaluation of PLA-lignin bioplastics properties before and after accelerated weathering, Compos B Eng 69 (2015) 342–349. https://doi.org/10.1016/j.compositesb.2014.10.006.

[227] T. Hatakeyama, S. Yamashita, H. Hatakeyama, Thermal properties of lignin-based polycaprolactones, J Therm Anal Calorim 143 (2021) 203–211. https://doi.org/10.1007/s10973-019-09161-0.

[228] D. Kai, K. Zhang, L. Jiang, H.Z. Wong, Z. Li, Z. Zhang, X.J. Loh, Sustainable and Antioxidant Lignin-Polyester Copolymers and Nanofibers for Potential Healthcare Applications, ACS Sustain Chem Eng 5 (2017) 6016–6025. https://doi.org/10.1021/acssuschemeng.7b00850.

[229] D. Li, M.W. Frey, Y.L. Joo, Characterization of nanofibrous membranes with capillary flow porometry, J Memb Sci 286 (2006) 104–114. https://doi.org/10.1016/j.memsci.2006.09.020.

[230] I.K. Park, H. Sun, S.H. Kim, Y. Kim, G.E. Kim, Y. Lee, T. Kim, H.R. Choi, J. Suhr, J. Do Nam, Solvent-free bulk polymerization of lignin-polycaprolactone (PCL) copolymer and its thermoplastic characteristics, Sci Rep 9 (2019) 1–11. https://doi.org/10.1038/s41598-019-43296-2.

[231] Z. Terzopoulou, E. Xanthopoulou, N. Pardalis, C.P. Pappa, S. Torofias, K.S. Triantafyllidis, D.N. Bikiaris, Synthesis and Characterization of Poly(lactic acid) Composites with Organosolv Lignin, Molecules 27 (2022). https://doi.org/10.3390/molecules27238143.

[232] R. Kumar Singla, S.N. Maiti, A.K. Ghosh, Crystallization, Morphological, and Mechanical Response of Poly(Lactic Acid)/Lignin-Based Biodegradable Composites, Polymer - Plastics Technology and Engineering 55 (2016) 475–485. https://doi.org/10.1080/03602559.2015.1098688.

[233] D. Wang, H. Yang, Q. Wang, Y. Lu, J. Yan, W. Cheng, O.J. Rojas, G. Han, Composite membranes of polyacrylonitrile cross-linked with cellulose nanocrystals for emulsion separation and regeneration, Compos Part A Appl Sci Manuf 164 (2023) 1–10. https://doi.org/10.1016/j.compositesa.2022.107300.

[234] J.L. Ferreira, S. Gomes, C. Henriques, J.P. Borges, J.C. Silva, Electrospinning polycaprolactone dissolved in glacial acetic acid: Fiber production, nonwoven characterization, and in Vitro evaluation, J Appl Polym Sci 131 (2014) 37–39. https://doi.org/10.1002/app.41068.

[235] J. Bae, H. kim, K.S. Kim, H. Choi, Effect of asymmetric wettability in nanofiber membrane by electrospinning technique on separation of oil/water emulsion, Chemosphere 204 (2018) 235–242. https://doi.org/10.1016/j.chemosphere.2018.04.003.

[236] Y. Liang, S. Kim, P. Kallem, H. Choi, Capillary effect in Janus electrospun nanofiber membrane for oil/water emulsion separation, Chemosphere 221 (2019) 479–485. https://doi.org/10.1016/j.chemosphere.2019.01.048.

[237] A.K. Kota, G. Kwon, A. Tuteja, The design and applications of superomniphobic surfaces, NPG Asia Mater 6 (2014) 1–16. https://doi.org/10.1038/am.2014.34.

[238] Y. Lin, M.S. Salem, L. Zhang, Q. Shen, A.H. El-shazly, N. Nady, H. Matsuyama, Development of Janus membrane with controllable asymmetric wettability for highly-efficient oil/water emulsions separation, J Memb Sci 606 (2020) 118141. https://doi.org/10.1016/j.memsci.2020.118141.

[239] N.A.M. Barakat, M.A. Kanjwal, F.A. Sheikh, H.Y. Kim, Spider-net within the N6, PVA and PU electrospun nanofiber mats using salt addition: Novel strategy in the electrospinning process, Polymer (Guildf) 50 (2009) 4389–4396. https://doi.org/10.1016/j.polymer.2009.07.005.

[240] A. Prasad Tiwari, M. Kumar Joshi, J. Lee, B. Maharjan, S. Won Ko, C. Hee Park, C. Sang Kim, Heterogeneous electrospun polycaprolactone/polyethylene glycol membranes with improved wettability, biocompatibility, and mineralization, Colloids and Surfaces A: Physicochem. Eng. Aspects 520 (2017) 105–113. https://doi.org/10.1016/j.colsurfa.2017.01.054.

[241] Y.J. Yeh, J.P. Chu, J. De You, T.H. Chang, J.R. Liou, W.H. Chiang, P. Yiu, C.H. Hsueh, Y.L. Shen, K.L. Tung, Tunable nanostructured stainless-steel coating for high-selective and high-permeable separation membranes for oil/water emulsions, NPJ Clean Water 6 (2023). https://doi.org/10.1038/s41545-023-00237-x.

[242] A. Asad, M. Rastgar, D. Sameoto, M. Sadrzadeh, Gravity assisted super high flux microfiltration polyamide-imide membranes for oil / water emulsion separation, J Memb Sci 621 (2021) 119019. https://doi.org/10.1016/j.memsci.2020.119019.

[243] F. Shijie, Z. Jiefeng, Z. Pengyu, G.A.O. Yunling, Y. Junxian, Superhydrophilic/underwater superoleophobic oil-in-water emulsion separation membrane modified by the co-deposition of polydopamine and chitosan-tripolyphosphate nanoparticles, J Environ Chem Eng 10 (2022) 107407. https://doi.org/10.1016/j.jece.2022.107407.

[244] C. Du, Z. Wang, G. Liu, W. Wang, D. Yu, One-step electrospinning PVDF/PVP-TiO2 hydrophilic nanofiber membrane with strong oil-water separation and anti-fouling property, Colloids Surf A Physicochem Eng Asp 624 (2021) 126790. https://doi.org/10.1016/j.colsurfa.2021.126790.

[245] Q. Wang, J. Cui, S. Liu, J. Gao, J. Lang, C. Li, Y. Yan, Facile preparation of halloysite nanotube-modified polyvinylidene fluoride composite membranes for highly efficient oil/water emulsion separation, J Mater Sci 54 (2019) 8332–8345. https://doi.org/10.1007/s10853-019-03482-z.

[246] L. Averous, L. Moro, P. Dole, C. Fringant, Properties of thermoplastic blends: starch-polycaprolactone, Polymer (Guildf) 41 (2000) 4157–4167.

[247] A.H. Bahremand, M. Mousavi, A. Ahmadpour, M. Taherian, Biodegradable blend membranes of poly (butylene succinate)/cellulose acetate/dextran: Preparation, characterization and performance, Carbohydr Polym 173 (2017) 497–507. https://doi.org/10.1016/j.carbpol.2017.06.010.

[248] A. Sadeghi, S.M. Mousavi, E. Saljoughi, S. Kiani, Biodegradable membrane based on polycaprolactone/polybutylene succinate: Characterization and performance evaluation in wastewater treatment, J Appl Polym Sci 138 (2021). https://doi.org/10.1002/app.50332.

[249] P.C. Chen, Z.K. Xu, Mineral-coated polymer membranes with superhydrophilicity and underwater superoleophobicity for effective oil/water separation, Sci Rep 3 (2013) 1–6. https://doi.org/10.1038/srep02776.

[250] W. Pronk, A. Ding, E. Morgenroth, N. Derlon, P. Desmond, M. Burkhardt, B. Wu, A.G. Fane, Gravity-driven membrane filtration for water and wastewater treatment: A review, Water Res 149 (2019) 553–565. https://doi.org/10.1016/J.WATRES.2018.11.062.

[251] X. Feng, D. Peng, J. Zhu, Y. Wang, Y. Zhang, Recent advances of loose nanofiltration membranes for dye/salt separation, Sep Purif Technol 285 (2022). https://doi.org/10.1016/j.seppur.2021.120228.

[252] P. Zhang, S. Rajabzadeh, Q. Song, R.R. Gonzales, Y. Jia, S. Xiang, Z. Li, H. Matsuyama, Development of loose nanofiltration PVDF hollow fiber membrane for dye/salt separation, Desalination 549 (2023). https://doi.org/10.1016/j.desal.2022.116315.

[253] M. Rastgar, A. Karkooti, A. Sohrabi, P. Karami, N. Nazemifard, M. Sadrzadeh, Osmotic dewatering accelerates inherent sluggish kinetics of electro-Fenton process: Toward sustainable removal of organic contaminants, Chemical Engineering Journal 394 (2020) 125043. https://doi.org/10.1016/j.cej.2020.125043.

[254] A.M. Abou-Elanwar, J. Oh, S. Lee, Y. Kim, Selective separation of dye/salt mixture using diatomite-based sandwich-like membrane, Chemosphere 330 (2023). https://doi.org/10.1016/j.chemosphere.2023.138725.

[255] M. Jiang, K. Ye, J. Deng, J. Lin, W. Ye, S. Zhao, B. Van Der Bruggen, Conventional Ultrafiltration As Effective Strategy for Dye/Salt Fractionation in Textile Wastewater Treatment, Environ Sci Technol 52 (2018) 10698–10708. https://doi.org/10.1021/acs.est.8b02984.

[256] Q. Gao, D. Bouwen, S. Yuan, X. Gui, Y. Xing, J. Zheng, H. Ling, Q. Zhu, Y. Wang, S. Depuydt, J. Li, A. Volodine, P. Jin, B. Van der Bruggen, Robust loose nanofiltration membrane with fast solute transfer for dye/salt separation, J Memb Sci 674 (2023). https://doi.org/10.1016/j.memsci.2023.121518.

[257] S. Tang, Y. Chen, H. Zhang, T. Zhang, P. Wang, H. Sun, A novel loose nanofiltration membrane with high permeance and anti-fouling performance based on aqueous monomer piperazine-2-carboxylic acid for efficient dye/salt separation, Chemical Engineering Journal (2023) 146111. https://doi.org/10.1016/j.cej.2023.146111.

[258] D. Zou, X. Chen, M. Qiu, E. Drioli, Y. Fan, Flux-enhanced A-alumina tight ultrafiltration membranes for effective treatment of dye/salt wastewater at high temperatures, Sep Purif Technol 215 (2019) 143–154. https://doi.org/10.1016/j.seppur.2018.12.063.

[259] R. Li, S. Cao, X. Feng, J. Don, X. Guo, H. Wang, Y. Zhang, Guanidinium-based loose nanofiltration membranes for dye purification and chlorine resistance, Sep Purif Technol 300 (2022). https://doi.org/10.1016/j.seppur.2022.121941.

[260] S. Liu, H. Jiang, Y. Li, G. Maria, Construction of tight ultrafiltration membrane for efficient dye/salt separation with physical and chemical self-healing property, Chemical Engineering Journal 467 (2023). https://doi.org/10.1016/j.cej.2023.143456.

[261] S. Varjani, P. Rakholiya, H.Y. Ng, S. You, J.A. Teixeira, Microbial degradation of dyes: An overview, Bioresour Technol 314 (2020). https://doi.org/10.1016/j.biortech.2020.123728.

[262] S. Wong, N.A. Ghafar, N. Ngadi, F.A. Razmi, I.M. Inuwa, R. Mat, N.A.S. Amin, Effective removal of anionic textile dyes using adsorbent synthesized from coffee waste, Sci Rep 10 (2020). https://doi.org/10.1038/s41598-020-60021-6.

[263] R. Al-Tohamy, S.S. Ali, F. Li, K.M. Okasha, Y.A.G. Mahmoud, T. Elsamahy, H. Jiao, Y. Fu, J. Sun, A critical review on the treatment of dye-containing wastewater: Ecotoxicological and health concerns of textile dyes and possible remediation approaches for environmental safety, Ecotoxicol Environ Saf 231 (2022). https://doi.org/10.1016/j.ecoenv.2021.113160.

[264] W. Ye, K. Ye, F. Lin, H. Liu, M. Jiang, J. Wang, R. Liu, J. Lin, Enhanced fractionation of dye/salt mixtures by tight ultrafiltration membranes via fast bio-inspired co-deposition for sustainable

textile wastewater management, Chemical Engineering Journal 379 (2020). https://doi.org/10.1016/j.cej.2019.122321.

[265] G. Jiang, S. Zhang, Y. Zhu, S. Gao, H. Jin, L. Luo, F. Zhang, J. Jin, Hydrogel-embedded tight ultrafiltration membrane with superior anti-dye-fouling property for low-pressure driven molecule separation, J Mater Chem A Mater 6 (2018) 2927–2934. https://doi.org/10.1039/c7ta09898g.

[266] D. Ji, C. Xiao, S. An, J. Zhao, J. Hao, K. Chen, Preparation of high-flux PSF/GO loose nanofiltration hollow fiber membranes with dense-loose structure for treating textile wastewater, Chemical Engineering Journal 363 (2019) 33–42. https://doi.org/10.1016/j.cej.2019.01.111.

[267] W. Sun, N. Zhang, Q. Li, X. Li, S. Chen, L. Zong, Y. Baikeli, E. Lv, H. Deng, X. Zhang, H. Baqiah, Bioinspired lignin-based loose nanofiltration membrane with excellent acid, fouling, and chlorine resistances toward dye/salt separation, J Memb Sci 670 (2023). https://doi.org/10.1016/j.memsci.2023.121372.

[268] S. Mohammad Nejad, S.F. Seyedpour, S. Aghapour Aktij, M. Dadashi Firouzjaei, M. Elliott, A. Tiraferri, M. Sadrzadeh, A. Rahimpour, Loose nanofiltration membranes functionalized with in situ-synthesized metal organic framework for water treatment, Mater Today Chem 24 (2022). https://doi.org/10.1016/j.mtchem.2022.100909.

[269] J. Cheng, Z. Li, X. Bao, R. Zhang, S. Yin, W. Huang, K. Sun, W. Shi, A novel polyester-amide loose composite nanofiltration membrane for effective dye/salt separation: The effect of long molecule on the interfacial polymerization, J Memb Sci 657 (2022). https://doi.org/10.1016/j.memsci.2022.120675.

[270] F. Seyedpour, M.M.H. Mizan, M. Sadrzadeh, Exploring biomimetic membranes: applications and challenges, Green Membrane Technologies towards Environmental Sustainability (2023) 113–148. https://doi.org/10.1016/B978-0-323-95165-4.00005-7.

[271] S. Li, X. Wang, Y. Guo, J. Hu, S. Lin, Y. Tu, L. Chen, Y. Ni, L. Huang, Recent advances on cellulose-based nanofiltration membranes and their applications in drinking water purification: A review, J Clean Prod 333 (2022) 130171. https://doi.org/10.1016/j.jclepro.2021.130171.

[272] M.M.H. Mizan, P.M. Gurave, M. Rastgar, A. Rahimpour, R.K. Srivastava, M. Sadrzadeh, "Biomass to Membrane": Sulfonated Kraft Lignin/PCL Superhydrophilic Electrospun Membrane for Gravity-

Driven Oil-in-Water Emulsion Separation, ACS Appl Mater Interfaces (2023). https://doi.org/10.1021/acsami.3c09964.

[273] S. Manholi, S. Athiyanathil, Poly (ε-caprolactone)-based porous membranes for filtration applications—effect of solvents on precipitation kinetics, performance, and morphology, J Appl Polym Sci 139 (2022). https://doi.org/10.1002/app.51720.

[274] M. Halanur Mruthunjayappa, C. Shachar, A. Imbar, O.A. Menashe, H. Mamane, Cellulose acetate and polycaprolactone based photoactive ultrafiltration membrane: A novel approach with UV-switchable photocatalytic activity, Sep Purif Technol (2023) 125102. https://doi.org/10.1016/j.seppur.2023.125102.

[275] A.K. Kota, Y. Li, J.M. Mabry, A. Tuteja, Hierarchically structured superoleophobic surfaces with ultralow contact angle hysteresis, Advanced Materials 24 (2012) 5838–5843. https://doi.org/10.1002/adma.201202554.

[276] M. Shakiba, M. Abdouss, S. Mazinani, M. Reza Kalaee, Super-hydrophilic electrospun PAN nanofibrous membrane modified with alkaline treatment and ultrasonic-assisted PANI in-situ polymerization for highly efficient gravity-driven oil/water separation, Sep Purif Technol 309 (2023) 123032. https://doi.org/10.1016/j.seppur.2022.123032.

[277] M. Hu, S. Yang, X. Liu, R. Tao, Z. Cui, C. Matindi, W. Shi, R. Chu, X. Ma, K. Fang, M. Titus, B.B. Mamba, J. Li, Selective separation of dye and salt by PES/SPSf tight ultrafiltration membrane: Roles of size sieving and charge effect, Sep Purif Technol 266 (2021). https://doi.org/10.1016/j.seppur.2021.118587.

[278] M. Dutta, S. Upadhyay, S. De, A facile method to estimate the effective membrane pore charge density through surface zeta potential measurement, J Memb Sci 637 (2021). https://doi.org/10.1016/j.memsci.2021.119655.

[279] Z. Ge, Y. Wang, Estimation of Nanodiamond Surface Charge Density from Zeta Potential and Molecular Dynamics Simulations, Journal of Physical Chemistry B 121 (2017) 3394–3402. https://doi.org/10.1021/acs.jpcb.6b08589.

[280] S. Kalam, S.A. Abu-Khamsin, M.S. Kamal, S. Patil, Surfactant Adsorption Isotherms: A Review, ACS Omega 6 (2021) 32342–32348. https://doi.org/10.1021/acsomega.1c04661.

[281] M. Diná Afonso, G. Hagmeyer, R. Gimbel, Streaming potential measurements to assess the variation of nanofiltration membranes surface charge with the concentration of salt solutions, 2001. www.elsevier.com.

[282] M. Sadrzadeh, S. Bhattacharjee, Rational design of phase inversion membranes by tailoring thermodynamics and kinetics of casting solution using polymer additives, J Memb Sci 441 (2013) 31–44. https://doi.org/10.1016/j.memsci.2013.04.009.

[283] C.A. Smolders, A.J. Reuvers, R.M. Boom, I.M. Wienk, Microstructures in phase-inversion membranes. Part 1. Formation of macrovoids*, Elsevler Science Pubhshers, 1992.

[284] X.M. Tan, D. Rodrigue, A Review on Porous Polymeric Membrane Preparation. Part I: Production Techniques with Polysulfone and Poly (Vinylidene Fluoride), Polymers (Basel) 11 (2019). https://doi.org/10.3390/POLYM11071160.

[285] X. Dong, D. Lu, T.A.L. Harris, I.C. Escobar, Polymers and Solvents Used in Membrane Fabrication: A Review Focusing on Sustainable Membrane Development, Membranes 2021, Vol. 11, Page 309 11 (2021) 309. https://doi.org/10.3390/MEMBRANES11050309.

[286] M.H. Abbasi Geravand, E. Saljoughi, S.M. Mousavi, S. Kiani, Biodegradable polycaprolactone/MXene nanocomposite nanofiltration membranes for the treatment of dye solutions, J Taiwan Inst Chem Eng (2021). https://doi.org/10.1016/j.jtice.2021.08.048.

[287] A. Bottino, G. Camera-Rodab, G. Capannelli, S. Munari, The formation of microporous polyvinylidene difluoride membranes by phase separation, J Memb Sci 57 (1991) 1–20.

[288] H. Yanagishita, T. Nakane, H. Yoshitome, Selection criteria for solvent and gelation medium in the phase inversion process, 1994.

[289] S.H. Yoo, J.Y. Jho, J. Won, H.C. Park, Y.S. Kang, Effect of solvent and cosolvent on the morphology and permeance of asymmetric polyimide membrane, Journal of Industrial and Engineering Chemistry 6 (2000) 129–132.

[290] R. Haase, H.-J. Jansen, B. Winter, Enthalpies of Mixing for Binary Liquid Mixtures of Acids, 1983.

[291] A.N. Campbell, J.M. T Rii Gieskes, Heats of mixing and heat capacities in the system: acetic acid-chloroform-water, at 25°C, Can. J. Chem. 43 (1965).

[292] P. Karami, M.M.H. Mizan, C. Ammann, A. Taghipour, J.B.P. Soares, M. Sadrzadeh, Novel lignosulfonated polyester membranes with remarkable permeability and antifouling characteristics, J Memb Sci 687 (2023) 122034. https://doi.org/10.1016/J.MEMSCI.2023.122034.

[293] L. Shamaei, B. Khorshidi, M.A. Islam, M. Sadrzadeh, Industrial waste lignin as an antifouling coating for the treatment of oily wastewater: Creating wealth from waste, J Clean Prod 256 (2020). https://doi.org/10.1016/j.jclepro.2020.120304.

[294] Y. Wang, Y. Hou, H. Li, W. Wu, S. Ren, J. Li, A New Structural Model of Enzymatic Lignin with Multiring Aromatic Clusters, ACS Omega 7 (2022) 18861–18869. https://doi.org/10.1021/acsomega.2c01812.

[295] B.Ş. Ayvazoğlu, M. Ceylan, A.A.I. Turan, E.B. Yılmaz, Biodegradable Polycaprolactone Fibers with Silica Aerogel and Nanosilver Particles Produce a Coagulation Effect, Polymers (Basel) 15 (2023). https://doi.org/10.3390/polym15092022.

[296] B. Van Der Bruggen, B. Daems, D. Wilms, C. Vandecasteele, Mechanisms of retention and flux decline for the nanofiltration of dye baths from the textile industry, 2001. www.elsevier.com/locate/seppur.

[297] A. Dukhin, S. Dukhin, P. Goetz, Electrokinetics at high ionic strength and hypothesis of the double layer with zero surface charge, Langmuir 21 (2005) 9990–9997. https://doi.org/10.1021/la050480d.

[298] B.D. Coday, T. Luxbacher, A.E. Childress, N. Almaraz, P. Xu, T.Y. Cath, Indirect determination of zeta potential at high ionic strength: Specific application to semipermeable polymeric membranes, J Memb Sci 478 (2015) 58–64. https://doi.org/10.1016/j.memsci.2014.12.047.

[299] C. Zhang, K. Wei, W. Zhang, Y. Bai, Y. Sun, J. Gu, Graphene Oxide Quantum Dots Incorporated into a Thin Film Nanocomposite Membrane with High Flux and Antifouling Properties for Low-Pressure Nanofiltration, ACS Appl Mater Interfaces 9 (2017) 11082–11094. https://doi.org/10.1021/ACSAMI.6B12826/SUPPL_FILE/AM6B12826_SI_001.PDF.

[300] A. Metecan, A. Cihanoğlu, S. Alsoy Altinkaya, A positively charged loose nanofiltration membrane fabricated through complexing of alginate and polyethyleneimine with metal ions on the polyamideimide support for dye desalination, Chemical Engineering Journal 416 (2021). https://doi.org/10.1016/j.cej.2021.128946.

[301] Y. Liu, J. Wang, Y. Wang, H. Zhu, X. Xu, T. Liu, Y. Hu, High-flux robust PSf-b-PEG nanofiltration membrane for the precise separation of dyes and salts, Chemical Engineering Journal 405 (2021). https://doi.org/10.1016/j.cej.2020.127051.

[302] X. Liang, P. Wang, J. Wang, Y. Zhang, W. Wu, J. Liu, B. Van der Bruggen, Zwitterionic functionalized MoS2 nanosheets for a novel composite membrane with effective salt/dye separation performance, J Memb Sci 573 (2019) 270–279. https://doi.org/10.1016/j.memsci.2018.12.015.

[303] L. Yu, Y. Zhang, H. Zhang, J. Liu, Development of a molecular separation membrane for efficient separation of low-molecular-weight organics and salts, Desalination 359 (2015) 176–185. https://doi.org/10.1016/j.desal.2014.12.044.

[304] J. Ding, H. Wu, P. Wu, Preparation of highly permeable loose nanofiltration membranes using sulfonated polyethylenimine for effective dye/salt fractionation, Chemical Engineering Journal 396 (2020). https://doi.org/10.1016/j.cej.2020.125199.

[305] J. Zhu, M. Tian, J. Hou, J. Wang, J. Lin, Y. Zhang, J. Liu, B. Van Der Bruggen, Surface zwitterionic functionalized graphene oxide for a novel loose nanofiltration membrane, J Mater Chem A Mater 4 (2016) 1980–1990. https://doi.org/10.1039/C5TA08024J.

[306] D. Yang, L. Gong, Q. Li, B. Fan, C. Ma, Y.C. He, Preparation of a biobased polyelectrolyte complex from chitosan and sodium carboxymethyl cellulose and its antibacterial characteristics, Int J Biol Macromol 227 (2023) 524–534. https://doi.org/10.1016/J.IJBIOMAC.2022.12.089.

[307] P.B. Kalahal, A.M. Sajjan, T.M. Yunus Khan, A.A. Rajhi, S. Achappa, N.R. Banapurmath, A. M, A.A. Duhduh, Novel Polyelectrolyte Complex Membranes Containing Carboxymethyl Cellulose–Gelatin for Pervaporation Dehydration of Azeotropic Bioethanol for Biofuel, Polymers (Basel) 14 (2022) 5114. https://doi.org/10.3390/POLYM14235114/S1.

[308] M. Dmitrenko, O. Mikhailovskaya, R. Dubovenko, A. Kuzminova, D. Myznikov, A. Mazur, K. Semenov, Y. Rusalev, A. Soldatov, S. Ermakov, A. Penkova, Pervaporation Membranes Based on Polyelectrolyte Complex of Sodium Alginate/Polyethyleneimine Modified with Graphene Oxide for Ethanol Dehydration, Polymers (Basel) 16 (2024). https://doi.org/10.3390/polym16091206.

[309] L.A.N. El-Din, A. El-Gendi, N. Ismail, K.A. Abed, A.I. Ahmed, Evaluation of cellulose acetate membrane with carbon nanotubes additives, Journal of Industrial and Engineering Chemistry 26 (2015) 259–264. https://doi.org/10.1016/j.jiec.2014.11.037.

[310] C. Bordes, V. Fréville, E. Ruffin, P. Marote, J.Y. Gauvrit, S. Briançon, P. Lantéri, Determination of poly(ε-caprolactone) solubility parameters: Application to solvent substitution in a microencapsulation process, Int J Pharm 383 (2010) 236–243. https://doi.org/10.1016/j.ijpharm.2009.09.023.

[311] J. Ruwoldt, M. Tanase-Opedal, K. Syverud, Ultraviolet Spectrophotometry of Lignin Revisited: Exploring Solvents with Low Harmfulness, Lignin Purity, Hansen Solubility Parameter, and Determination of Phenolic Hydroxyl Groups, ACS Omega 7 (2022) 46371–46383. https://doi.org/10.1021/acsomega.2c04982.

[312] W. Ding, Y. Tong, L. Shi, W. Li, Superhydrophilic PVDF Membrane Modified by Norepinephrine/Acrylic Acid via Self-Assembly for Efficient Separation of an Oil-in-Water Emulsion, Ind Eng Chem Res 61 (2022) 130–140. https://doi.org/10.1021/acs.iecr.1c03953.

[313] M. Shakiba, S.R. Nabavi, H. Emadi, M. Faraji, Development of a superhydrophilic nanofiber membrane for oil/water emulsion separation via modification of polyacrylonitrile/polyaniline composite, Polym Adv Technol 32 (2021) 1301–1316. https://doi.org/10.1002/pat.5178.

[314] Reactive Red 120 | C44H30Cl2N14O20S6 | CID 73264 - PubChem. https://pubchem.ncbi.nlm.nih.gov/compound/Reactive-Red-120 (accessed November 12, 2023).

[315] Reactive Black 5 | C26H21N5Na4O19S6 | CID 135442967 – PubChem. https://pubchem.ncbi.nlm.nih.gov/compound/Reactive-Black-5#section=Structures (accessed November 12, 2023).

[316] Methyl orange | C14H14N3NaO3S | CID 23673835 - PubChem. https://pubchem.ncbi.nlm.nih.gov/compound/Methyl-orange (accessed November 12, 2023).

Appendix A

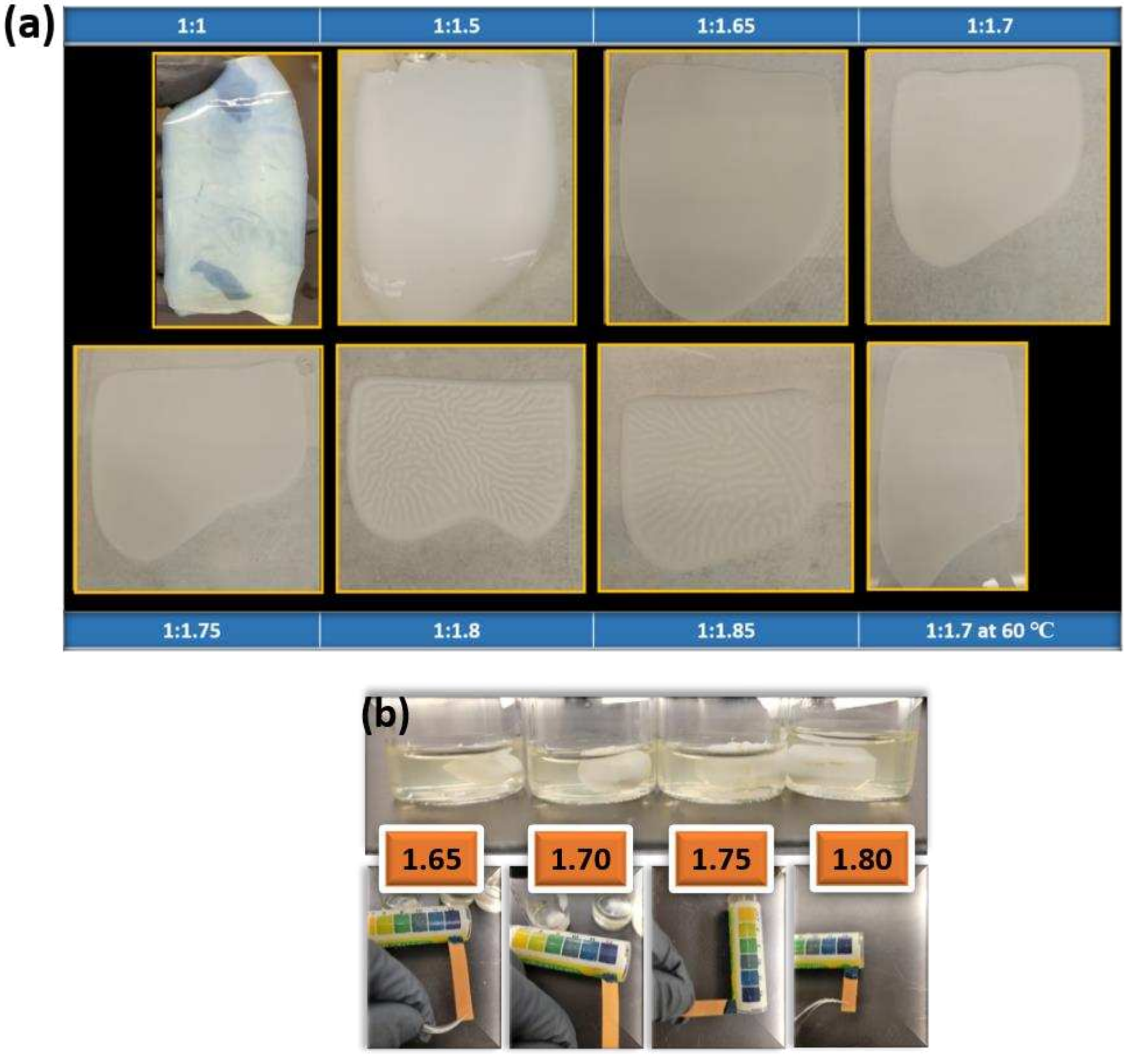

Figure A.S1. Photographs of (A) membranes prepared at different monomer ratios, and casting solution temperatures and (B) casting solutions and their pH at different monomer ratios.

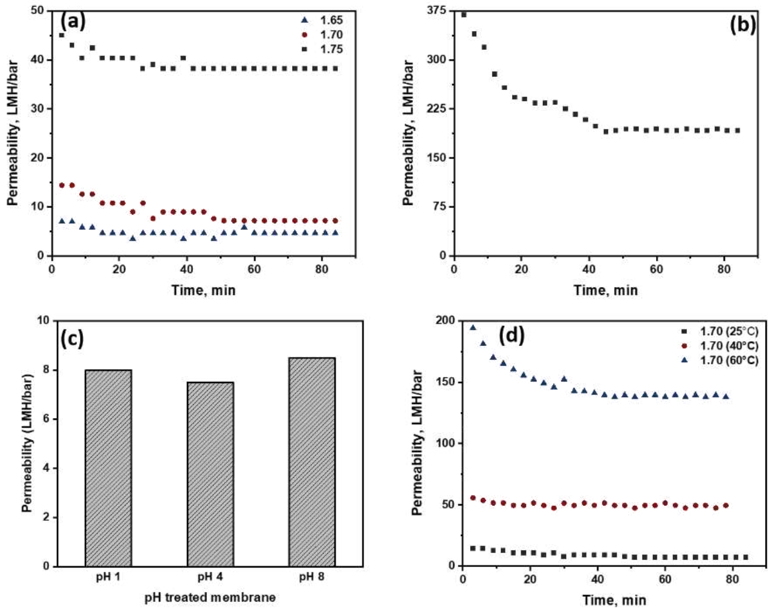

Figure A.S 2. (A) Pure water permeability vs time of membranes prepared at different monomer ratios (1:1.65, 1:1.70, and 1:1.75), (B) Pure water permeability vs time of membranes prepared at 1:1.80 monomer ratio, (C) Pure water permeability of membrane (1:1.70) after treated with pH 1, 4, and 8 for 7 days and (D) Pure water permeability vs time of membranes prepared from different casting solution temperatures (25 to 60°C)

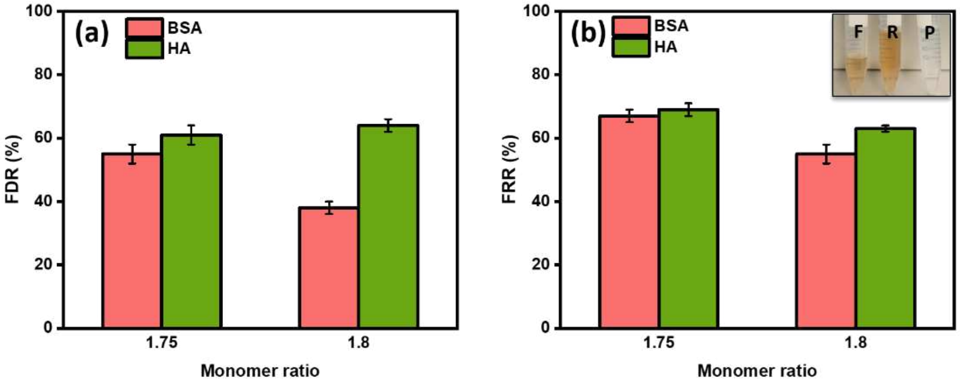

Figure A.S3. (A) Flux decline rate (FDR) and (B) Flux recovery rate (FRR) of membranes prepared at different monomer ratio (1:1.75 and 1:1.80) after filtering BSA and HA solution; Images of the feed (F), retentate (R) and permeate (P) of HA solution are shown in the inset.

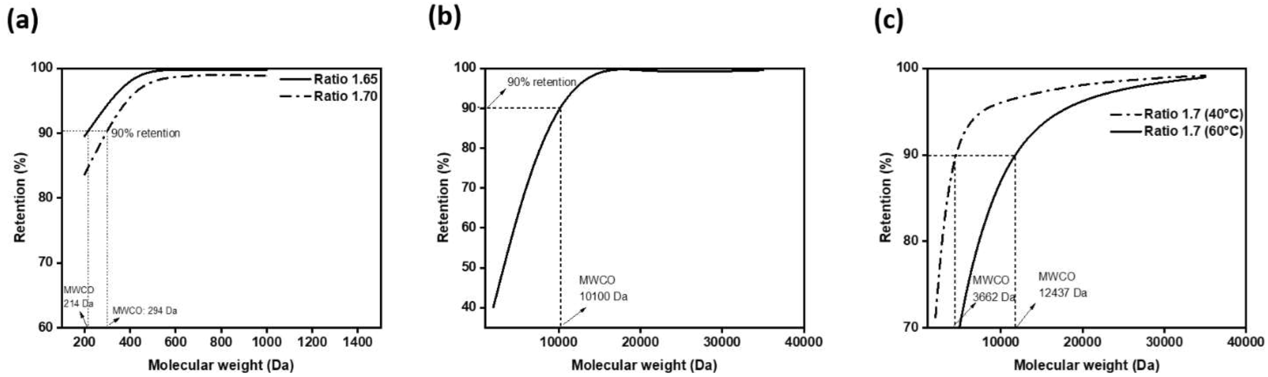

Figure A.S4. (a) Sieving curve to determine MWCO for membranes prepared at 1:1.65 and 1:1.70 monomer ratio (b) Sieving curve to determine MWCO for membranes prepared at 1:1.75 monomer ratio, (c) Sieving curve to determine MWCO for membranes prepared from different casting solution temperatures (25 to 60°C). Different MW of PEG, i.e., 0.2, 0.4, 0.6, and 1 kDa were used for nanofiltration membranes, and 0.2, 6, 10, 20, and 35 kDa were used for ultrafiltration membranes.

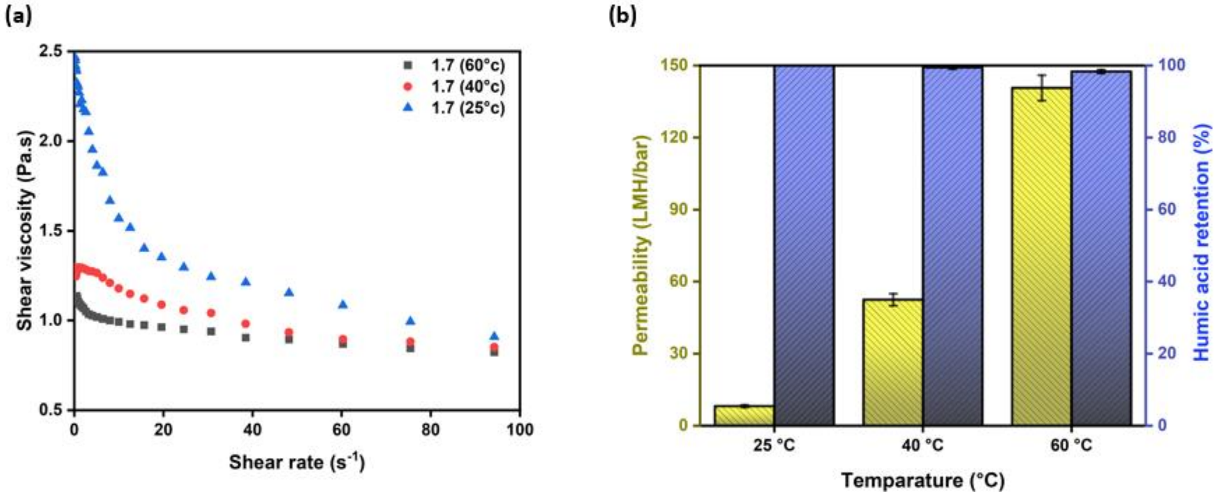

Figure A.S5. (a) Change of shear viscosity with the shear rate for membranes prepared from different casting solution temperatures (25 to 60°C), (b) Change of pure water permeability with time and HA retention results for membranes prepared from different casting solution temperatures (25 to 60°C)

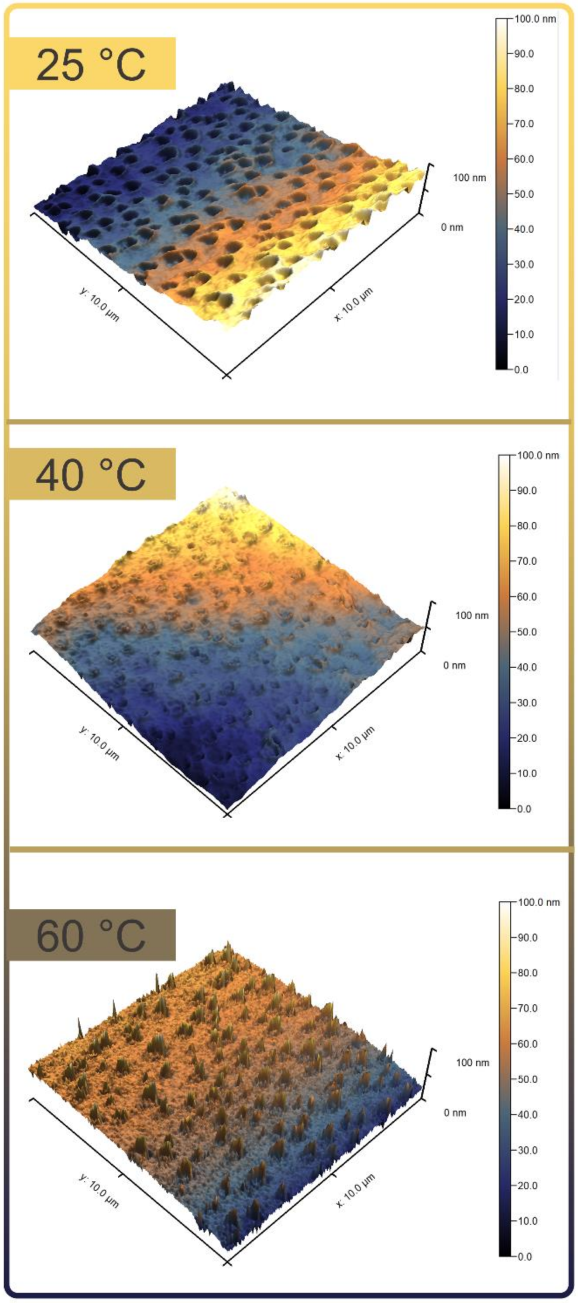

Figure A.S6. AFM images and surface roughness values of the membranes prepared at different temperatures of the casting solution. PSS-PEI at a ratio of 1:1.70 was used for preparing the casting solution.

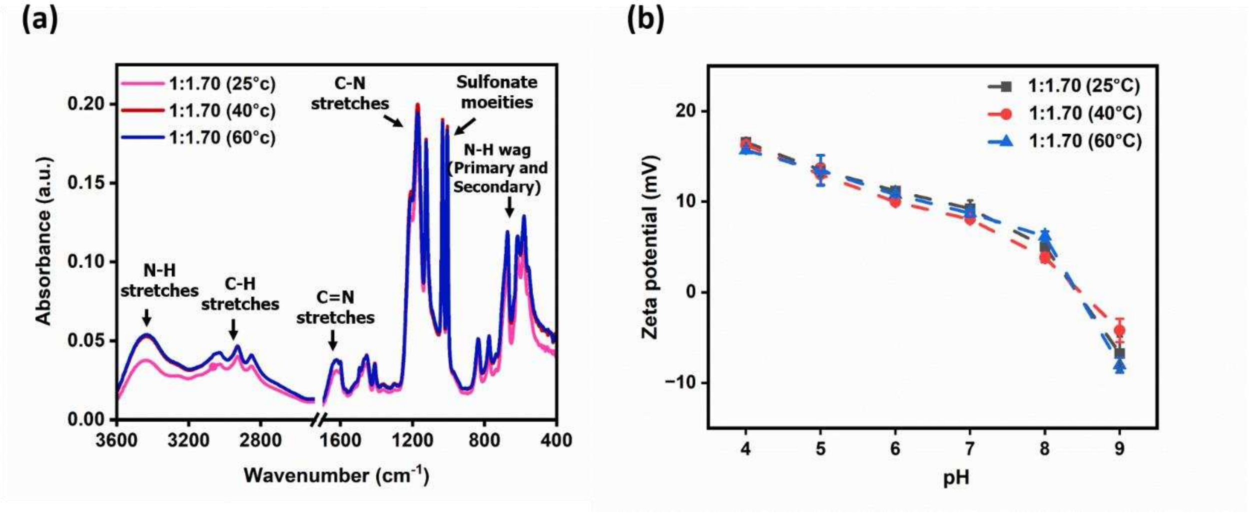

Figure A.S7. (a) FTIR images showing the chemical composition of membranesprepared from different casting solution temperatures (25 to 60°C), (b) Zeta potential vs pH of membranes prepared from different casting solution temperatures (25 to 60°C)

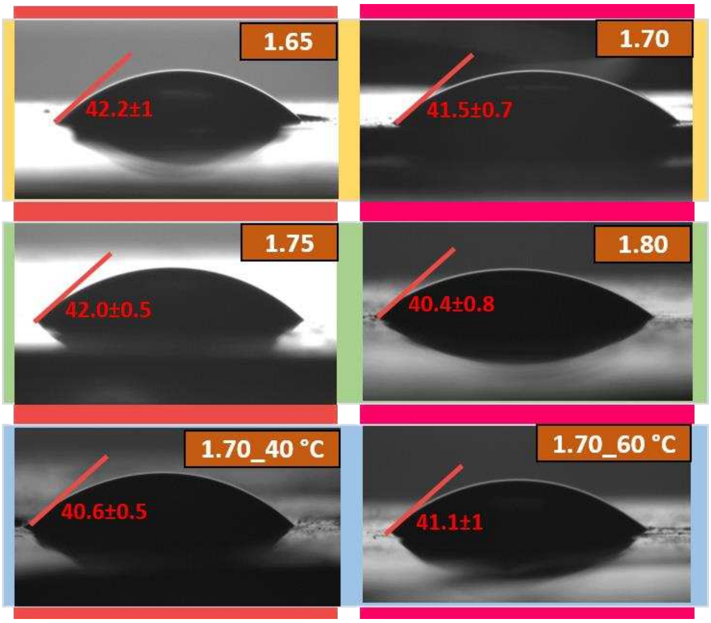

Figure A.S8. Contact angle images of membranes prepared from different monomer ratios (1.65 to 1.80) and casting solution temperatures (40 and 60°C).

Appendix B

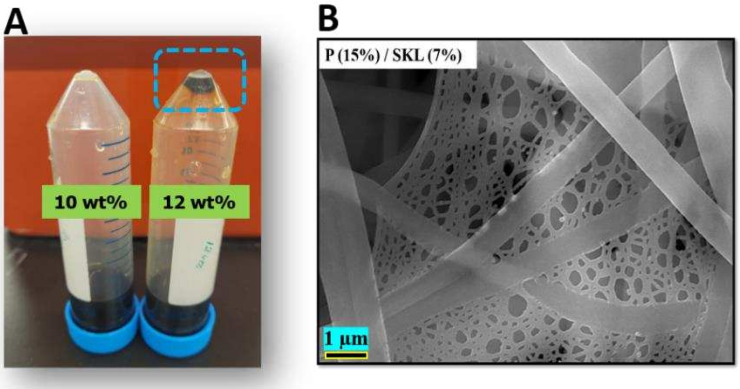

Figure B.S1. (A) SKL solution in Acetic acid at 10 wt% and 12 wt%. Some undissolved SKL can be noticed at 12 wt% (in rectangular box); (B) Nanonet structure in PCL (15 wt%) / SKL (7 wt%) electrospun membrane.

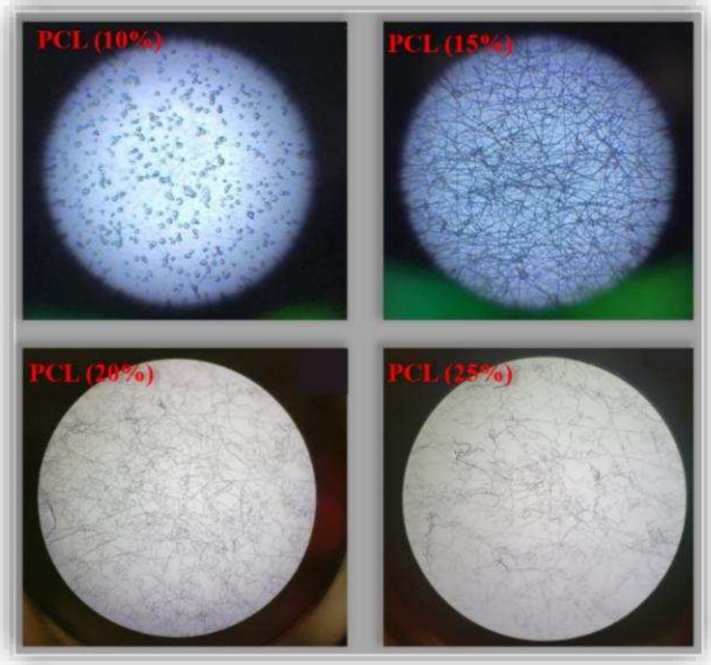

Figure B.S2. Optical images of the fibers formed from dope solutions at different concentrations of PCL, i.e., 10 wt%, 15 wt%, 20 wt%, and 25 wt% of PCL solution

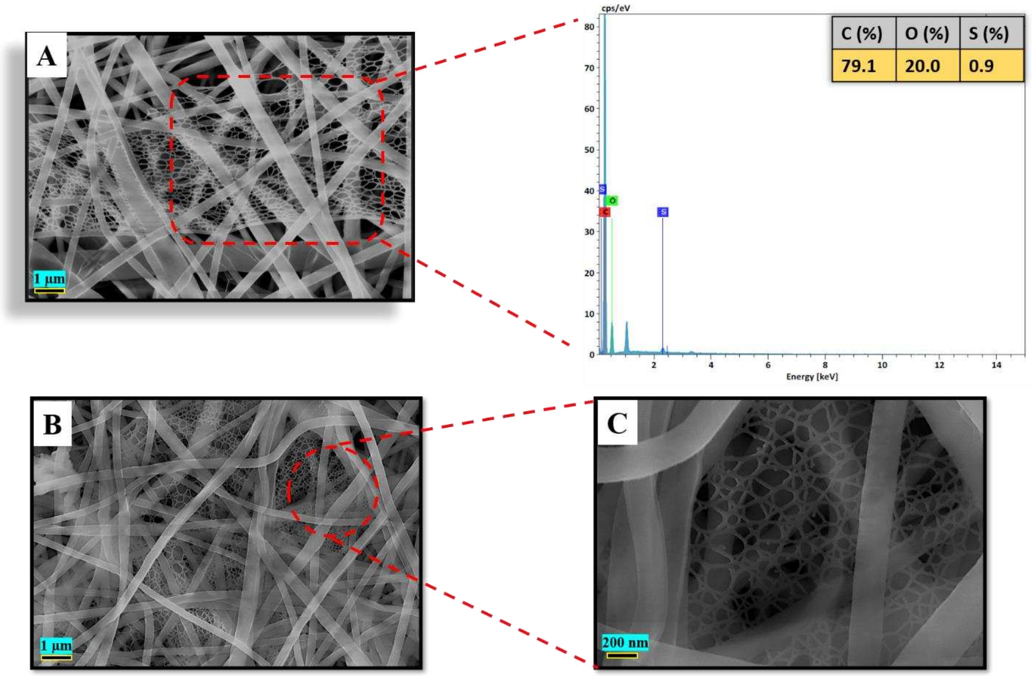

Figure B.S3. (A) Energy dispersive spectrum analysis of PCL/SKL electrospun membrane (L-10) obtained at 10 wt% SKL concentration. Fishnet-like nano webs were observed both on top and underneath the surface: (B) Fishnet-like nano webs underneath the surface, C) Zoomed image of the nano webs underneath the top surface

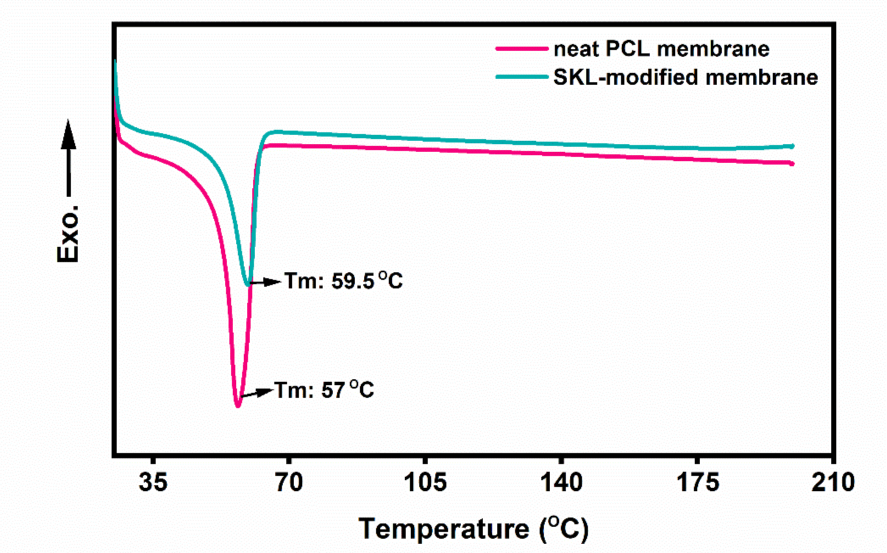

Figure B.S4. Differential scanning calorimetry curves of neat PCL and SKL-modified electrospun membrane (L-10) (second run)

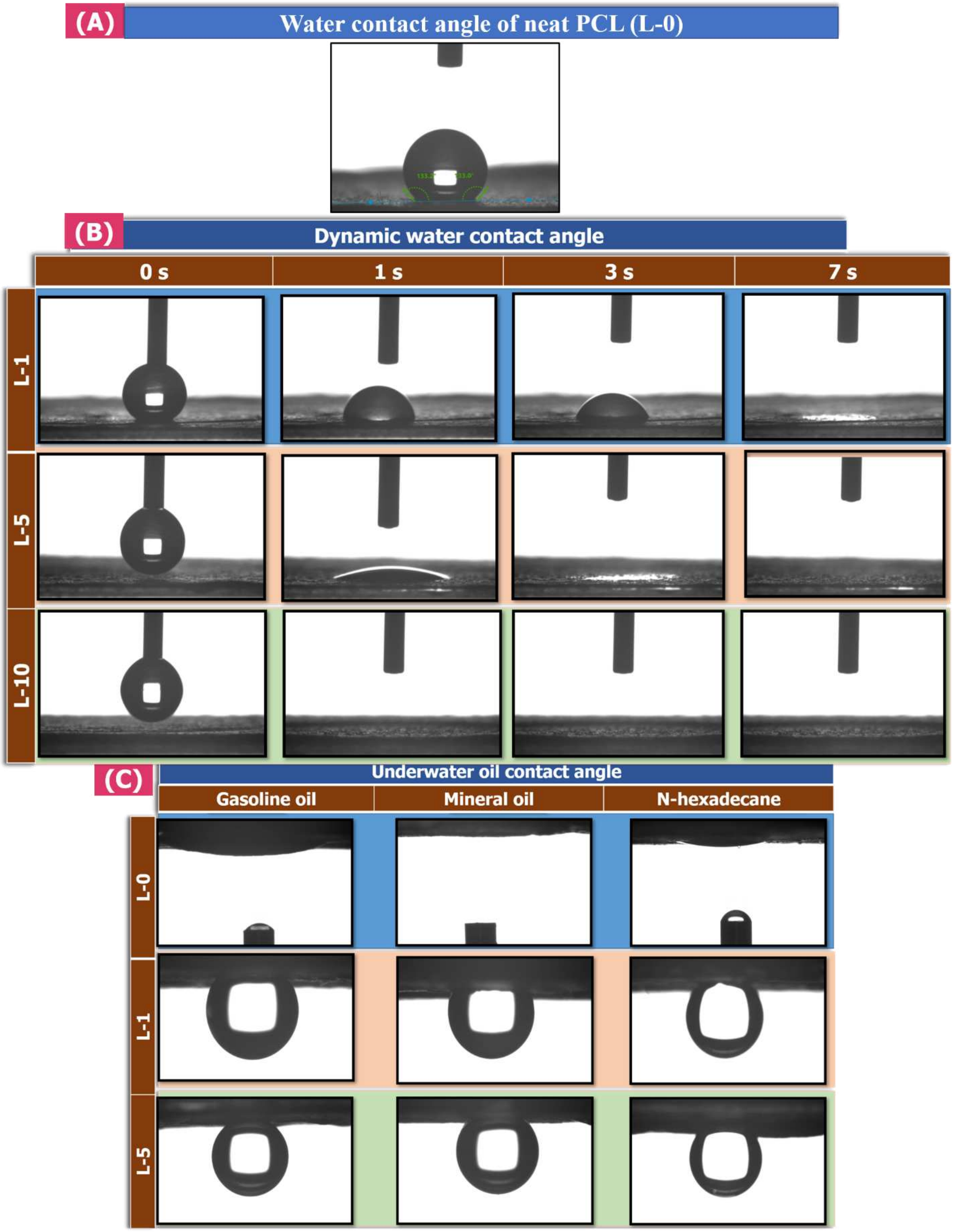

Figure B.S5. (A) Water contact angle of neat PCL (L-0), (B) Dynamic water contact angle of L-1, L-5, and L-10 electrospun membranes, and (C) Underwater oil contact angle of L-0, L-1, and L-5 membranes.

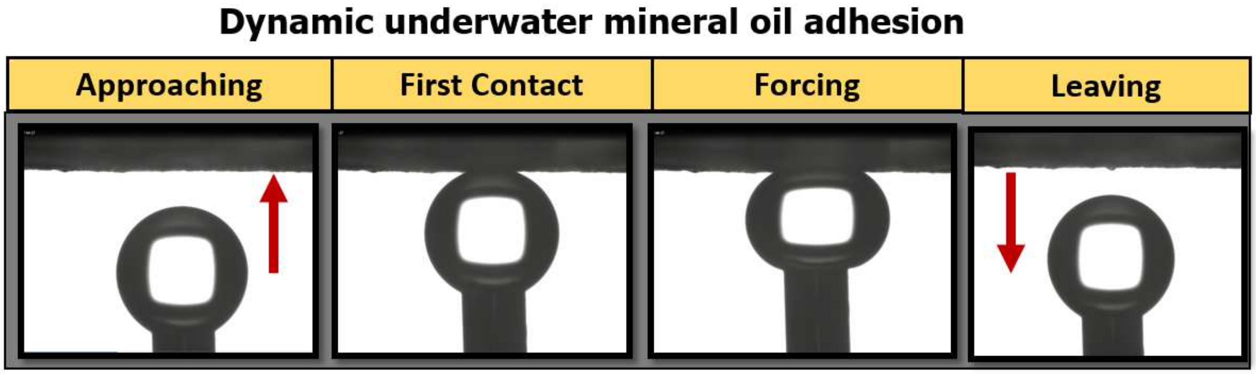

Figure B.S6. Dynamic underwater mineral oil contact angle of L-10 membrane after the cyclic test

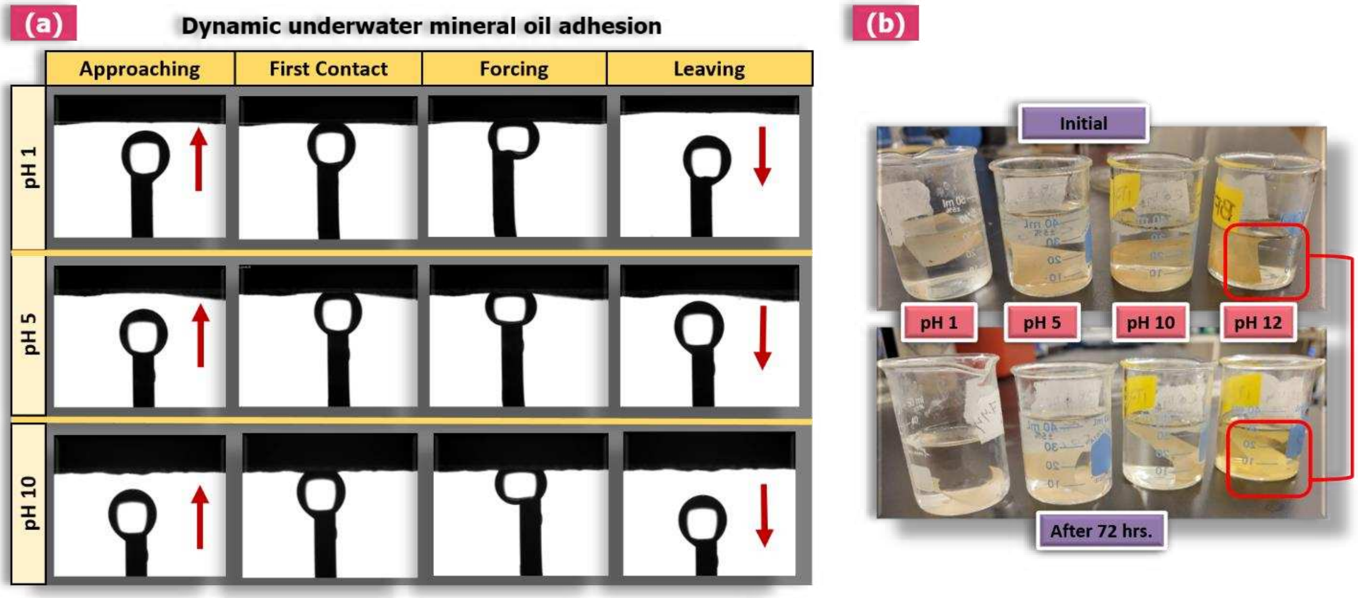

Figure B.S7. (a) Dynamic underwater mineral oil adhesion behavior of L-10 membraneafter pH stability test for 72 h, (b) L-10 membrane at different pH mediums, red rectangle shows the brownish solution after the stability test, indicating lignin leaching at pH 12. This sample at pH 12 was too fragile to handle, and hence could not be used for contact angle analysis.

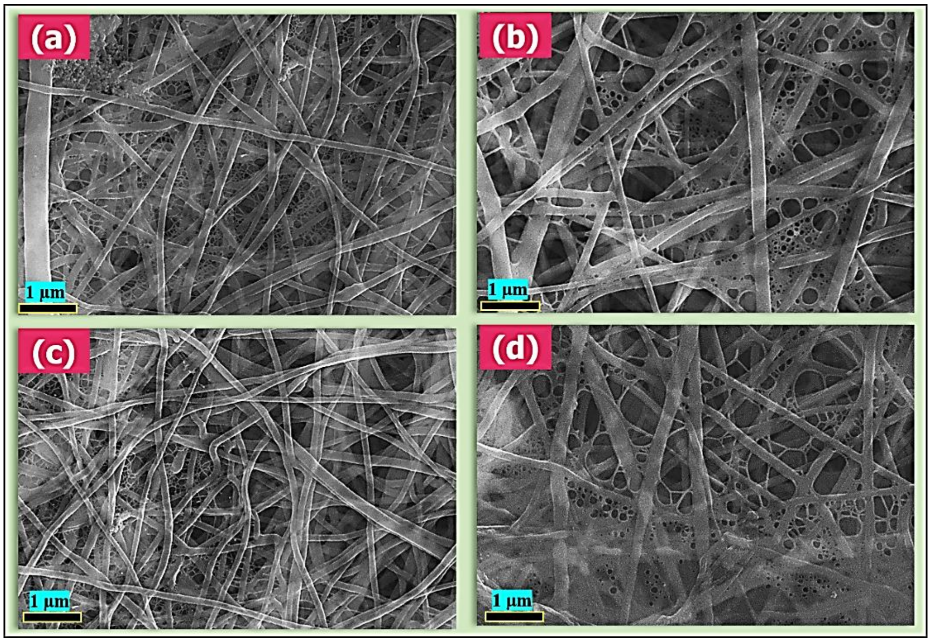

Figure B.S8. SEM images of L-10 electrospun membrane after long-term use and pH stability test (a) after 10 cycle test, (b) pH 1, (c) pH 5, and (d) pH 10. The pore sizes on the nanonet structure in the SKL-modified membranes were not uniform all over the membrane surface. In some parts, it contains tiny pores; in others, it may contain larger pores (as seen in Figure S8 for the electrospun membrane after the pH 10 stability test). To further clarify, the pore sizes of the nanonets in SKL-modified membranes after and before pH stability tests were estimated using Image-J software (at least for 100 nanonet pores). The nanonet pore size before the pH stability test was ~730 ± 234 nm, whereas after the pH stability test, pore sizes were ~683± 384 nm and ~637 ± 409 nm for membranes tested at pH1 and pH10, respectively. This indicates that the pore sizes were almost the same (within the range) before and after pH stability tests. It is worth noting that the nanonet pore sizes are smaller than the oil droplet sizes (1-4 µm). Moreover, as a proof of concept, the mineral oil/water separation test was performed for electrospun membranes (after the pH 10 stability test). The emulsion flux and mineral oil rejection were ~470 LMH and ~98.9%, respectively, which were similar to the membrane performance before the pH stability test.

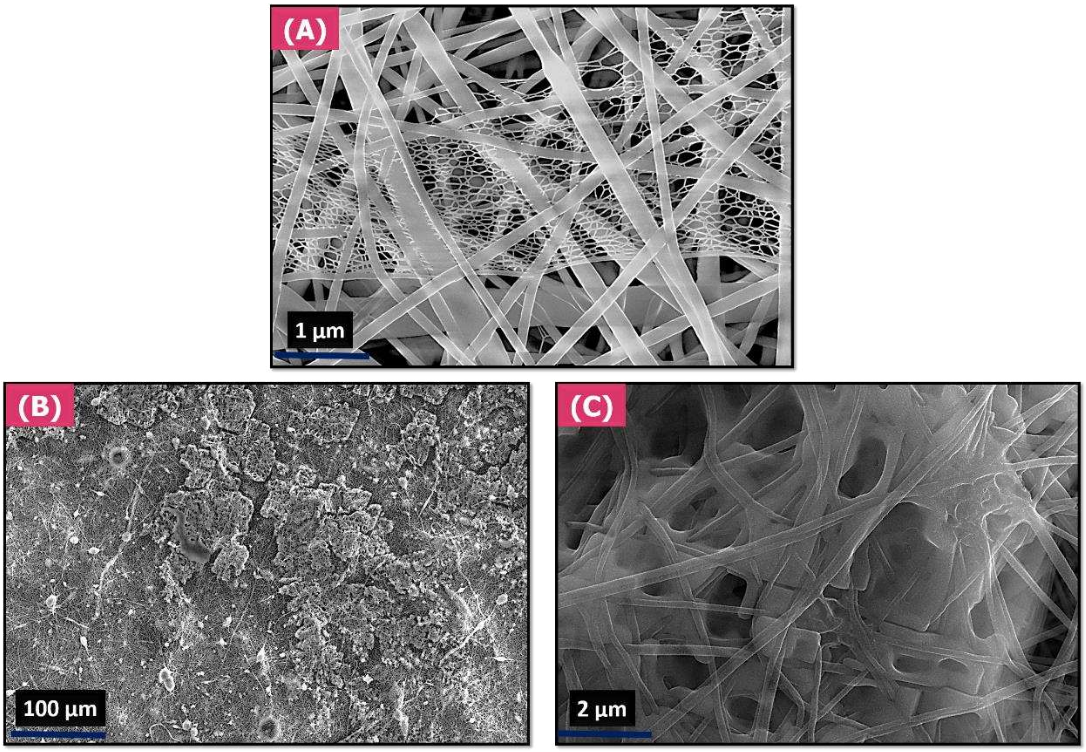

Figure B.S9. SEM images of L-10 electrospun membrane before (A) and after (B) the soil burial test for 2 months. The SEM image (C) shows the magnified image of the membrane after the burial test.

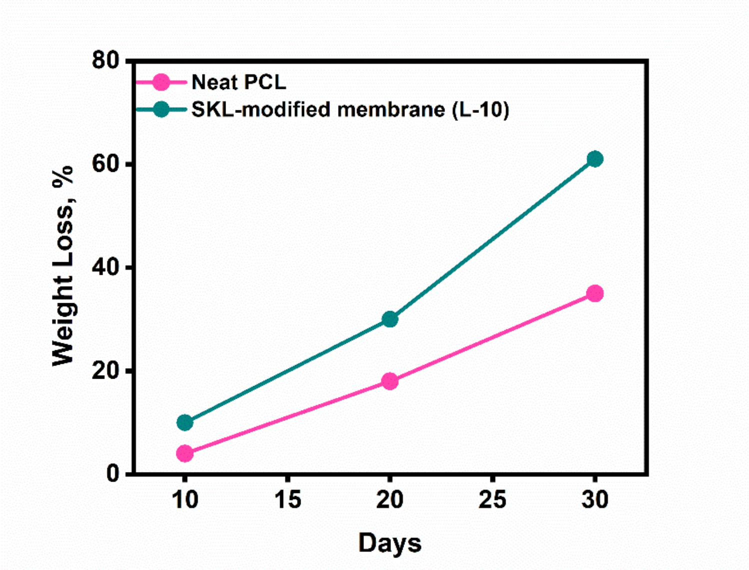

Figure B.S10. Weight loss of neat PCL and SKL-modified L-10 electrospun membranesduring soil burial test for one month

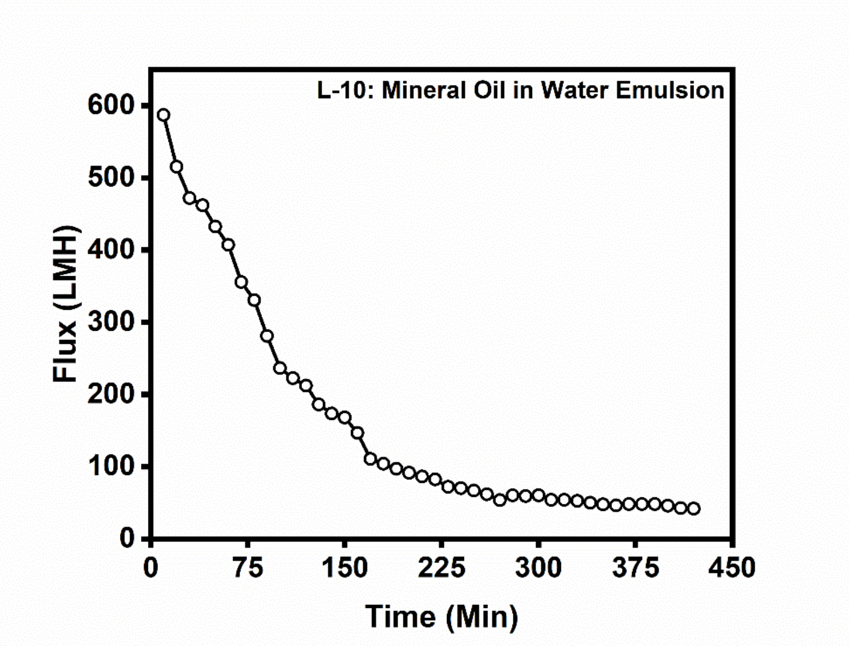

Figure B.S11. Gravity-driven mineral oil in water emulsion filtration using SKL-modified L-10 electrospun membrane. The oil/water emulsion filtration experiment was performed for 7 hrs.

Table B.S1. Details of the composition and electrospinning operationparameters used for PCL composition optimization.

PCL (wt%)	Glacial acetic acid (wt%)	Electrospinning parameter			Result
		Voltage (kV)	Distance (cm)	Flowrate (mL/h)	
10	90	18	18	1	Small droplets; Fiber starts forming
15	85	18	18	1	Smooth, uniform, and interconnected fiber formation
20	80	18	18	1	Less fiber formation; highly viscous solution
25	75	18	18	1	Less fiber formation; highly viscous solution

Table B.S2. HSP values for PCL, SKL, and AA.

Polymer/Solvent	δ_D	δ_P	δ_H	δ, calculated	Ref
PCL	17.7	6.2	7.8	20.31181922	[310]
SKL	17.6	2.8	12.6	21.82567296	[311]
Glacial AA	14.5	8	13.5	21.36586062	[310]

The Hansen solubility parameter (HSP) is a useful tool for evaluating the compatibility between two materials [32,33]. The HSP method involves assigning three parameters to each molecule, which quantitatively represent different aspects of bonding: the polar (atomic) bonding (δ_P), the permanent dipole-permanent dipole (molecular) bonding (δ_D), and the hydrogen (molecular) bonding (δ_H). The total parameter, δ, is then calculated as follows:[32,33]

$$\delta^2 = \delta_D{}^2 + \delta_P{}^2 + \delta_H{}^2$$

The solubility parameters are typically expressed in $\mathrm{MPa}^{½}$ units. The smaller the difference between two polymers δ, the higher the likelihood of compatibility between them. When the δ values of two materials are similar, it suggests that their solubility parameters are closely matched, making them more likely to form a compatible blend or solution. The HSP distance between two molecules, conventionally called R_a, can also be utilized to assess the similarity between two molecules as follows:

$$R_a{}^2 = 4(\delta_{D1}-\delta_{D2})^2 + (\delta_{P1}-\delta_{P2})^2 + (\delta_{H1}-\delta_{H2})^2$$

The Hansen solubility parameter δ for PCL, SKL, and glacial AA is presented in **Table B.S2**. Based on these parameters, the R_a of PCL and SKL in glacial AA are measured to be 8.75 and 8.14, respectively. The calculations indicate a very small difference in δ values between PCL and SKL, confirming their compatibility. This suggests that the polymers will likely form a compatible blend or solution due to their closely matched solubility parameters. Additionally, based on the R_a values, glacial AA appears to be an excellent solvent for dissolving both polymers.

Table B.S3. ICP-OES results after the leaching experiment

Days	Sulfur concentration, mg/L	Leaching rate, (mg/m^2.h)
7	0.004	0.0023
14	0.001	0.0005
21	0	0

Table B.S4. Comparison of oil/water emulsion separation performanceof various superhydrophilic membranes reported in the literature and this work.

Membrane	**Fabrication method**	**Modification**	**Oil/water emulsion**	**Transmembrane pressure**	**Water flux (LMH)**	**Oil/water emulsion flux (LMH)**	**Separation efficiency, %**	**FRR, %**	**Reference**
P(NIPAAm-co-NMA)/ChNWs	Electrospinning	Crosslinking	Toluene/water	0.3 bar	--	1100-1300	>99.5	--	[202]
PAN/Silica	Electrospinning	Electrospraying	Hexane/water	Gravity	--	1120	>99	--	[210]
CS-TPP@PDA@nylon	Commercial Nylon	Dipcoating	Diesel/water	Vacuum	--	291.3	97.5-99.94	89	[243]
PVDF-g-PNE	Commercial PVDF	Surface modification/grafting	Edible oil/water	0.1 bar	3200	734.8	99.21	87.82	[312]
PAI	Phase inversion	Surface modification	Diesel oil/water	Gravity	440	420	>99	100	[242]
PCL/Chitosan	Electrospinning	Blending	Hexane/water	Gravity	2609	627	99.9	--	[224]
PAN/PANI	Electrospinning	Blending	Toluene/water	0.5 bar	--	2280	98	--	[313]
PAN/CNC	Electrospinning	Alkaline treatment	Diesel/water	Gravity	2186	724	99.5	>90	[233]
PCL/SKL	Electrospinning	Blending	Gasoline/water, n-hexadecane/water, mineral oil/water	Gravity	800-900	170-480	~99	>99	This work

Appendix C

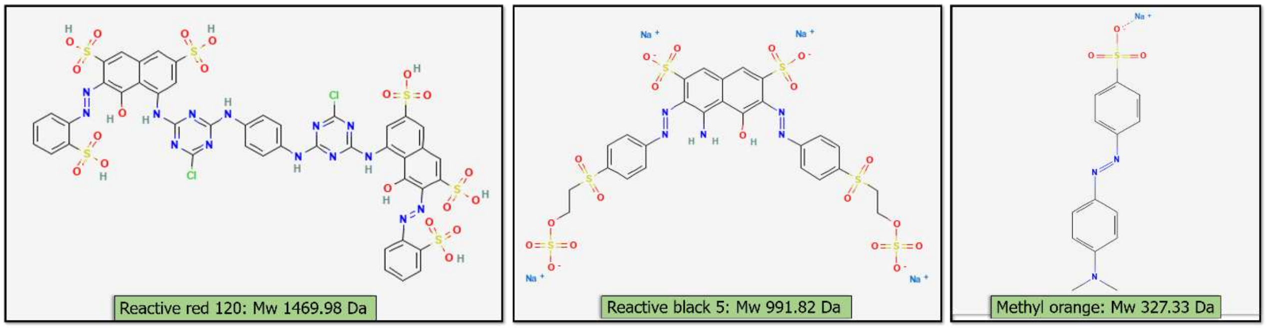

Figure C.S1. Molecular structure of anionic dyes: Reactive red 120[314], Reactive black[315], and Methyl orange [316].

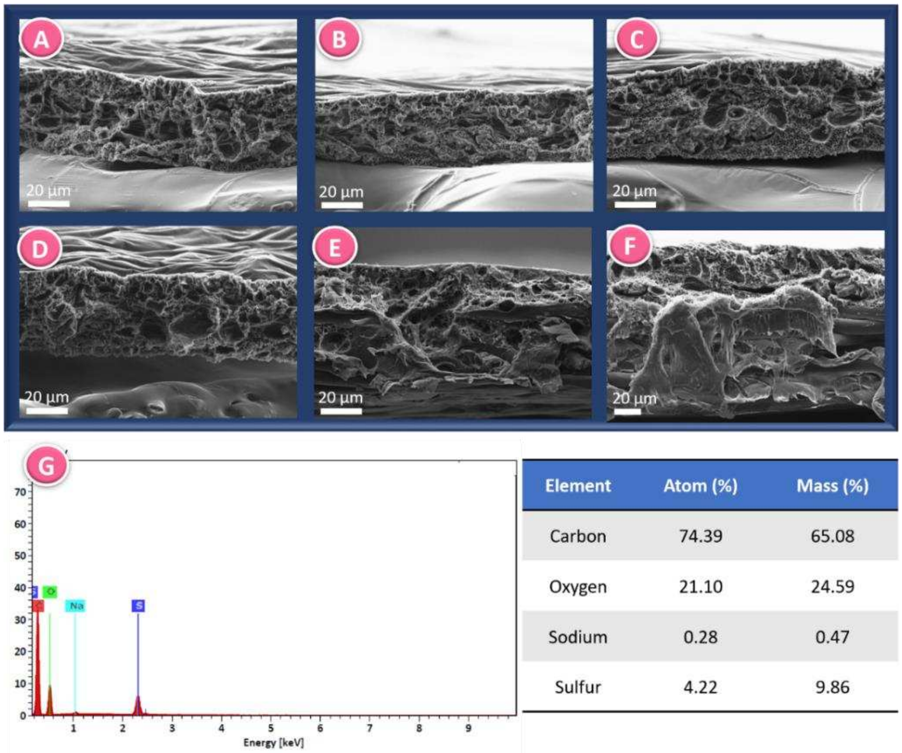

Element	Atom (%)	Mass (%)
Carbon	74.39	65.08
Oxygen	21.10	24.59
Sodium	0.28	0.47
Sulfur	4.22	9.86

Figure C.S2. Cross-section SEM images of PCL/SKL membranes: M1 (A), M2 (B), M3 (C), M4 (D); and cross-section of M3 membrane (E, F) with support showing formation of membrane inside the non-woven polyester support which favors strong attachment of the PCL/SKL membrane with the support.

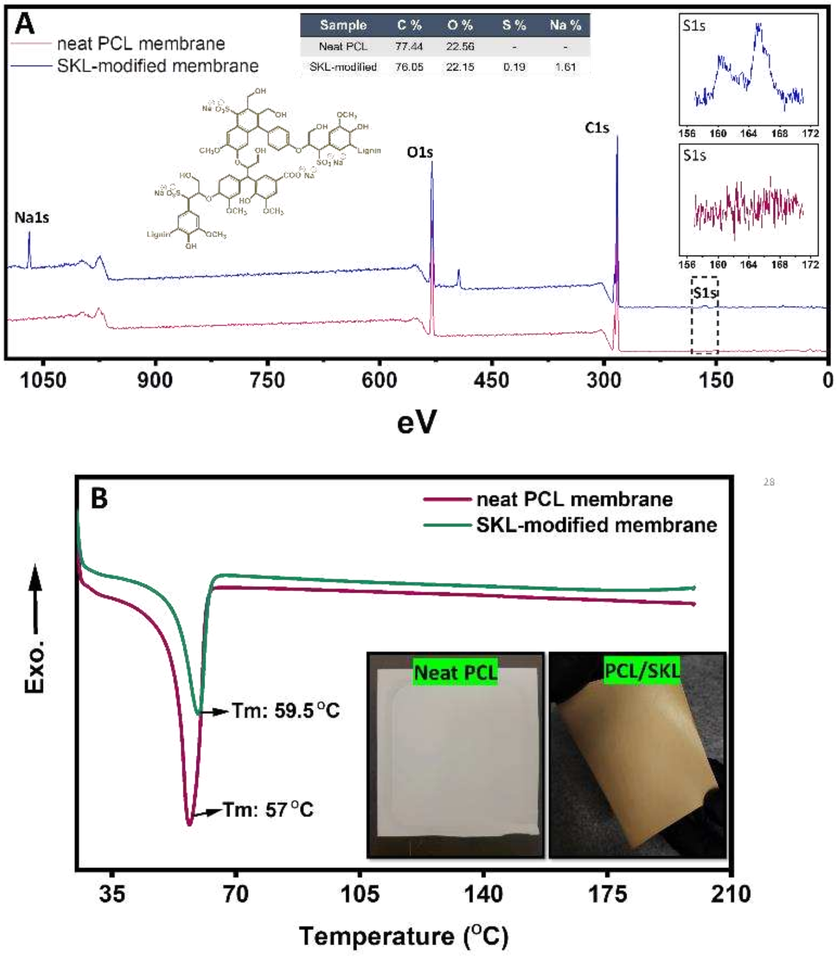

Figure C.S3. (A)XPS survey spectra of neat PCL and SKL-modified membrane (M3); the elemental composition of the membrane is provided in the embedded table; the zoomed image of S1s spectra is also shown inside the figure. (B) Differential scanning calorimetry of neat PCL and SKL-modified membrane; digital images of neat PCL and SKL-modified membrane are shown in the inset.

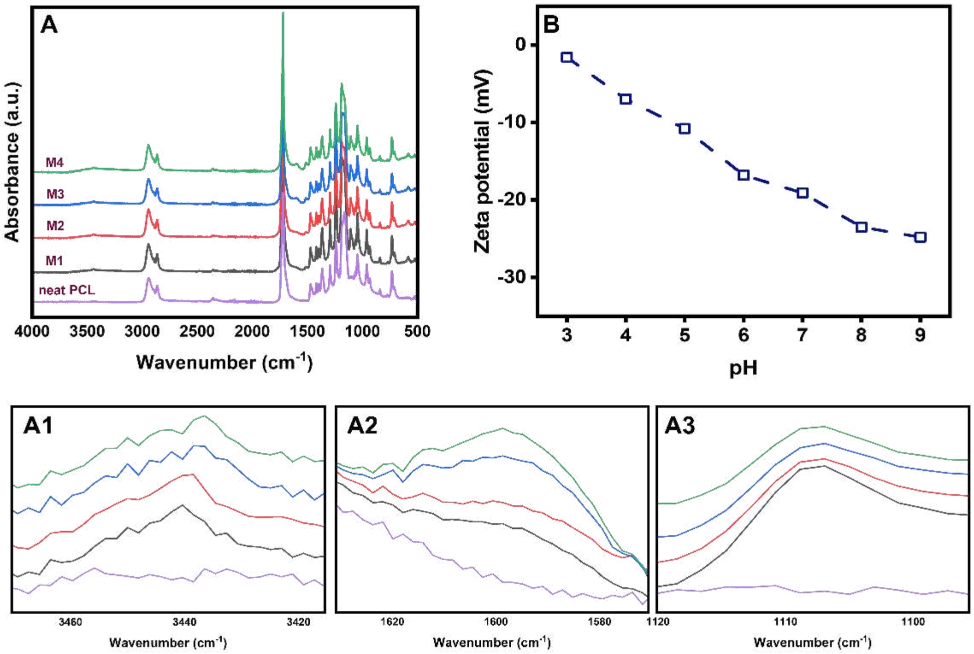

Figure C.S4. (A) FTIR spectra of neat PCL and SKL-modified membranes; (A1-A3) magnified FTIR spectra at different wavelengths, i.e., from 3000 to 3500 cm^{-1}, 1580-1620 cm^{-1}, and 1100-1120 cm^{-1}, clearly showing the effect of SKL inclusion in PCL matrix; (B) Zeta potential values of neat PCL membrane.

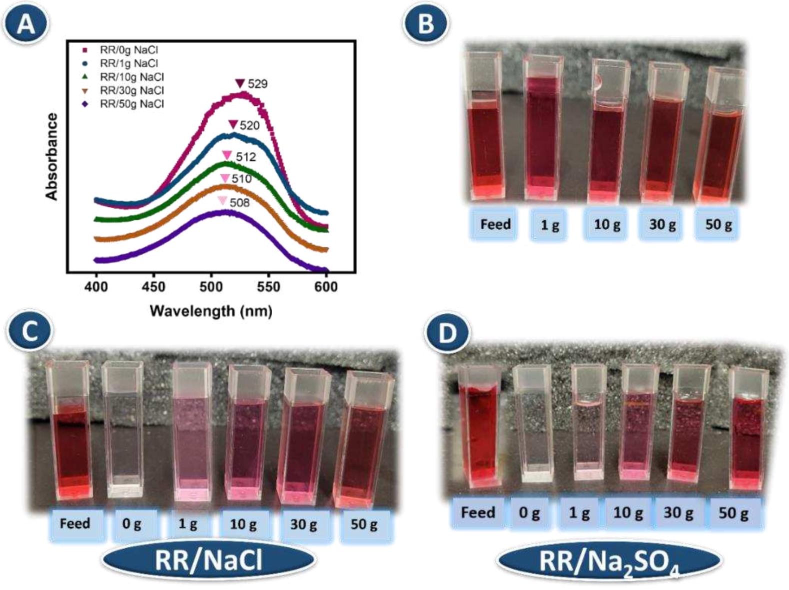

Figure C.S5. (A) UV-vis spectra for RR feed solutions with different amount of NaCl salt (0-50 g/L); (B) digital images of RR feed solution at different NaCl concentrations (1-50 g/L); digital images of RR feed solution and permeate after separating different RR/salt concentrations through membrane: (C) RR/NaCl mixture, (D) RR/Na_2SO_4 mixture.

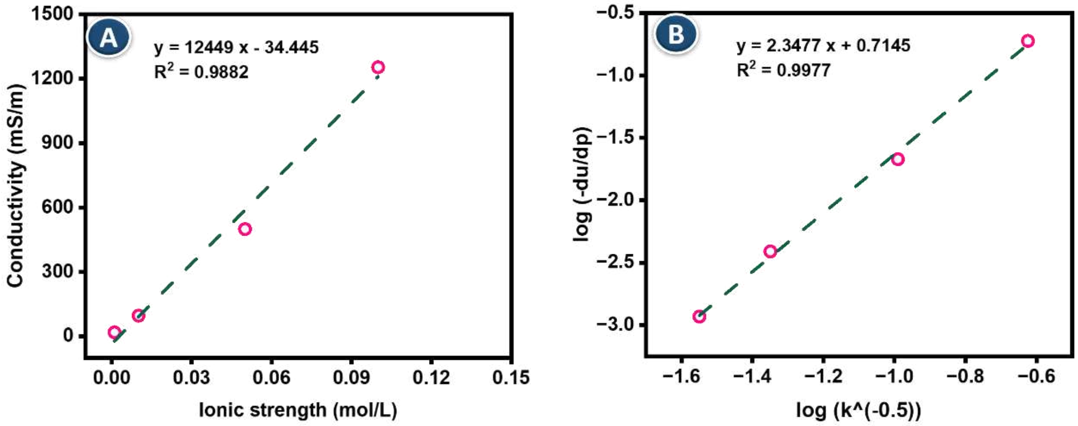

Figure C.S6. (A) conductivity vs ionic strength calibration curve, (B) plot of streaming potential coefficient (-dU/dP) vs conductivity ($k^{-1/2}$) in log-log scale.

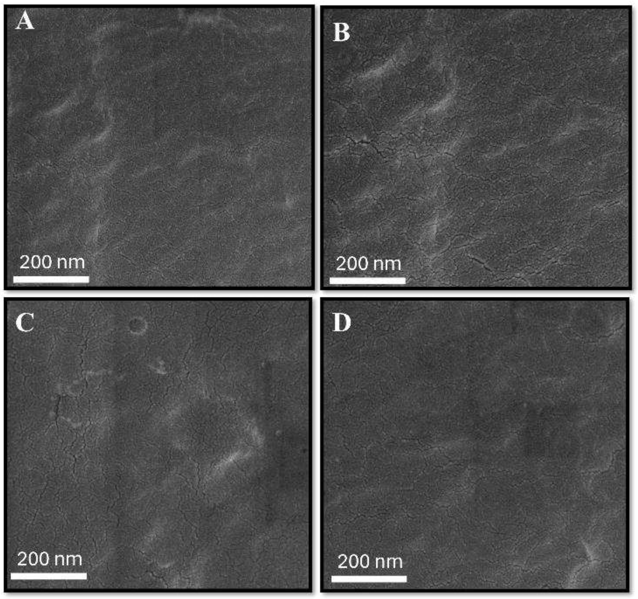

Figure C.S7. SEM images of M3 membrane (A) before fouling test, (B) after dye/salt mixture filtration, (C) after BSA filtration, and (D) after Humic acid filtration tests.

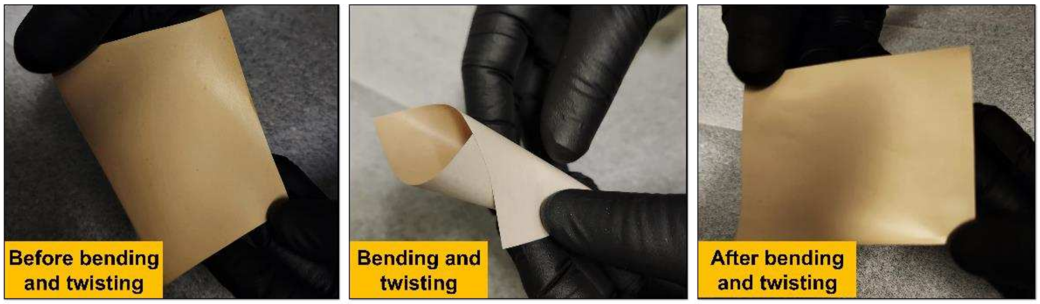

Figure C.S8. Digital images of membrane before and after bending and twisting.

Table C.S1.HSP values for PCL, SKL, and AA.

Polymer/Solvent	**δ_D**	**δ_P**	**δ_H**	**δ, calculated**	**Ref**
PCL	17.7	6.2	7.8	20.31181922	[310]
SKL	17.6	2.8	12.6	21.82567296	[311]
Glacial AA	14.5	8	13.5	21.36586062	[310][326]

Table C.S2. Ionic strength, charge density and streaming potential values

Ionic strength	du/dp (V/Pa)	Viscosity (PaS)	Electrolyte conductivity, mS/m	Zeta potential, mV	Debye length, nm	Charge density, C/m^2
0.001	-1.89E-06	0.000872018	17.71	-42.32	9.62	-3.03E-03
0.01	-2.43E-07	0.000889752	95.64	-29.81	3.05	-6.77E-03
0.05	-3.99E-08	0.000849124	499.26	-24.60	1.35	-12.44E-03
0.1	-1.1711E-08	0.000854027	1253.82	-18.23	0.96	-13.05E-03